Thesis for the Master's degree in chemistry

Marius Westgård Erichsen

The methanol-to-hydrocarbons reaction: Influence of acid strength on the mechanism of olefin formation

60 study points

DEPARTMENT OF CHEMISTRY
Faculty of mathematics and natural sciences
UNIVERSITY OF OSLO 05/2010

Acknowledgements

This thesis is a result of experimental work performed at the Department of Chemistry, University of Oslo, during the period from August 2008 to May 2010. Supervisors during the project have been Prof. Unni Olsbye, Assoc. Prof. Stian Svelle, Dr. Merete Hellner Nilsen and Prof. Karl-Petter Lillerud. I would like to offer my sincerest thanks to them all for allowing me to perform and complete the work presented herein, and for all their help along the way. Special thanks are due to my main supervisor Unni Olsbye, whose inspirational guidance during the past two years has been invaluable.

The whole of the catalysis group is also acknowledged for providing a friendly and stimulating environment for learning. I am especially grateful to those who have helped with proof-reading and quality control of this thesis, namely Francesca, Anlaug and Shewangizaw. Dr. Stig Rune Sellevåg, Dr. Sandro Usseglio Nanot and Assoc. Prof. Morten Bjørgen (NTNU) are acknowledged for their help on FTIR spectroscopy, while both Dr. Rune Wendelbo (Abalonyx AS) and Prof. Em. Stein Kolboe also deserves thanks for valuable help along the way. In addition, Haldor Topsøe AS and Dr. Pablo Beato are acknowledged for performing NH_3 TPD measurements.

Lastly, I would like to thank my high school teacher Terry Baine. If not for him, it is unlikely that I would ever have considered studying chemistry.

Abstract

The methanol-to-hydrocarbons (MTH) reaction is a flexible alternative step in the upgrading of natural gas, coal or biomass. By tuning the catalyst and process conditions, methanol can be converted into a variety of hydrocarbon products including gasoline and polymer-grade olefins. While the reaction has been known for many years, reaction mechanisms are still not fully understood. Most previous mechanistic studies have been performed on aluminosilicate zeolites, so the aim of the present work was to investigate the effect of a less acidic catalyst on the mechanisms of olefin formation. For this reason, the silicoaluminophosphate H-SAPO-5 was synthesised, characterised and tested for methanol conversion.

During the synthetic effort to produce H-SAPO-5 samples suitable for mechanistic studies it was found that samples with plate-like morphology could be obtained after a short crystallisation time from mixtures containing triethylamine. While the competing growth of other zeolitic phases proved a challenge, several parameters were investigated and conditions favouring growth of the desired phase was found. Characterisation of synthesised materials revealed numerous structural defects, but also that the materials possessed similar acidic strength to the commercial silicoaluminophosphate catalyst H-SAPO-34.

Catalytic studies revealed that MTH over H-SAPO-5 yields primarily light olefins, especially propene and isobutene. A series of catalytic tests at different conditions and use of both labelled methanol and co-feeding of benzene and methanol revealed that methylbenzene intermediates are not as important as what has been observed in aluminosilicates such as H-Beta. While methylbenzenes were found to be active for olefin formation, it was found that isobutene and larger olefins were primarily generated via other intermediates. A mechanism where olefins are produced both by a cycle of successive methylation and cracking, where 2,2,3-trimethylpentene is a key intermediate, and from methylbenzenes was thus proposed. The decreased importance of methylbenzenes may be caused by the less acidic H-SAPO-5 not catalysing hydride transfers as efficiently as aluminosilicate catalysts. The mechanistic proposal shares many similarities with observations in zeolitic catalysts during low-temperature processes and when steric effects hinder the formation of methylbenzenes.

List of abbreviations used in this thesis

*BEA	IZA code for the framework of zeolite Beta
a. u.	Arbitrary unit
AEI	IZA code for the framework of $AlPO_4$-18 and SAPO-18
AFI	IZA code for the framework of $AlPO_4$-5 and SAPO-5
$AlPO_4$	Aluminophosphate (zeolitic material composed of Al, P and O)
B/H	A sample synthesised and used in this work (Barrel-shaped/high-silica)
B/L	A sample synthesised and used in this work (Barrel-shaped/low-silica)
BET	Braunauer-Emmet-Teller
CHA	IZA code for the framework of Chabazite, SSZ-13 and SAPO-34
DME	Dimethyl ether
EDS	Energy dispersive x-ray spectroscopy
FID	Flame ionisation detector
FTIR	Fourier transform infrared spectroscopy
GC	Gas chromatography
GC-MS	Gas chromatography with MS detector
Hexa-MB	Hexamethylbenzene
HMB	Hexamethylbenzene
HMMC	1,2,3,3,4,5-hexamethyl-6-methylene-1,4-cyclohexadiene
HTI	Hydrogen transfer index
IUPAC	International Union of Pure and Applied Chemistry
MeAPO	Metal-aluminophophate (a metal containing $AlPO_4$ material)
MeAPSO	Metal-silicoaluminophophate (a metal containing SAPO material)
MeOH	Methanol

MFI	IZA code for the framework of ZSM-5
MS	Mass spectrometry
MTG	Methanol-to-gasoline
MTH	Methanol-to-hydrocarbons
MTO	Methanol-to-olefins
MTP	Methanol-to-propene
MWE##(#)	Denotes the number of an experiment performed in this work
NMR	Nuclear Magnetic Resonance
P/H	A sample synthesised and used in this work (plate-like/high-silica)
P/L	A sample synthesised and used in this work (plate-like/low-silica)
Penta-MB	Pentamethylbenzene
PMB	Pentamethylbenzene
SAPO	Silicoaluminophosphate (zeolitic material consisting of Si, Al, P and O)
SC	A sample synthesised and used in this work (small crystals)
SDA	Structure directing agent
SEM	Scanning electron microscopy
TEA	Triethylamine
TGA	Thermogravimetric analysis
TIGAS	Topsøe integrated gasoline synthesis
TOS	Time on stream
TPA	Tri-n-propylamine
TPD	Temperature-programmed desorption
WHSV	Weight hourly space velocity (often referred to simply as space velocity)
XRD	X-ray diffraction

Table of contents

1 Introduction

As world oil reserves are limited and the oil prices are increasing, interest in the utilisation of other feedstocks, such as natural gas or biomass, for production of chemicals usually produced from oil is increasing. The mounting environmental concerns of recent years are also leading to increased interest in cleaner processes for production of base chemicals and gasoline. In addition to this, world demand for polyolefins is expected to grow in the future, thus further increasing demand for ethene and propene. Supply of these base chemicals is mostly provided today from steam cracking of naphtha and fluid catalytic cracking (FCC) processes. However, especially for propene, more dedicated processes for their production is expected to be required to meet future demands.[1]

Catalytic conversion of methanol over acid catalysts is a process that is potentially able to contribute to the supply of both gasoline and light olefins. This process, known collectively as methanol-to-hydrocarbons (MTH), can be tuned for production of different hydrocarbon products by varying process conditions and/or catalyst used. Production of methanol is already well known and can be achieved, via synthesis gas, from a variety of feedstocks including natural gas, biomass and coal. It has even been suggested that methanol is a more viable choice than hydrogen for energy storage in the future[2]. MTH might well become an important and flexible contribution to world hydrocarbon demand, especially in an economy where methanol plays an important part. Unfortunately, the reaction mechanisms for the process are not fully understood.

The aim of this work has been to provide insight into how (or if) the acid strength of the catalyst used affects reaction mechanism. For this purpose a material called H-SAPO-5 was synthesised, characterised and used in catalytic tests of methanol conversion. While this material is not commercially attractive as an MTH catalyst, its acid strength is not very different from the commercial catalyst H-SAPO-34. The relatively open and simple structure of H-SAPO-5 should make it viable as a model catalyst in the reaction and allows co-feeding of large aromatic intermediates. Added to this, its structure is somewhat similar to another structure of stronger acidity often used in mechanistic studies of the reaction (H-Beta).

While striving towards this end several obstacles were encountered, leading to less time for actual mechanistic studies. The synthesis of a suitable catalyst sample proved difficult and characterisation of synthesised materials also revealed the material to be more complex than originally assumed. On top of this, problems with reproducibility were encountered during the catalytic testing. While all these problems were solved in their turn, the end result is a thesis where catalytic testing and mechanistic studies only constitute part of the total work. Due to this, it seemed reasonable to divide it into several (more or less) independent parts. Part I deals with the synthesis of a suitable sample of H-SAPO-5, while part III comprises all catalytic studies performed. Part II, which includes all characterisation results of the samples to be used, is meant to tie the two parts together. An introduction and summary of previous work on MTH and H-SAPO-5 is included first, which relevant for all three parts.

2 Zeolites and catalysis

2.1 Catalysis

2.1.1 What is catalysis

A catalyst accelerates a chemical reaction without itself being consumed and without altering the overall thermodynamics of the reaction. This usually occurs by the catalyst bonding to the reactants, allowing them to react with lower activation energy than what would have been the case if they had reacted directly without the presence of a catalyst. The bond between the catalyst and the product is then broken, leaving the catalyst free for another cycle. Figure 2.1 illustrates the difference between a catalysed and an uncatalysed reaction:

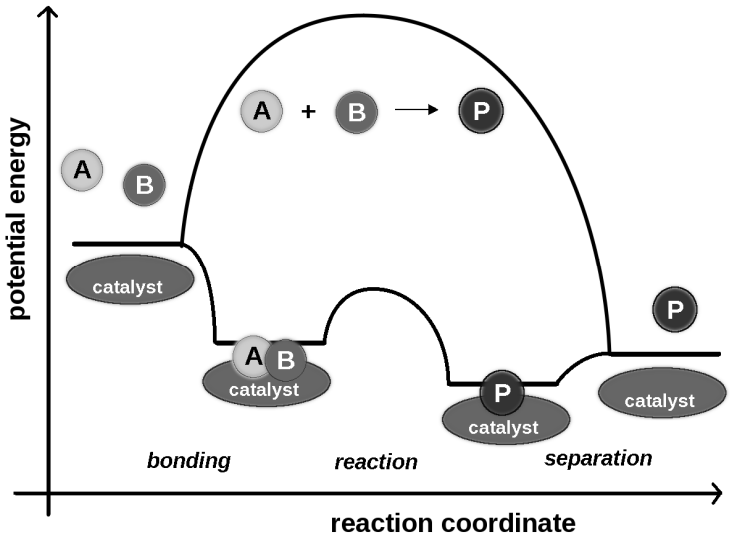

Fig. 2.1: Potential energy diagram of an uncatalysed (upper line) and a catalysed reaction (lower reaction path). Note the added complexity of the catalysed reaction path and that the activation barrier is much lower than the uncatalysed reaction. Note also that the overall energy change is the same in both paths. Figure adapted from [3].

From figure 2.1 it is evident that the catalytic reaction path in involves more steps than the uncatalysed path. In many cases a catalytic reaction is indeed much more complex than reactions not involving catalysts, but the lowered activation barrier(s) still make the catalytic reaction favourable. An important fact is apparent when looking at the reaction scheme in figure 2.1, namely that the backwards reaction is accelerated as much as the forward one. This means there will be no change in the equilibrium position between the reactants and products.

A catalyst can in principle take any form, including atoms, molecules and larger solids like metal or oxide surfaces. The next section highlights some different types of catalysis.

2.1.2 Different types of catalysis

Generally, a division is made between homogeneous and heterogeneous catalysis. In homogeneous catalysis the catalyst, reactants and products are in the same phase, most commonly the liquid- or gas-phase. Examples of homogeneous catalysis include the decomposition of ozone in the atmosphere catalysed by chlorine atoms and the industrial production of acetic acid from methanol over an iridium complex catalyst. Heterogeneous catalysis, on the other hand, has the catalyst in another phase than the reaction mixture. Most often the catalyst is a solid, while reactants and products are in the gas or liquid phase. Many processes in oil refining utilise heterogeneous catalysis to provide base chemicals for everyday items like plastics and the production of gasoline.

In addition to homogeneous and heterogeneous catalysis a third type called biocatalysis or enzyme catalysis is usually differentiated from the others. This is the type of catalysis that takes place in living organisms, where complex molecules called enzymes catalyse numerous processes with very high selectivity.

The focus of this thesis focuses lies on a specific heterogeneous reaction: the conversion of methanol to hydrocarbons. This reaction is catalysed by zeolitic materials, which are acidic solids, while both reactants and products are in the gas phase.

2.2 Zeolites and related materials

2.2.1 History

Zeolites are a class of naturally occurring aluminosilicates first reported by the Swedish geologist Cronstedt in 1756. They were later found to be one of the most abundant mineral crystals in the world (see fig 2.2 for an example of natural appearance). The name “zeolite” is derived from from the Greek words “zeo” and “lithos” meaning “to boil” and “a stone”, respectively. This name was chosen because of the natural zeolites exhibition of intumescence

upon rapid heating makes the stone appear to boil. The mineral class is characterized by its three-dimensional structures comprised of corner sharing TO_4 tetrahedra, where T can indicate a multitude of elements, most commonly silicon or aluminium. These frameworks are generally very open and contain channels and cages usually filled with water and loosely held cations. It is this water, which is readily lost and regained, that gives rise to the intumescence and apparent boiling of the materials.[4, 5]

Fig. 2.2: Zeolite Edingtonite from British Columbia, Canada[6].

Even though reversible ion exchange in zeolites was demonstrated as early as 1858 by Eichhorn and the molecular sieving properties were described by Weigel and Steinhoff in 1925, zeolites experienced little commercial interest apart from as jewelry for close to 200 years. This changed in the forties and fifties, when R. M. Milton managed to synthesise zeolites by low temperature hydrothermal methods. The fifties saw increased usage of zeolites as desiccants and molecular sieves, while in the sixties the potential for use in catalytic applications was realized, most notably as cracking catalysts in oil refining. Since then the market for zeolites has grown steadily, with the major applications being ion exchange, catalysis and use as adsorbents.[4]

The number of zeolite structures has also increased greatly during later years, and many of the structures that have been synthesised have no natural counterparts. Related materials comprising other elements than aluminium and silicon have also been synthesised, with at least 20 types of T-atoms apart from Al and Si reported in different zeolitic frameworks[7]. Some of these materials even have novel structures not observed for aluminosilicates. In 2010, the structure commission of the International Zeolite Association reported that 194 different framework types had been approved and each given a three letter code.[8]

This large number of closely related structures based on several different elements has led to difficulties concerning the definition of zeolites. By some, zeolites are regarded as any mineral consisting of TO_4 tetrahedra formed into frameworks with open cavities[9], while others consider only the structures consisting of Si and Al as true zeolites[4]. The latter group usually refers to similar structures containing other elements as zeotypes. In addition IZA recommends the use of framework density to distinguish zeolites and zeotypes from denser tectosilicates, as zeolites usually have framework density lower than ~20 T-atoms per 1000$Å^3$[10]. This work will consider all materials consisting of IZA approved frameworks with only SiO_4 and AlO_4 tetrahedra as zeolites, and refer to structures containing other elements as zeotypes. The term "zeolitic" is used as a common name to mean both zeolites and zeotype materials.

2.2.2 Structure and properties

As established above, zeolitic materials consist of TO_4 tetrahedra with shared corners forming a three dimensional framework. The tetrahedra are often referred to as the primary building blocks of the zeolite, and the structure is formed by the connections between these primary building blocks. Figure 2.3 illustrates these relations:

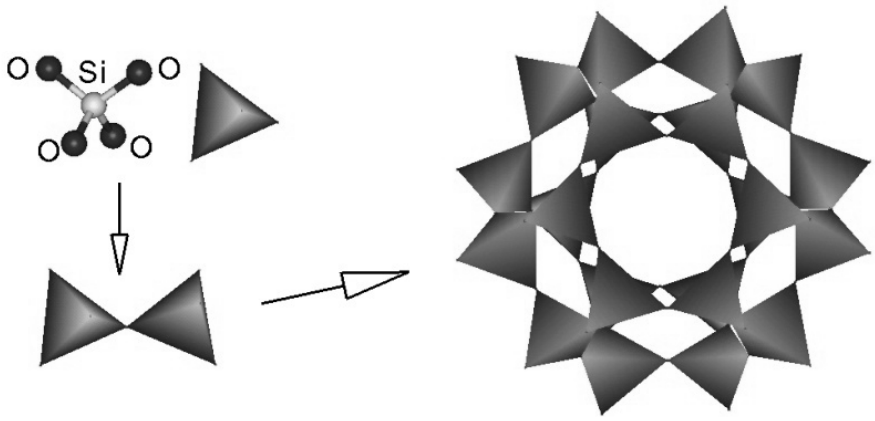

Fig. 2.3: Illustration of how the TO_4 tetrahedra connect to form a zeolite structure. From the webpage of the British Zeolite Association (BZA)[11].

In addition to this, a number of secondary and composite building units that are present in many structures have been recognized. Secondary building units (SBUs) are finite units derived on the assumption that the entire framework can be made from one type of unit only.

SBUs are invariably achiral and the unit cell of a material always contains an integral number of these units[8]. However, several frameworks may be built from more than one type of SBU and some of the SBUs (especially the 4, 6 and 5-1 units) can be used to build a plethora of different frameworks. Composite building units (CBUs) are larger units that are not necessarily achiral and can be infinitely extended (i.e. chains or layers). They appear in more than one framework type and are useful in ascertaining relations between different framework types, but cannot necessarily be used to construct whole frameworks. Understanding zeolitic structures from these bigger units is usually easier than from primary units and unit cell parameters only. Some examples of SBUs and CBUs are presented in figure 2.4.

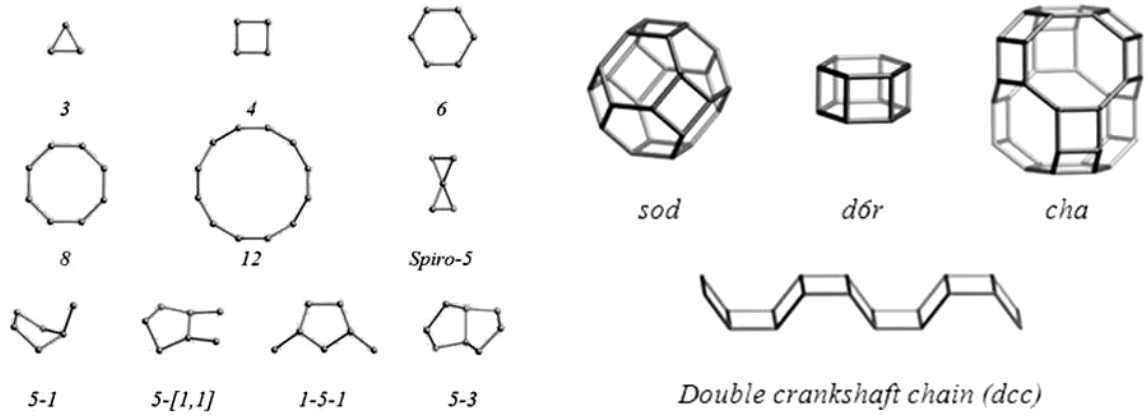

Fig. 2.4: Some examples of SBUs (left) and CBUs (right) from the IZA webpage[8]. Oxygen bridges have been omitted for clarity in the drawings.

The building units described so far are useful in visualizing the full framework, but the most useful initial description of a zeolitic structure is often in terms of its pore system. A description of the dimensionality of the channel system, the aperture of the pore opening and whether larger internal cages are present allows recognition of the framework's key features. Pore openings are usually characterized by the size of the smallest ring in the pore and named after how many T-atoms it contains. The most common sizes are 8, 10 and 12 rings, with free diameters of roughly 4.1, 5.5 and 7.4 Å respectively if not distorted[12]. Larger rings also exist, including the 18 ring of the VPI framework, but they are all below 20 Å and thus fall in the range referred to by IUPAC as microporous[13].

While the framework and porosity provides the molecular sieving ability of the materials, since only certain molecules are small enough to enter the structure, other properties are dependent on the nature of the T-atoms. A framework consisting of SiO_4 tetrahedra only will

be electronically neutral, but the presence of an Al atom induces a negative charge in the framework, which must be compensated by a cation inside the framework. These cations are often loosely bound and easily exchangeable, giving rise to the ion-exchange properties of zeolites[4]. The amount of aluminium in zeolites is usually limited to half of the total T-atoms as per Löwensteins rule[14], which states that Al-O-Al bonds in the frameworks are forbidden.

As briefly mentioned before, zeolitic materials can contain other T-atoms than silicon and aluminium. For instance, inclusion of boron or elements from period three of the periodic table in zeolite frameworks has been frequently reported[15]. One class of zeotypes prepared by combining the elements on either side of silicon in the periodic system, called aluminophosphates ($ALPO_4$'s), was synthesised by workers at Union Carbide in 1982[16]. In these materials the T atoms are half Al and half P in a strictly alternating fashion, providing the framework with localized charges but keeping the net neutrality of the material. The properties of such materials differ somewhat from aluminosilicates. While these materials do not possess ion-exchange properties when net framework charge is zero, this is obtainable by substitution of tetravalent elements for phosphorous or divalent elements for aluminium[17, 18]. Most notable among zeotypes with ion-exchange abilities are the silicoluminophosphate (SAPO) materials, first reported in 1984[19, 20]. In these materials silicon mainly substitutes for phosphorous in the lattice to produce a net negative charge. In addition to silicon, numerous other elements have been incorporated into $AlPO_4$ frameworks[7, 21] and zeolitic materials containing neither Al nor Si, such as gallophosphates, have also been synthesised. In addition to this, the possibility of intergrowths between different frameworks[12] and compositional gradients[22] makes the chemistry of zeolitic materials rich indeed.

If the balancing cations of a net negative material are protons, Brønsted acidic sites located at defined sites in the material are obtained. Such materials, usually denoted by an H before their name (e.g. H-SAPO-5), are highly suited for heterogeneous catalysis. Figure 2.5 shows such a Brønsted site where the bridging oxygen between two different T-atoms holds a proton. Although solid acidity is a very ambiguous term[23] it is possible to distinguish between Brønsted acidity (proton donor) and Lewis acidity (electron acceptor). While most solid acids contain large numbers of Lewis sites, an ideal zeolite contains only

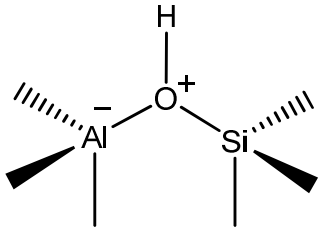

Fig. 2.5: A bridging Brønsted acidic site in a zeolite or SAPO material.

Brønsted sites. When zeolites contain Lewis acid sites, these are usually related to defects or extra-framework species present in the material[24].

The acid strength of zeolitic materials is related both to the surrounding structure (framework type) and the chemical composition of the material. In SAPO materials, acid strength of bridging Brønsted sites is also affected by the number of neighbouring Si T-atoms[25]. It should be noted that the term acid strength is used somewhat ambiguously in different situations to describe both the density of acid sites and the actual acid strength (related to the ease of removing the proton). In this thesis, however, the term will be used only relating to the actual strength of the O-H bond at an acid site, while the density of the sites will be referred to as acid site density. The composition of a zeolite is often given as Si/Al (or sometimes SiO_2/Al_2O_3) or in a SAPO as (Al + P)/Si, and the acid site density is inversely proportional to this number.

2.2.3 Synthesis of zeolitic materials

Most zeolite syntheses are based on sol-gel and hydrothermal synthesis methods[26]. Usually the reaction mixture of a zeolite consists of amorphous silica and alumina in an aqueous solution containing mineraliser and cations or organic molecules. This mixture forms a gel by condensation reactions at low temperature and is then heated in a sealed autoclave above the boiling point of the water. The function of a mineraliser is to speed up crystallisation, usually by increasing solubility of the reactants[26]. This role is commonly fulfilled by OH^- ions[27].

The role of cations and organic molecules in the mixture is poorly understood, but in addition to acting as charge balance for the zeolite framework, they appear to have a structure determining effect. They have been thought to act as templates by filling the voids of the zeolite structure, but more complex interaction between them and the framework might also occur. Typical cations are from group I or II, while amines and ammonium ions are the most common organic molecules utilised. All these species when used in zeolite synthesis are often referred to as templates or structure-directing agents (SDAs). It should be noted that while these species are regarded as structure-directing, the same structure can in many cases be formed with more than one type of SDA, and an SDA can often be used to form more than one type of structure. A brief overview of templating in zeolite synthesis can be found in [28].

As the diversity of zeolitic structures is enormous, synthesis conditions are critical to obtaining the wanted phase and composition. Factors such as pH, the nature and amount of the reactants and SDA used, temperature, crystallisation time, ageing time of the initial gel, whether the mixture is stirred or not during crystallisation and many more factors determine what end product is obtained. The IZA handbook "verified synthesis of zeolitic materials"[29] provides a series of general articles on some zeolite synthesis parameters, while Cundy and Cox[30] have written a detailed review on the hydrothermal synthesis of zeolites.

Synthesis of aluminophosphate-based zeotypes is performed in much the same way as zeolite synthesis, but where zeolites are usually synthesised at high pH aluminophosphates are usually synthesised in the pH-interval 3-10. The same sources of aluminium utilised in zeolite synthesis can be used to produce aluminophosphates as well, while phosphorous is nearly always introduced in the form of orthophosphoric acid. Usually, there is no alkali cations present, and the SDA is an amine or quaternary ammonium hydroxide ion. Silicon or other heteroatoms to be incorporated are added to this mixture, which is crystallised hydrothermally at 100-200°C.[7]

2.2.4 Zeolite catalysis

Although the largest use of zeolites on a volume basis is for ion exchange in detergents, use in catalysis is still the largest value market[5]. The vast majority of zeolite used for catalysis is used for the fluid catalytic cracking (FCC) process, where heavy oil fractions are converted to lighter, more useful lighter fractions over a zeolite Y catalyst (a zeolite composed of large cavities connected by twelve-ring apertures). Other notable catalytic processes utilising zeolites include hydrocracking, isomerisation of light gasoline or xylenes, and alkylation of benzene[24]. In addition, another potential application of zeolitic catalysts is in the conversion of methanol conversion to hydrocarbons (more on this in the next section).

In general, what makes zeolites attractive for catalysis is their high surface area, defined crystal structures, high thermal stability, possibility of modulating active sites (including the incorporation of metal sites to the lattice) and the shape selectivity brought about by their pores of molecular dimensions. Shape selectivity is often divided into three types, as shown

schematically in figure 2.5. Reactant selectivity occurs when reactants are too large to enter the channels of the zeolite, while transition-state- and product- selectivity prevents the formation of transition-states that are too large to exist inside the pores and products too large to diffuse out of the crystal, respectively.[31] If the molecules formed inside the zeolitic pores are too large to diffuse out of them, these must either react further to species that are able to leave the structure or be left inside, possibly reacting to form even larger species which may cause deactivation of the zeolite catalyst. It is important to bear in mind that shape-selectivity only occurs in the bulk volume of a zeolitic material. This means that the smaller the crystals are, the less effective the shape selectivity properties will become as more of the reactions take place on the surface or in the pore mouths[32].

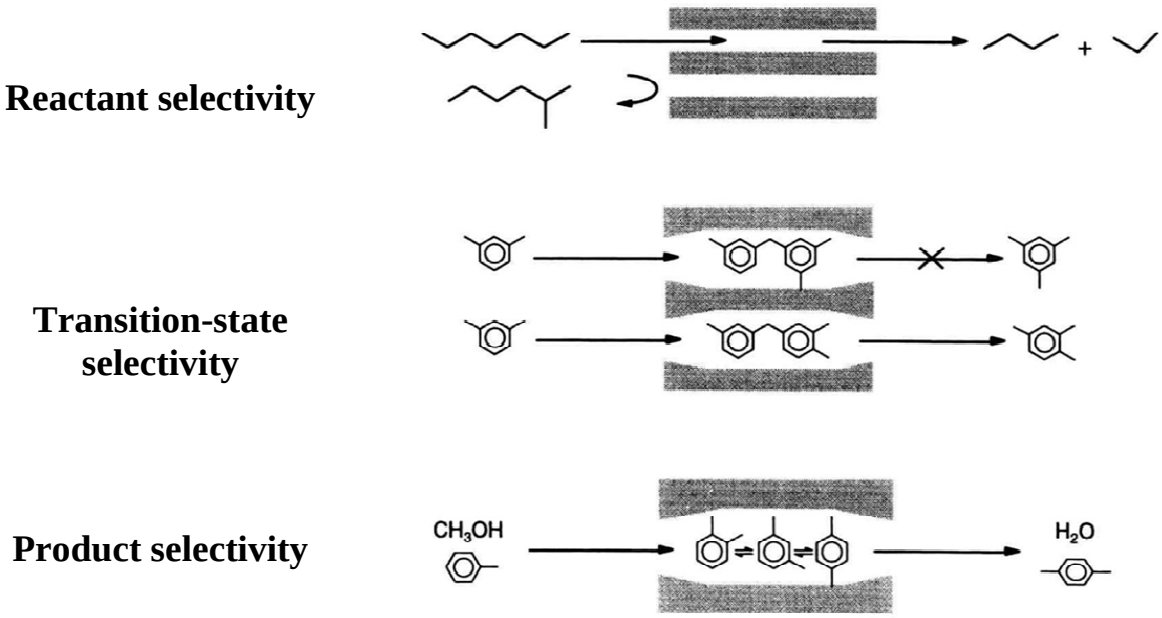

Fig. 2.6: The three types of shape-selectivity (adapted from [31])

3 The Methanol-to-Hydrocarbons process (MTH)

3.1 History and overview of the process

The methanol-to-hydrocarbons (MTH) process is, as its name suggests, a process where methanol is converted into a mixture of hydrocarbons. The reaction proceeds over acidic catalysts such as zeolitic materials and a general stoichiometric equation of the reaction can be written as:

$$CH_3OH \rightarrow \text{“}CH_2\text{”} + H_2O$$

The “CH_2” in the equation above represents a variety of hydrocarbons, both of aliphatic and aromatic character. The exact species formed depends on process conditions and the shape-selectivity properties of the zeolite catalyst used[33]. In industrial applications, reactant methanol is produced from synthesis gas (syn-gas, a mixture of H_2 and CO/CO_2) through well known processes utilising a $Cu/Zn/Al_2O_3$ catalyst at high pressure and intermediate temperature. The syn-gas itself is produced from a carbon containing feedstock (usually coal or natural gas), usually by steam reforming[3]. Structures of H-SAPO-34, a framework of cages with 8-ring apertures, and H-ZSM-5, with 10-ring pores, are shown below in figure 3.1 together with the structure of H-Beta. The first two are the most common industrial catalysts for MTH processes, while the 12-ring pores of H-Beta makes this structure useful for studying reaction mechanisms.

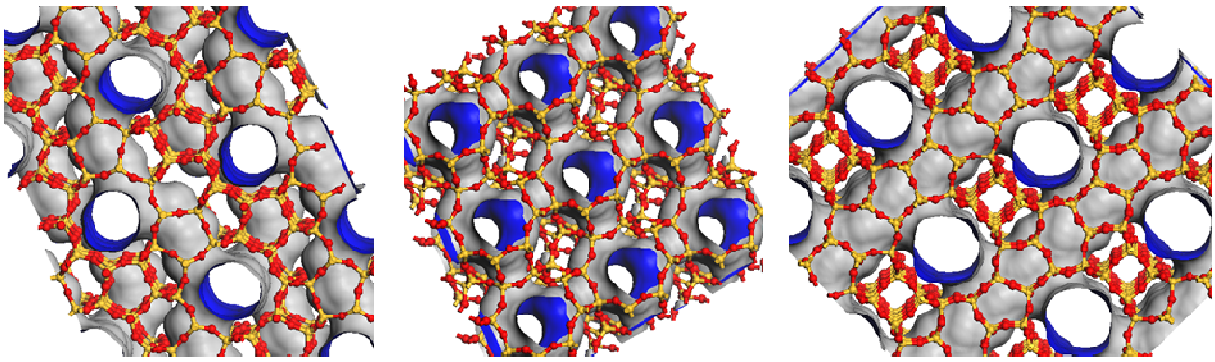

Fig. 3.1: The structures of H-ZSM-5 (MFI framework), H-SAPO-34 (CHA) and H-Beta (*BEA) are shown from left to right. Note that all structures have three dimensional channel systems. Oxygen and T-atoms differ in colour, while channel systems are drawn with outsides grey and insides blue

The process was discovered by accident when Chang & Silvestri at Mobil's research division were working on methods to produce high octane gasoline from methanol and isobutane over zeolite catalysts in the 1970s. They discovered that even though the isobutane was not consumed, a mixture of alkanes and aromatics similar to high octane gasoline was produced from the methanol alone.[33-35] The ongoing energy crisis at the time had led to great interest in synthetic fuels and provided favourable conditions for continuing the research into this new methanol process[33]. This led to the construction in 1986 of a plant in New Zealand utilising Mobil's patented methanol-to-gasoline (MTG) process, in which methanol is converted to gasoline over H-ZSM-5. However, the oil prices soon dropped and gasoline production was closed down not long after coming on-line[1, 33, 35].

Even after the somewhat decreased industrial interest, methanol catalysis remained an important research topic. This has led to several articles and patents on methanol conversion over zeolitic materials, including a more selective catalysis of methanol to light olefins[35]. This process, called methanol-to-olefins (MTO), gained more interest from industry as worldwide demand for polyolefins is growing[1]. Available technologies of these processes include UOP/Hydro's MTO process using H-SAPO-34 catalyst and Lurgi's MTP (methanol-to-propylene) process, catalysed by H-ZSM-5[1].

As the awareness of environmental factors and depletion of oil reserves is increasing, an interest in the exploitation of hydrocarbon sources other than oil has grown once again. As a consequence, industrial interest in MTH has been renewed. Since production of methanol is well known and can in principle be produced from any carbon-containing feedstock, MTH presents a flexible process to produce various hydrocarbons from whatever feedstock is available. The increased interest is evident as several MTO/MTP/MTG plants both of commercial and demonstrative scales have been built recently or are under construction[36-40]. Included in this is a demonstration plant to be built in the US producing gasoline from wood. This will be based around the Topsøe Integrated Gasoline Synthesis (TIGAS) process (a process combining production of syn-gas and methanol with MTG in one process loop)[40].

3.2 Reaction mechanisms

3.2.1 Early efforts and the first C-C bond

Investigations into the methanol-to-hydrocarbons reaction started immediately after its discovery and, as the reaction was completely unexpected, much attention was focused on elucidating the reaction mechanisms. Despite the efforts, this remains a challenge since the mechanisms involved appear to be both complex and numerous. Chang and Silvestri[34] concluded, based on the effects of contact time and the fact that a dimethyl-ether feed produced the same products, that the reaction path over H-ZSM-5 could be described reasonably well by the following scheme (Figure 3.2):

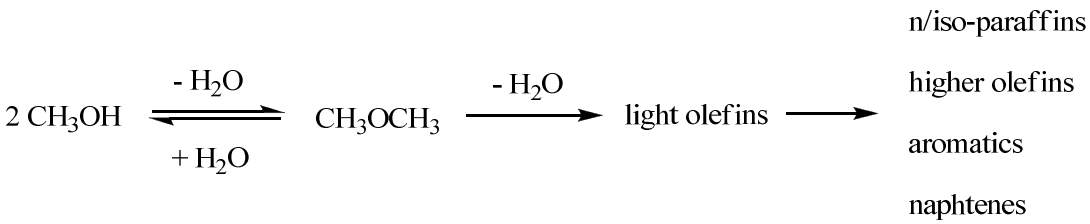

Fig. 3.2: Simplified scheme of the reaction path for the methanol-to hydrocarbons reaction adapted from [34].

The scheme implies that methanol is first dehydrated to dimethyl ether and water. This equilibrium mixture is then converted to light olefins, which in the last step is converted into higher hydrocarbon products. Although this scheme lacks mechanistic insight, it is still a useful simplification and helps to keep track of the species present in a typical MTH reaction.

Early efforts in mechanistic investigations were strongly focused around the question of how the first C-C bond was formed[1, 35]. According to a review by Stöcker, more than 20 mechanisms have been proposed for forming this bond[33]. Chief among these were mechanisms based on carbenes, carbocations, radical mechanisms, and a mechanism involving oxonium ylide intermediates. However, no consensus on how such a bond would form was reached and focus later shifted towards more indirect methods of olefin formation.

As none of the mechanisms proposed for direct C-C bond formation could explain the kinetic induction period observed in the reaction or was able to explain the initial product selectivities

adequately, the idea that the reaction is autocatalytic was born[35]. Dessau and co-workers proposed in the 80's that a direct mechanism may operate during an induction period, but that a more efficient route through olefin chain growth and cracking (see figure 3.3) dominates once initial olefins are formed.[41, 42]

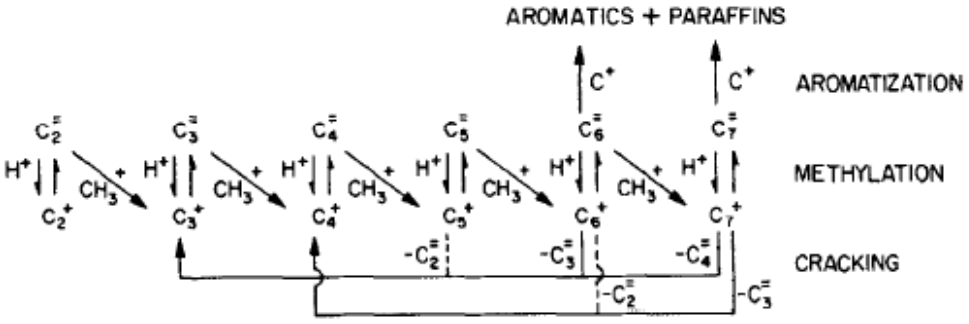

Fig. 3.3: Dessau's scheme of a mechanism based on successive methylation and cracking[41].

Before this, Mole[43] and Langner[44] had also showed independently that Toluene and cyclohexene, respectively, had a co-catalytic effect on the reaction, thus diminishing the importance of direct C-C bond formation. Their findings and theories were very insightful and likely contributed greatly to later mechanistic studies.

3.2.2 Hydrocarbon pool

A major advance in the mechanistic understanding of methanol conversion came about when Dahl and Kolboe suggested the concept of a hydrocarbon pool in the 1990's. Their co-feeding experiments of labelled methanol with ethene or propene over SAPO-34[45-47] show that propene/butene products are not chiefly formed by methylation of ethene/propene, discrediting any mechanism based on alkene chain growth. Instead, they suggested that a pool of adsorbed hydrocarbons was continuously adding methanol and splitting off hydrocarbons as shown schematically in figure 3.4:

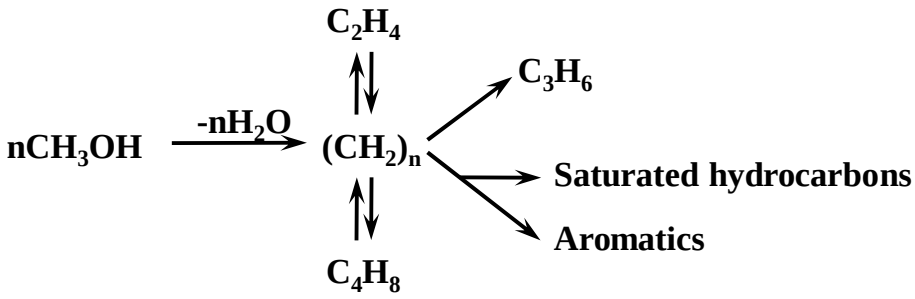

Fig 3.4: Kolboe's phenomenological scheme of the hydrocarbon pool mechanism for MTO catalysis. Adapted from [35].

Over the years, the hydrocarbon pool mechanism has gained general acceptance (see e.g. [1, 23, 35, 48]), and the importance of direct C-C formation is now considered minor. Indeed, studies by Song et al[49] suggest that this is completely insignificant as, if it even occurs, it is so slow as to be eclipsed by the contribution of even trace impurities in the feed. In addition to this, calculations by Lesthaeghe et al[50] show that the direct reaction from methanol to ethene is improbable.

Although the nature of the hydrocarbon pool was not initially specified, more recent research has shown that methylbenzenes play a central role in the reaction. Mikkelsen et al[51] observed substantial isotopic scrambling when cofeeding ^{12}C-toluene and ^{13}C-methanol over H-ZSM-5, H-mordenite and H-Beta, indicating the participation of methylbenzenes in olefin formation. Findings by Arstad and Kolboe[52, 53] from studying the organic material retained in SAPO-34 after short reaction periods also strongly suggest that polymethylbenzenes are the reaction centres in H-SAPO-34. Song et al[54] also arrived at essentially the same conclusions using NMR spectroscopy. Indeed, when seen together with the earlier findings of Mole et al[43, 55] that toluene acts as co-catalyst for methanol conversion over H-ZSM-5, a strong case can be made for the role of methylbenzenes as reaction centres in a hydrocarbon-pool mechanism. In addition to this, Sassi et al[56] have also showed that polymethylbenzenes fed over H-Beta are active for olefin formation.

Although the conclusion that polymethylbenzenes are reaction centres in hydrocarbon pool chemistry seems to hold for several different zeotypes, the exact nature of the active species seems to vary with catalyst type and reaction conditions. In addition to polymethylbenzenes, both polymethylnaphtalenes (although less active than polymethylbenzenes in SAPO-34)[57, 58] and cyclopentenyl species[59, 60] have been identified as active hydrocarbon pool centres.

Observations also point to different active polymethylbenzes in H-ZSM-5 compared to H-beta and H-SAPO-34, with less substituted methylbenzenes active in the former than in the latter two[61]. Different active hydrocarbon pool species have also been linked to differences in product selectivities as methylbenzenes. Those with two to four methyl groups apparently splits off predominantly ethene, while those with more methyl substituents appears to preferentially split off propene or butene[61].

Product formation from polymethylbenzenes is thought to occur either via a ring-contraction/expansion or through methylation of an exocyclic double bond. The first of these, called the "paring" reaction, was suggested by Sullivan et al in 1961[62] to explain isobutene formation from hexamethylbenzene and is shown below in figure 3.5:

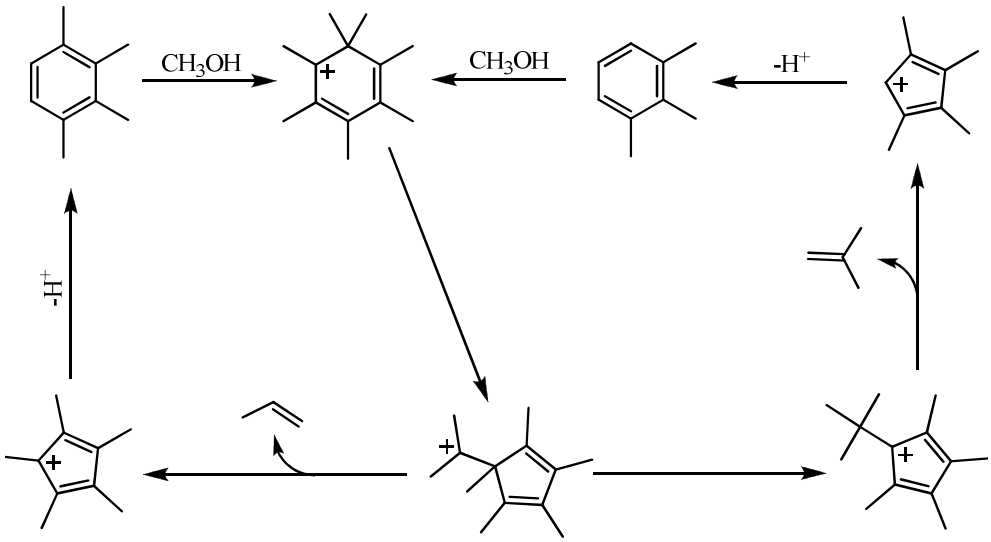

Fig. 3.5: Scheme of the paring reaction indicating formation of propene or isobutene from heptamethylbenzene cation via a ring contraction adapted from [1].

The second mechanism was proposed by Mole et al[43, 55] to account for the cocatalytic effect of toluene and suggests the formation of an exocyclic double bond that is subsequently methylated before the resulting alkene is split off. It was further refined by Haw et al[35] and is usually referred to as the exocyclic methylation reaction (shown below in figure 3.6). Although the heptamethylbenzenium cation is the starting point of both mechanisms in figures 3.5 and 3.6, benzenes with fewer methyl substituents presumably take part in similar reactions.

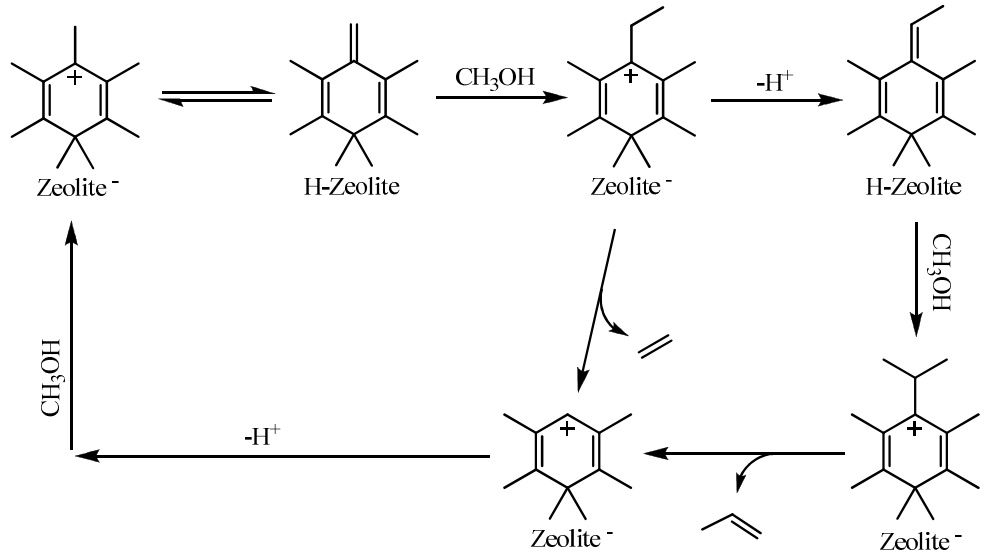

Fig. 3.6: Scheme, adapted from [1], of the exocyclic methylation reaction forming ethene or propene from a heptamethylbenzene cation.

Most studies of olefin formation from polymethylbenzenes has been done on the large-pore zeolite H-Beta as this structure allows the direct feeding of these species[1]. It has been found that hexamethylbenzene is far more reactive for product formation than the lower methylbenzenes over this zeolite[56], and that the amount of this species retained in the material decreases quickly when methanol feed is stopped and the catalyst is flushed with inert gas.[58] It has been known for a long time[63] that hexamethylbenzene can form the heptamethylbenzenium ion under methylating conditions. Both this and its corresponding base 1,2,3,3,4,5-hexamethyl-6-methylene-1,4-cyclohexadiene (HMMC) have been observed in H-Beta[64, 65] and are assumed to be very reactive. The group of Haw et al has produced several papers on the exocyclic methylation mechanism and adopts this as the most likely (see e.g. [23, 35, 56, 66]) mechanism. On the other hand, Bjørgen et al[64] produced results in 2004 which fit very well with a paring type mechanism over H-Beta. They also invoke the large amounts of isobutene produced as an argument for a considerable participation of a paring type mechanism, as isobutene is not an obvious product from the exocyclic methylation mechanism. Recently, McCann et al[67] have modelled a complete catalytic cycle for formation of isobutene over H-ZSM-5 involving a paring type mechanism which contains no major bottlenecks and is compatible with experimental observations. While this undoubtedly adds credibility to the occurrence of a paring type mechanism for isobutene formation,

whether the same mechanism is responsible for production of other olefins as well is not certain. It has also been speculated whether the exocyclic route could be favoured by using a catalyst with a lower acid strength.[1]

Considering acid strength, it is noteworthy that studies of the protonation of polymethylbenzenes in H-Beta by IR and UV/visible spectroscopy shows that tetra-methylbenzenes and higher homologues are protonated while tri-methylbenzene is not[68, 69]. On the other hand, recent results from Bleken et al[70] on H-SAPO-34 and H-SSZ-13 (the isostructural zeolite) indicate that while tetra-, penta- and hexa-methylbenzene seems to decompose over the zeolite, only penta- and hexa-methylbenzene decomposes in the SAPO (confirming the findings of Arstad et al[52, 53]). This could hint to the inability of the less acidic SAPO material to protonate the lower methylbenzenes.

3.2.3 Competing mechanisms

Aromatics based hydrocarbon pool mechanisms have received much attention and this is confirmed to be an important mechanism for olefin formation in methanol-to-olefin catalysis. However, it has also been reported during the last decade that the methylation/cracking mechanism proposed by Dessau et al[41] might operate under certain conditions. For instance Svelle et al[71, 72] showed that methylation of ethene, propene and n-butene by methanol occurs at elevated alkene pressures over H-ZSM-5. Further isotopic labelling studies performed on this material by Svelle et al[73] and Bjørgen et al[74, 75] suggests that the formation of ethene over this catalyst is mechanistically separated from the formation of higher alkenes. This led to their proposal of a dual cycle concept, where methylbenzene intermediates are responsible for ethene formation while alkene methylation and cracking accounts for formation of higher alkenes. This concept is illustrated in figure 3.7.

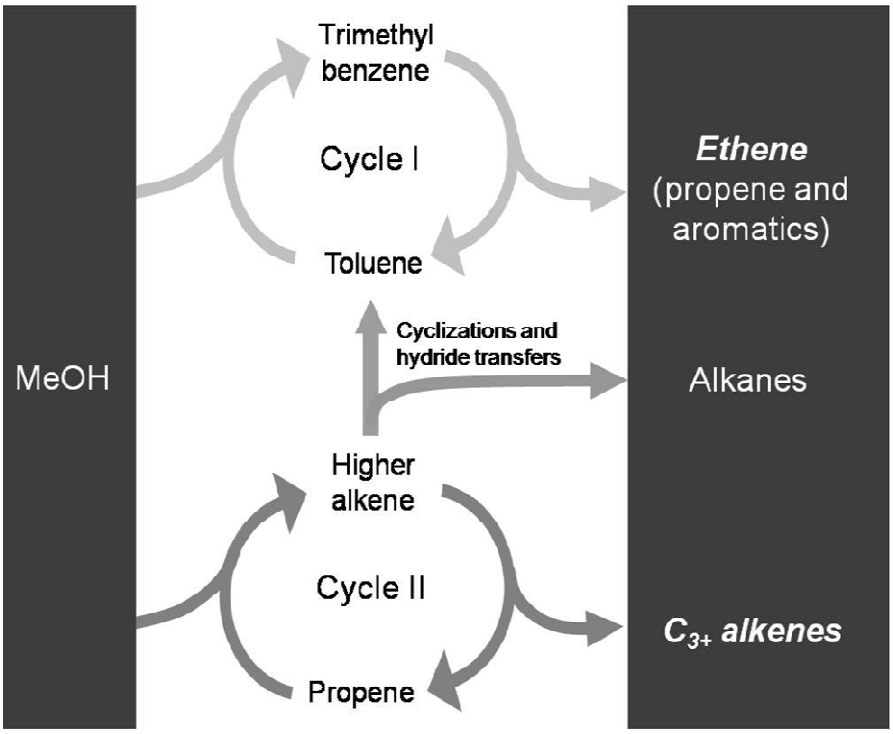

Fig. 3.7: The dual cycle concept proposed by Bjørgen et al[74] to account for the mechanistic separation of ethene and higher alkene products in methanol conversion over H-ZSM-5. Note that there is a link between the two cycles so that formation of alkanes and aromatics through hydride transfers is accounted for.

Further studies by the same groups[61, 76] also led to the conclusion that both the aromatic and the alkene cycle operates over H-Beta as well. However, the aromatic cycle in H-Beta is more efficient since the more spacious pores allow larger and more reactive polymethylbenzenes to form than in H-ZSM-5. Some of the differences in selectivity over these two catalysts are thus accounted for by the pore sizes favouring either cycle I or cycle II, and other by a difference in products formed from cycle I due to different methylbenzene intermediates. The narrower channels of H-ZSM-5 favours the alkene cycle and an aromatic cycle based on lower polymethylbenzes leading to ethene formation, while an aromatic cycle based on higher methylbenzenes causes H-Beta to produce mostly propene and butenes. With this knowledge, it should be possible to fine-tune the selectivity of methanol conversion by choosing a catalyst with a pore-size favouring the wanted intermediate. An example of a catalyst strongly favouring the alkene cycle while the aromatic cycle is hardly active has been provided by Teketel et al[77-79] studying the zeolite ZSM-22. This zeolite has one-dimensional 10-ring channels that are narrower than those of ZSM-5 and produces large amounts of branched C5+ alkenes while hardly producing aromatics at all. Isotopic labelling studies confirm that nearly

all products are formed from an alkene cycle and that the small amount of polymethylbenzenes retained in the material is nearly inactive for product formation.

3.2.4 Catalyst deactivation

As in many other hydrocarbon reactions, the formation of coke along with the desired products can be a challenge, as this leads to deactivation of the catalyst. It should be noted that when the term coke is used here it does not necessarily refer to graphitic coke, but also to smaller aromatic structures capable of blocking zeolite micropores. These species can lead to catalyst deactivation either by poisoning of the active sites and/or through pore blockage[80]. In principle, coke formation is reversible as the catalyst can be regenerated by oxidation at high temperature. Regeneration is, however, often incomplete either due to leftover coke or through damage of the catalyst from severe treatments leading to diminished catalyst activity[80, 81]. Diminished activity in zeolites after regeneration is often assumed to be an effect of dealumination during the high temperature oxidation, leading to a decrease in acid site density[82]. Similar processes can also be imagined to occur in SAPO materials.

Deactivation mechanisms in MTH are subjects of much interest, as catalysts used are prone to quite rapid deactivation compared to the metal catalysts used in other processes. Despite this, deactivation mechanisms are only partly understood as separation between aromatics that are required for product formation and those responsible for deactivation is difficult. The subject is further complicated by the fact that deactivation seems to occur for different reasons over different zeolite topologies.

The deactivation of SAPO-34 is thought to occur as methylbenzenes inside the structure are converted to larger aromatics (as large as pyrene), leading to greatly reduced mass transport once a significant fraction of the cages are occupied by the polycyclic aromatics[35]. Studies by Hereijgers et al[83] seem to support the idea of lower diffusivity leading to deactivation, but also that the polycyclic aromatics are mainly formed after deactivation has taken place and that the diffusion limitations must be caused by lighter species. A different example is the deactivation of H-ZSM-5, for which studies seem to conclude that deactivation is not related to coke formation inside the zeolite channels, but is more likely an effect of coke on the external surface on the catalyst[74]. Indeed, in-situ spectroscopy of coke formation on H-ZSM-

5 and H-SAPO-34 during methanol conversion performed by Mores et al[84] confirms significant differences in coke formation over the two catalysts.

The mechanisms of forming polyaromatic compounds in zeolites have also been studied. Guisnet and Magnoux[80] suggest that condensation and rearrangement steps are possible at low temperatures, but lead to non-polyaromatic species with compositions dependent on the reactants. At higher temperatures, multiple hydride transfer steps also occur, leading to polyaromatic species with compositions practically independent of the reactant species. A relation between the ability to perform hydrogen transfers and deactivation has also been suggested by Yuen et al[17], together with a hypothesis that for this to occur, stronger acid sites are needed than for other reactions in methanol conversion. Another notable contribution in the understanding of coke formation is the finding by Bjørgen et al[58] that the hetpamethylbenzenium-ion seems to rapidly form dihydro-trimethyl-naphtalene, which again can be methylated to hexamethylnaphtalene. It can be envisaged that coke may be formed from naphthalenes and since there is a tendency to form heptamethyl-benzenium ion in any acidic zeolite with sufficiently large pores under methylating conditions, this could be an important mechanism in other catalysts as well. Their proposed scheme for formation of coke-precursors in H-Beta is shown in figure 3.8:

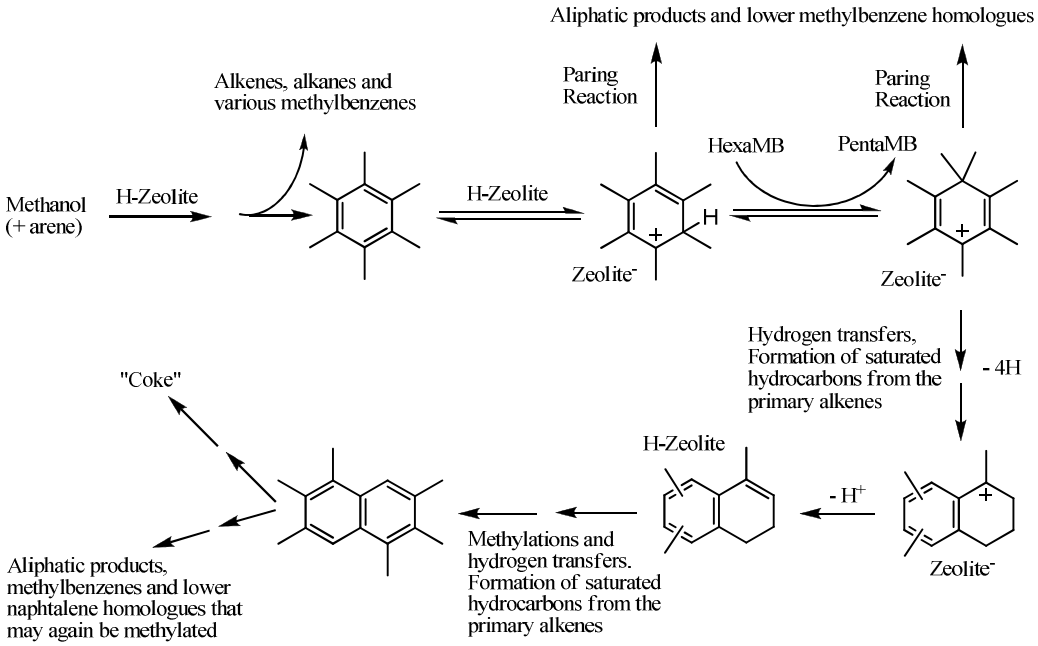

Fig. 3.8: Proposed scheme for formation of coke precursors from hexamethylbenzene in H-Beta adapted from [58]. Note the numerous hydrogen transfers that must occur for coke to form.

An interesting article by Janssens[81] has recently been published, proposing that deactivation, by whatever method or reason, can be modelled as a simple loss of an active site. If this line of thinking is taken a bit further, it is possible to imagine the catalyst simply as a number of active sites which over time become inactive, leading to lower conversion capacity in the catalyst bed as a whole. A catalyst bed which has had half its sites deactivated should thus perform similarly to a fresh catalyst bed made with half as many active to begin with.

4 SAPO-5 and the AFI structure

4.1 Introduction

$AlPO_4$-5 was discovered in 1982 along with the first aluminophosphates by Wilson et al[16] working at the Union Carbide labs. Its structure (framework type AFI) was solved soon after[85]. The same structure was also among the first synthesised silicoaluminophosphates (SAPOs) in 1984, and was then named SAPO-5[19, 20]. Later, it has been shown that many metals can be incorporated into the $AlPO_4$-5 and SAPO-5 structure, creating MeAPO and MeAPSO materials respectively[21]. In addition, an isostructural zeolite called SSZ-24 has also been synthesised, initially only in pure siliceous form by van Nordstrand et al[86], but later also with aluminium incorporated.

As the possibilities for varying composition, and thus tailor its properties, is large for the AFI topology, such materials have been studied extensively over the years. The perceived potential of the materials was originally limited to adsorptive, catalytic and ion-exchange applications, but more exotic uses like nonlinear optics[87] and containers for single walled carbon nanotubes[88] have also been explored.

SAPO-5 provides an interesting model system for methanol conversion because its open structure provides ample opportunity to co-feed larger reagents in a similar manner to what has been done with H-Beta. As silicoaluminophosphates generally possess lower acid strength than high-silica aluminosilicates[20, 89, 90], it is not certain whether reaction mechanisms over these two types of catalysts are identical. The regular structure of SAPO-5, with only one type of pore and one type of T-atom should make the material well suited as a model system. When comparing results directly with the most common SAPO catalyst, H-SAPO-34, it should be noted both that the larger space available in SAPO-5[91], and the somewhat lower acid strength than H-SAPO-34[92] could mean that mechanistic differences in product formation exist in the two materials.

4.2 Structure

As suggested by the name SAPO-5, T-atoms of the material are aluminium, phosphorous and silicon. Each Si atom in the lattice that is bonded to Al through an oxygen bridge, gives a Brønsted acidic site (vide supra). The framework of SAPO-5 and isostructural materials is made up of columns of twisted four- and six- rings, together forming a one-dimensional twelve ring parallel to the c-axis.[93] The three-letter code given to the topology by the International Zeolite Association (IZA) is AFI, and it can be constructed from either of the secondary building units 4, 6 or 12. Alternatively it can be viewed as a composition of the composite building units *afi*, *bog* and the *nsc* (narsarsukite) chain[8], shown in figure 4.1.

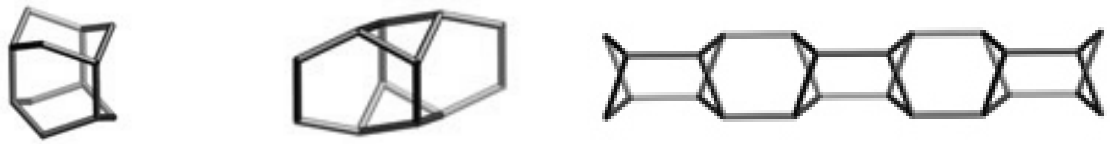

afi *Bog* *nsc chain*

Fig. 4.1: The composite building units of SAPO-5.[8]

Furthermore, the unit cell can be classified by the space group P6/mcc which has a hexagonal unit cell with the dimensions a = 13.827 Å and c = 8.580 Å[8], giving a unit cell volume of 1420.64 Å. The twelve ring channels of the structure are nearly circular with a diameter of 7.3 Å.[8] Figure 4.2 shows the structure and channel system in more detail.

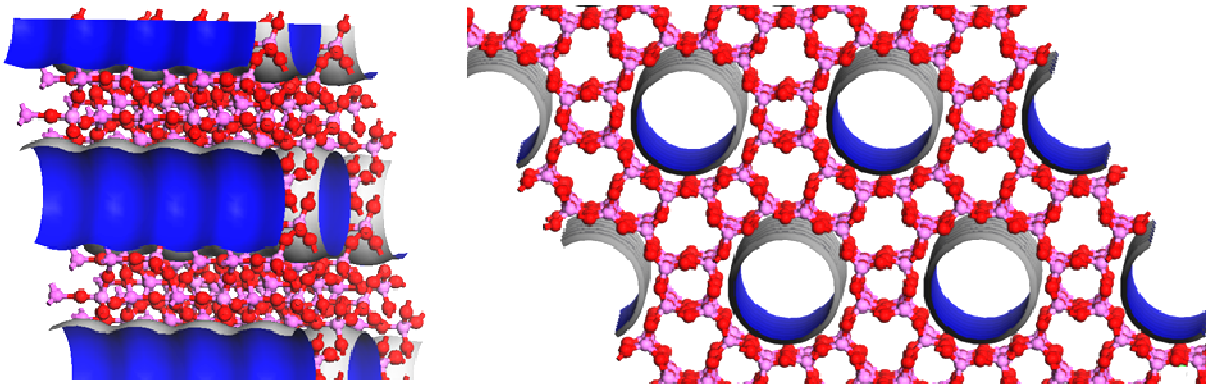

Fig. 4.2: The AFI topology seen along the a-axis (left) and c-axis (right). The twelve ring channels have been drawn with blue insides and grey outsides.

4.3 Synthesis

The synthesis of $AlPO_4$-5 and SAPO-5 can be executed using many different conditions and is not particularly template specific. Already in the first $AlPO_4$-5 reports Wilson et al[16] reported the ability to synthesise the material with 23 different amine and quaternary ammonium compounds as SDAs. Later, Wilson[7] has stated that more than 85 different SDAs can be used to form AFI frameworks. Likewise, numerous different templates and conditions have been used to synthesise SAPO-5 as well. For instance, Weyda and Lechert[93] compared crystallisation kinetics using six different SDAs in addition to varying several other parameters. The most commonly used templates for syntheses of SAPO-5 appear to be tri-n-propylamine (TPA) and triethylamine (TEA).

Morphologies of reported SAPO-5 and $AlPO_4$-5 materials vary, most commonly between aggregated sphere, hexagonal rod or hexagonal plate, depending on synthesis conditions. Large aggregated spheres are reported among others by Weyda and Lechert[93] using TPA, by Campelo et al[94] and as the product of the verified method of Young and Davis[95] using a cyclohexylamine template. Hexagonal rod morphologies varying greatly in size from the huge crystals (averaging 220 x 50µm) obtained by Demuth et al[96] to the smaller rods (~1 x 3µm) obtained by Qinhua et al[97] are reported using triethylamine as SDA. Hexagonal (or somewhat rounded hexagonal) plate-like crystals have been reported by several groups including Wang et al[98], using diethylamine and high temperatures, and Qinhua et al[97] using triethylamine.

Two studies on morphology control worth mentioning have been published by Tian et al[99] and by Jhung et al[100]. The former showed that an added surfactant in the synthesis mixture could hinder growth in the c-direction of metal-substituted AlPO-5, while the latter systematically varied the conditions of SAPO-5 synthesis under microwave irradiation. The trends found by Jhung et al[100] are summarised in figure 4.3.

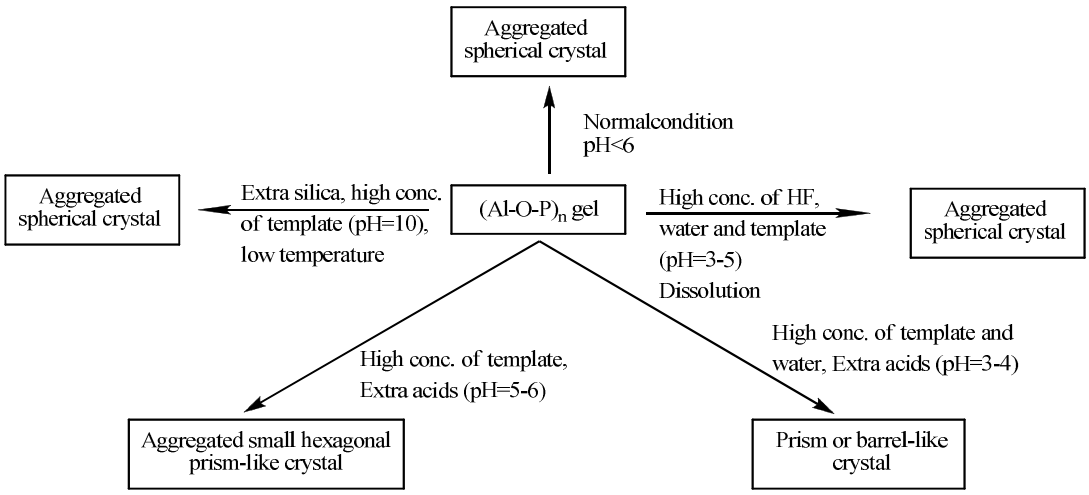

Fig. 4.3: Morphology changes as a function of varying parameters. Adapted from [100].

In the same and other studies of synthesis parameters on microwave synthesis of SAPO-5 by Jhung and Yoon et al[100-104], it is also reported that there is a competitive growth of the AFI and CHA frameworks. Which phase dominates is determined mainly by the pH and silicon content in the synthesis mixture, and whether microwave or conventional heating is applied. The competition between AFI and CHA frameworks has also been reported by many before them (see e.g. [105-108]). Vistad et al[108] also showed that the heating rate was of critical importance when synthesising SAPO-34 in the presence of HF using morpholine as SDA. Their research showed that if the synthesis mixture was heated too rapidly a key prephase for SAPO-34 would not form, resulting in formation of SAPO-5 instead. This is consistent with the results of Jhung et al[102] that SAPO-5 would form almost exclusively when crystallised under microwave irradiation, while SAPO-34 would dominate under hydrothermal conditions using both TEA and N,N,N',N'-tetraethylenediamine (TEEDA). While the heating rate is undoubtedly important, that other factors such as pH and temperature play a part is evident from the fact that Qinhua et al[97] reports successful synthesis of pure SAPO-5 hydrothermally from a mixture very similar to that reported by Jhung et al[102] to produce exclusively SAPO-34.

Summing up the different synthesis studies it seems that TPA produces mostly SAPO-5, while many other amines and ammonium ions (especially TEA) can produce both SAPO-5 and SAPO-34. In these cases rapid heating, low silicon content in the synthesis mixture and low pH seems to favour the crystallisation of the AFI phase. In addition, it seems as if SAPO-5 can be converted into SAPO-34 if the crystallisation is allowed to continue for long enough,

indicating that SAPO-34 is more stable under the synthesis conditions. Most reported synthesis methods produce large crystals, which could lead to diffusion limitations in catalytic applications, so producing small crystals may pose a challenge. Plate-like shapes are interesting because even if the crystals remain large, the effective length of the pores will decrease the thinner the plates are. The directions of the pores in hexagonal crystals are evident from the hexagonal unit cell of the AFI framework.

4.4 Catalysis

Catalytic measurements for the cracking of n-butane[20], cumene and isomerisation of o-xylene[97] show that while $AlPO_4$-5 is more or less inactive, H-SAPO-5 shows reasonable activity. H-SAPO-5 has also been tested for methanol conversion by a few research groups and shown to be active. The most noteworthy of these are summarized below.

Yang et al[109] tested and compared H-SAPO-5, -11 and -34 with low space velocity (Weight Hourly Space Velocity, WHSV, refers to the amount of reactant fed per gram of catalyst, per hour) of methanol at different temperatures. They found that H-SAPO-5 showed higher selectivity towards C7+ hydrocarbons than the others and that the predominant low olefin was butene, while H-SAPO-11 and -34 were more selective toward ethene and propene. Increasing contact time increased the selectivity toward both light olefins and aromatics, but the selectivity towards olefins was inversely proportional to the partial pressure of methanol while the selectivity towards aromatics was proportional to it. In addition, the selectivity to aromatics reached a maximum at temperatures between 300 and 350°C, with light olefin selectivity increasing at higher temperature.

Yuen et al[17] also compared selectivity in methanol conversion over the AFI framework to that over CHA, using many different material classes including zeolites, borosilicates, MAPOs and SAPOs. They found that the AFI materials produced substantial amounts of aromatics, mostly penta- and hexa-methylbenzenes together with smaller amounts of other methylated benzenes and even smaller amounts of naphthalenes. Aromatics are not present in the products of methanol conversion over the CHA topology. However, they found little difference in selectivity among the AFI materials even if the acidity was shown to differ.

Campelo et al's[94] study of deactivation during methanol conversion of several silicoaluminophosphates showed that both H-SAPO-5 and -34 was initially more active, but deactivated faster than H-SAPO-11, 31 and 41 at 400°C. It should, however, be noted that the acid site densities of the five materials were not the same. The reported initial selectivities showed that H-SAPO-5 was more selective toward C4 and C5+ hydrocarbons than the others.

Part I: Synthesis

5 Background for characterization methods

5.1 Scanning electron microscopy (SEM)

Scanning electron microscopy (SEM) can be used to study the microstructure of materials, including the size and shape of crystals. The basic principle of SEM is that a narrow beam of electrons is scanned in a raster pattern over a sample, while the yield of backscattered and/or secondary electrons is detected.[110] These signals are then used to create a "picture" of the sample. The backscattered electrons are high energy electrons and detection of these yields information about the sample composition, as heavy elements are more efficient scatterers and will thus appear brighter in the created image. Secondary electrons, on the other hand, are lower in energy and originate from the surface of the sample. Detection of these provides an analysis on the local curvature of the surface as the detector receives a greater amount of secondary electrons from protruding features of the sample than from recessed regions.[111]

The electron beam in SEM is produced from a filament through which a voltage, called the acceleration voltage, is applied to eject the electrons. The beam is then focused to a small spot by a series of lenses before reaching the sample as shown in figure 5.1. Vacuum conditions are required in the microscope both to ensure the stability of the electron source and to avoid scattering of the electron beam, but in some instruments the possibility of introducing small amounts of gas is available. This feature can be useful to avoid build-up of charge on the surface of non-conducting samples.[110]

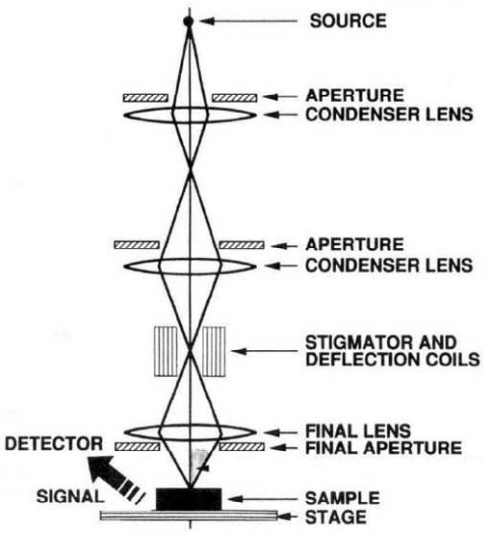

Fig. 5.1: Schematic representation of a scanning electron microscope, showing the path of the electron beam.[112]

5.1.1 Energy dispersive X-ray spectroscopy (EDS)

In addition to backscattered and secondary electrons, interactions of materials with electron also induce emission of x-rays. When an electron in the core shell of an atom has been ejected, the energy of the atom can decay by an electron transition from a higher orbital into the now vacant state. Such transitions are accompanied by the emission of x-rays with a wavelength characteristic of the emitting element.[110, 111] With an EDS detector, which is often part of a SEM instrument, these x-rays can give a quantitative analysis of the chemical composition of studied samples.

5.2 X-ray diffraction (XRD)

Crystalline materials consist of an ordered lattice of atoms that can be represented as parallel planes of atoms separated by a distance d. In x-ray diffraction (XRD), x-ray photons are elastically scattered by the atomic layers to give information on the crystal structure of the material studied. When a monochromatic ray of photons hits a crystal plane it will be reflected with an angle θ. The reflections from different planes will be in phase if the difference of photon path length is an integer number of wavelengths. In this case, constructive interference of the photons will lead to a strong signal in the detector while a difference in path length of a fractional number of wavelengths will lead to destructive interference. A simple schematic of two photons hitting two atomic layers of a crystal is shown in figure 5.2.

If either the sample or the detector is moved during radiation, the angles at which constructively interfering x-rays leave the sample can be measured. The Bragg's relationship:

$$n\lambda = 2d\ sin\ \theta$$

can then be used to calculate the spacing of the planes, which are characteristic of a crystal structure.[110] X-ray diffraction can be applied both to single crystals and powder samples.

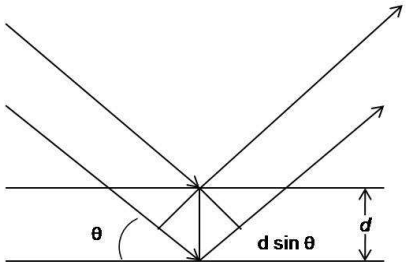

Fig. 5.2: Schematic representation of photons reflected from atomic planes. Adapted from [110].

As zeolites rarely form large enough crystals for single crystal diffraction, powder diffraction is most often used. The positions and intensities in a powder diffractogram can be compared to reference diffractograms to determine what phase(s) are present in the sample. Relative peak widths give information on the types of atoms present and their positions, while for crystals below ~100nm the peak width will be indicative of the crystallite size[110]. The background of the powder pattern will also indicate whether or not amorphous material is present in the sample as long as fluorescence or poor sample preparation can be neglected[12]. It is also possible to obtain unit cell parameters from good quality diffraction patterns. No matter what information is sought, care should be taken when crystallites of a morphology that favours a certain orientation is analysed, as this could cause significant changes in peak intensities.

5.2.1 In-situ XRD of crystallisation

In-situ XRD during crystallisation can be performed by using a capillary to hold the synthesis mixture (instead of an autoclave). The capillary is then placed in the x-ray beam and heated with a hot-air blower to crystallise the sample. Diffractograms are collected consecutively during the crystallisation time. To ensure hydrothermal conditions and prevent the synthesis mixture from leaving the capillary a pressure of inert gas, higher than the vapour pressure of water at the crystallisation temperature, is applied onto the capillary. The method is described by Norby[113] and a schematic of the capillary micro-reactor is provided in figure 5.3.

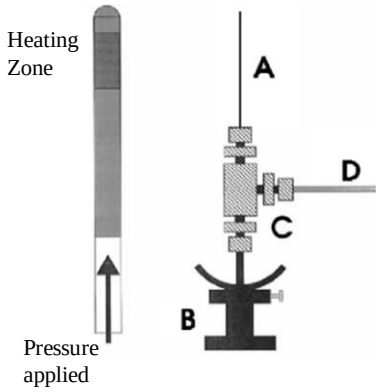

Fig. 5.3: Schematic of a micro-reactor used for in-situ studies of zeolite crystallisation. Adapted from Norby[113].

6 Experimental

6.1 Synthesis of SAPO-5

Syntheses were in all conventional experiments performed in stainless steel autoclaves with Teflon liners. The Teflon liners were washed with 15wt-% hydrofluoric acid (HF) and distilled water before before each experiment. Synthesis mixtures both with tri-n-propylamine (TPA) and triethylamine (TEA) were prepared in the following manner:

1. Distilled water and orthophosphoric acid were mixed
2. Alumina (Catapal B) was added and the mixture was stirred for a few minutes, usually turning the mixture into a very viscous gel.
3. To this, both silica (Cab-O-Sil unless otherwise mentioned, but Ludox AS-40 in some cases) and template were added, before the mixture was vigorously stirred or shaken until it appeared homogeneous. Upon mixing, the solution would produce significant amounts of heat and the viscosity would decrease greatly.

For syntheses performed in 40 ml or 150 ml liners, mixtures would usually be prepared directly in the liner to avoid losses during transfer. When other liners were used, reagents were mixed in a plastic vessel and later transferred to the liner. Autoclaves were then closed and placed in a preheated oven. Liners were most often be filled to between 60 and 80 % of maximum volume, except for microwave autoclaves which were never filled above 50 %.

Autoclaves were removed from the oven after a set time and quench-cooled by immersing in ice water. Recovery of product was accomplished by centrifuging the contents of the autoclave with copious amounts of distilled water before decanting. Standard procedure was four rounds of centrifugation (3000 rpm) for 15 minutes each. After the last centrifugation, the samples were dried at 60 °C.

6.1.1 Methods of heating

Several different ovens and heating methods were used in this work, and a description of these is given below:

- Static heating was performed in Termaks TS8000 series ovens and stainless steel autoclaves with 50ml liners were used as crystallisation vessels.
- Two different tumbling ovens were used. These were custom-made with a motor-controlled axis, around which the autoclaves could rotate. The difference between the two ovens was that the "old" tumbling oven was constructed around an older model Termaks oven which was slow to heat and had poor temperature control. It was observed to fluctuate with more than 10 °C during a synthesis and would use up to an hour to regain crystallisation temperature again after opening to insert the autoclaves. The "modern" tumbling oven was built around a Termaks TS8000 series oven with much better temperature control and the ability to reach crystallisation temperature in less than 10 minutes after insertion of autoclaves. In addition, the "old tumbler" used 40 ml liner autoclaves, while syntheses in the "new tumbler" were performed in autoclaves using 50 ml liners. In both ovens, a Teflon coated magnet was included to ensure thorough mixing of reactants during tumbling. Until chapter 7.2.4, only the "old" tumbling oven was used.
- The magnetic stirring oven used was a custom-made Termaks TS8000 series oven. This was built with magnetic stirrers under the autoclaves, so that Teflon coated magnets in the synthesis mixtures could provide fast stirring. Stainless steel autoclaves with 40ml liners were used with this oven.
- Mirowave syntheses were performed in a Milestone MicroSYNTH labstation (max. power: 1000 W) using plastic autoclaves with 80 ml liners. Teflon coated magnets were used for stirring.

6.2 SEM

Scanning electron microscopy (SEM) was performed to determine particle sizes and morphologies of synthesised samples. This was performed on a FEI Quanta 200 FEG-ESEM. The microscope was equipped with both an Everhart-Thornley secondary electron detector and a detector for backscattered electrons in addition to the possibility of performing energy dispersive x-ray spectroscopy (EDS). Microscopy was usually performed at working distances of around 10 mm with acceleration voltages between 5-10 kV. High vacuum conditions were used for all samples.

6.3 XRD

All XRD performed in this thesis was done on powders. The method was used to determine the phase identification and purity of the synthesised samples and was in addition shown to give some insight into the morphology of the crystals. The instrument used was a Siemens D-500 with primary Ge monochromator and Bragg-Brentano geometry. The radiation used was CuKα with a wavelength λ = 1.5406 Å.

Samples were prepared by mixing the powder with ethanol or water before dispersing it on a glass plate and allowing the liquid to evaporate. The diffractograms were collected in the area 2θ = 3-60° using a count time of 0.5 minutes and step size of 0.015°.

6.4 In-situ XRD

In-situ crystallisation studies were performed in a similar diffractometer as above, with capillary set-up. The synthesis mixture was introduced into a 1 mm quartz capillary, and the goniometer holding it was modified with Swagelock fittings to allow the introduction of a pressurised N_2 gas to ensure hydrothermal conditions in the capillary. Pressure used was > 15 bar and the capillary was heated with a hot air blower. The count time was 0.2 seconds, giving a time from the start of one analysis to the start of the next of approximately 13 minutes. To simulate the slow heating of an autoclave, the capillary was heated linearly to the crystallisation temperature during a period of ~90min.

7 Results and discussion

7.1 Synthesis of SAPO-5 using tri-n-propylamine (TPA) as template

7.1.1 Synthesis under static conditions

Synthesis mixtures based on example 13 in the original silicoaluminophosphate patent[19] were prepared and crystallised at 200 °C under static conditions using tri-n-propylamine (TPA) as SDA and Cab-O-Sil silica source. The amount of orthophosphoric acid relative to the other reactants was varied to see the effect of this parameter. The relative molar amounts used are given in table 7.1, below.

Table 7.1: Synthesis conditions and composition of mixture in relative molar amounts. Note that the composition is given as the oxides of the possible T-atoms.

H_2O	Al_2O_3	P_2O_5	SiO_2	TPA	Time	Temp.
50	1.0	0.6 – 1.0	0.4	2.1	24 hours	200 °C

Representative SEM micrographs and diffractograms of the products from three syntheses with differing phosphorous content are shown in figures 7.1 and 7.2 respectively. The diffractograms are compared to a standard diffraction pattern of an AFI material and it is evident that this phase has been obtained in all syntheses. The background of the diffraction patterns suggests the presence of amorphous material in addition to the crystalline AFI phase. This background is less prominent for the sample containing the highest amount of phosphorous.

SEM confirms the similarity of the samples as the crystals of all three consist of slightly deformed hexagonal “barrels” of varying sizes, with a mean size of approximately 10 µm. Material of less pronounced shape and size, assumed amorphous, is also present in all samples. In the sample with P/Al = 1, small amounts of intergrown needle shaped material is also observed. EDS of all samples confirm that the crystals in all samples contain silicon in similar amounts. The presumed amorphous material consists primarily of Al and O, with some Si and P. The amount of phosphorous relative to aluminium increases with the P/Al ratio in the synthesis mixture.

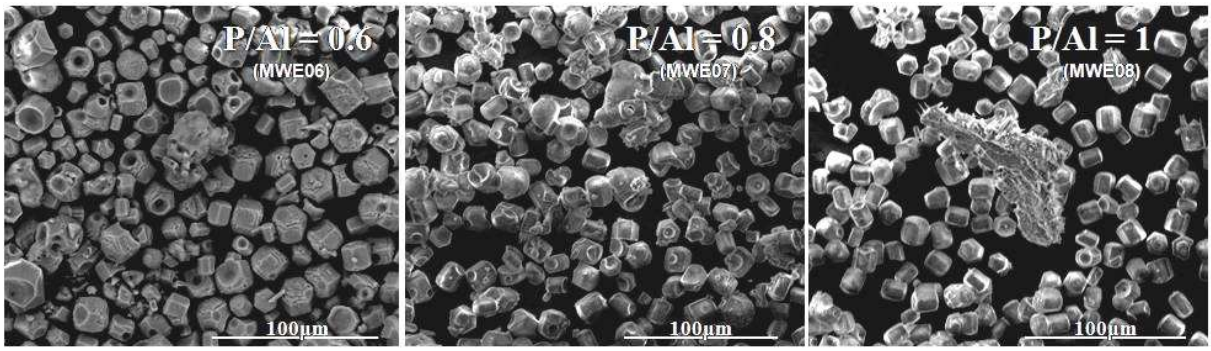

Fig. 7.1: SEM micrograph showing the effect varying the P/Al ratio in the synthesis mixture. Note the needle-like shapes in the middle of the rightmost image (P/Al =1).

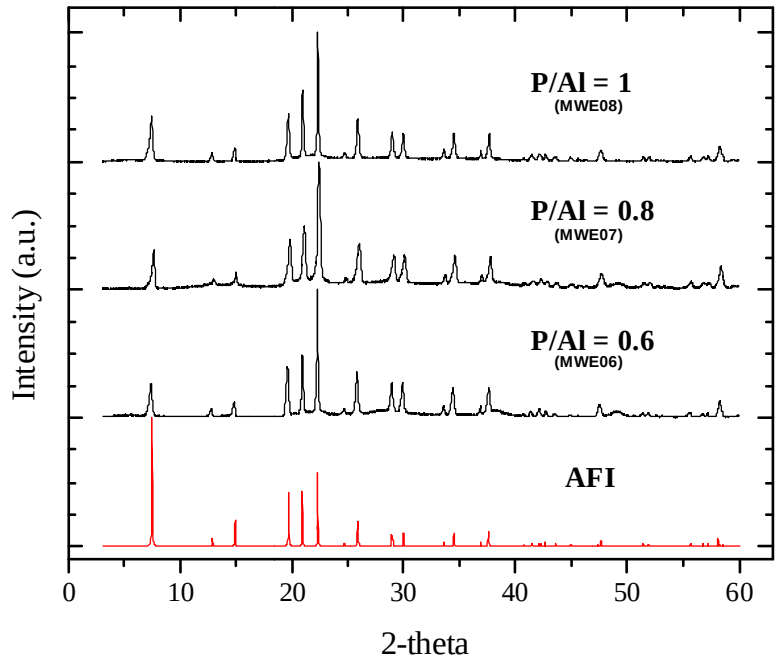

Fig. 7.2: Diffractograms for samples synthesised with different P/Al ratio compared to a standard diffraction pattern from IZA.[8] All peaks present in the reference are present in all three sample diffractograms and no extra peaks are present.

Reproduction of the sample with least phosphorous (P/Al = 0.6) was performed a few times and an attempt at scale-up was performed in a 150 ml autoclave (mixture with P/Al = 1). In addition, ageing the mixtures between 1 hour and 3 days before heating was attempted on a series of syntheses containing equal amounts of P and Al. In all cases except one, AFI was the only phase present in XRD, but SEM micrographs revealed the products of some syntheses to consist of more rounded crystals than those shown above. The morphology of these crystals were similar those shown in the next section (fig 7.4), but no systematic reason for when rounded or hexagonal crystals were produced could be found. In the one sample where a crystalline impurity was present, this was identified as a tridymite phase.

7.1.2 Crystallisation under tumbling conditions

As stirring during crystallisation has been found to decrease crystal size in other zeolites[114], attempts were made to synthesise SAPO-5 using a tumbling oven. Keeping in mind the observation of Jhung et al[100] that high concentration of SDA leads to plate like crystals in microwave synthesis, variation of the amount of TPA relative to the other compounds in the synthesis mixture was also performed. Synthesis conditions and contents of synthesis mixture for the series with varying template amount are given in table 7.2.

Table 7.2: Synthesis conditions and composition of mixture in relative molar amounts.

H_2O	Al_2O_3	P_2O_5	SiO_2	TPA	Time	Temp.
50	1.0	1.0	0.4	2.1 – 3.9	24 hours	200 °C

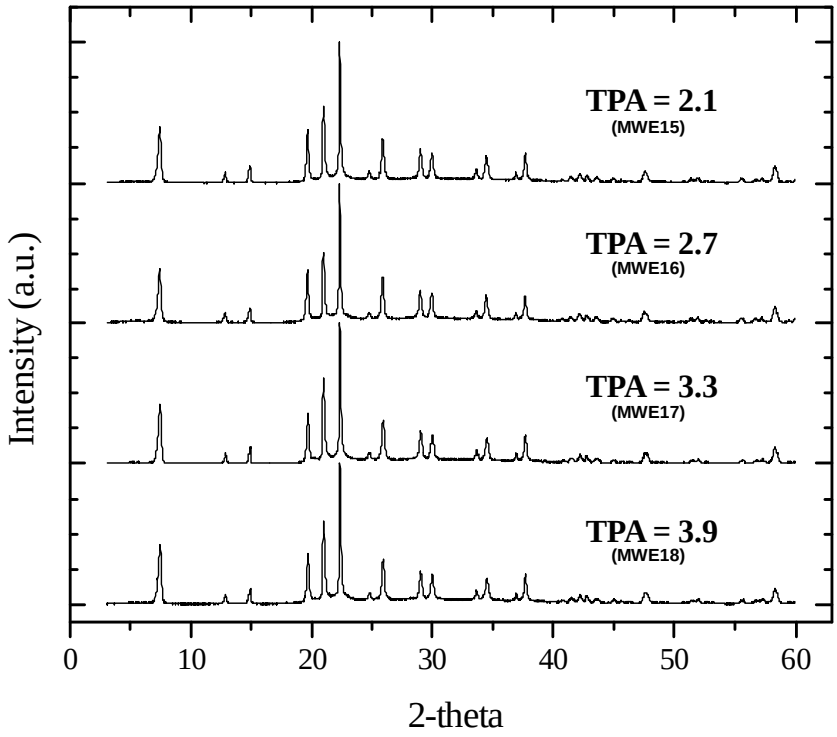

Fig. 7.3: Diffraction patterns of the synthesis series with varying concentration of TPA. All patterns indicate AFI as the only phase present and intensities are similar.

X-ray diffraction of all samples show pure AFI phase (see figure 7.3) with no observable difference induced by the varying amount of TPA template. SEM micrographs (shown in figure 7.4) of the samples reveal roundish crystals of varying size but with the majority of the crystals having a diameter of around 10 µm. Only traces of the seemingly amorphous material observed after static crystallisation is visible when tumbling conditions are employed. EDS

indicates that the silicon content of the small amounts of amorphous material present was much higher than in the crystals. No apparent differences between the samples can be found, neither in the morphology nor phase purity.

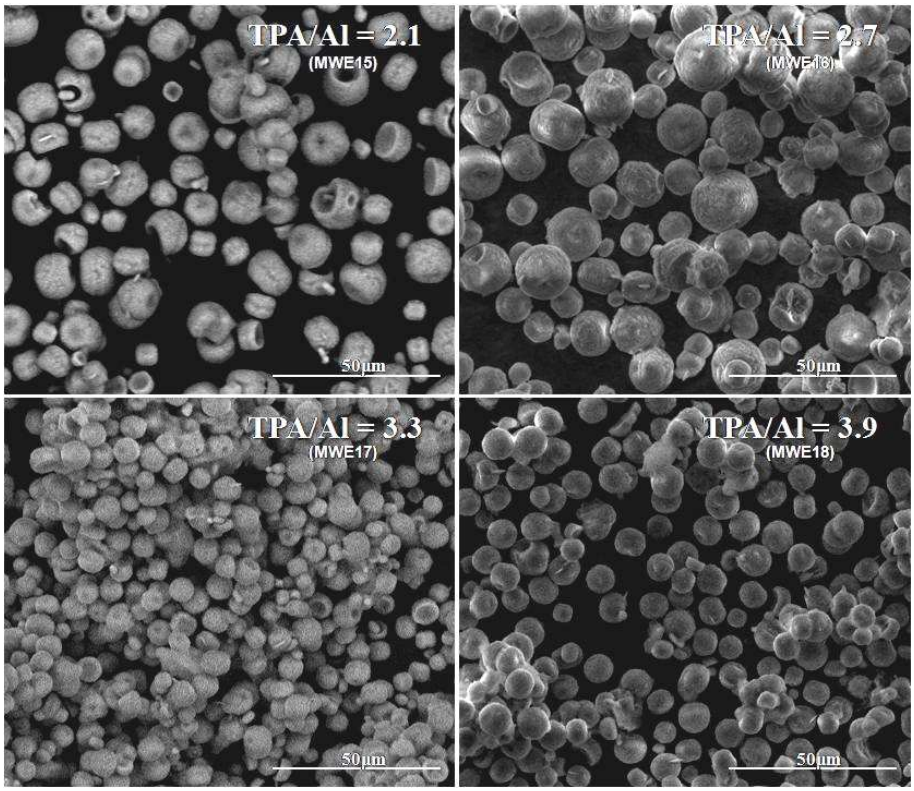

Fig. 7.4: SEM of samples synthesised with different amounts of template. Morphology or size does not appear to change much with this.

Weyda and Lechert[93] have reported that fully crystalline SAPO-5 can be obtained after only 3-4 hours of crystallisation under similar conditions as those employed here. In addition, Ganschow et al[115] report that the morphology of $AlPO_4$-5 crystals, synthesised with triethylamine and microwave heating, changes as the synthesis time is increased. In an attempt to produce SAPO-5 of different (plate-like) morphology, the effect of decreasing crystallisation time was investigated. In addition, a parallel series of differing crystallisation times at a lower temperature (180 °C) was performed. The range of conditions studied is displayed in table 7.3.

Table 7.3: Synthesis conditions and composition of mixture in relative molar amounts.

H_2O	Al_2O_3	P_2O_5	SiO_2	TPA	Time	Temp.
50	1.0	1.0	0.4	3.9	4 - 24 hours	180 or 200 °C

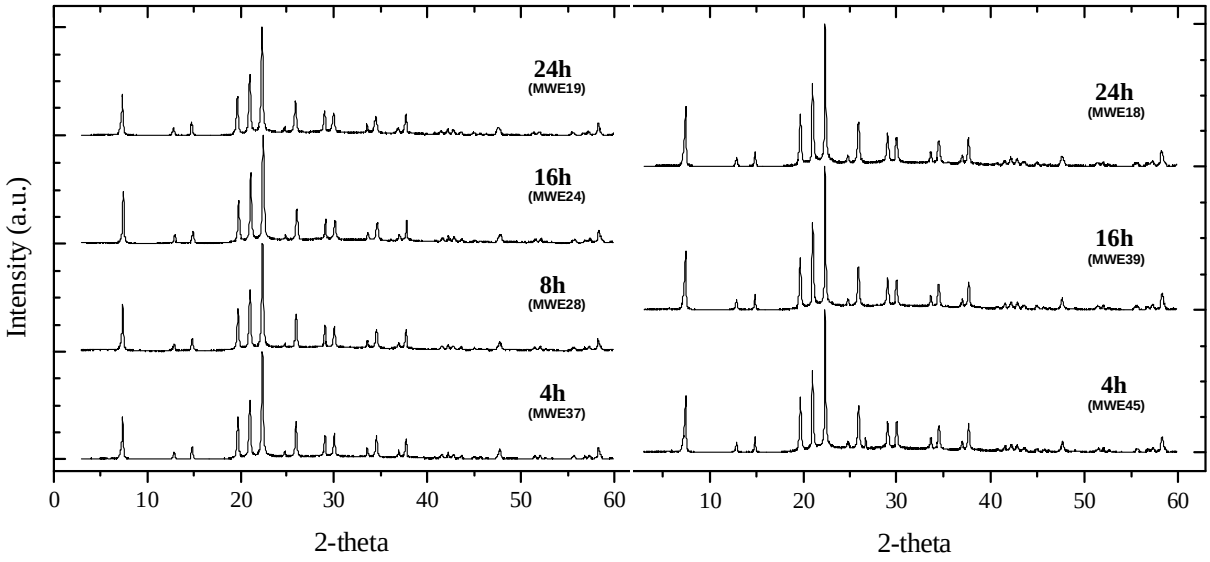

Fig. 7.5: Effect of changing crystallisation time at 180°C (left series) and 200°C (right series). No change in crystallinity or phase purity can be observed by XRD upon either changing temperature or crystallisation time.

The diffraction patterns at all crystallisation times and both temperatures, shown in figure 7.5, reveal no differences between the samples. Thus, it was confirmed that no more than 4 hours of crystallisation time is required to achieve fully crystalline AFI phase at these conditions. SEM reveals the presence of somewhat more plate-like crystals in the samples crystallised at 180°C, as shown in figure 7.6. However, the morphology and size is varied in all samples at this temperature, and the majority of the crystals are roundish. Samples crystallised at 200 °C are indistinguishable from previous samples such as those shown in figure 7.4.

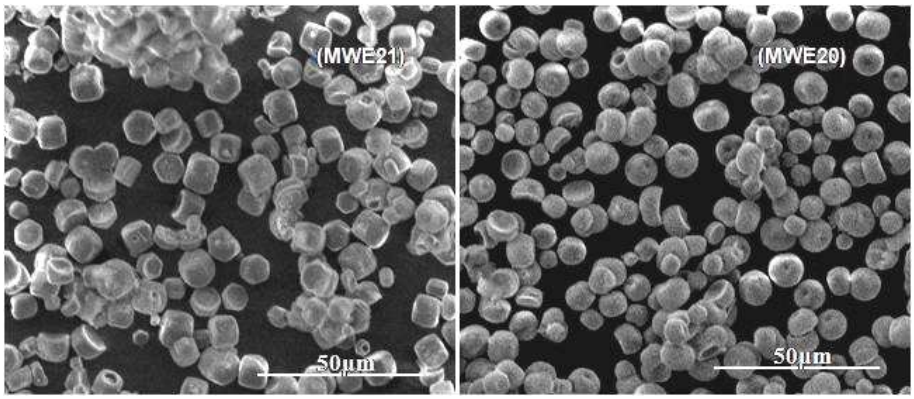

Fig. 7.6: SEM micrographs of samples crystallised 180°C. These two samples have been crystallised for 24 hours and with different amounts of water, but they are still representative of all samples crystallised at 180 °C.

Attempts to obtain different morphology or size of crystals by varying the amount of silica relative to alumina in the range of Si/Al = 0.05 – 0.5 in the synthesis mixture were also performed. Both Demuth et al[96] and Jhung et al[103] report that the amount of silica in the synthesis mixture influences the crystal morphology. In spite of this, no change in the product compared to the previous samples was observed even when also varying the crystallisation time and temperature. For the sake of brevity, XRD patterns are not shown here and only the range of conditions studied are given in table 7.4. For a more complete overview of the conditions and results, the reader is referred to appendix A.

Table 7.4: Composition of synthesis mixture in relative molar amounts in addition to the range of conditions employed.

H_2O	Al_2O_3	P_2O_5	SiO_2	TPA	Time	Temp.
50	1.0	1.0	0.2 – 1.0	3.9	4 - 24 hours	180 or 200 °C

Similarly to this, a variation of water content (from 30 to 100, relative to Al) in the synthesis mixture did not appear to cause any changes in the product. It is again referred to appendix A for specifications on synthesis mixture compositions and conditions.

7.1.3 Summary of TPA synthesis

All syntheses performed with TPA as template (except one) yielded a pure AFI phase product of good crystallinity. Where SEM has been performed, EDS confirms the presence of silicon

in the crystals, indicating that the products are indeed SAPO-5 crystals. The relative amount of silicon in the crystals has not been studied, but the presence of silicon-rich seemingly amorphous material suggests lower relative Si content in the crystals than in the synthesis mixtures. It has been previously reported that the amount of incorporated silicon in SAPO-5 is limited (see e.g. [116]).

It can be established from these results that TPA is very selective towards producing the AFI framework under the conditions employed in this work. This is likely the reason why Lok et al[20], in the original publications on silicoaluminophosphates, reported this amine as the typical template for producing SAPO-5.

Morphology of the crystals appears to vary between spherical and hexagonal shapes, but what conditions produce which morphologies is not obvious from the studies. It is possible that lower temperature produces more plate-like crystals, and that hexagonal crystals can only be obtained by static heating. However, as reproductions do not always produce the same morphology, these observations may also be coincidental. Either way, little success in morphology control has been achieved using TPA as template during this work. Some amorphous material is present in all samples, but the amount appears to decrease when using tumbling conditions.

7.2 Synthesis of SAPO-5 using triethylamine (TEA) as template

As Jhung et al[100-104] has demonstrated a large degree of morphology control with the use of TEA template and microwave irradiation, attempting to follow in their footsteps appeared like a reasonable way to obtain either smaller or plate-like crystals. Unfortunately, the lack of microwave facilities at the time excluded this heating method. Although Jhung et al[102, 104] claim that only SAPO-34 is formed under hydrothermal conditions, both Qinhua et al[97] and Weyda and Lechert[93] report pure SAPO-5 using this template and hydrothermal heating. Syntheses described in chapters 7.2.1 - 7.2.3 are all crystallised in the “old” tumbling oven.

7.2.1 Variation of crystallisation time

Synthesis mixtures with reactant molar ratios as outlined in table 7.5 were prepared and crystallised at 180 °C. Initial findings revealed that only CHA was formed after 24 hours of crystallisation time. For this reason, syntheses with shorter crystallisation times were attempted.

Table 7.5: Synthesis mixture compositions used in study of crystallisation time with TEA template. Temperature and range of crystallisation times employed are also indicated.

H_2O	Al_2O_3	P_2O_5	SiO_2	TEA	Time	Temp.
50	1.0	1.0	0.4	3.9	4 - 24 hours	180 °C

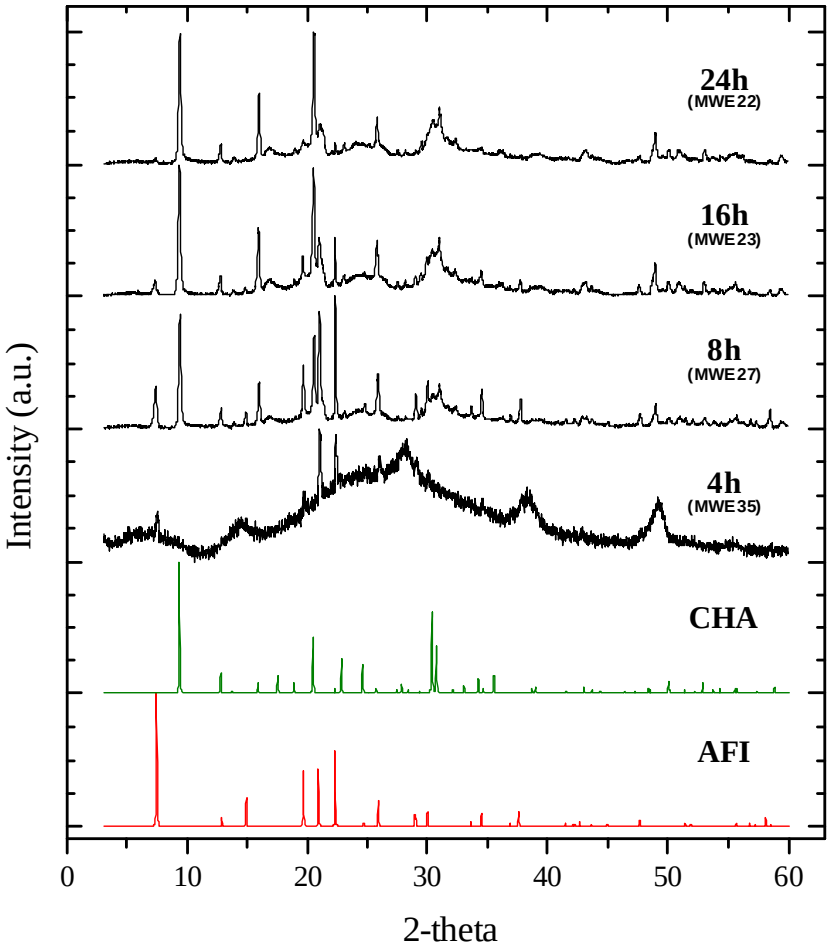

Fig. 7.7: Diffraction patterns of samples crystallised for x hours. Mixture compositions are given in table 7.5. Reference diffractograms of AFI and CHA are included for comparison.

As figure 7.7 shows, a decrease in crystallisation time clearly yielded more of the AFI phase. When crystallised for 4 hours, no reflections indicative of the CHA phase were visible. Thus,

it may be possible to form highly crystalline AFI phase if the crystallisation time is increased slightly above 4 h.

7.2.2 Variation of silica content

In the same manner as with TPA syntheses, silica content in the synthesis mixtures was varied over a relatively large range. A comparison of the 4 h sample shown in figure 7.7 and a sample of higher silica content is shown in figure 7.8. While both samples are mostly amorphous, there is a clear indication that the silica content determines which phase is formed initially. The exact synthesis conditions of the two samples are given in table 7.6.

Table 7.6: Synthesis mixture composition in relative molar amounts of oxides and the time and temperature of crystallisation.

H_2O	Al_2O_3	P_2O_5	SiO_2	TEA	Time	Temp.
50	1.0	1.0	0.4 or 1.0	3.9	4 hours	180 °C

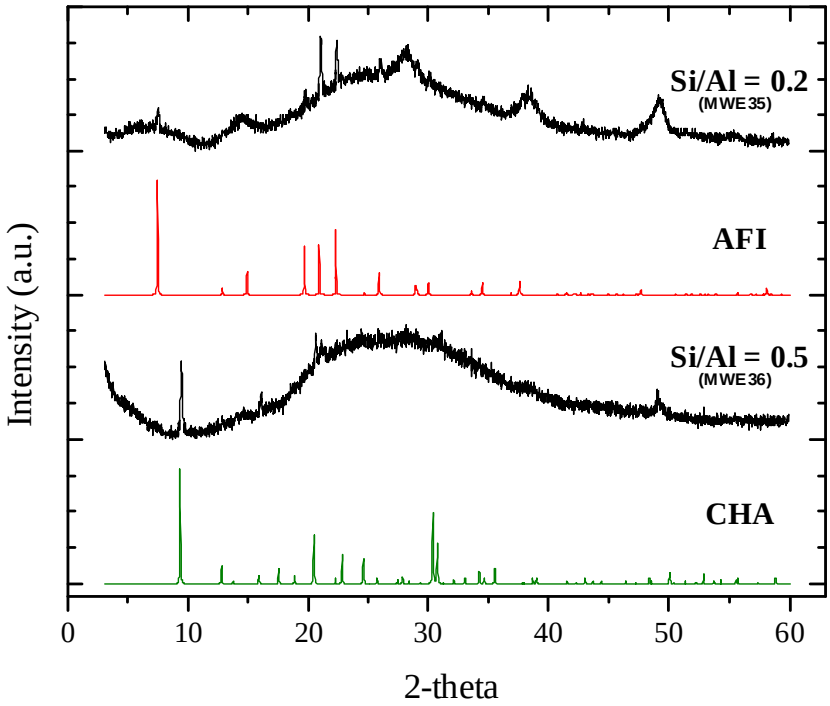

Fig. 7.8: Diffraction pattern of samples crystallised with high Si content (no. 2 from bottom) and intermediate Si content (top) compared with the reference AFI and CHA patterns.

When increasing the crystallisation time slightly to 4.5 h, the crystallinity of the samples improves significantly. A series of syntheses mixtures containing different amounts of silica

(composition shown in table 7.7) were prepared. Diffraction patterns of the products after 4.5 hours of crystallisation are displayed in figure 7.9.

Table 7.7: Composition, in relative molar amounts of oxides, and synthesis conditions.

H_2O	Al_2O_3	P_2O_5	SiO_2	TEA	Time	Temp.
50	1.0	1.0	0 – 1.0	3.9	4.5 hours	180 °C

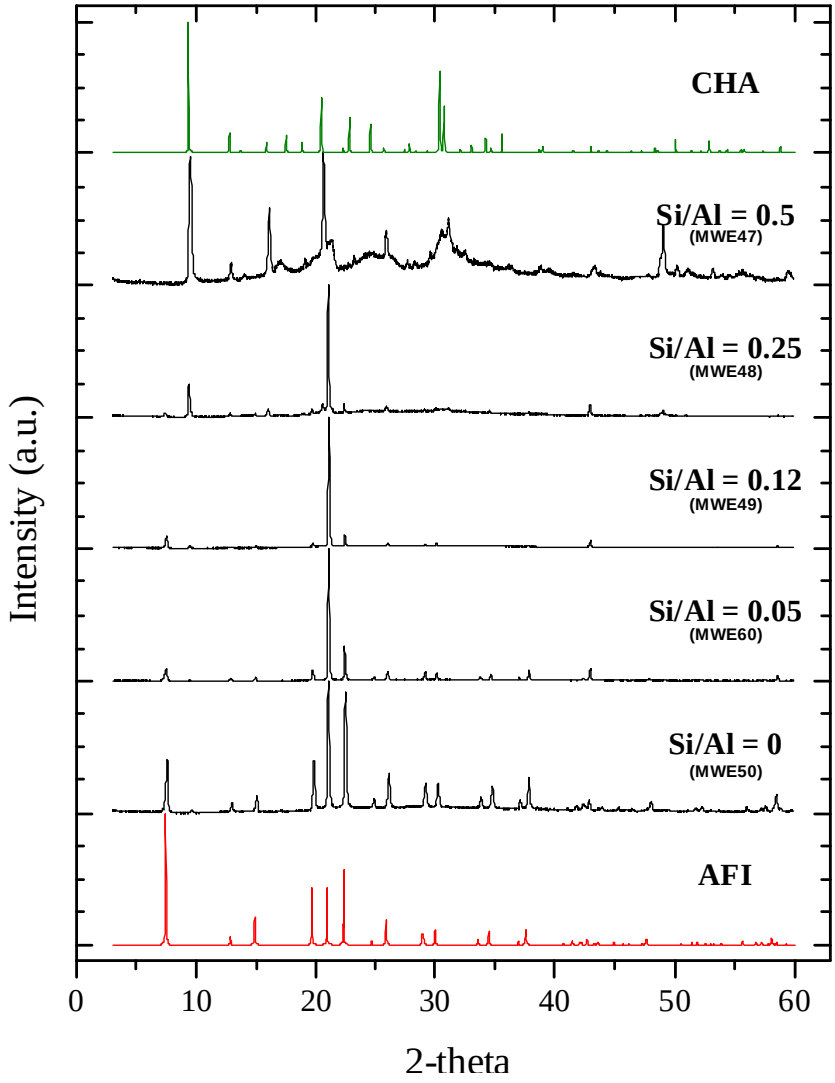

Fig. 7.9: Diffractograms revealing the effect of varying the Si content at 180°C.

Figure 7.9 clearly shows that when the silica content is decreased, the formation of the CHA phase is repressed in favour of the AFI phase. Another interesting observation is that in the AFI phase, the intensity of the peak at 21° is more intense than the two peaks surrounding it (at 19.7° and 22.3°). This differs both from the reference diffractogram and the samples synthesised with TPA. According to the "Collection of Simulated XRD Powder patterns for Zeolites"[117], this peak is a result of reflections from the 002 plane, and the intensity of this

peak has been attributed to the aspect ratio of AFI crystals by several groups[99, 100]. A high intensity of this peak usually indicates a plate-like morphology of the crystals. The effect itself is most likely caused by a preferential orientation effect of the sample, as relative intensities vary significantly with sample preparation method.

SEM of the nearly pure AFI samples reveal crystals of hexagonal plate-like morphology with dimensions of around 10 x 3μm. Some smaller hexagonal crystals are also present, in addition to small amounts of small cubic CHA crystals and some shapeless, presumably amorphous matter. EDS confirms that the crystals contain silicon, but the relative amount is higher in the CHA than the AFI crystals. While the exact crystal sizes vary between samples, the micrographs shown in figure 7.10 are representative of most samples synthesised at this temperature and similar conditions, when the product is predominantly of the AFI phase.

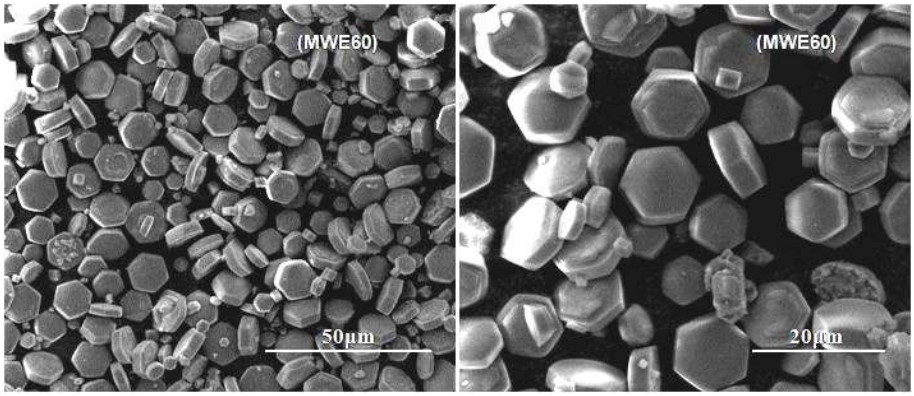

Fig. 7.11: SEM micrographs of samples with Si/Al = 0.05 (left and middle) showing plate-like morphology. With careful study, it is possible to spot a few small cubic crystals.

One exception to this is the sample prepared without any addition of silica, for which SEM (figure 7.11) reveals crystals of much less defined shape and widely varying crystal sizes. XRD (figure 7.9) also revealed a higher amorphous background in this sample than those of low Si content. The seemingly lower crystallinity of this sample may indicate that Si in the synthesis mixture is advantageous for crystal growth. Demuth et al[96] have also reported that Si-free AFI crystals synthesised with TEA often exhibit shingle-like growth patterns and partially blocked channel systems. Jhung et al[103] also observed similar, inhomogeneous, morphologies during microwave

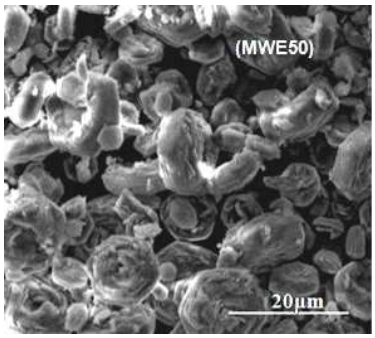

Fig. 7.10: AFI crystals prepared without added Si

syntheses when crystallisation time was short, but report more homogeneous and defined crystals with longer crystallisation. If this is the case in the hydrothermally crystallised sample as well, it could hint to a faster crystallisation when silica is present. While the reason for this is uncertain, it is possible that a more heterogeneous synthesis mixture provides more favourable conditions for nucleation. No further studies of crystallisation without added Si were performed in this thesis.

In summary it is evident that at the conditions employed here, the silica content in the synthesis mixtures is a deciding factor of which phase is obtained. A low amount of silica results in formation of the AFI rather than the CHA phase and at low crystallisation time (4.5 hours), pure SAPO-5 can be obtained. The yield of this is very low, however, with less than 500 mg calcined crystals produced from close to 4 g of reactant oxides.

Curiously, a sample crystallised from a synthesis mixture with very high content of silica (Si/Al = 1) under the same conditions as above (4.5h at 180°C), yielded a crystalline product seemingly containing more AFI than CHA phase. While this may be due to random experimental errors, a similar result at higher temperature (vide infra) decreases the likelihood of this. This could suggest that an upper limit of Si content where CHA is no longer the most stable phase exists. EDS of the latter sample also indicate that the Si content of the latter sample's crystals is not particularly high, begging the question of where the silica ends up. Too much speculation on this topic is not warranted as few experiments were performed with this much silica, and not all the results agree (see list of syntheses in appendix A).

7.2.3 Variation of temperature

In order to determine whether crystallisation temperature would affect the synthesis products, several synthesis mixture compositions were crystallised at varying temperatures (180 °C - 220 °C). Assuming that stopping the synthesis as soon as possible after crystals were formed was beneficial for obtaining AFI phase, the crystallisation time was in most cases lowered as the temperature was increased.

Diffractograms of products obtained from identical, high-silica, mixtures at 180°C, 200°C and 220°C are shown in figure 7.12. The samples were crystallised for 4.5, 4 and 3.5 hours

respectively, and the composition of the synthesis mixture is given in table 7.8. While high-silica mixtures such as this was previously shown to lead to product exclusively of the CHA phase at 180 °C, an increase in temperature evidently yields more of the AFI phase. At 220 °C, AFI is the dominant phase.

Table 7.8: Composition, in relative molar amounts of oxides, and synthesis conditions.

H_2O	Al_2O_3	P_2O_5	SiO_2	TEA	Time	Temp.
50	1.0	1.0	1.0	3.9	4.5 - 3.5 hours	180 - 220 °C

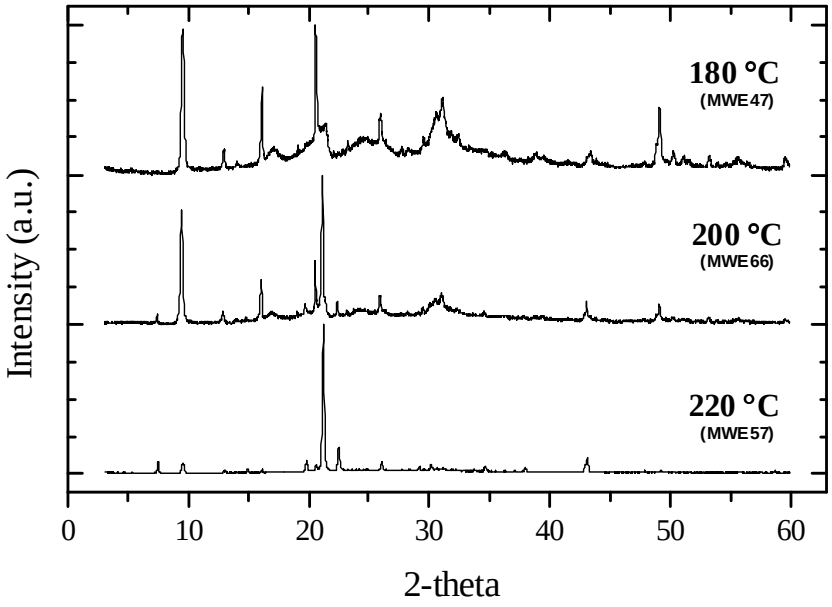

Fig. 7.12: Effect of temperature on a synthesis mixture with high silica content.

When the synthesis mixture contains less silica, the diffraction patterns shown in figure 7.13 also reveal an increased yield of AFI phase with higher temperature. The series chosen for display has intermediate silica content and produces an AFI phase with some CHA impurity at 180°C, while at the higher temperatures the CHA reflection at 9.5° is markedly smaller. The compositions and synthesis conditions are given in table 7.9.

Table 7.9: Composition, in relative molar amounts of oxides, and synthesis conditions.

H_2O	Al_2O_3	P_2O_5	SiO_2	TEA	Time	Temp.
50	1.0	1.0	0.3	3.9	4.5 - 3.5 hours	180 - 220 °C

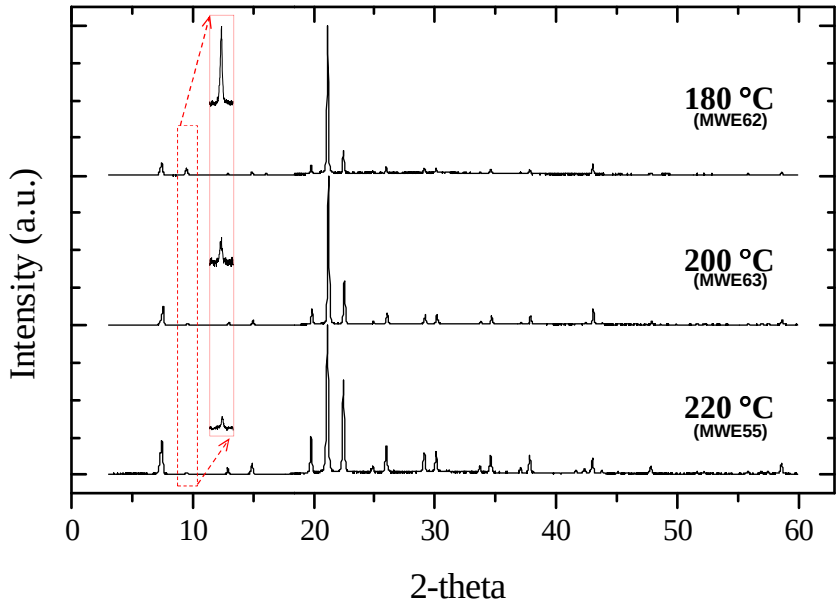

Fig. 7.13: Effect of temperature on a synthesis mixture with intermediate silica content. The CHA peaks at 9.5, indicated and magnified, can be seen to decrease with higher temperature.

As displayed by the SEM micrographs of (nearly) pure AFI samples in figure 7.14, the crystal size appears to increase with increasing temperature. All the crystals possess hexagonal plate-like morphology, but the thickness of the plates appears to increase with higher crystallisation temperature. While very few pure-phase samples are available for comparison, the assumption that the crystal size of SAPO-5 is dependent on crystallisation temperature is not unreasonable as similar results have been found for other zeolites, such as Na-X and silicalite[114]. An increase in crystal size with temperature could indicate that the crystal growth rate is more affected than the nucleation rate by temperature changes[114].

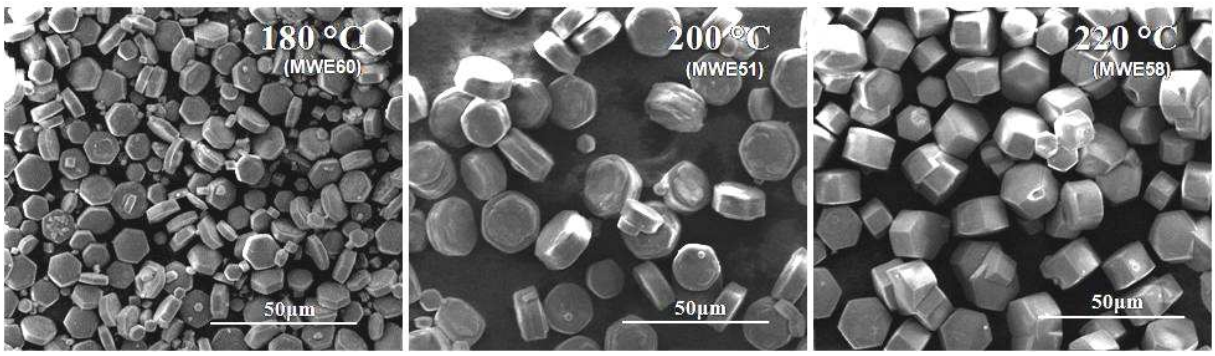

Fig. 7.14: SEM micrographs of pure AFI crystals synthesised from mixtures of low Si content at 180 °C (left), 200 °C (middle) and from a very Si-rich mixture at 220 °C (right).

Knowing that low silica content, high temperature and short crystallisation time all favour crystallisation of the AFI phase, production of pure SAPO-5 is possible. However, the yield of crystals is low and it is not easy to reproducibly obtain samples free of CHA impurities, while at the same time maintaining high crystallinity. Also, while 220 °C seemed to be the ideal temperature for producing the AFI phase, several attempts at this often led to a mixture of poorly crystalline phases (AFI and CHA, in addition to one or more unidentified phases). Even though this was likely due to a poor choice of silica source (as Ludox AS-40 was later discovered to cause such problems during microwave syntheses), no more experiments at this temperature were performed. In fact, the only pure SAPO-5 obtained at this temperature was made from a synthesis mixture containing a Si/Al ratio of 1 (SEM micrograph shown in figure 7.14).

7.2.4 Effect of faster heating, autoclave size and stirring method

The effect of a number of parameters, including use of a more modern oven than the tumbling oven used previously, was investigated. In general, the use of the "modern", faster heating tumbling oven (see experimental section 6.1.1 for details on ovens) resulted in results similar to previous syntheses in the "old" tumbling oven. Optimal conditions for producing plate-like AFI crystals were low-silica synthesis mixtures and short crystallisation time. Very few attempts at varying the temperature were performed, but no reason to doubt that an increased temperature is favourable for AFI crystallisation was apparent. Samples free of CHA impurities were still difficult to obtain, but this was somewhat easier than in the "old" oven. The yield of crystals was also slightly improved. The fact that faster heating of the synthesis mixtures is more favourable for crystallisation of AFI than CHA is in agreement with the results of Vistad et al[108], namely that slow heating is beneficial for crystallisation of CHA.

One notable difference when using "modern" ovens was the additional crystalline phase formed under conditions where nearly pure CHA would be formed in the "old" oven. The diffractograms shown in figure 7.15 are peculiar in that the reflection at ~9.5 ° is very intense and the accompanying SEM micrograph clearly shows an additional phase of pyramid-shaped crystals. The additional phase was identified as AEI ($AlPO_4$- or SAPO- 18), and the intense

~9.5 ° reflection is caused by partial overlap of reflections from crystal planes in both CHA and AEI.

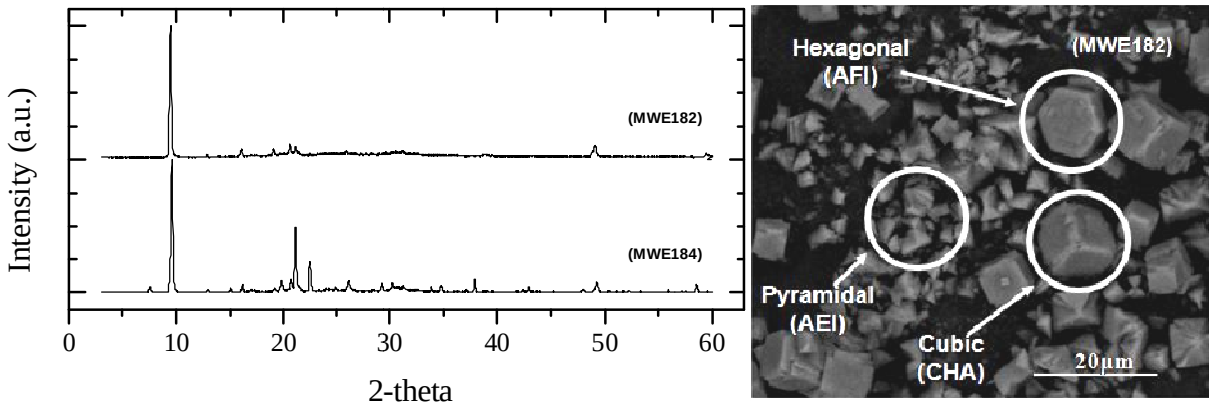

Fig. 7.15: Diffraction patterns of mixed phase crystalline products (left) and SEM showing hexagonal plate-like, cubic and pyramid-like crystals (right).

Syntheses performed at 200°C utilising magnetic stirring instead of tumbling shows the exact same trend as previously observed when varying crystallisation time. Yields and reproducibility are also similar to syntheses in the "modern" tumbling oven. Under synthesis conditions like those outlined in table 7.10, an AFI phase is formed at short time while CHA dominates at longer synthesis times. This is evident from the diffraction patterns in figure 7.16. However, the diffraction pattern at long crystallisation time also indicates the presence of the AEI phase. As this phase was only observed when the modern ovens were used, and then irrespectively of autoclave size or stirring method, it is assumed that crystallisation of AEI is favoured by faster heating rate.

Table 7.10: Composition, in relative molar amounts of oxides, and synthesis conditions.

H_2O	Al_2O_3	P_2O_5	SiO_2	TEA	Time	Temp.
50	1.0	1.0	0.1	3.9	3.5 - 4.5 hours	200 °C

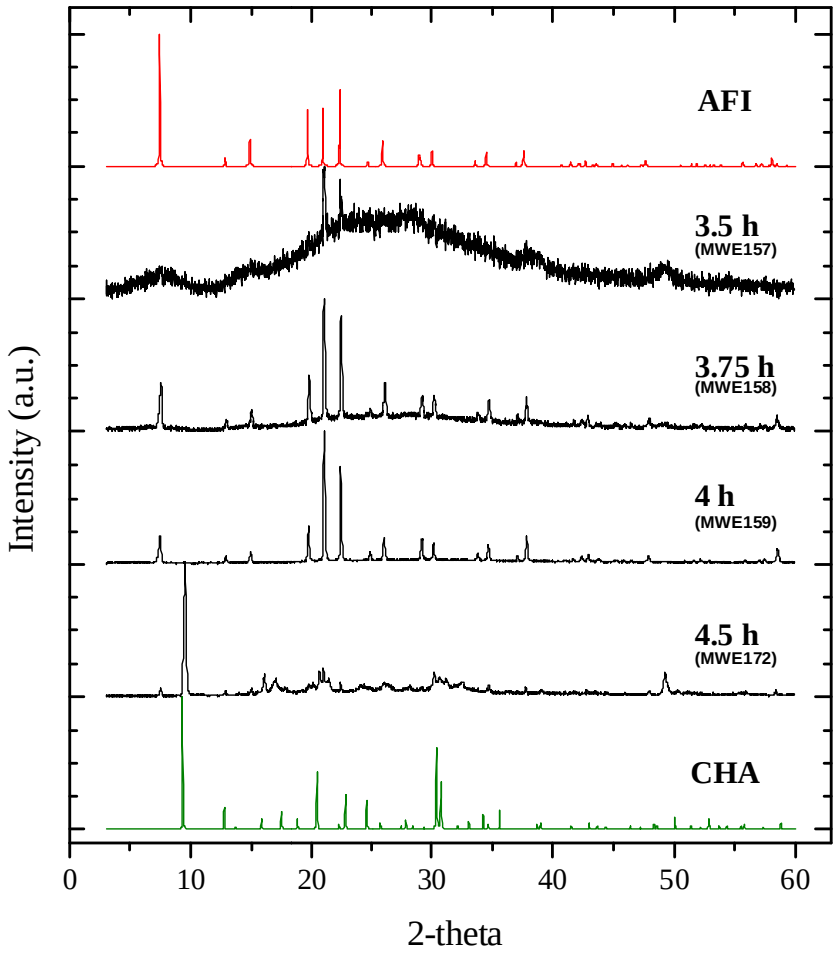

Fig. 7.16: XRD patterns showing the effect of synthesis time at 200 °C with magnetic stirring.

When characterised by SEM (micrographs shown in figure 7.17), samples which have been magnetically stirred are less homogenous than those crystallised under tumbling conditions. Also, when a temperature of 180 °C is employed, the crystals look like they are stuck together with amorphous matter. Thus, it was concluded that tumbling conditions are more favourable for producing homogeneously sized crystals.

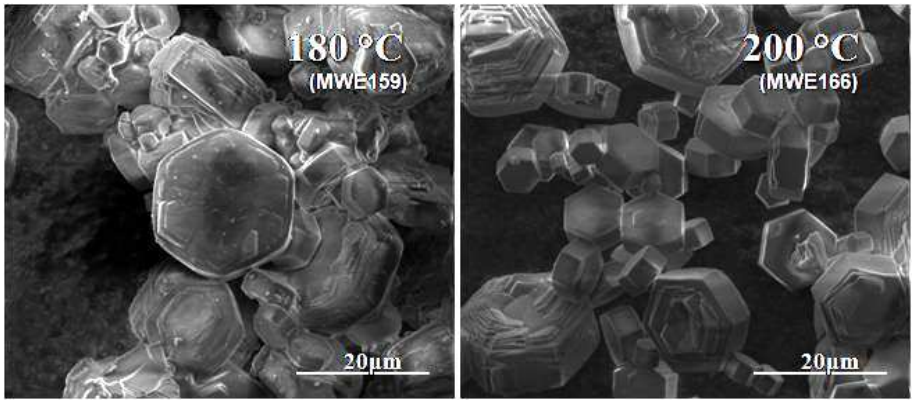

Fig. 7.17: Micrographs of samples crystallised with magnetic stirring at different temperatures.

7.2.5 Seeding

Even though conditions where formation of the AFI phase dominates have now been found, the syntheses still suffer from poor reproducibility and low yield of crystals. In an attempt to remedy this, small amounts of seed crystals from earlier syntheses of pure, plate-like, SAPO-5 was added to some synthesis mixtures. Such addition of small amounts of crystals to a synthesis mixture is known to be an effective method to "direct" the crystallisation towards the seeded phase[30, 114]. All syntheses with seeding were crystallised in the modern tumbling oven with synthesis conditions as shown in table 7.11. This practice was very successful as highly crystalline pure AFI phase was formed in most syntheses. Yields were also better than previous syntheses, with 2-3 g of (calcined) product formed from 6.5 g reactant oxides.

Table 7.11: Composition, in relative molar amounts of oxides, and synthesis conditions.

H_2O	Al_2O_3	P_2O_5	SiO_2	TEA	Time	Temp.
50	1.0	1.0	0.1	3.9	4 hours	200 °C

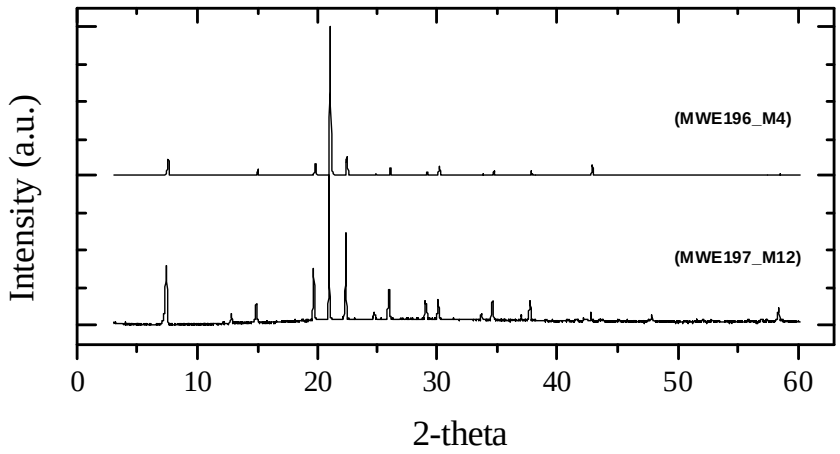

Fig. 7.18: XRD patterns of two batches of crystals obtained using seeded synthesis mixtures.

Figure 7.18 shows two representative diffraction patterns of seeded syntheses in tumbling oven. All samples displayed a very intense reflection from the 002 plane (at 21°), indicative of plate-like samples (usually of intensity between the two patterns in figure 7.18). Variations in this intensity between the samples are likely to be primarily caused by the sample preparation, as no systematic variations in morphology were detected by SEM. Figure 7.19 displays SEM micrographs of crystals from seeded syntheses. The samples are composed of hexagonal crystals with sharp edges, and thus appear very similar to non-seeded samples crystallised in the "modern" tumbling oven. Crystal sizes are quite homogenous, with cross-

sections of ~10 µm and thickness between ~2-4 µm. An interesting feature not observed in previous syntheses is the large crystals visible in the left image of figure 7.19. While these represented very few of the total number of crystals, they were nevertheless present in all plate-like seeded samples. A possibility is that these are the seed crystals themselves which, in addition to promoting nucleation, has grown larger during the heating period.

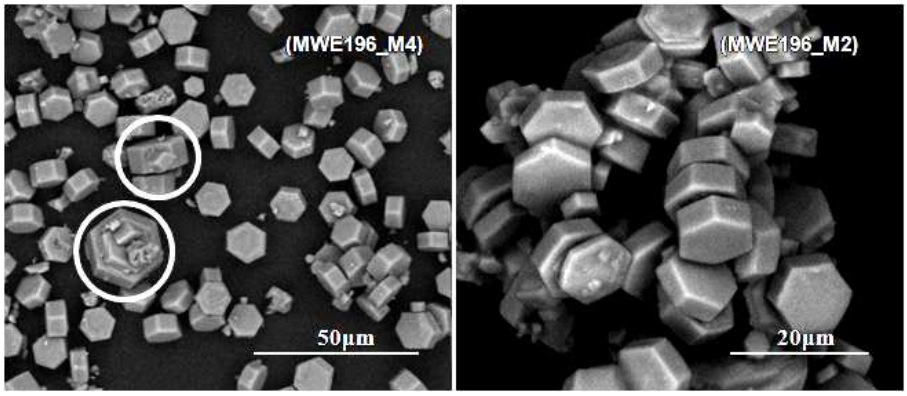

Fig. 7.19: Crystals obtained from seeded synthesis mixtures. Note the two large crystals in the image on the left.

Several different samples of plate-like crystals were used as seeds without observing any difference in the product. However, the addition of the hexagonal barrel-shaped crystals from TPA synthesis (such as those of figure 7.1) led to a product with less homogeneous morphology, but smaller crystal size, as shown in the SEM micrograph of figure 7.20. The reason for the dramatic change in crystal size and morphology is unknown, but the obtained crystals are of high crystallinity and significantly smaller than previously observed.

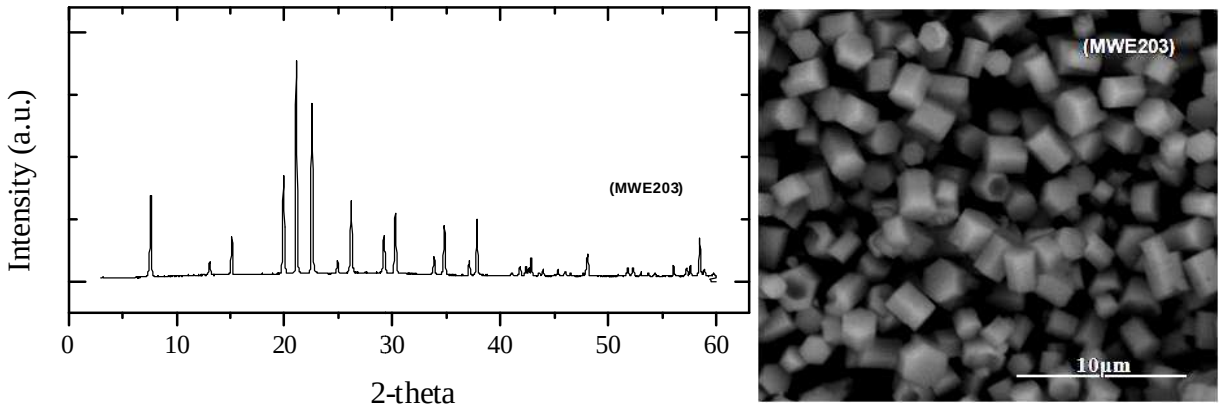

Fig. 7.20: XRD and SEM of a sample crystallised with seeds from a static TPA-templated synthesis. The largest crystals in the micrograph on the right are approximately 2x2.5 µm.

7.2.6 Syntheses performed with microwave irradiation

Advantages to microwave synthesis include faster crystallisation[30, 106, 118] and also in some cases the crystals formed are reported to possess more uniform and perfect habits[106]. In addition, Jhung and Yoon et al[102, 104] have reported that synthesis mixtures containing TEA subjected to microwave irradiation selectively form the AFI phase. When microwave facilities became available, syntheses with variation of several parameters were performed. These included temperature, heating rate, crystallisation time, amount of template and amount of silica in synthesis mixture. However, the experiments were largely unsuccessful and the majority of them suffered from poor temperature control caused by the controlling thermocouple being in contact with water only, whose interaction with microwaves was very different from that of the synthesis mixtures. Only a brief summary of highlights and lessons learned is given here, and the interested reader is referred to appendix A for an overview of what syntheses were performed.

The first synthesis attempt following the procedures used earlier (i.e. stopping the synthesis shortly after crystallisation) appeared to yield plate-like crystals in high yield. This led to the assumption that the method was appropriate with microwave syntheses, and many attempts to reproduce the early success were made. Three main problems were encountered: uneven heating caused the autoclaves to frequently ventilate their contents, the appearance of unwanted (dense) phases and profound difficulties in trying to predict the exact crystallisation time.

The first of these obstacles has already been mentioned, and was due to the controlling thermocouple being immersed in water instead of a synthesis mixture. After changing standard practice and always placing the thermocouple in one of the synthesis mixtures, unwanted ventilation of the autoclaves ceased to be a problem. The unwanted by-products are described by Jansen[118] and are ascribed to inadequate stirring of the mixture before crystallisation. While this is not a problem in hydrothermal heating, the fast crystallisation during microwave irradiation makes complete mixing of the reagents critical for a successful synthesis. Allowing at least 15 minutes of vigorous stirring before heating appeared to solve the problem, as unwanted phases were hardly ever observed after this was made standard practice. Predicting crystallisation time proved difficult, as it varied greatly between experiments. In most of the microwave syntheses Ludox AS-40 was used as the silica source

(as opposed to most of the conventional syntheses, where Cab-O-Sil was used), and this seemed to cause further randomisation of the crystallisation time. The reason for its adverse effect on synthesis control is thought to be due to its low purity, as larger silica particles introduced in the synthesis mixture could influence the nucleation of the mixture. While Ludox AS-40 allowed easier handling of synthesis mixtures by reducing their viscosity, the discovery of the reproducibility problems it caused led to Cab-O-Sil being used again.

Even after all these problems were solved and Cab-O-Sil was used, crystals made with microwave heating displayed large variations in morphology. Table 7.12 shows the synthesis conditions of four pure AFI phase samples produced with microwave irradiation, while figure 7.21 and 7.22 contains diffraction patterns and SEM micrographs for the same samples.

Table 7.12: Composition, in relative molar amounts of oxides, and synthesis conditions.

Sample	H_2O	Al_2O_3	P_2O_5	SiO_2	TEA	Time	Temp.
a	50	1.0	1.0	1.0	3.9	40 min	190 °C
b	50	1.0	1.0	1.0	3.9	25 min	190 °C
c	50	1.0	1.0	0.1	3.9	1 hour	180 °C
d	50	1.0	1.0	0.1	3.9	45 min	180 °C

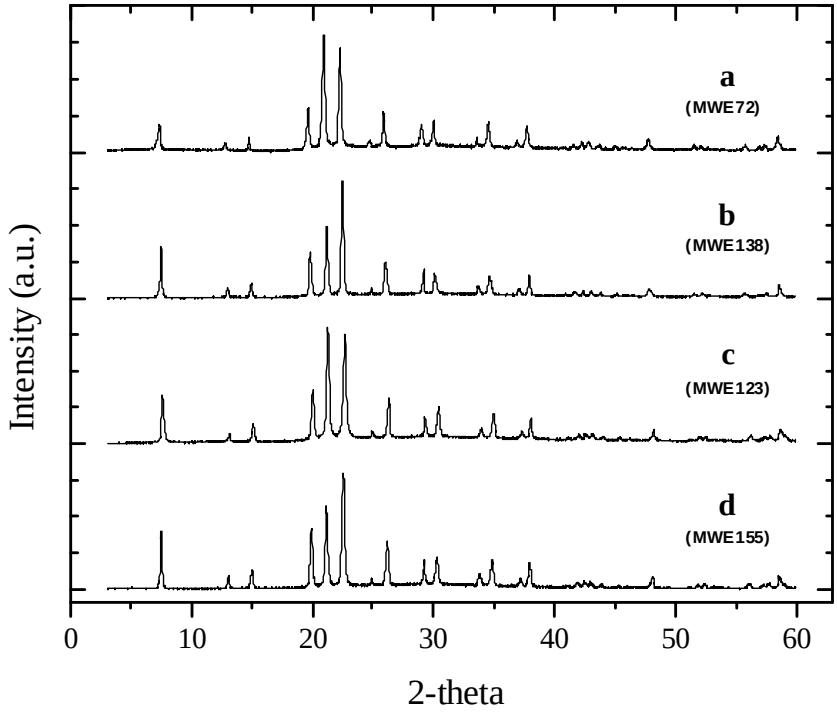

Fig. 7.21: XRD patterns of the samples detailed in table 7.12. All are pure AFI phase.

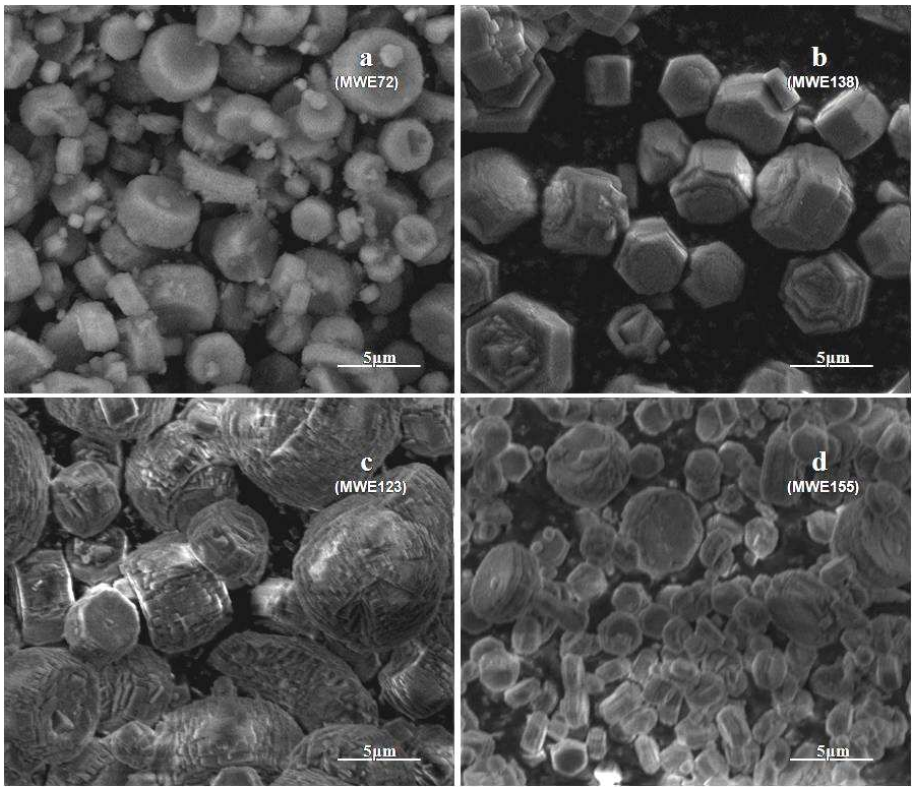

Fig. 7.22: Examples morphologies of microwave-crystallised samples. Note the much smaller crystal size than previously observed from hydrothermal heating.

While the use of microwave irradiation for production of SAPO-5 was abandoned after these observations, some useful knowledge can still be gleamed from the results. Firstly, although a great many parameter variations were attempted, no CHA impurities were observed in any of the samples crystallised by microwave irradiation. This could indicate that when the heating of the mixture is very rapid, CHA formation is repressed. This would be in line with earlier results found by Vistad et al[108]. When trying to synthesise SAPO-34 using a morpholine template they found that a key pre-phase for CHA formation does not form when heating is too rapid. The other interesting observation from microwave synthesis is the fact that all crystals studied with SEM are small. While crystals prepared with other methods mostly fall in the 10-20 µm range, those prepared by microwave irradiation are typically smaller than 5 µm.

7.2.7 Summary of syntheses with TEA

Using TEA as template, both CHA and AFI phases can be formed by hydrothermal synthesis. Several factors influence the relative amounts formed of the two phases and the effects of the investigated parameters on phase selectivity is given in table 7.13. It should be noted that while higher Si content generally promotes CHA formation (as indicated in the table), some experiments indicate that very large amounts of silica in the synthesis mixtures favours the AFI phase.

Table 7.13: Effects of varying synthesis parameters for a synthesis mixture containing TEA

Parameter	Effect
Higher Si content	Promotes CHA formation
Longer crystallisation time	Promotes CHA formation
Higher T	Promotes AFI formation Size of AFI crystals is increased
Faster heating rate	Promotes AFI formation
Seeding	Greatly favours growth of the seeded phase
Stirring	Tumbling increases homogeneity in size and morphology of AFI crystals

It is possible to produce pure SAPO-5 by optimising conditions to favour AFI formation (low Si, high T) and stopping the synthesis as soon as crystallisation occurs. Unfortunately, reproducibly stopping the synthesis at the point where only AFI has formed is difficult and often leads to either amorphous samples or CHA impurities. This may be a result of heterogeneity in the mixtures leading to differences in the time before crystallisation occurs. Even though all liners were washed with HF before use, there could still be a variable amount of particles introduced into the mixture which would supply a surface for nucleation. By adding seeds of pure AFI phase, this problem is circumvented since formation of CHA is strongly repressed. In nearly all syntheses, the morphology of the AFI phase is hexagonal and plate-like.

In microwave syntheses, the CHA phase is not observed. Whether this is due only to the faster rate of heating or some other interaction with the radiation is not known. However, it appears likely that the heating rate is the dominant factor as SAPO-34 has previously been shown not to form at fast heating rates, since the time is then too short for a key pre-phase to form before crystallisation of SAPO-5 starts[108]. Despite this, microwave irradiation at short synthesis times proved unpredictable for morphology control and subject to several problems. In hindsight, more effort should perhaps have been focused on microwave irradiation at longer synthesis time as this is a proven method[100-104] of morphology control.

7.3 In-Situ XRD

To study the formation of SAPO-5, crystallisation was followed by in-situ XRD. The experiment used a standard low-silica synthesis mixture and was crystallised at 200°C. The synthesis conditions are given in table 7.14.

Table 7.14: Synthesis conditions of the in-situ XRD experiment. See text for detail of synthesis time. The maximum temperature was reached after approximately 90min.

H_2O	Al_2O_3	P_2O_5	SiO_2	TEA	Time	Temp.
50	1.0	1.0	0.1	3.9	*	200 °C

Figure 7.23 shows the evolution of the synthesis mixture over time and already at scan number 7, the pattern of AFI is visible. This corresponds to just a bit more than 90 minutes of synthesis time (13 minutes between scans), meaning that the crystallisation has proceeded significantly faster in the capillary micro-reactor than in a regular autoclave. Further along in time we see that another phase starts growing. However, contrary to most conventional syntheses, this phase does not seem to be the CHA phase as the characteristic peak at 9.5°C is not present. The observed peaks appear to fit a number of denser phases of silica or alumina, but its exact nature has not been determined. Five hours after the first appearance of this phase, all traces of the AFI phase had vanished, leaving only the unidentified reflections. Another interesting feature is the bump centred around 5° which appear just before crystallisation starts, which could be due to an ordering of the reactants into some amorphous precursor. In figure 7.23, only data from the first three hours of synthesis is included in order to preserve the clarity of the figure.

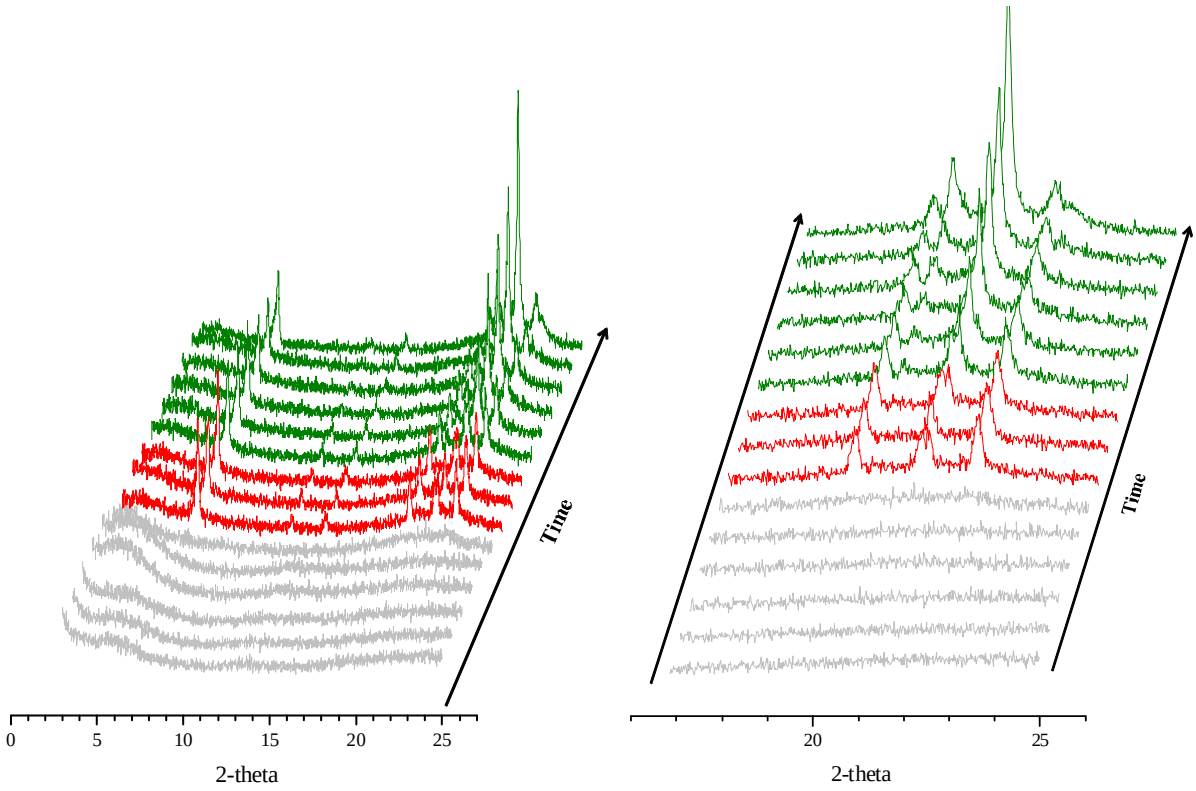

Fig. 7.23: XRD patterns from synthesis of SAPO-5. The left figure shows the complete diffraction range, while the right shows a close up of the 15-25° region to more clearly show the impurity peaks growing at 20° and 21.5°. The red area shows the time interval where AFI is the dominating phase. The time between each pattern is approximately 13 minutes, with the earliest scans shown at the bottom (closest to the reader).

Differences between syntheses carried out in an autoclave and a capillary have been documented before, but whether the crystallisation proceeds faster or slower in a capillary seems to differ.[113, 119] The main difference between this setup and an ordinary autoclave synthesis is the volume of the container, but other factors such as the fact that only a small part of the capillary is heated could also lead to differences in crystallisation even though the heated area is much larger than the X-ray beam. While it is difficult to directly compare the synthesis methods, both show that the AFI phase has a tendency to form early, but dissolves over time in a mixture containing TEA.

The smaller volume of the capillary leads to more interaction with the reactor walls, which would lead to a higher relative area for heterogeneous nucleation to occur on. The fact that the crystallisation was significantly faster in the smaller reaction volume could indicate that heterogeneous nucleation is very important for formation of the AFI phase.[113]

8 Conclusions and further work

Several samples of pure SAPO-5 have been produced with differing crystal sizes, morphologies and Si content. While the largest crystals might be affected by diffusion limitations when used in catalytic testing, crystals where the lengths of the micropores are only a few µm long have also been produced and should be suitable for this purpose.

Large differences between the two templates used for synthesis (TPA and TEA) have been uncovered, both in morphology and in phase selectivity. While synthesis mixtures containing TPA appear to crystallise as pure AFI phase under a large range of conditions, TEA containing mixtures show selectivity towards other phases as well. Most notable of these is the CHA phase. While factors such as silica content, temperature, heating rate and synthesis time can be tuned to lower the amount of impurities in the crystalline products of a TEA containing synthesis mixture, the addition of seeds is necessary to consistently obtain a pure SAPO-5 product. Morphologies of the AFI crystals are also seen to vary with the template used, as TPA seems to preferentially crystallise hexagonal barrels or (presumably polycrystalline) roundish morphologies, while TEA mixtures produce almost exclusively plate-like crystals.

Effects of heating methods and stirring have also been investigated. It was found that tumbling of the synthesis mixtures decreases the amount of amorphous material formed in syntheses with TPA. For TEA syntheses a more homogeneous size distribution was found under these conditions. Microwave crystallisation was shown to have a large impact on the production of impurities in TEA syntheses, with no other zeotype phases formed, and also to decrease the average size of crystals produced. The morphologies did not appear controllable at the conditions investigated, though.

The results also provide a small hint to the crystallisation kinetics of the AFI phase in TEA syntheses. The apparent growth in crystal size with temperature could indicate that the growth rate increases more than the rate of nucleation upon temperature, possibly due to a higher activation energy for growth than for nucleation[114]. The importance of heterogeneous nucleation rather than homogeneous is also suggested by the significantly faster

crystallisation in the smaller volume of a capillary than in an autoclave. However, this might also be due to a significantly faster heating of the mixture under these conditions.

Many possibilities for further work are apparent after the results here. Especially the competitive growth of CHA and AFI phases, which seems to be present under many different synthesis conditions, is worth studying. As crystallisation mechanisms of zeolites are generally poorly understood further studies of which parameters affect the two phases, and in what way, may provide valuable insight for more directed future syntheses.

While the morphologies of the hexagonal AFI phase have been proven variable over a large range of aspect ratios[96, 99-101, 103, 120], more investigations could yield even further variations. Tian et al[99] succeeded in producing different morphologies of transition-metal substituted AFI crystals by adding surfactant to the synthesis mixtures. Such a procedure could be attempted for the silicon-containing SAPO-5 as well. The fact that Choi et al[121] recently succeeded in synthesising single-unit-cell MFI crystals from a surfactant containing synthesis mixture proves the applicability of this type of compound for control of zeotype morphology. Very thin plate-like AFI could be interesting as e.g. membrane material.[96]

Part II: Spectroscopy and adsorption studies

9 Theory of experimental techniques

9.1 Thermogravimetric analysis (TGA)

Thermogravimetric analysis allows monitoring of a sample's changes in mass with variations in temperature. The instrument consists of a small precision balance, upon which the sample is placed, and an oven encapsulating the volume around the sample. It is often possible to introduce controlled atmospheres inside the oven. In this work, TGA set-ups were used both for temperature-programmed desorption (TPD) measurements and for the adsorption of tri-n-propylamine (TPA) in the samples. In the latter case, the mass was monitored at constant temperature.

9.2 Characterisation by adsorption or desorption of probe molecules

9.2.1 Surface area measurements by N_2 adsorption

The surface area of solids can be determined by adsorption of small molecules. Most commonly, characterisation of porous materials is carried out by adsorption of N_2 at its liquefaction temperature of 77 K (- 196 °C). The Braunaer-Emmet-Teller (BET) isotherm[122] can then be employed to find the specific surface area of the material. This isotherm assumes equivalent adsorption sites for all molecules in the first layer, no adsorbate-adsorbate interactions and that adsorption on top of the previous layer with adsorption energy equal to the condensation energy proceeds to infinity at the saturation pressure. The linearised version of the isotherm is given as:

$$\frac{P}{V_a(P_0 - P)} = \frac{1}{\chi V_0} + \frac{\chi - 1}{\chi V_0}\frac{P}{P_0}$$

Where χ is the ratio of the desorption rates from the second and first adsorbate layer, V_a is the volume of adsorbed gas, V_0 is the volume of adsorbed gas in the first monolayer, P_0 is the equilibrium pressure of the adsorbed gas while P is the partial pressure of the adsorbed gas. From a plot of $\frac{P}{V_a(P_0-P)}$ vs. $\frac{P}{P_0}$, a straight line through the points at low P/P_0 can be used to find the number of molecules in the first layer. From this, the surface area is available if the molecular diameter is known. While the assumptions of the BET isotherm are not strictly

applicable to zeolitic materials as very little multilayer adsorption takes place in the pores, BET areas can still be used for comparison of similar materials[123].

In addition to the surface area, the shape of an adsorption isotherm can also reveal characteristics of a material. Hysteresis loops caused by capillary condensation may indicate the presence of mesopores. The IUPAC has published guidelines on the characterisation of porous materials by physisorption, including descriptions of common isotherm shapes[124].

9.2.2 Characterisation of pore size and diffusion

The adsorption rate versus time for large probe molecules with dimensions similar to the zeolitic pores can provide valuable information on pore structure in zeolitic materials. For example, Chen and Zones[125] have demonstrated that adsorption of 2,2-dimethylbutane can be used to distinguish both between 10- and 12-ring structures and between different structures of similar pore dimensions. The uptake rate will be indicative of the diffusivity of the probe inside the pores of the material. A good overview of the use of probe molecules for characterisation purposes is given by Traa et al[126]. It is possible that by using a probe of suitable dimensions, differences in diffusivity can be detected in samples of the same structure. For use on H-SAPO-5 samples a larger probe than 2,2-dimethylbutane (kinetic diameter 6.2 Å[125]) is likely needed as pore diameters in this structure is 7.3 Å[10]. Chen et al[127] have reported that essentially no adsorption of 1,3,5-triisoprobylbenzene (kinetic diameter 8.5 Å) is observed in SSZ-24 (AFI structure), while Traa et al[126] recommends the use of tertiary alkylamines for characterisation of 12-ring structures.

9.2.3 Temperature - programmed desorption (TPD)

Acidic sites of zeolitic materials can be investigated by temperature-programmed desorption of a suitable base such as NH_3. The principle of the method is to adsorb a basic compound on the material before increasing the temperature slowly and observing at what temperature the adsorbates desorb. Desorption can be monitored either by mass spectrometry or by thermogravimetric methods. When investigating zeolitic materials, it is common to use NH_3 as the probe molecule and to leave it at a slightly elevated temperature for some time to ensure removal of physisorbed molecules before heating commences. As NH_3 will desorb

from weaker acid sites at lower temperatures than from stronger sites, the method provides a measure of acidic strength. The amount of NH_3 desorbing also provides a measure of the amount of available sites.

9.3 Fourier Transform Infrared Spectroscopy (FTIR)

Transitions between vibrational (and rotational) energy levels of molecules and materials can occur by absorption of photons with frequencies ν in the infrared range. However, absorption will only occur when a change in dipole moment is associated with the transition. This means that molecules must either possess an electric dipole moment or one must be induced during vibration for successful use of infrared spectroscopy. In Fourier transform infrared spectroscopy (FTIR), the sample is irradiated with infrared radiation and an interferogram is produced. The interferogram is a complex signal of intensity as a function of time, containing all the frequencies of the infrared spectrum and to convert this into the more useful spectra of intensity versus frequency, a mathematical operation known as a Fourier transform is used. The vibrational frequencies of a chemical bond will increase with increasing bond strength and with decreasing mass of the vibrating atoms. A more thorough coverage of infrared spectroscopy can be found in the references [110, 128, 129].

In catalysis, infrared spectroscopy is commonly used to study probe molecules and the manner in which these interact with the catalyst[110]. For zeolites, characterisation of acidic sites in the frequency region of O-H stretching vibrations has proven valuable and it is possible to monitor the interaction of the acidic site with various probe molecules. For instance, the strength of the acidic sites in zeolitic materials has been frequently measured by the adsorption of a weak base such as CO. In such an experiment, the O-H bond of the zeolite will weaken upon adsorption (shifting it to a lower frequency) and the range of the shift can be used as a measure of the acidic strength. The same type of information can also be obtained from the change in vibrational frequency of the adsorbate. For a thorough discussion on FTIR spectroscopy of zeolites, see [130, 131]. FTIR spectra of zeolites are usually presented as absorbance versus wavenumber ($\bar{\nu}$), where $\bar{\nu}$ is inversely proportional to the wavelength (λ) (or proportional to the frequency ν):

$$\bar{\nu} = {}^{1}/_{\lambda} = {}^{\nu}/_{c}$$

10 Experimental

10.1 Calcination of the samples

Except for SEM and XRD (which has been previously shown), all characterisation and testing was performed on samples that had been calcined to remove the templating agent used in the synthesis. Samples B/H, SC, P/H and B/L were calcined in a muffle-furnace for 2-3 hours and were removed when the powder was completely white. The exact time varied between the samples and depending on the amount of powder being calcined. For sample P/L, some black spots (possibly indicating the presence of a small amount of denser phase zeolitic material) were visible in the powder after this treatment. Further calcination was performed on this sample by heating it to 600 °C under an N_2 flow in a tube furnace. After reaching 600 °C, the flow was changed to pure O_2 and the sample left at this temperature for three days.

10.2 Surface area measurements by N_2 adsorption

Isotherms were measured using a BEL BELSORP-mini II, where N_2 was adsorbed and desorbed at 77 K. Between 50 and 100 mg sample was used for each experiment. All samples were pre-treated under vacuum, first at 80 °C for 1 hour and then at 300 °C for 3 hours, to remove water and other adsorbates.

10.3 Adsorption of TPA

Tri-n-propylamine (TPA) was adsorbed on the samples at 50 °C while the weight increase was monitored in a Rheometric Scientific STA 1500 Thermogravimetric instrument. The adsorption experiments were performed to provide insight into diffusive properties of the samples. 10 mg sample was used and 15 ml/min of N_2 saturated with TPA at 25 °C was allowed to flow into the TG. The vapour pressure of TPA at this temperature (3.5 mbar[132]) provides an equivalent WHSV of 0.4 h^{-1}, although a significant bypass will result in the set-up. All samples were pre-treated at 550°C under pure O_2 for 1 hour prior to adsorption.

10.4 NH_3 TPD

NH_3 TPD was performed thermogravimetrically at Haldor Topsøe AS in Lyngby, Denmark, and a detailed description of the method and experimental procedure can be found in [133]. 20 -50 mg sample was dried at 500°C for 1h under a flow of helium and then cooled down to 150°C before an excess of NH_3 was introduced. The sample was then left at 150 °C under inert atmosphere until the mass of the sample stabilised so all physisorbed NH_3 would be desorbed. Heating to 615 °C at a rate of 10 °C/min was then performed to monitor desorption of NH_3 from acidic sites.

10.5 FTIR spectroscopy

FTIR spectroscopy was used in an attempt to get a qualitative impression of the degree of defects in the materials (by comparing relative signals of different hydroxyl groups) and to study the acidity of the materials. In addition, it was attempted to determine whether H-SAPO-5 would protonate tetra- and/or hexamethylbenzene. The instrument used was a Vertex 80 with MCT detector and a transmission setup. 64 subsequent scans were performed to obtain each displayed absorbance spectrum.

Sample P/H was prepared by pressing the powder into a self-supporting wafer, but for the other samples a high degree of scattering and weak OH-signals made it impossible to record intelligible spectra in this way. Instead, the other samples were prepared by depositing the powder as a thin layer on a silisium substrate using distilled water. For sample SC, both methods were viable and produced similar results, but the background was heavily sloped and thus the spectra obtained using a silisium wafer are shown instead. Before measurement, all samples were pre-treated *in-situ* under vacuum at 120 °C for 1 hour, at 300 °C for 1 hour and finally at 450 °C for 1 hour in order to remove adsorbed water and hydrocarbons.

When adsorbing CO, the samples were cooled to 77 K with liquid nitrogen before CO was allowed into the sample cell. The CO was then gradually pumped out of the cell while spectra were recorded at regular intervals. When adsorbing methylbenzenes, either tetra- or hexamethylbenzene powder was introduced into the sample cell under vacuum before the cell was closed and disconnected from the vacuum line and put into an oven to increase the

vapour pressure of the compounds. For hexamethylbenzene it was found that 150°C for 2 hours was necessary to ascertain that the molecules had diffused into the sample and interacted with the acidic sites. The same conditions were then also used to adsorb tetramethylbenzene, although the same results were also obtained when lower temperature was used. To remove physisorbed methylbenzene the sample cell was outgassed, first at room temperature and later at 100 °C.

All spectra shown have been corrected for water and CO_2 present in the air around the sample cell.

11 Results and discussion

11.1 Overview of samples studied

As shown in part I of this work, a large number of syntheses were performed, but very few yielded suitably pure H-SAPO-5 samples for catalytic studies. A few of these samples were selected for further studies, and this section is dedicated to provide details of the synthesis conditions together with SEM and XRD results for these samples. The names given to each sample will be used extensively throughout the remainder of the thesis.

The original idea for selecting these exact samples was to have two plate-like samples with short (2-3 μm) channels and two samples with longer (~10 μm) channels in order to study the effect of diffusion length through the crystals on the selectivities and deactivation behaviour. Of these, one sample of each would have a low density of acid sites, while the other would be higher. They were then named either P for plate-like or B for barrel-like to account for morphology, and either L or H for low or high silica content. It should however be noted that the amount of silica actually incorporated into the barrel-like samples was not very different after all, and in fact has the opposite order as the nomenclature suggests. In addition to this, a fifth sample was introduced when a later attempt at synthesis produced crystals of much smaller size. The most logical name for this sample was then simply SC, for small crystals.

All samples were calcined as described in the experimental section. Some changes to the low angle reflections were noticed, but no apparent decrease in crystallinity was observed. Non-framework species are known to affect the low angle region of the pattern, and a change in these are expected when the organic template is removed[12].

B/H (Barrel, high Si content)

A catalyst sample synthesised in the old tumbling oven (see chapter 6.1.1. for details on ovens used), with TEA template and Cab-O-Sil as silica source. Synthesis conditions are given in table 11.1, while figure 11.1 gives XRD patterns and a representative SEM image. The synthesis number of the sample was MWE58.

Table 11.1: Synthesis conditions and composition in relative molar amounts.

H_2O	Al_2O_3	P_2O_5	SiO_2	TEA	Time	Temp.
50	1.0	1.0	2.0	3.9	3.5 hours	220 °C

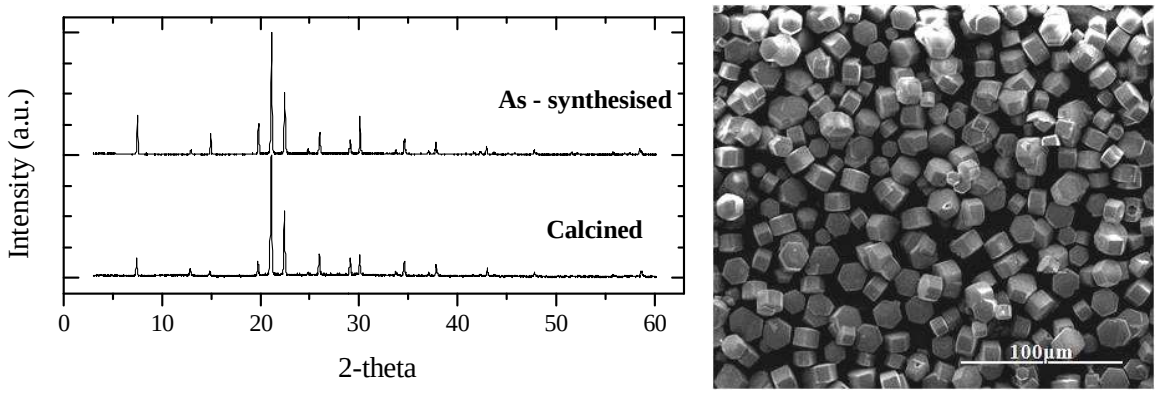

Fig. 11.1: XRD patterns for as-synthesised and calcined material (left) and representative SEM image (right). The sample seems to have good crystallinity and consist of mostly large 20x10 µm hexagonal nuts/barrels, with some of them seemingly fusing together.

B/L (Barrel, low Si content)

This sample was crystallized under static conditions. The template used was TPA and Cab-O-Sil was used as silica source. Synthesis conditions, diffraction patterns and SEM micrograph are displayed in table 11.2 and figure 11.2, below. The synthesis number for the sample was MWE01 (see appendix A).

Table 11.2: Synthesis conditions and composition in relative molar amounts.

H_2O	Al_2O_3	P_2O_5	SiO_2	TPA	Time	Temp.
50	1.0	0.6	0.4	2.1	24 hours	200 °C

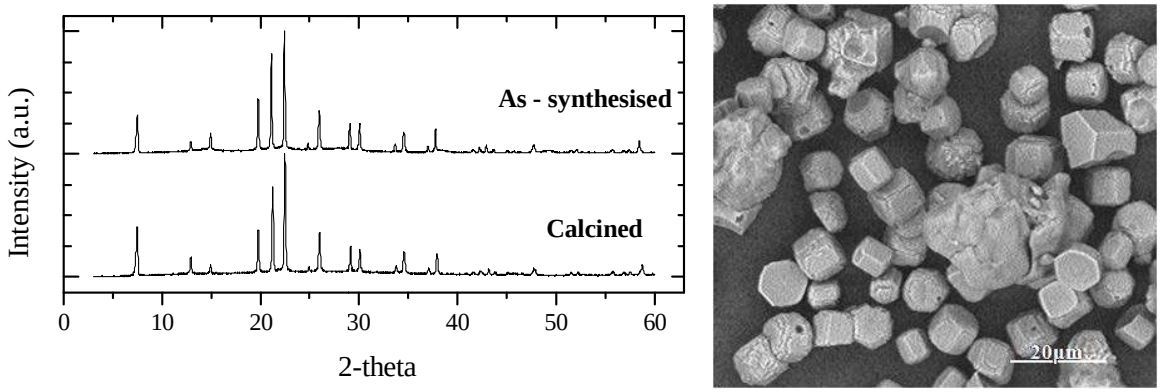

Fig. 11.2: XRD patterns for as-synthesised and calsined material (left) and representative SEM image (right). The sample has a high content of amorphous material and the crystals are somewhat unevenly shaped. The c-axis length seems to average about 10 µm.

P/L (plate, low Si content)

P/L was crystallized in new tumbling oven using TEA as template, with Cab-O-Sil silica source and seeded with a small amount of pure, plate-like, SAPO-5 to obtain pure phase. The sample is a mixture of the combined yield of syntheses MWE196 and MWE197 (see appendix A), produced with synthesis conditions as outlined in table 11.3. Figure 11.3 provides XRD and SEM data of the sample.

Table 11.3: Synthesis conditions and composition in relative molar amounts.

H_2O	Al_2O_3	P_2O_5	SiO_2	TEA	Time	Temp.
50	1.0	1.0	0.1	3.9	4 hours	200°C

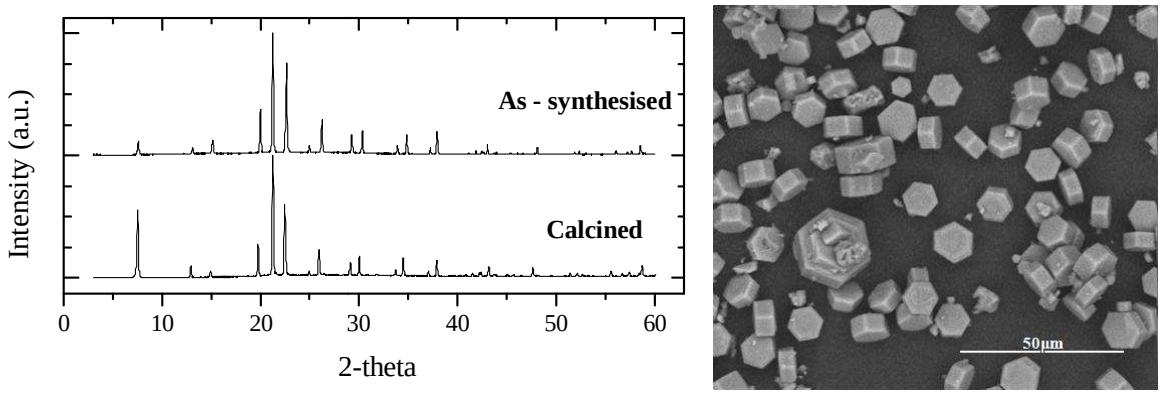

Fig. 11.3: XRD patterns for as-synthesised and calcined material (left) and representative SEM image (right). The morphology of the sample is mostly plate-like with diameter averaging 10 µm and thickness 3 µm. A few larger or smaller crystals are also observed, but variations in crystal size in the majority of the sample are very small.

P/H (plate, high Si)

This catalyst batch crystallized in microwave oven using TEA as template and Cab-O-Sil as silica source. Details on synthesis conditions are given in table 11.4, while characterisation data is provided in figure 11.4. The synthesis number of the sample is MWE72.

Table 11.4: Synthesis conditions and composition in relative molar amounts.

H_2O	Al_2O_3	P_2O_5	SiO_2	TEA	Time	Temp.
50	1.0	1.0	1.0	3.9	40 minutes	190°C

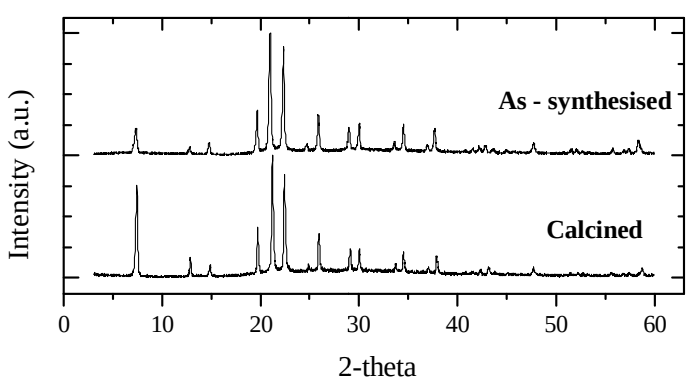

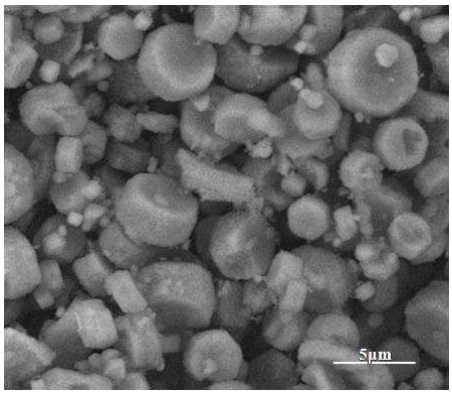

Fig. 11.4: XRD patterns for as-synthesised and calcined material (left) and representative SEM image (right). The crystals are mostly roundish and plate-like, with varying diameter and thickness. As is also implied by the diffractogram, there is a substantial amount of amorphous matter present in addition to the crystals. Note that the crystals are smaller than P/L, but the average thickness is approximately the same (3 µm).

SC (small crystals, 203)

This sample was crystallized in new tumbling oven using TEA as template, with Cab-O-Sil silica source, and seeded with a small amount of pure SAPO-5 (from sample B/L) to obtain pure phase. This sample consists of the combined yield from syntheses MWE203 and MWE204. Synthesis conditions are given in table 11.5, while XRD and SEM results are given in figure 11.5.

Table 11.5: Synthesis conditions and composition in relative molar amounts.

H_2O	Al_2O_3	P_2O_5	SiO_2	TEA	Time	Temp.
50	1.0	1.0	0.1	3.9	4.25 hours	200°C

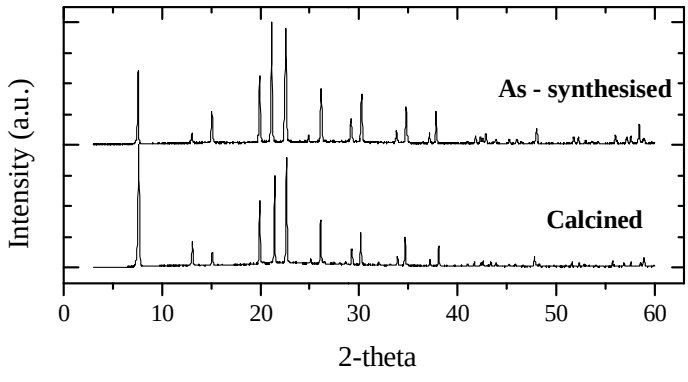

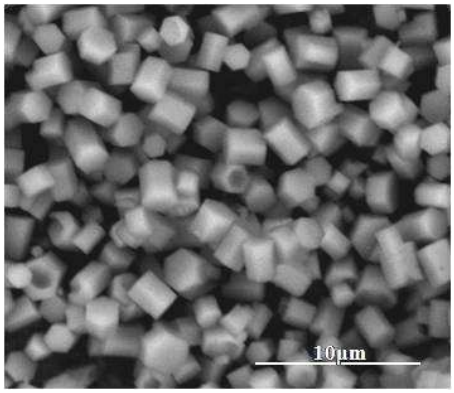

Fig. 11.5: XRD patterns for as-synthesised and calcined material (left) and representative SEM image (right). The crystals are all hexagonally shaped and smaller than 2 µm. Crystallinity appears to be very high.

11.2 BET

N_2 adsorption was performed on all samples and a measure of the surface area was found using the BET equation. The adsorption isotherms of the samples SC, B/H and P/L are shown in figure 11.6. All three isotherms are of type I, which is typical for microporous materials with relatively small external surfaces[124]. This suggests that the materials possess well-defined micropores and that few or no defective regions containing larger pores or cavities exist. Differences in adsorption capacities up to the plateau region are evident from the figure, with the capacities of the samples increasing in the order P/L < SC < B/H.

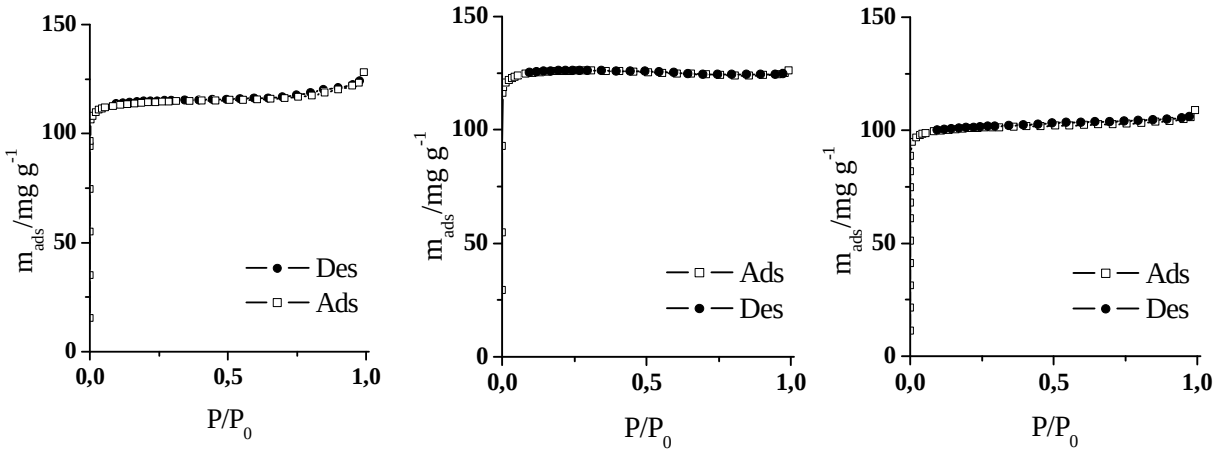

Fig. 11.6: Adsorption isotherms for samples SC (left), B/H (middle) and P/L (right).

The adsorption isotherms for B/L and P/H (shown in figure 11.7) are quite different from the samples already discussed. The plateau regions of the isotherms are not as flat and well defined as those in figure 11.6. At high pressures there is also a significant rise in the amount of adsorbed gas. Both samples also show a slight hysteresis on desorption. Hysteresis is usually associated with capillary condensation in mesoporous structures[124], but from the synthesis methods of these samples there is no reason to assume that the crystals are mesoporous. Instead, it is assumed that the hysteresis is caused by agglomeration and possible intergrowths and defects in the crystals. Indeed, the isotherm for P/H is very similar to type H3 and H4 hysteresis loops observed for slit shaped pores resulting from aggregation of plate-like particles[124]. The hysteresis loop of B/L, more akin to a H1 or H2 type hysteresis loop, is somewhat more difficult to interpret. Hystereses of these kinds are often associated with agglomerates of particles, but have also previously been ascribed to a difference in

condensation and evaporation mechanisms caused by pores with narrow necks and wide bodies (ink bottle pores)[124].

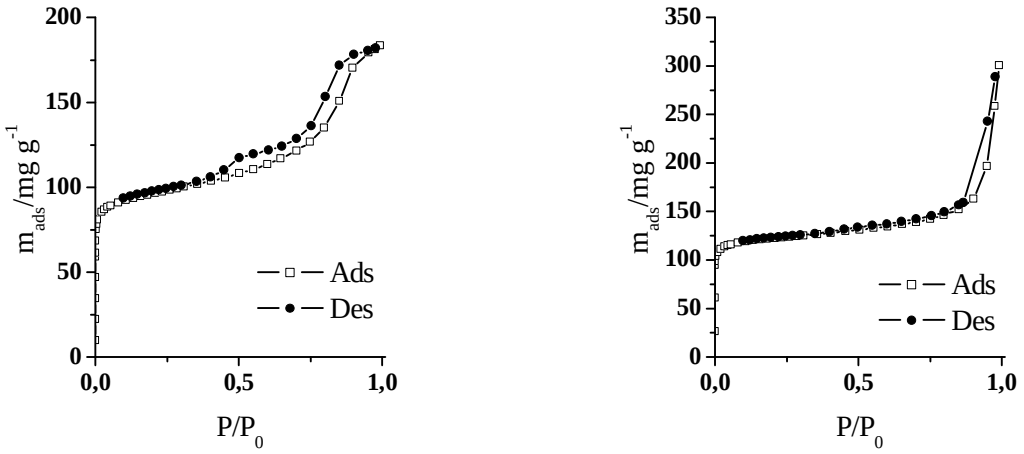

Fig. 11.7: Adsorption isotherms for samples B/L (left) and P/H (right).

When comparing these results to the SEM micrographs of the same samples (figures 11.2 and 11.4), explanations of the isotherms which involve agglomerates or aggregates seem plausible. Even though the ink bottle pore explanation is probably an oversimplification[124], there is still a possibility that defects or intergrowths in the crystals of B/L could be responsible for its strange adsorption isotherm.

Table 11.6: BET surfaces of all studied samples.

Sample	BET surface (m^2/g)
SC	341
B/H	375
B/L	269
P/H	347
P/L	295

When calculating the BET surfaces of the samples (given in table 11.6), significant differences are apparent. The difference between samples B/H and B/L is greater than 100 m^2/g, while BET surfaces of the other samples are distributed between those two. Surface areas reported by other groups also vary quite widely. Jhung et al[100, 101, 103] report mostly

surfaces in the range 320 - 380 m^2/g, while crystals with high silica content are reported by Seelan et al[116] to possess surface areas smaller than 200 m^2/g.

The main reason for differences in surface area is assumed due to differences in the amount of blocked or distorted channels in the material. Considering then that the calculated accessible surface for N_2 in a perfect $AlPO_4$-5 is around 450 m^2/g (For a discussion on calculated accessible surface, see [134]) and silicoaluminate AFI structures (SSZ-24) have been reported with BET surfaces of 414 m^2/g[135], it is evident that the synthesised SAPO-5 samples possess defective structures.

In summary, the surface areas vary between the samples, with B/H having the highest BET area while that of B/L is significantly lower. The other samples are intermediate between these two. Samples B/H, SC and P/L appears to be perfectly microporous from their adsorption isotherms, while B/L and P/H show some degree of hysteresis indicating agglomeration/aggregation and/or defective structures.

11.3 Adsorption of TPA

The kinetic diameter of tri-n-propylamine (TPA) is ~0.8 nm[136, 137], which is larger than the reported diameter of the pores in an AFI framework (7.3 Å[10]). However, the molecular kinetic diameter and the pore size are not necessarily consistent with each other, and in many instances molecules are known to diffuse into pores considered narrower than the molecular diameter[126]. Considering the large size of TPA and the fact that it can be used to template the synthesis of AFI frameworks, it seems plausible to assume that the molecule fits into the pores, but that the effective size of the pore opening is critical to its diffusivity. If so, it might be possible to detect small variations in pore size and accessibility by monitoring the rate of adsorption of this molecule in the synthesised samples.

Figure 11.8 shows the increase in weight versus time for all five synthesised H-SAPO-5 samples when exposed to a continuous flow of N_2 saturated with TPA at 25°C (3.5 mbar partial pressure[132]). While adsorption was monitored for most samples for as long as 20 hours, the samples did not appear to become saturated and still showed a slow increase in weight with time. Only the first 100 minutes of adsorption are shown in figure 11.8, as this

represents the most interesting information. After this, all measured samples (P/H was only measured for 2 hours) simply continue to increase slowly. Whether they would all eventually have converges to a similar level of weight gain (or an order related to their BET surface areas), is not known. While it is evident from figure 11.8 that reproducibility of the experiment for sample B/L is not very good, repetitions of the experiments for both P/L and SC are in good agreement. The poor reproducibility of B/L is attributed to sample inhomogeneity as the sample contains amorphous material and a larger degree of agglomeration than the other samples. Inhomogeneity might thus also be a problem for P/H, but this sample has not been tested for reproducibility.

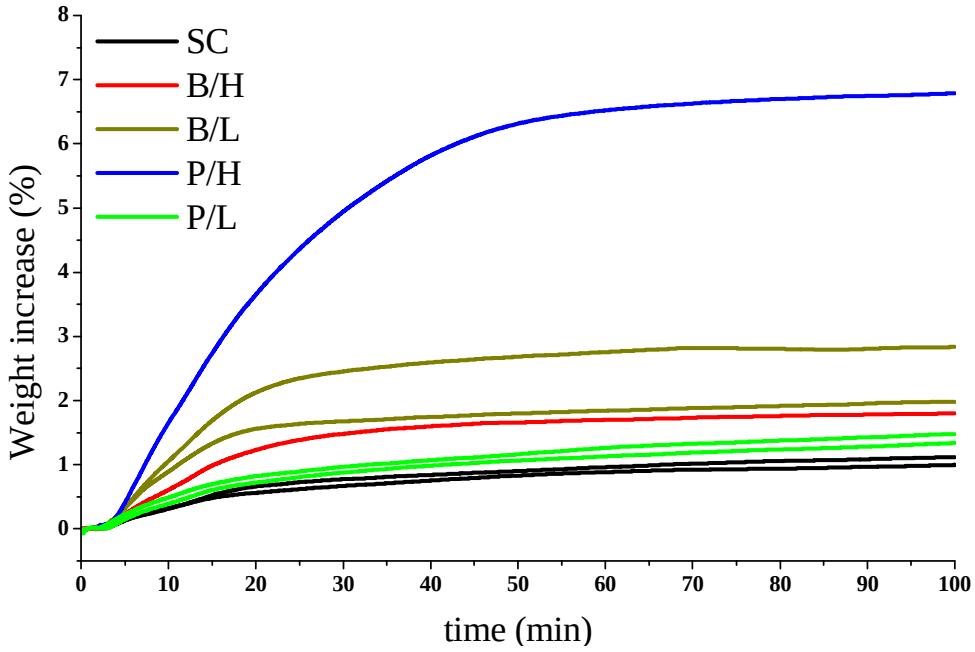

Fig. 11.8: adsorption isotherms for adsorption of TPA. Where there are two lines of the same colour, these are reproductions of the same experiment.

The experiment reveals that there are clear differences between the amounts of TPA adsorbed during the time shown in figure 11.8, and that the amounts adsorbed does not appear to follow the same trend as amounts of N_2 adsorbed (see chapter 11.2). P/H and B/L adsorb TPA fastest, which might be related to the same phenomena causing hysteresis during N_2 adsorption. If larger pores (mesopores) exist in the interfaces between crystals or in amorphous material in these samples, it seems plausible that large amounts of TPA could be adsorbed in these. In addition the possibility exists that defects in the materials might create somewhat larger pores, into which TPA may diffuse more easily. The difference observed between the three other samples, which all look highly crystalline both with SEM and XRD

and strictly microporous from N_2 adsorption, is also very interesting. The adsorption rate increases in the order SC < P/L < B/H, which is different from the order of increasing BET surface areas (P/L < SC < B/H) and opposite of what would be expected based on crystal sizes. This indicates that the TPA uptake is governed by some other property of the samples than the surface area and crystal size.

The most likely cause of the differences in diffusion is thought to be a difference in the effective channel dimensions, due to defects either creating larger or narrower pores in the crystals. The ease of diffusion into the crystals appear to increase in the order SC < P/L < B/H < B/L < P/H.

11.4 NH_3 TPD

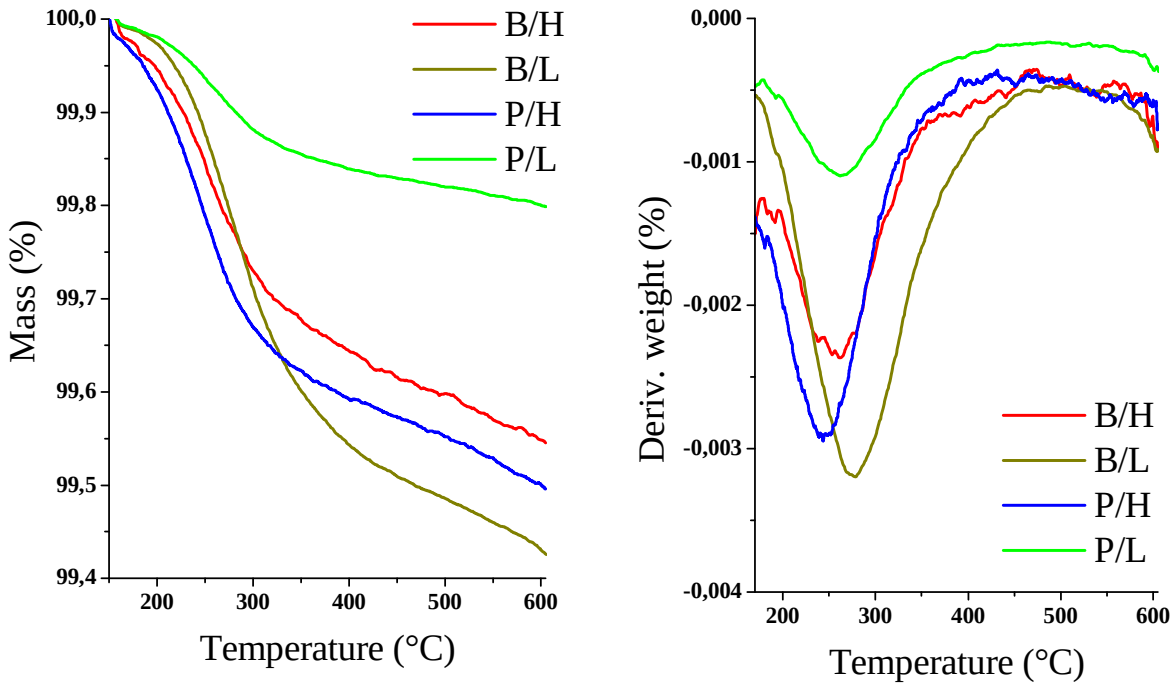

Fig. 11.9: Results of NH_3 TPD plotted as mass % (left) and mass change (right) versus temperature.

To study the acidic properties of the samples, NH_3 TPD was performed on all samples except SC. The results of the experiments are shown in figure 11.9, where the mass of the samples can be seen to decrease throughout the temperature interval studied. The mass decreases most rapidly between ~200°C and ~350°C, with some variation between the samples. The variations between the samples in the temperature where most rapid desorption is observed

might indicate small differences in acid strength. However, as the variations are small and the curves somewhat noisy, it is difficult to establish whether this difference is significant or not. Small variations in heating rate could also cause shifts in the desorption maxima.

The temperatures found to correspond with maximum NH_3 desorption from figure 11.9 is between 245°C and 275°C. Even though previous studies have reported different temperature maxima for H-SAPO-5, they mostly fall into the range observed here. Lee et al[138] reports a desorption maximum at 275°C, while both Chen et al[92] and Qinhua et al[97] report maxima at 240°C. Tapp et al[139] found a somewhat lower maxima at 220°C. While all of the aforementioned report only one peak corresponding to desorption from acidic sites, Halik et al[140] reports a second maximum occurring at 307°C, but provide indications that this might be caused by amorphous impurities. Only one maximum is observed for the samples studied in this work and this is assumed to be caused by desorption from Brønsted acidic sites.

Compared to other zeotype materials like H-SAPO-34 and H-Beta, TPD reveals H-SAPO-5 to be a significantly weaker acid. H-SAPO-34 is known to possess a desorption maximum at as high temperatures as 390°C[92] or 400°C[141] (with an additional maximum for weaker sites at 250°C reported in [141]). H-Beta has also been reported to have NH_3 desorption maxima higher than 300°C by Bjørgen[142]. As many of the other works utilise somewhat different methods and conditions for the TPD experiments, they are not necessarily directly comparable with this work. However, as similar heating rates have been applied they should still give good approximations of relative acid strengths.

Table 11.7: Acid site density ((Al+P)/Si ratios) of the studied material found by TPD and EDS compared. The "Synth" column details the relative amounts in the synthesis mixtures.

Sample	(Al+P)/Si TPD	(Al+P)/Si EDS	(Al+P)/Si Synth
SC	-	80	40
B/H	59	28	2
B/L	47	25	8
P/H	53	20	4
P/L	135	96	40

The acid site density of the materials was determined from the amount of NH_3 desorbed (see appendix E for details). Table 11.7 lists the calculated (Al+P)/Si ratios found by NH_3 and EDS, and compares them to the amount of silica added to their synthesis mixtures. It is evident from this that the amount of silica incorporated into the materials is much lower than the content in the synthesis mixture, but also that there is little correlation between silica content in the crystals and the amount of acidic sites. For B/H, B/L and P/H it appears that only about half of the incorporated silica produce an acid site, while for P/L a somewhat higher proportion of the silica seems to produce acidity. It is well-known that Si can substitute not only for P to generate a bridging Brønsted site, but can also produce siliceous regions by substituting for both P and Al in SAPO structures (see e.g. [25]). Such siliceous regions produce less than one acid site per Si atom and would explain the deficiency of acid sites compared to silica content in the materials. It has also been reported that the tendency for generation of siliceous regions increases with increasing amount of silica in H-SAPO-5[98, 143].

In summary, the acid strengths of the samples studied appear to be similar while the acid site density is seen to vary. B/H, B/L and P/H all have a higher (and comparable) acid site density than P/L. SC has not been studied, but based on EDS and amount of silica in synthesis mixture, it is expected to have an acid site density close to, but somewhat higher than, P/L.

11.5 FTIR Spectroscopy

11.5.1 Comparison of hydroxyl stretching region

Figure 11.10 shows the FTIR spectra in the region of hydroxyl stretching for all (pre-treated) samples recorded at room temperature. Two absorptions at ~3524 cm^{-1} and ~3626 cm^{-1} are present in all samples, while most of the samples also show absorptions at ~3674 cm^{-1} and ~3742 cm^{-1}. In addition, a small absorption band at ~3792 cm^{-1} is also visible in some spectra. Although the exact wavenumbers vary a little, these five bands have been reported numerous times for H-SAPO-5 in the literature[25, 92, 97, 138, 140, 144-147]. They have been assigned to bridging Si-OH-Al (~3524 cm^{-1} and ~3626 cm^{-1}), P-OH (~3674 cm^{-1}), Si-OH groups (~3742 cm^{-1}) and Al-OH groups (~3792 cm^{-1}), respectively.

As all T-atoms in the AFI structure are crystallographically equivalent[10], it is interesting to note that there are two different absorption bands for the Si-OH-Al groups. The reason for this has been studied by Zibrowius et al[144], both by IR and NMR spectroscopy. Their conclusion was that the band at lower wavenumber (~3524 cm^{-1}) is due to hydroxyls pointing into the six- membered rings of the framework while the ~3626 cm^{-1} band is caused by hydroxyls pointing into the twelve-rings. The exact nature of the Al -, Si - and P-OH bands is somewhat less clear as they have been attributed both to amorphous impurities[140], to surface hydroxyls[147] and to terminal OH groups associated with structural defects in the materials[146].

It should be noted that the spectra in figure 11.10 are not normalised with respect to each other, meaning that a quantitative analysis of the amounts of different OH groups present is not possible. However, a comparison of the relative absorptions of the P-OH and Si-OH groups with Si-OH-Al reveals clear differences between the samples. The silanol (Si-OH) band at ~3742 cm^{-1} is clearly present in the spectra of B/H, B/L and P/H, while it is very small or absent in the spectra of P/L and SC. This higher ratio of silanol groups to bridging Brønsted groups for materials with higher Si content seems to support the previous findings of primarily Si for P substitution at low Si content, but that other substitution mechanisms become more likely when more silica is incorporated[98, 143].

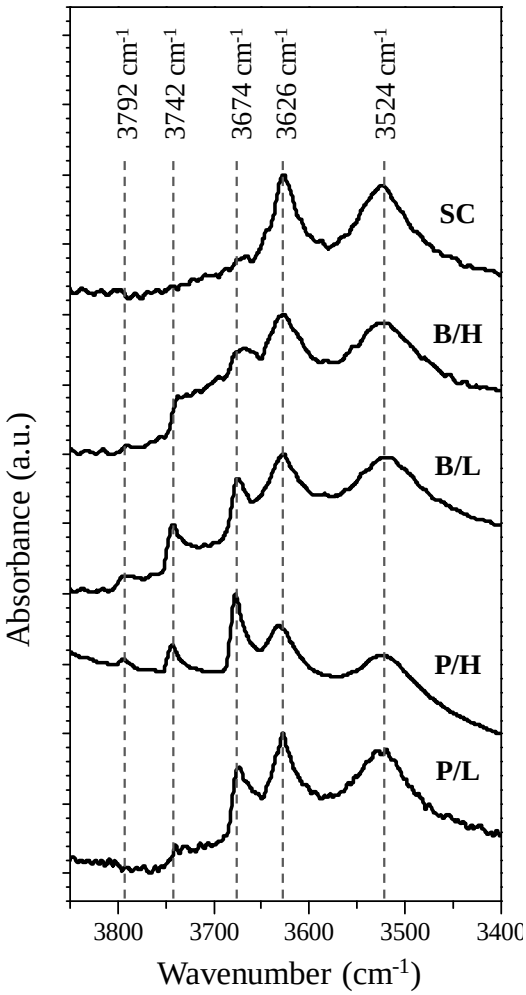

Fig. 11.10: Comparison of IR spectra of all samples in the ν(OH) region at room temperature. Wavenumbers of the peaks discussed in the text are indicated on the figure.

The P-OH band at ~3674 cm^{-1} is quite strong in all samples except SC, and especially strong in P/H. As this sample is known to contain amorphous material rich in phosphorous from SEM and EDS, there might be a connection. Al-OH groups are visible in B/H, B/L and P/H, while the spectrum of P/L is too noisy to determine if it is present or not. This absorbance is quite broad in B/L, possibly signifying that slightly different Al-OH groups exists within the sample.

While all other samples contain a mixture of different OH, it is remarkable that the spectrum of SC is virtually free from any other bands than bridging Si-OH-Al (some P-OH is visible on close examination). Even though a reproduction of SC (measured as a self-supporting wafer) showed a more visible P-OH band, the absorbance was still significantly lower than for any of the other samples.

11.5.2 Acidity measurements by probing with CO

To study the acidity of the samples, they were exposed to CO at 77 K in order to monitor the change in frequency of the OH groups. Upon cooling to 77 K, and before CO adsorption, the Si-OH-Al band at ~3626 cm^{-1} broadens and is blue-shifted between 0 and 15 cm^{-1}. The range of the shift differs between the samples, with SC hardly shifting at all while B/H shifts as much as 15 cm^{-1}. The band for protons pointing into the six-rings (~3524 cm^{-1}) is hardly affected on most samples, but a significant blue shift is observed for P/L and SC (12 cm^{-1}). No change in frequency is observed upon cooling for the other OH groups and the peaks returned to their original position (3626 cm^{-1}) when heated back up to room temperature. There are many possible explanations for this observed behaviour, and definite conclusions are not warranted without further studies. When the temperature of a material or molecule is increased, it is expected that higher vibrational energy levels become more populated. Due to anharmonicity in the molecular vibrations, these levels become more closely spaced as the energy is increased. This may lead to absorption at lower frequency when the temperature increases, but would also be expected to lead to a narrower band at low temperature than at high[148]. From this, it is possible that different degrees of anharmonicity in the material cause the difference in shift ranges. An explanation for the band broadening at low temperature may be based on increased hydrogen bonding interaction between OH groups close together (such as the edges of a silica patch). This would lead to broadening, but would also be assumed to cause a shift in the opposite direction as that observed. These explanations do not account for the fact that the absorption frequencies are equal for all materials at room temperature. One possibility that would explain this is that while the Si-OH-Al groups are different at low temperatures, the increased proton and framework mobility at higher temperatures results in equalisation. In this latter case, it is uncertain whether acid strengths measured by CO

adsorption are relevant for high temperature applications such as catalytic conversion of methanol.

When exposed to CO the spectra of all samples are affected in a similar manner, although the exact shift values of the Si-OH-Al vary between the samples. The general features of the spectra will be discussed first, before the exact positions and shifts of all samples' Si-OH-Al bands are given in table 11.8 at the end of the section.

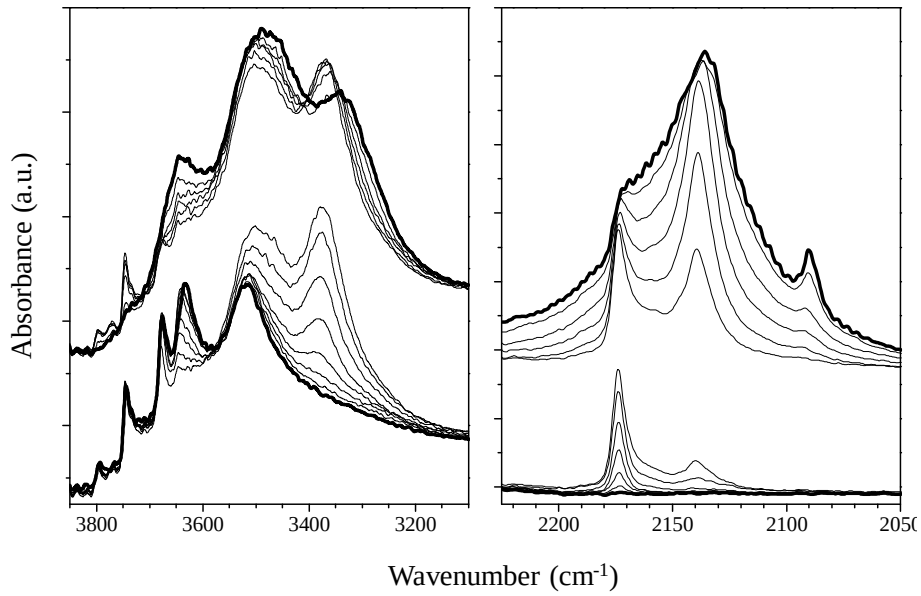

Fig. 11.11: FTIR spectra showing the O-H stretching region (left) and the C-O stretching region (right, background subtracted) of B/L exposed to different amounts of CO. The spectra are divided into two groups to separate overlapping interactions of the Al-OH and Si-OH from the P-OH and Si-OH-Al bands. The top spectra represent high CO coverage and the bottom low coverage. Thicker lines indicate maximum and minimum CO coverage.

The FTIR spectra of B/L are shown in figure 11.11. At maximum CO coverage (thicker line in the upper group of spectra in figure 11.11) three broad peaks are visible in the OH stretching region at wavenumbers 3650 cm^{-1}, 3495 cm^{-1} and 3345 cm^{-1}. As CO is removed from the sample, the bands of Al-OH and Si-OH (at 3742 cm^{-1} and 3792 cm^{-1}, respectively) start appearing while the peak at 3650 cm^{-1} disappears. In addition, the peak at 3345 cm^{-1} sharpens and is blue-shifted to 3367 cm^{-1} and the intensity of the peak at 3495 cm^{-1} decreases. At lower CO coverages (lower group of spectra in figure 11.11) the P-OH and Si-OH-Al bands reappear (at 3676 cm^{-1} and 3634 cm^{-1}), while at the same time the 3367 cm^{-1} peak disappears and the 3475 cm^{-1} is reduced to the original peak at 3524 cm^{-1}.

In the CO stretching region of B/L (figure 11.11 right), two peaks at 2171 cm^{-1} and 2137 cm^{-1} dominate the spectra at high CO coverage. These peaks are assigned respectively to CO adsorbed on strong Brønsted sites and "liquid-like" CO condensed in the channels, based on similar observed absorbances in related materials under the same conditions[90, 130, 131]. Another peak is also visible at the highest coverages at 2090 cm^{-1}, which is ascribed to CO bonded to a hydroxyl group through the O-atom[130]. As CO is removed from the sample the O-bonded and "liquid-like" CO disappear, making the band for CO on strong Brønsted sites dominant. All peaks in the CO stretching region blue shifted slightly when coverage was decreased, with the two major peaks ending at 2174 cm^{-1} and 2140 cm^{-1}. There is also some indication of absorbance between the "liquid-like" and strongly adsorbed CO, which is most likely caused by adsorption on the Al-, Si- and P-OH sites.

The samples B/H and P/H (spectra shown in figure 11.12) show similar responses to CO as B/L except that the value of $\Delta\bar{\nu}$(Si-OH-Al) is a bit larger in B/H and smaller in P/H. Apart from small differences in intensity, peak widths and wavenumbers, the appearance and disappearance of the same peaks in the same order is observed for all three samples.

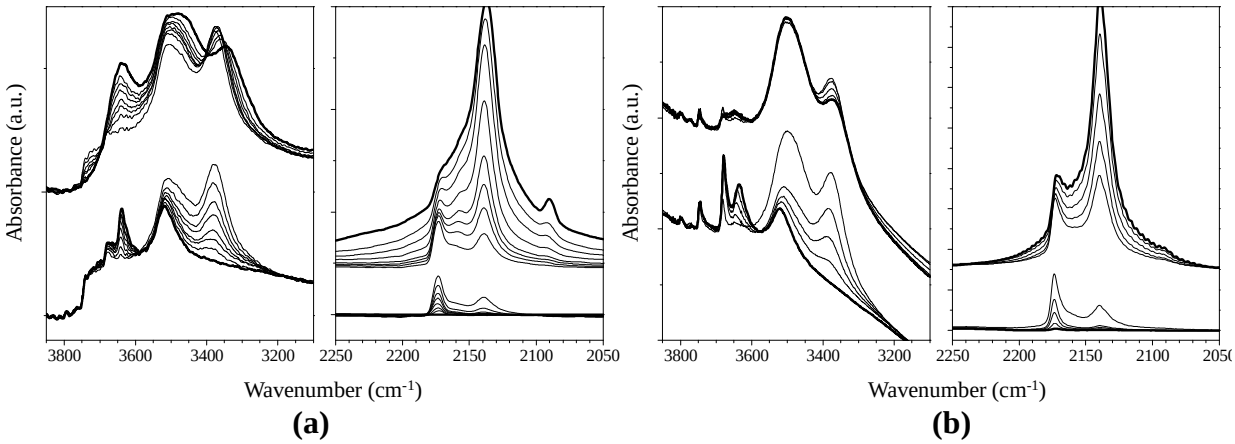

Fig. 11.12: FTIR spectra of B/H (a) and P/H (b), both divided into O-H (left) and (background subtracted) C-O (right) stretching regions. The top group of spectra represent high CO coverage while bottom group of spectra show lower coverage. These are separated to distinguish between overlapping interactions. Thicker lines indicate maximum and minimum CO coverage.

On the basis of these experiments it appears that adsorption of CO causes a shift of the Al- and Si-OH bands from 3742 cm^{-1} and 3792 cm^{-1} to a broad absorption around 3650 cm^{-1}. The

individual shifts for these two cannot be determined, but it is assumed that the centre of the shifted peak is Si-OH H-bonded to CO while the Al-OH adducts are less visible at higher wavenumbers. This would give $\Delta\nu$(Si-OH) equal to -90 cm^{-1}, which is about the same as expected for Si-OH in aluminosilicates[131]. The P-OH can likewise be linked to the peak around 3495 cm^{-1}, especially from the spectra of P/H where a large decrease here coincides with a large increase in the P-OH peak. This gives a shift value $\Delta\bar{\nu}$(P-OH) equal to -181 cm^{-1}. However, the 3495 cm^{-1} band continues to decrease a bit after the P-OH band has returned, begging the question whether something else is associated with this absorbance. Of the two bands from Si-OH-Al, it appears that only the one at higher wavenumber is interacting with CO. The interacting band shifts to around 3360 cm^{-1}, depending on the sample. The shift of this OH group, $\Delta\bar{\nu}$(Si-OH-Al), is then longer than 250 cm^{-1} for all samples, indicating that this group is more acidic than the other interacting OH groups[131]. As Si-OH-Al groups are assumed responsible for the catalytic activity of the material, this is expected. The observed blue shifts of many of the peaks when CO is desorbed can be attributed to multilayer coverage of CO when coverage is very high[90].

The observed inaccessibility of protons pointing into the six-rings is in accord with the kinetic diameter of CO compared to the size of a zeolitic six-membered ring (3.76 Å and 2.8 Å, respectively[149]). Despite this, indications that these sites interact with stronger bases or at higher temperatures exist in the literature. Kustov et al[145] have shown that both types of bridging OH groups are deuterated during oligomerisation of deuteroethylene at 300 K, while Schüth et al[150] report interactions with p-xylene at 373 K. Because of this, it appears likely that the protons are mobile enough to participate in catalytic reactions at elevated temperatures.

The spectra of CO exposed samples with low Si content (SC and P/L, shown in figure 11.13) differ somewhat from previously shown spectra in the OH stretching region. The Si-OH-Al (~3628 cm^{-1} in SC and ~3641 cm^{-1} in P/L) appear very broad compared to their low intensity, and it appears that a peak at 3460 cm^{-1} must be related to CO adsorption on these bridging Brønsted bands. The most likely cause of two peaks related to CO H-bonded to bridging sites would be that there are two different strengths of these acidic sites. It has been found that the acidic strength of a bridging OH will vary depending on the first neighbours of Si in SAPO materials, increasing in the order Si(4Al) < Si(3Al) < Si (2Al) < Si (1Al) [25]. In addition,

Halik et al[140] observed a shoulder on the accessible Si-OH-Al band and attributed it to another type of strong Brønsted site. However, the large difference in red shift (close to 100 cm^{-1}) on CO adsorption between the two sites is surprising. The strength of the weakest site would then be comparable to the P-OH groups which, again according to Halik et al[140], are not active for catalytic cracking of n-butane or n-hexane.

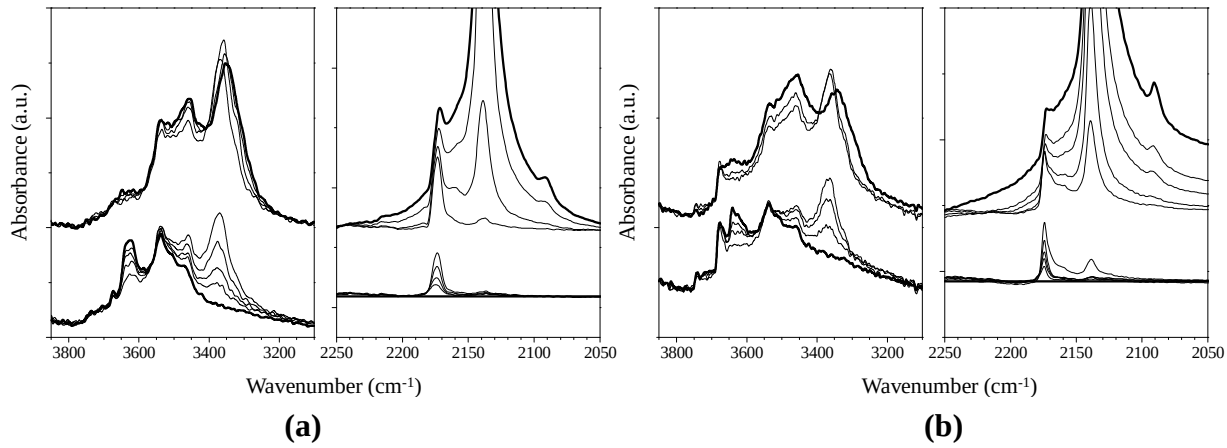

Fig. 11.13: FTIR spectra of SC (a) and P/L (b), both divided into O-H (left) and (background subtracted) C-O (right) stretching regions. The top group of spectra represent high CO coverage while bottom group of spectra show lower coverage. Thicker lines indicate maximum and minimum CO coverage respectively.

While it is difficult to explain the presence of these extra peaks as anything else than more weakly acidic sites, their exact nature is somewhat unclear. If there is more than one type of bridging Brønsted site this should be visible in the samples containing more Si as well, as more variation in Si environments are observed when silica content is increased[98, 143]. It is possible that the large P-OH shifts overlaps and hides this peak in P/L, P/H and B/L, but more experiments would be required if a satisfactory explanation is to be found.

Table 11.8: position of Si-OH-Al bands at 77 K for all samples and their shifts, $\Delta\bar{\nu}$(OH), after exposure to CO.

Sample	$\bar{\nu}$(OH) Si-OH-Al	notes	$\Delta\bar{\nu}$(OH)
SC	3628cm^{-1}	Very broad peak	273 cm^{-1} (and 170 cm^{-1})
B/H	3642 cm^{-1}		273 cm^{-1}
B/L	3634 cm^{-1}		267 cm^{-1}
P/H	3634 cm^{-1}		254 cm^{-1}
P/L	3641 cm^{-1}	Tailing on red side	276 cm^{-1} (and 181 cm^{-1})

As previously mentioned, the exact positions and shapes of the Si-OH-Al absorption (3626 cm^{-1} at RT) differed between the samples when cooled to 77 K, and the shift induced by adsorbed CO also differed. Exact peak positions and shift values are given in table 11.8. These significant (reproducible) variations indicate that the samples have slightly different acid strengths, with especially P/H and B/L showing a weaker acidity than the others. In addition to this, extra peaks are observed when SC and P/L were exposed to CO, possibly indicating the presence of even weaker acid sites (vide supra). It should be noted that the TPD results shown in chapter 11.4 indicated that B/L was more strongly acidic than the other samples, although delving into the variations in TPD was avoided due to the noisy plots obtained. Kubelóva et al[146] also reported two quite different shift values for two H-SAPO-5 samples exposed to CO ($\Delta\bar{\nu}$(OH) = 254 cm^{-1} and 280cm^{-1}), so it is not improbable that these samples also vary in acidic strength. In any case, further studies on acidity of the samples would be desirable.

If the H-SAPO-5 samples are compared to the more frequently used MTH catalyst H-SAPO-34 as measured in [141] and [90], it is seen that the tendency to form terminal OH groups is much higher in H-SAPO-5. The acid strengths also seem comparable as the largest shifts measured for H-SAPO-34 are 270 cm^{-1}. While it was concluded by Chen et al[92] that H-SAPO-34 is a stronger acid than H-SAPO-5, the FTIR experiments performed here indicates that this is not necessarily true of all H-SAPO-5 samples.

11.5.3 Interaction of acidic sites with methylbenzenes

When performing flushing experiments on H-SAPO-34 and the isostructural zeolite H-SSZ-13, Bleken et al[70, 151] found that the amount of tetramethylbenzene retained in the catalysts decreased with flushing in the latter material, but not the former. They attributed this to the relative acid strengths of the materials, and speculated on whether the acid strength of H-SAPO-34 was too low to protonate this species. As the proton affinity of methylbenzenes increase with increasing number of methyl groups, it is possible that the difference in acid strength between the two materials is sufficient to cause a difference in how many methyl substituents is required before protonation can occur. H-SAPO-5 has a similar acid strength to H-SAPO-34 and grants the possibility to introduce methylbenzenes into the structure for studies with FTIR spectroscopy. By monitoring absorptions related to benzene ring

asymmetry, it may be determined whether symmetrically substituted aromatics (such as 1,2,4,5-tetramethylbenzene or hexamethylbenzene) are protonated inside the zeolitic framework. Such experiments were successfully performed by Bjørgen et al[68, 69] on zeolite H-Beta. They reported that tetramethylbenzene is the least substituted methylbenzene that is protonated inside this structure.

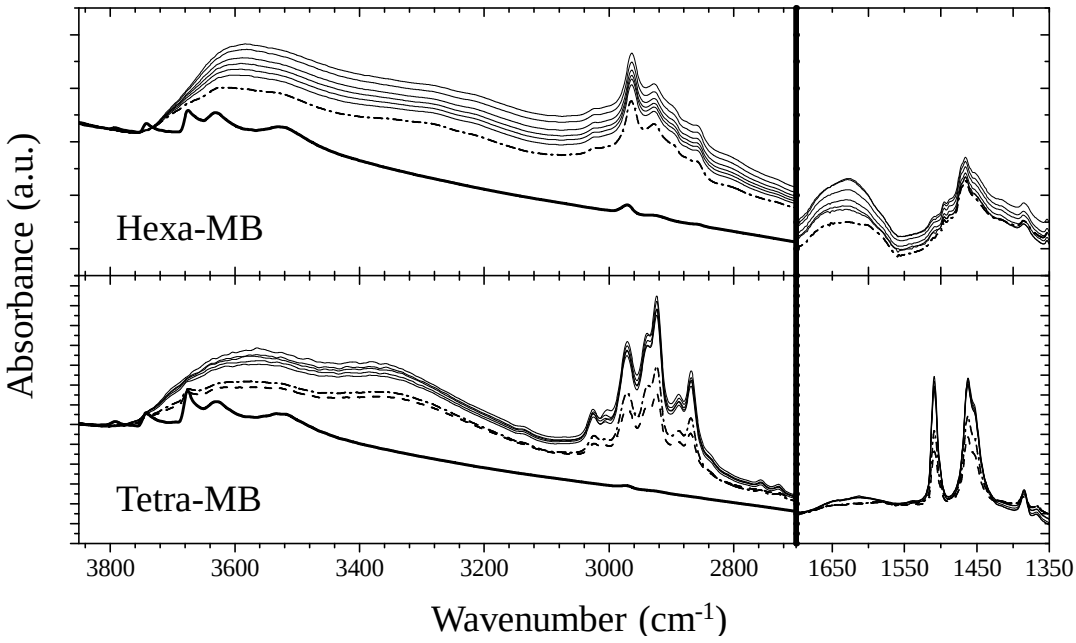

Fig. 11.14: Hexa- (top) and Tetra- methylbenzene (bottom) adsorbed on P/H. The bottom lines in each of the left frames are from the pretreated P/H sample without adsorbate. The series of fully drawn thin lines represent outgassing of methylbenzenes at room temperature under vacuum, while the dash-dotted lines have been heated to 100 °C while degassing. The right parts of the spectra have been subtracted for the clean P/H sample.

Figure 11.14 displays the FTIR spectra of H-SAPO-5 sample P/H containing adsorbed 1,2,4,5-tetra- and hexa- methylbenzene. While the bottom spectra in each frame represent the clean (pretreated) samples, the series of successive lines show the evolution of the spectra as the sample cell is outgassed at room temperature. Weakly bound methylbenzene was removed during this period. The dash-dotted lines show the spectra after outgassing at 100 °C until no change was observed on further degassing.

When hexamethylbenzene was adsorbed on the sample (top spectra in figure 11.14), absorptions from the molecule was visible between wavenumbers 2800 - 3100 cm^{-1} and 1350 - 1500 cm^{-1}. Similar, but sharper, bands also appeared on the sample with adsorbed tetramethylbenzene. These bands correspond well with previously observed infrared spectra

of the same methylbenzenes[68, 69, 152]. In addition, broad bands appeared in both samples after adsorption, covering the region between the ~3700 cm^{-1} and ~3100 cm^{-1}. These were assigned to interactions between the zeolitic O-H groups and the methylbenzenes. The broad absorption region could also be seen to possess two maxima for each sample. Both samples displayed one maximum at ~3600 cm^{-1} while the position of the other differs for the samples. For the sample with adsorbed tetramethylbenzene, this maximum was at ~3350 cm^{-1}, while the sample with hexamethylbenzene showed a less pronounced maximum at ~3250 cm^{-1}. In both samples, the absorptions were significantly broader than what was observed during adsorption of the same species in H-Beta[68, 69].

A band near 1600 cm^{-1} was clearly visible when hexamethylbenzene is adsorbed on H-SAPO-5, but is less clear during tetramethylbenzene adsorption. This is the area where Bjørgen et al[68, 69] reported the band caused by ring asymmetry corresponding to protonated methylbenzenes in H-Beta. Unlike what was observed in H-Beta, however, this band could be seen to decrease when the sample was outgassed. While the much higher intensity of this absorption in the sample with hexamethylbenzene than tetramethylbenzene may indicate protonation in the former but not the latter, this is far from certain. Although precautions were made to avoid water in the sample cell, its presence cannot be completely ruled out. As water absorbs in this region (above 1600 cm^{-1}), it is possible that this is what is removed when the cell is outgassed. The fact that there is an absorption in this region in the tetramethylbenzene loaded sample at high loadings which seemingly disappears during outgassing is also puzzling. Benzene and p-xylene in H-SAPO-5 has previously been reported to cause absorptions at ~3356 cm^{-1}[140] and ~3327 cm^{-1}[150] respectively. As tetramethylbenzene is a stronger base than either of these[153, 154], hydrogen-bond interactions with Si-OH-Al groups would be expected to cause absorption at lower wavenumbers than these. The fact that it does not complicates the interpretation of the spectra.

From these spectra (figure 11.14), there appears to be a difference in the interaction of the two methylbenzenes with the acidic sites of H-SAPO-5, but whether this is related to protonation is uncertain. A clear conclusion is unlikely to be found without better spectra or further experiments, but it is likely from these results that protonation of hexamethylbenzene occurs. For tetramethylbenzene, it is hard to conclude anything at all.

12 Conclusions and further work

Five of the samples synthesised in part I of this work have been more extensively characterised. These samples are the same as will be used for part III. It has been found that relatively large differences in surface areas and accessibility to large molecules exist between the samples, and FTIR has shown varying amounts of terminal OH groups in addition to possible variations in acid strength. Acid site density has been found to be similar for all samples except when very little silica has been used in the synthesis mixture. This indicates that above a certain amount, additional silica does not create acidic sites with the synthesis methods employed in this work. Table 12.1 gives a rough summary of the results of the different characterisation techniques employed.

Table 12.1: Summary of characterisation data for all samples. Acid strength and amount of OH-groups are from FTIR measurements. Amounts of OH groups and accessibility to TPA are somewhat arbitrary but give a good idea of how the samples compare. The reader is referred to the relevant chapter for specifics. SEM and XRD data is given in chapter 11.1.

Sample	S_{BET} (m^2/g)	(Al+P)/Si TPD	(Al+P)/Si EDS	Accessibility to TPA	Acid strength $\Delta\bar{\nu}$(OH) (IR)	(IR) Amount of [1] P-OH	Al-OH	Si-OH
SC	341	-[2]	80	(Very) poor	273 cm^{-1} [3]	Low	None	None
B/H	375	59	28	Medium	273 cm^{-1}	Medium[4]	None	High[4]
B/L	269	47	25	High	267 cm^{-1}	Medium	High	High
P/H	347	53	20	Very high	254 cm^{-1}	High	Medium	Medium
P/L	295	135	96	poor	276 cm^{-1} [3]	Medium	None	Low

(1) Intensity of signal relative to Si-OH-Al signal from FTIR at room temp compared with other samples.

(2) TPD of SC has not been performed, but acid site density is expected to be somewhat higher than P/L.

(3) These samples have an additional shift value approximately 100 cm^{-1} shorter.

(4) Spectra of B/H are poorly resolved, so determination of relative amounts of Si-OH and P-OH is hard.

The interactions of two methylbenzenes (1,2,4,5-tetramethylbenzene and hexamethylbenzene) with the zeolitic acid sites of P/H has also been studied. While results indicate that protonation of hexamethylbenzene occurs, the nature of the interaction with tetramethylbenzene is less certain. Complimentary UV-VIS spectroscopy may provide further clarification of this. In addition, it would be informative to perform the measurements again, but add a strong base after methylbenzene adsorption. If the bands around 1600 cm^{-1} disappear upon contact with strong base, it would indicate deprotonation of the

methylbenzene. Such an observation would add credibility to any claim that protonation occurs.

It has been observed that the H-SAPO-5 synthesised here is prone to formation of defects, especially when silica content is increased. The nature of the defects have, however, been poorly characterised and generation and strength of acid sites has proven quite complex based on the variations found between the samples by FTIR measurements. If more knowledge is to be gained in this area, more extensive characterisation will be required. Both NMR spectroscopy and more IR spectroscopy studies using other probe molecules would likely yield valuable information on Si substitution mechanisms and generation of acidity. Moving to diffuse reflectance FTIR spectroscopy (DRIFTS) might also be a better alternative than the transmission methods used in this work, as DRIFTS allows easier investigation of strongly scattering samples[110, 155].

If producing SAPO-5 with less defective structure and/or with higher density of acidic sites is desirable, more synthesis experiments might also be performed. Some examples of reasonably successful attempts to produce H-SAPO-5 with higher content of silica with little formation of siliceous regions is available in the literature. For example, syntheses based on the methods of Franco[156] or Ojo[143] (where the latter also achieved a BET surface higher than 400 m^2/g) could be attempted.

Part III: Catalytic Testing

13 Theory of experimental techniques

13.1 Gas Chromatography (GC)

Gas chromatography (GC) has been used extensively in this work to analyse the distribution of products during catalytic reactions, and also to study hydrocarbons retained in the catalysts after reaction. Chromatography is a method for separating compounds based on their differing distribution between two phases, the mobile phase and the stationary phase[157]. In gas chromatography the mobile phase is usually He, N_2 or H_2, and this gas carries the mixture to be separated through a column containing the stationary phase. Depending on the compounds degree of interaction with the stationary phase, the time used to travel the length of the column will differ. In columns with non-polar stationary phases, Van der Waal interactions dominate and similar compounds are eluted in (roughly) boiling point order. Compounds can be observed with a detector as they are eluted from the column.

Most analyses using GC employs long open tubular capillary columns with the stationary phase lining the inner wall of the column, either in the form of a film or solid particles. The column is placed in an oven to ensure a sufficient vapour pressure for compounds to elute in a reasonable amount of time. Many chromatographs also have the possibility to control both the temperature and the flow rate of mobile phase during analyses, and both these factors will influence the degree of separation and time before elution of the analysed compounds[158]. A schematical representation of a gas chromatograph is shown in figure 13.1. Numerous detectors can be used to observe and analyse the eluted fractions, but in this work either a flame ionisation detector or mass spectrometry were used.

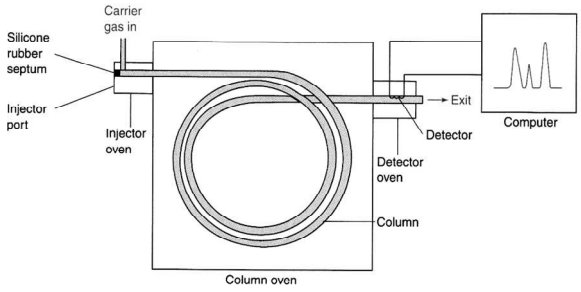

Fig. 13.1: simple depiction of a gas chromatograph. From [158]

13.1.1 The flame ionisation detector (FID)

In a flame ionisation detector (FID), the eluted compounds are burned in a mixture of H_2 and air. As carbon atoms are burned, about 1 in 10^5 produce an ion according to the scheme:[158]

$$CH + O \rightarrow CHO^+ + e^-$$

The charge separation produces a current between the flame and the collector, which can be detected and converted to a digital signal. The response factor of carbon atoms in oxygen containing compounds will be different from hydrocarbons and have been corrected for this throughout this work based on previous calibration. The response factor of all hydrocarbons has been assumed equal in all quantifications. A schematical representation of a FID detector is included in figure 13.2.

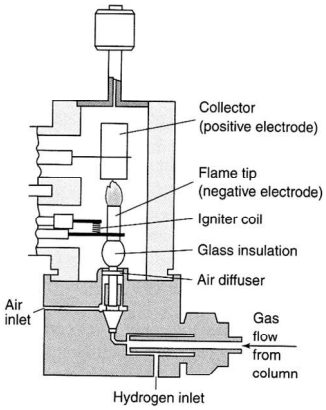

Fig. 13.2: Schematics of a FID detector. From [158].

13.1.2 Mass spectrometry (MS)

Mass spectrometry (MS) is a method that can be used not only as a detector system for chromatography, but also as a separate spectrometric technique. Either way, the method is based on converting the sample into positive ions by bombarding them with high energy electrons. These ions are then accelerated by an electrical potential and separated based on their deviation from a straight line of flight in a magnetic field. In addition to providing the molecular mass of the sample, the ions will also fragment into smaller ions. The fragmentation pattern can then be used for a more detailed analysis of the molecular structure.[157] Figure 13.3 displays the layout of a single focusing mass spectrometer.

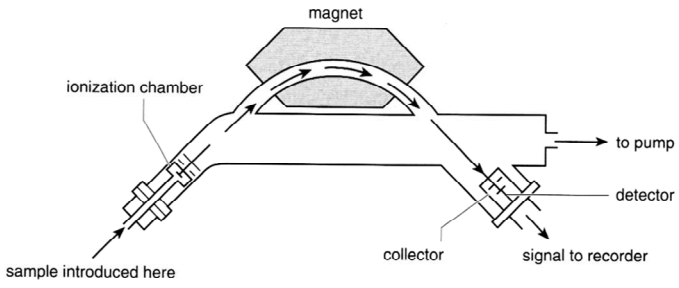

Fig. 13.3: Schematic diagram of a single focussing mass spectrometer. From [157].

13.2 Isotopic labelling

When using a feed containing ^{13}C labelled carbons, it is desirable to determine the distribution of labelled and unlabelled atoms in the product compounds. This is possible by performing a linear regression analysis on the ion fragments found by mass spectrometry. The method used here is based on previous work by P.O. Rønning[159]. The calculations assume that there is no kinetic isotope effect and only molecular ions and fragments with intact carbon skeletons are analysed.

As ^{13}C make up 1.11 % all naturally occurring carbon atoms, it is necessary to correct for this amount in order to obtain a pure ^{12}C mass spectrum. For an ion of mass m/z consisting of N carbon atoms, the probability of containing n ^{13}C atoms is given by:

$$P_n = \left[\frac{N!}{n!\,(N-n)!}\right] * 0.0111^n * 0.9889^{N-n}$$

Where the bracketed part of the equation is the number of permutations possible for n ^{13}C atoms in an ion of N carbon atoms. The single ion peak area corrected for naturally occurring ^{13}C is thus given by:

$$A_{corr}(i) = A_{obs}(i) - \frac{\sum_{n=1}^{N} A_{corr}(i-n) * P_n}{0.9889^N}$$

Where $A_{corr}(i)$ is the corrected ion peak area, $A_{obs}(i)$ the observed ion peak area and $A_{corr}(i - n)$ is the Corrected peak area of ions with mass i-n. When the corrected peak areas are known, the distribution of ions in a pure ^{12}C spectrum is obtainable.

The isotopic composition of a compound can then be found by integration of single ion peaks from MS data. Each single ion peak will contain contributions from ions of the same mass number but different number of hydrogen atoms and/or ^{13}C atoms. Based on this knowledge, a general formula for the observed area as a linear combination of the fractions of ^{13}C atoms in the ions can be constructed:

$$A_{obs}(i) = A_{sum}D_{12C}(i)X_{12C} + \sum_{n=1}^{N} A_{sum}D_{12C}(i-n)X(n)$$

Where A_{sum} is the sum of ion peak areas, $D_{12C}(i)$ the fraction of ions with mass number i in a purely ^{12}C spectrum of the compound while X(n) and X_{12C} is, respectively, the fraction of ions containing n ^{13}C atoms and the fraction of ions containing ^{12}C atoms only.

For every mass number there will be a linear equation and a set of these can be solved by linear regression analysis to give the fractions of ions containing n ^{13}C atoms. Such a linear regression was performed using a Microsoft Excel™ spreadsheet. The total content of ^{13}C in any given compound can be found from the observed distribution in the molecule.

14 Experimental

14.1 Catalytic testing

Catalytic testing experiments were performed in a u-shaped glass reactor with an inner diameter of 9 mm containing inlet, outlet and a septum for insertion of a thermocouple into the catalyst bed. Catalyst particles were pressed, gently crushed and sieved to obtain particle sizes between 0.25 - 0.42 mm. The reactor was constructed specifically to ensure room for more than 10 particles on all sides of the thermocouple as detailed by Dautzenberg[160] in his instructions on laboratory reactor design. It was also made so that the entire catalyst bed would always sit in the isothermal zone of the oven during testing. To comply with another of Dautzenberg's guidelines (height of catalyst bed should be at least 50 particles) without using overly large amounts of sample, the height of the catalyst bed was increased by diluting the catalyst with quartz, crushed and sieved to the same dimensions as the catalyst. This would also limit the increase in temperature during the reaction as methanol to hydrocarbons is an exothermic process. However, the practice of diluting with quartz caused problems during analyses of spent catalyst while at the same time seemingly not causing any significant differences on test results. The practice was therefore abandoned when performing flushing experiments and co-feeding with labelled methanol.

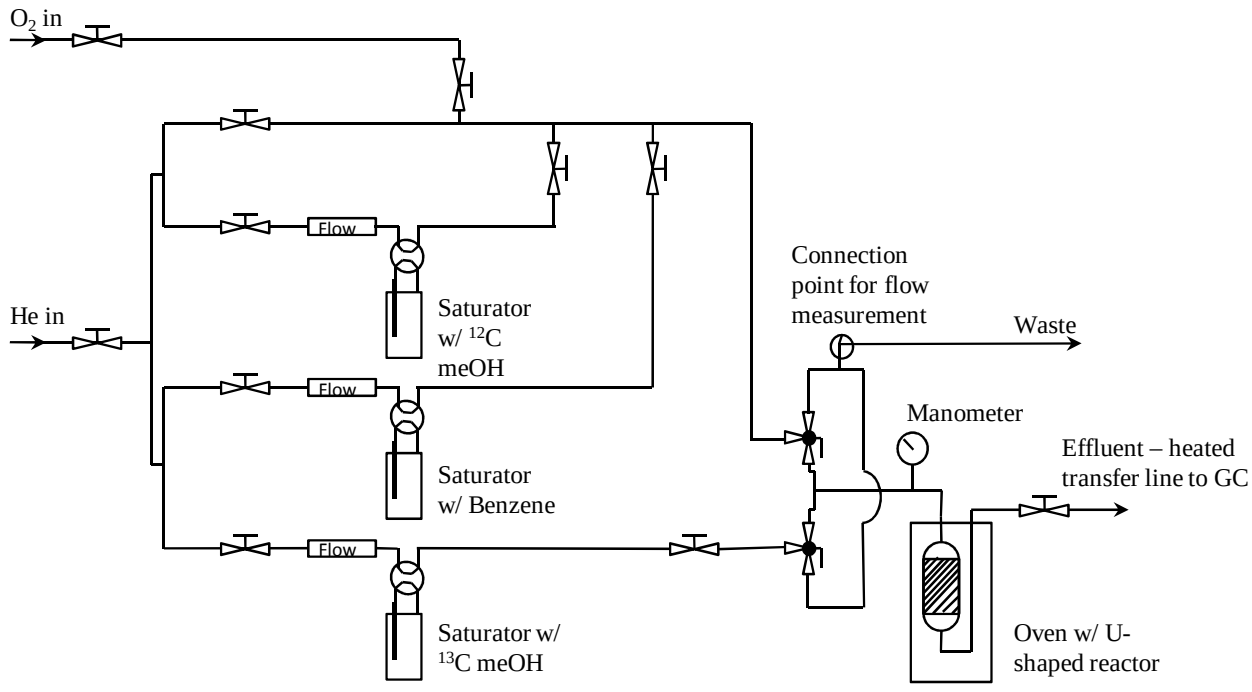

Fig. 14.1: Schematic map of the reactor setup.

Figure 14.1 shows a schematic flowchart of the setup used for most of the testing displayed in this work. The GC used was of the type Agilent 6890 with FID detector and the transfer line leading the effluent to it was heated to 250 °C. Saturators were immersed in water baths to control the saturation temperature, while flowmeters of the type Porter P150 were used. Early tests with methanol feed, (all at 450 °C and WHSV 0.93 except for sample SC) were performed on a simpler version of the testing rig containing only one feed line, but it was later rebuilt to that shown in figure 14.1 to allow easier co-feeding. This change also corresponded with a change of the GC column from an Agilent J&W HP PONA (50 m x 0.2 mm x 0.50 µm) column to an Agilent J&W PLOT-Q column (15 m x 0.32 mm x 20 µm). This change was made as the HP PONA column could not separate methanol from isobutene. Even though the PLOT-Q column could do this, in addition to also separating C2 and C3 alkenes from alkanes, it instead had problems eluting large aromatics. The columns and reactor setups will be referred to in the text simply as Pona and Plot-Q. Details and comparisons of the columns and setups are given in appendix G. Temperature and flow programs of the GC used with the different columns are given in table 14.1, below.

Table 14.1: Oven and flow programs used in the GC analysis of effluent with Pona and Plot-Q columns.

HP PONA			**PLOT-Q**		
Temperature program			Temperature program		
Ramp (°C/min)	Temp (°C)	Hold time (minutes)	Ramp (°C/min)	Temp (°C)	Hold time (minutes)
	40	6.2		90	5
25	260	25	20	220	5
			20	270	16
Total time:		40	Total time:		35
Flow program			Flow program		
Constant inlet pressure:			Ramp (Flow /min)	Flow (ml /min)	Hold time (minutes)
1.52 bar				1.5	5
Resultant initial flow:			0.5	2.5	7
1.94 ml /min			0.5	4	18
			Total time:		35

A list of all catalytic testing performed with more specific details is given in appendix B, but the most common conditions used (at WHSV 0.93 h^{-1}) was 50 mg catalyst diluted with 250 mg quartz. Helium carrier gas flowing at 15 ml /min would then be saturated with methanol at 0 °C and led through the catalyst bed at the desired temperature. When co-feeding more than one type of reactant, the saturated flows were mixed in the piping before being led through the reactor. If analysis of the spent catalyst was desired, the reaction was quenched at predetermined time by transferring the catalyst powder to a glass vial at room temperature. The setup in figure 14.1 also allow easy change from one gas flow to another, and in the flushing experiments the methanol feed was changed to a pure helium feed after the desired reaction time.

Before each test, the catalyst was activated in-situ by heating and leaving it at 550°C under a pure O_2 flow for 1 hour. This was done to remove water and ensure that no hydrocarbons remained in the structure as it was found that reproducibility was not optimal when the O_2 treatment was not performed. Oxygen treatment of this kind directly before experiments has been found necessary and successful during the group's previous work on another one-dimensional zeolitic material: ZSM-22[77].

14.2 Offline analysis of effluent and isotopic distributions

When using isotopically labelled feed, the effluent was analysed by taking gas samples from the outlet of the reactor (through a septum) using syringes. The gas samples were then analysed on a HP 6890 GC with a J&W GS-GasPro column (30 m x 0.32 mm) and HP 5973 MS detector. Temperature and flow conditions of the GC during analyses are detailed in table 14.2. This system could elute and analyse compounds up to trimethylbenzene. For analysis of larger effluent fractions, an aliquot of gas was also injected into the same GC-MS used for analysis of retained hydrocarbons (see next section). The MS detector provided the possibility of

Table 14.2: Temperature and flow conditions used in GC MS for offline analysis of effluent.

GS-GasPro		
Temperature program		
Ramp (°C/min)	Temp (°C)	Hold time (minutes)
	100	10
10	250	35
Total time:		60
Flow		
Constant flow: 1 ml /min		

determining isotopic distributions by performing regression analyses of the mass spectra obtained in each peak.

14.3 Investigation of retained material

Investigation of retained hydrocarbons in catalyst exposed to reactant was performed by quenching the reaction at a predetermined time. The samples were then dissolved in 15 % hydrofluoric acid (HF) and the hydrocarbons extracted for the aqueous solution with CH_2Cl_2. In the experiments with quartz dilution 2 ml HF to 100 mg (sample and quartz) was used, while 2 ml HF was used to dissolve 80 mg catalyst in the other cases. In the former case, 1 ml CH_2Cl_2 was used for extraction, while this was reduced to 0.5 ml for the latter experiments in order to increase the concentration of aromatics. The CH_2Cl_2 used contained C_2Cl_6 as an internal standard and a phenol impurity (likely from of the HF bottle) was always present in the same relative amounts in all analyses performed.

Extracts were analysed on an Agilent 6890 GC with an Agilent J&W HP-5MS column (60 m x 0.25 mm x 0.25 µm) and an Agilent 5973 MS detector. Isotopic distributions could be determined in the same manner as for the effluent from regression analyses of MS spectra. Temperature and flow conditions during analysis are detailed in table 14.3.

Table 14.3: Temperature and flow conditions used in GC MS for analysis of retained hydrocarbons.

HP-5MS		
Temperature program		
Ramp (°C/min)	Temp (°C)	Hold time (minutes)
	50	3
10	300	2
Total time:		30
Flow		
Constant flow: 1 ml /min		

15 Results and discussion

15.1 Catalyst activity and lifetime

15.1.1 At 450 °C and WHSV 0.93 h^{-1}

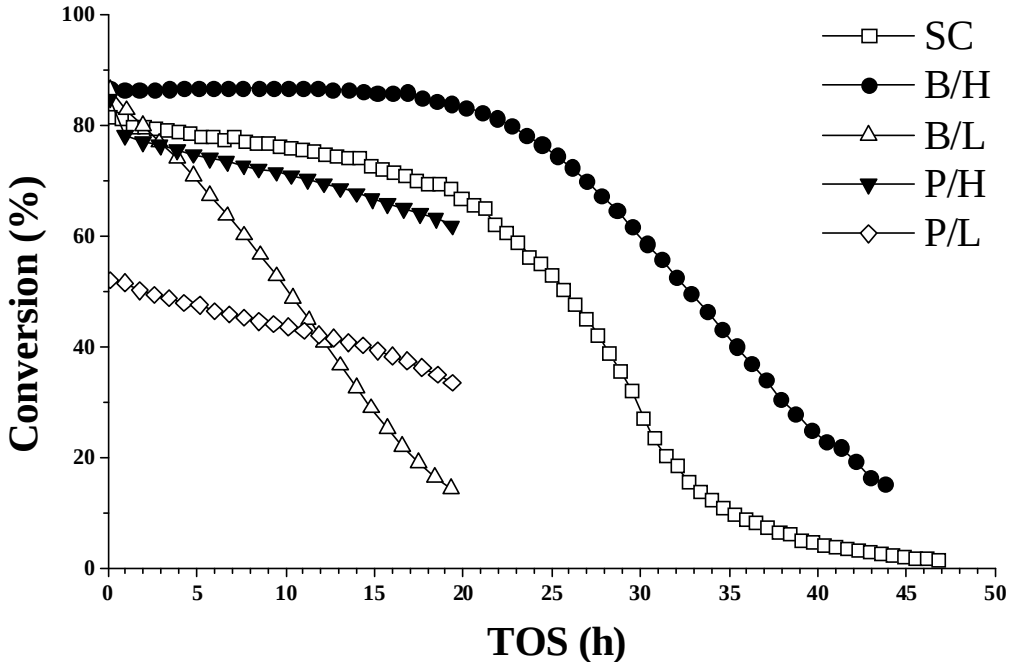

Fig. 15.1: methanol conversion as a function of time in stream (TOS) for the different catalyst samples at WHSV 0.93 h^{-1} and 450 °C. Note that SC is measured with the new rig.

Figure 15.1 shows the evolution of activity with time on stream (TOS) at 450 °C and WHSV = 0.93 h^{-1} for the five catalyst samples used in this work. When calculating conversion levels, dimethyl ether has been counted as a reactant instead of a product, as equilibration between methanol and dimethyl ether (and water) is assumed to occur before production of hydrocarbons[33]. As can be seen from the figure, the initial conversion of most samples are very similar and between eighty to ninety percent. The exception is P/L, which starts out at the significantly lower conversion of ~52 %. These initial activities correspond quite well to the acid site densities of the catalysts as the acid site density of P/L is low while it is higher and similar for the others.

SC has a higher activity than expected following this logic (initially just slightly below B/H, B/L and P/H), which could mean that its acid site density is higher than expected from the amount of silica used in the synthesis mixture. However, if there are significantly fewer

siliceous regions in this material than in the others, which is likely since no Si-OH groups were observed in IR (see chapter 11.5.1), the ratio of acid sites to Si atoms in the material may be much larger than for the other samples. Thus, it cannot be ruled out that the acid site density of this material is closer to P/H, B/H and B/L than to P/L. Some care should be taken in comparing the activity SC directly to the others as this is the only sample of these which was measured on the PLOT-Q GC column after rebuilding the testing rig. While the two set-ups and column perform very similarly, the results are not identical. See appendix G for a comparison between the two GC columns. In general, it has been found that activities found with the new PLOT-Q system is usually slightly lower than for the old PONA system.

While initial conversion levels are similar for most of the samples, and differences can be partly explained by the acid site density, the deactivation rates differ substantially. The conversion of SC slowly decreases throughout the whole testing period and a more rapid deactivation begins after about 20 hours on stream. While the conversions of the plate-like samples (P/L and P/H) have not been measured for long enough to see this deactivation, they follow a very similar, slowly decreasing, conversion curve to SC during the measured time on stream. The two other samples, however, strongly contrast this deactivation trend. B/H shows little or no decrease in conversion until approximately twenty hours on stream, when a rapid deactivation takes place, while B/L deactivates rapidly from the beginning of the experiment.

When integrating under the deactivation curves in figure 15.1, the total conversion capacity for methanol can be found. While the catalysts are active for a long period of time, the low space velocity means that only a moderate amount of methanol is converted. B/H (the catalyst with longest lifetime) converts just under 30 gram methanol per gram catalyst before deactivation, while B/L (which deactivates fast) converts only about 9 gram per gram catalyst. Although 30 g/g_{cat} is more than the conversion of H-SAPO-34 at its optimum temperature (~22 g/g[70]), the time on stream for H-SAPO-5 before reaching this number is very long compared to H-SAPO-34. Dealuminated H-Beta has been reported to convert up to nearly 200 g/g_{cat}[161] before deactivation, while NaOH treated H-ZSM-5 has been reported to convert 550 g/g_{cat} before deactivation[162]. It is also interesting to note that while Chen et al[92]and Campelo et al[94] report conversion capacities similar to those seen here, Tapp et al[139] reports a conversion capacity an order of magnitude higher. Whether it is possible to achieve higher conversion capacity under other conditions has not been studied in detail here.

Both B/L and B/H were originally expected to deactivate fast due to their large crystal sizes, as slow diffusion in large crystals are often assumed to make the catalysts less efficient[114]. For instance, both Chen et al[163] and Hereijgers et al[83] found that 2-5 µm H-SAPO-34 crystals displayed a lower total conversion capacity for methanol than crystals of 1 µm or smaller. While B/L displays a rapid deactivation as intuitively expected, the even larger crystals of the B/H sample are seemingly more resistant to deactivation than any of the other samples. TPA adsorption (see chapter 11.3) also indicates that the diffusivity of large molecules is better in B/L than in B/H. This should in principle make B/L more resistant to coke formation instead of less, and thus also more resistant to deactivation, assuming that pore blockage is the main cause of catalyst deactivation. The fact that neither crystal size nor the measured ease of diffusion is reflected in the order of which the catalysts deactivate most likely indicate that diffusion limitations are not an issue at the conditions utilised here. Whether this would still be the case at higher feed rates or with samples containing a greater density of acid sites is an open question.

A fact worth noting is that the highest and lowest BET surface areas are possessed by, respectively, B/H and B/L. If the lower BET area of B/L is due to a more defective structure, it is possible to imagine that larger cavities exist inside the crystals due to "missing" framework atoms. Formation of larger aromatic species in such cavities could then cause blockage of one or more of the crystals' micropores. Another possible explanation for the difference in deactivation would be that the more defective structures have a higher degree of blocked pores, a feature Demuth et al[96] reports to have observed with $AlPO_4$-5. It appears plausible to imagine that diffusion of molecules out of a deep pore with only one opening would be problematic. This might then lead to a build-up of coke in the pores and further to deactivation of the catalyst.

15.1.2 At 350 ℃ and WHSV 0.93 h^{-1}

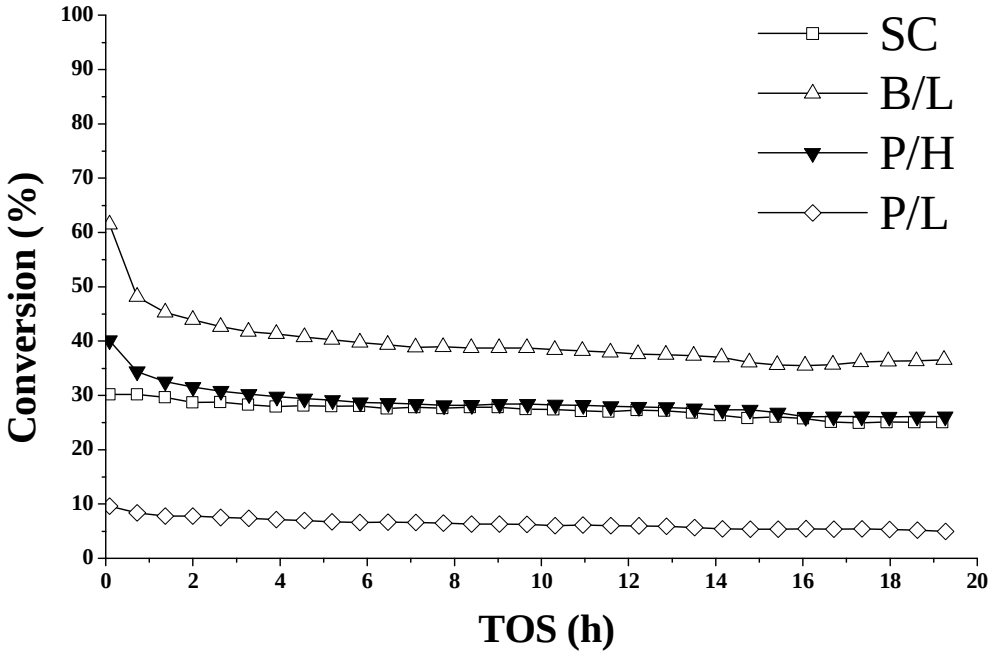

Fig. 15.2: Methanol conversion as a function of time on stream (TOS) at T = 350 °C and WHSV = 0.93h^{-1} for samples SC, B/H, P/H and P/L.

As figure 15.2 shows, the activity of all measured samples (B/H was not measured due to low sample availability) is much lower at 350°C than it was at 450°C (recall figure 15.1). This is in accordance with the results of Chen et al[92]: that SAPO-5 requires relatively high temperatures to reach a significant activity level. Results by Bleken et al[70] indicate that SAPO-34 also has a optimum temperature for methanol conversion which is above 350°C. The initial activity of the samples differs, with P/L again being the least active, in accordance with its low density of acid sites. While the order of initial conversions is the same as at 450 °C for the other three samples, they show a greater spread at 350°C. Initial conversion at 350 °C is 20 % higher for B/L than for P/H, which is again 10 % higher than SC. That B/L is this much more active than P/H is surprising as even though the acid site density of B/L is higher, the difference is quite small. It is possible that the lower acidic strength of P/H (recall chapter 11.5.2) comes into play here. That SC is comparable in activity to P/H strengthens the assumption that its acid site density is higher than expected based on amount of Si used in the synthesis.

What is also evident from figure 15.2 is the lack of any significant deactivation during the 19.5 hours on stream for the catalysts, which is in stark contrast especially to the rapid deactivation exhibited by P/L at higher temperature. As no deactivation takes place it is hard to determine total methanol conversion capacity, but this is assumed to be lower than at 450 °C due to the initially much lower conversion. Both P/H and B/L display an initial loss of activity during the first hour before reaching a more stable, slowly decreasing, conversion level. This behaviour was also visible for P/H at 450°C where conversion dropped by almost 10 % between the first two sampling points. This drop is present in every reproduction of the test (even those considered failed), so it is a real effect inherent to this sample. It also coincides with some changes in selectivity for the same samples, as will be discussed in the section on catalyst selectivity (chapter 15.2).

While it is hard to find a definite explanation for this effect, the two samples exhibiting the activity drop do have several features in common. They both show a hysteresis loop upon N_2 adsorption and desorption in addition to amorphous material being present in both samples. FTIR also revealed two differences compared to the other samples, namely the presence of Al-OH groups and a seemingly lower acid strength than the other samples. These Al-OH groups may stem from extra-framework aluminium inside the zeolite cavities, which has been previously linked to strong Lewis acidic sites[131]. Thus, it is tempting to ascribe the initially higher conversion to strongly acidic sites that deactivate very fast. However, it should be noted that no interaction of CO with strong Lewis sites was observed using FTIR, so this explanation is not completely satisfactory.

15.1.3 Variation of WHSV at 450 ℃

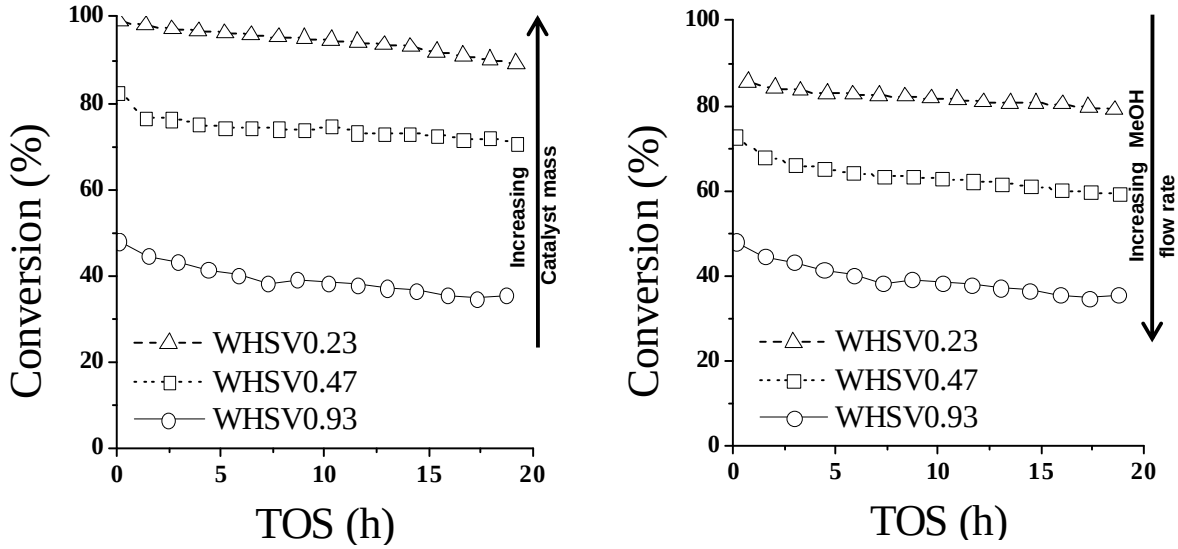

Fig. 15.3: Conversion curves for varying WHSV by varying the mass of catalyst (left) and varying the flow rate (right). Catalyst is P/L at WHSV 0.93 h^{-1} and 450 °C.

A series of experiments investigating the effect of varying space velocity was performed. The catalyst used was P/L and the temperature 450 °C in all experiments. WHSV was lowered both by increasing the mass of catalyst used and by decreasing the flow rate of methanol. The effect of decreasing the space velocity on the conversion of methanol is shown in figure 15.3, from which it is evident that when space velocity is decreased the percentage of methanol feed converted to products is increased. As the catalyst does not show any significant signs of deactivation during any of the experiments, it is not known whether the total conversion capacity for methanol per gram catalyst is affected in any way.

It can also be observed that the manner in which the space velocity is varied is of importance, as a higher percentage conversion is obtained when increasing the amount of catalyst used than if the flow is reduced. A possible reason for this is that some of the methanol bypasses the catalyst bed when only 50 mg catalyst is used, thus increasing the height of the catalyst bed promotes the reaction more than reducing flow. While the reactor used here has been built with a sufficiently large diameter to avoid influence of the reactor walls on the flow pattern, Dautzenberg[160] also recommends that the height of a catalyst bed in a laboratory reactor should be much higher than 50 times the size of the catalyst particles. This is not at all the case in the experiments performed in this work as even when the catalyst is diluted with quartz in a 1:5 ratio, the height of the bed is still < 50 times the particle size. It is also

unknown if the quartz dilution has any effect at all on flow pattern as it does not seem to affect selectivity or lifetime to any large extent (see appendix H). It should also be noted that Dautzenberg[160] recommends use of high flow as good experimental practice. The 3.75 ml/min flow used to obtain a WHSV of 0.23 (figure 15.3, right) can hardly be said to stand up to this criterion.

15.1.4 Summary of catalyst activity and lifetime

Initial activity for methanol conversion of the samples appears to be governed primarily by the acid site density of the samples, assuming a similar acid site density for SC as for B/L, B/H and P/H. At 450 °C and WHSV 0.93 h^{-1}, all samples except P/L convert between 80 and 90 percent of the methanol feed after 5 minutes on stream, while P/L converts a bit more than 50 %. When the temperature is decreased at the same WHSV, the activity of all samples is significantly reduced and a greater spread in activity becomes apparent. P/L now converts less than 10 % of the methanol feed while B/L, P/H and SC convert between 60 and 30 %. As space velocity is lowered, it is observed that P/L converts more of the methanol feed to products. Observed changes in conversion was larger when varying WHSV by increasing the size of the catalyst bed rather than lowering the flow rate of methanol.

At 450 °C and WHSV 0.93 h^{-1}, the catalysts show very different rates of deactivation. While P/L, SC and P/H show a slightly downward sloping activity, B/H show a long period of stable conversion before deactivating and B/L deactivates rapidly from the beginning. The reason for this has not been satisfactorily determined. At 350 °C, none of the samples show deactivation, but P/H and B/L both show an initial drop in activity between 5 and ~45 minutes. The reason for this is also uncertain, but defective structures might be part of the answer.

15.2 Product selectivities

15.2.1 At 450 ℃ and WHSV 0.93 h^{-1}

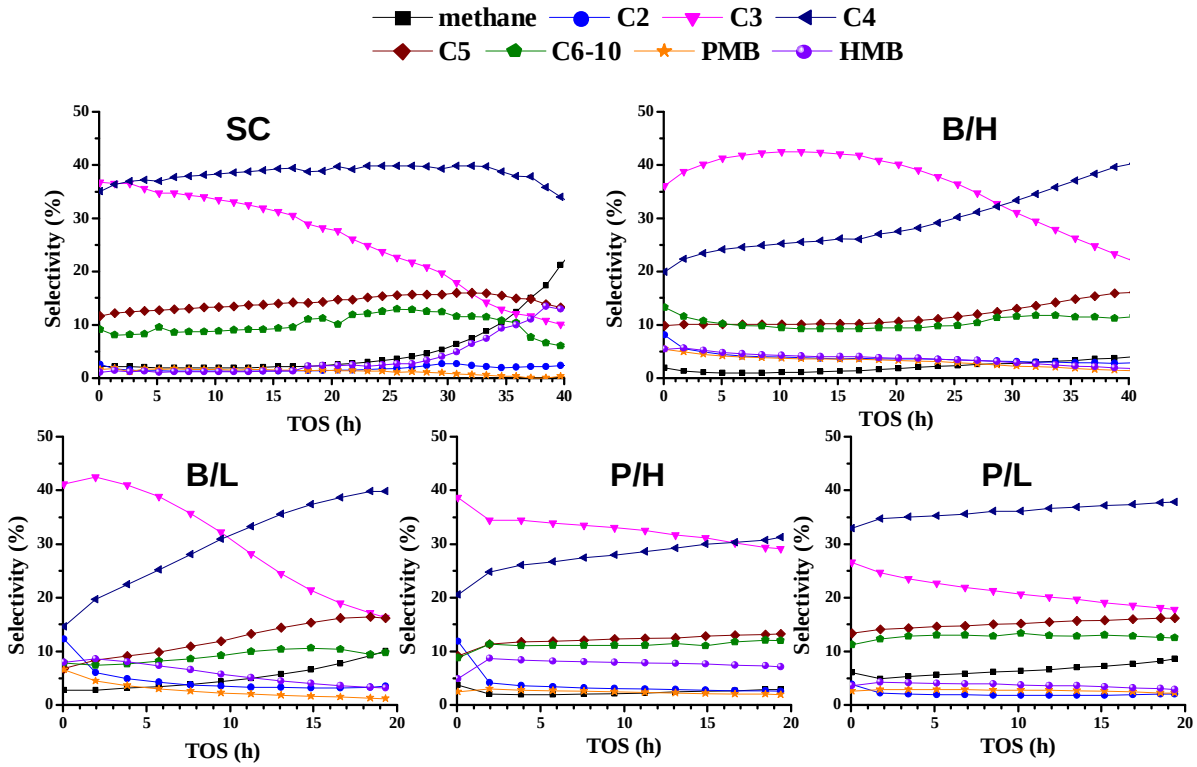

Fig. 15.4: Selectivities vs. TOS for all five samples at 450 °C. CX indicates hydrocarbons with X carbon atoms. The C6-10 fraction contains both aliphatics and aromatics. PMB and HMB are penta- and hexa- methylbenzene, respectively.

Figure 15.4 shows selectivities plotted versus time on stream (TOS) for all samples. In line with previous reports[94, 109] C4 hydrocarbons (butenes and butanes) constitute large amounts of the products, while larger compounds are also eluted in substantial amounts. However, the C3 (propene and propane) fraction is the largest initially in all samples except in P/L, whose initial conversion level is much lower than the others. When conversion is decreased for B/H, B/L and SC, the selectivity towards C4 becomes greater than the selectivity towards C3. The C2 (ethene and ethane) selectivity is low for all samples and the curve remains mostly stable during the testing period, except for a drop in selectivity after the first point in some of the samples (especially in B/L and P/H). Methane selectivity is initially low for all samples except P/L, and is seen to increase sharply as the catalysts deactivate and SC deactivated down to below 10 % conversion has a higher than 20 % selectivity to methane. It is tempting to ascribe the methane formation to increased diffusion resistance caused by coking of the

catalyst. However, the fact that P/L produces similar amounts of methane when fresh as SC does when deactivated to ~50 % conversion indicates that while this might be a factor, it does not appear to be dominant until severe deactivation is reached.

As is shown by figure 15.5 (next page), the product selectivities of the catalysts appear to depend mostly on the level of conversion rather than other factors. While there are small differences in selectivities at the same conversion levels for the different catalysts, the same trends are observed for all samples irrespective of the TOS and degree of deactivation. It should also be noted that, as previously mentioned, the PONA GC column was used for all samples except SC. This then means that comparisons with SC should be performed with caution. The observation from figure 15.5 corresponds well with Janssens' idea of envisioning deactivation simply as the loss of active surface[81], as deactivation does not appear to influence selectivity to any large degree.

The trends observed for all catalysts was that the C2 and C3 fraction together with penta- and hexa- methylbenzene clearly grows with increasing conversion while the methane, C4, C5 and C6-10 fractions all diminish as conversion levels increase. It should be noted that the ration between C4 and C5 selectivities does not appear to change upon changing conversion. The hexamethylbenzene fraction is seen to show a different trend for SC, but it is believed that this is due to the GC column not being suited for elution of products this large, causing a build-up when too many successive runs are performed, and not because of a real selectivity difference (appendix G has more details on differences and problems with the PONA and PLOT-Q columns). The selectivity to hexamethylbenzene is the lowest of all samples before the sudden increase, indicating a low sensitivity for this compound in the PLOT-Q column.

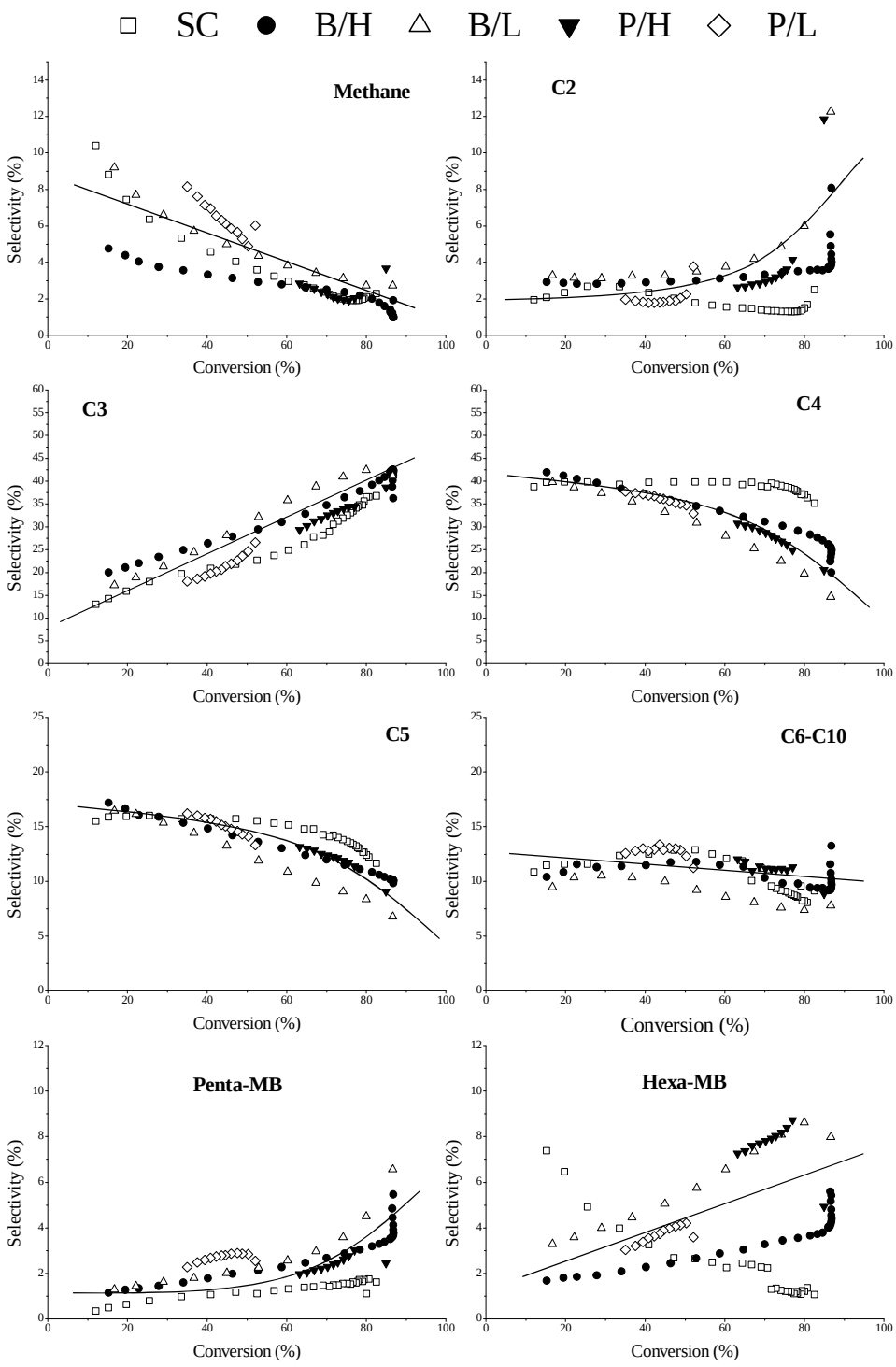

Fig. 15.5: Plots of selectivity versus conversion level for all product fractions at 450 °C. The trend lines are approximations and a guide to the eye only, and not calculated in any way, but illustrate the changes in selectivity quite well. The strange selectivity towards hexa-MB for sample SC is assumed to be due to GC problems (see text for explanation) and was not accounted for when the trend line was drawn.

Aromatic products in all samples are dominated by penta- and hexa-methylbenzene, in line with what has been reported by Yuen et al[17] and Tapp et al[139]. The contents of the C6-10 fraction in figure 15.2 have not been identified properly for tests performed with the PONA column, but for SC (tested with the PLOT-Q column) the fraction has been determined to consist of ~5 times as much aliphatic as aromatic products at short TOS (high conversion) and increasing to more than ten times as much at long TOS (low conversion). Toluene and xylenes are present in marginally larger amounts than tri- and tetra-methylbenzenes, while even smaller amounts of benzene and ethylbenzene are also present. Testing of P/L on the PLOT-Q column (not shown in previous figures) also reveal similar compositions of these fractions. For both of these samples the total amount of C6-10 aromatics is lower than either of the penta- or hexa-methylbenzene fractions. Trace amounts of polymethylnaphthalenes and ethyl substituted benzenes are also found in the samples when effluent is analysed by GC-MS, but they cannot be observed during normal testing due to the lower sensitivity of the GC.

The composition of the C5 fraction has not been properly identified, but it appears as if the major fractions are isopentenes. Of these, the peak presumably caused by 2-methyl-2-butene becomes dominant at low conversion. The assignment of peaks is based solely on mass spectra of the compounds (from ex-situ GC-MS analysis) and the boiling points of the C5 alkenes (that are related to the order of elution in GC analysis). The aliphatics in the C6-10 fraction consists of a multitude of small, unidentified, peaks. GC-MS analysis confirms the presence of C6, C7 and C8 alkenes with MS spectra of most compounds giving best fits with branched isomers. There also appears to be trace amounts of C7 and C8 dienes present. These may possibly be precursors to aromatic species. The compositions of the C2, C3 and C4 fractions, on the other hand, are known with certainty for the samples analysed with the PLOT-Q column (SC and P/L). This column is able to separate ethane from ethene and propane from propene, in addition to separating iso-butane from methanol (which was not possible with the PONA column).

Figure 15.6 shows the compositions of the C4 fractions at different conversion levels of methanol for SC and P/L. The C4 fractions of both SC and P/L (analysed with PLOT-Q column) are confirmed to consist mostly of butenes, with butanes accounting for less than 10 % of the fraction. While the iso- and 1-butene fractions are not completely separated in the GC, they are well enough separated to see that iso-butene is dominating at all conversion levels, while the 1-butene peak usually appears smaller than the cis- and trans-2-butene peaks.

The C4 fraction of SC (figure 15.4) reveals clear trends, with the relative amount of 1/i-butene decreasing with higher total conversion, while the 2-butenes and iso-butane amounts are increasing with higher conversion. The relative amount of n-butane is very small at all times, and does not change much with conversion.

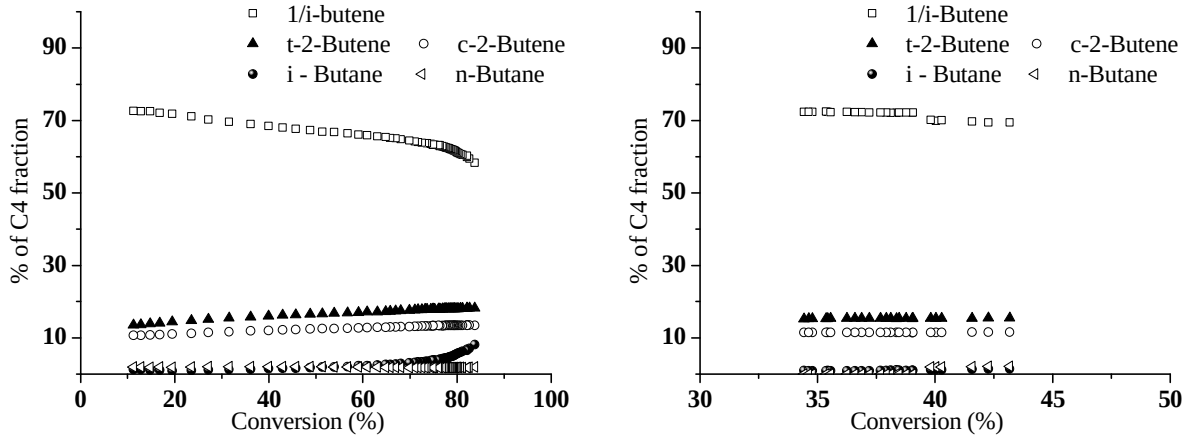

Fig. 15.6: The distribution of C4 species as a function of total methanol conversion for SC (left) and P/L (right). Note that the conversion range for P/L is much narrower than for SC.

For the distribution of the butenes only, the equilibrium positions at three different temperatures are given in table 15.1. It is obvious from this and from figure 15.4 that the amount of 1/i-butene is significantly higher than the equilibrium value, especially at lower conversion levels. As the amount of 1-butene is known to be much lower than isobutene (from partial separation by GC analysis), it seems likely from the trends in figure 15.6 that i-butene is closer to a primary product than the linear butenes.

Table 15.1: Equilibrium distribution of butenes at different temperatures[164]

Temperature (K)	1-butene	i-butene	Sum 1+i-butene	c-2-butene	t-2-butene
600	7.5	54.6	62.1	14.4	23.4
700	10.8	49.2	60.0	15.8	24.2
800	14.0	44.9	58.9	16.6	24.5

For saturated molecules to form during methanol conversion over zeolites, a transfer of hydrogen from another molecule is necessary. This leads to the formation of a more saturated molecule and one which is less saturated, i.e. an aromatic compound. Hydrogen transfer reactions, and the rate of these, are thus of great importance in methanol catalysis. To discuss it, it is useful to define a hydrogen transfer index (HTI), defined as follows:[142]

$$HTI = \frac{Sum\ of\ alkanes}{Sum\ of\ alkenes + alkanes}$$

This can then be calculated for different species (e.g. C2, C3 or C4) to yield the ratio of alkenes and alkanes, in addition to information on the amounts of aromatic compounds produced. The C4 HTI of SC and P/L are shown in figure 15.7, where it can be seen that C4 HTI increases with higher conversion. For SC, the HTI starts at ~0.03 and increases slowly to ~0.04 at ~60 % conversion before increasing more rapidly to 0.1 at 83 % conversion. Curiously, even though P/L has a lower C4 HTI at its lowest conversion (~35 %) the HTI value increases sharply after 40 % up to a maximum value of 0.16 at 48 % conversion, a significantly higher value than ever obtained for SC. This shows that even though the C4 HTI values are quite low at all times, there are variations between the samples. Also, it implies that the rate of hydrogen transfers is also affected by the degree of deactivation as both samples show a steep decrease in HTI at the start of their lifetime and a more stable HTI value at longer TOS.

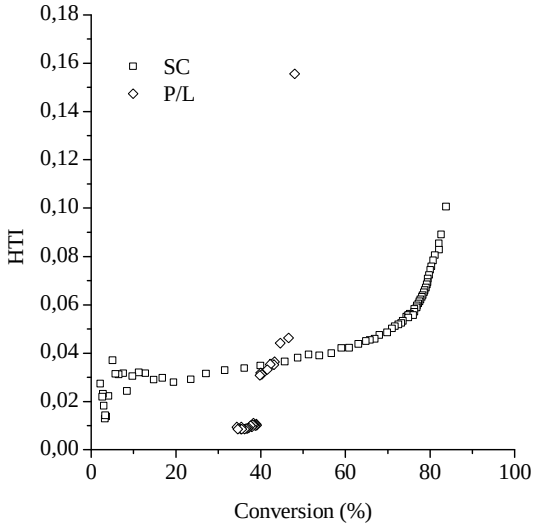

Fig. 15.7: C4 HTI, plotted as a function of conversion for samples SC and P/L

The amount of propane formed for both samples is very low throughout the entire time they were tested, with C3 HTI values smaller than 0.01 at all conversion levels for SC and too low to measure at all for P/L. While hard to measure accurately as the C2 fractions are very small, the C2 HTI value is found to show the opposite trend of the C4 HTI for SC. The value is quite high when conversion is less than 25 %, reaching 0.2 at the lowest conversion, while it decreases from ~0.06 to ~0.02 in the conversion range 25-83 %.

15.2.2 At 350 ℃ and WHSV 0.93 h^{-1}

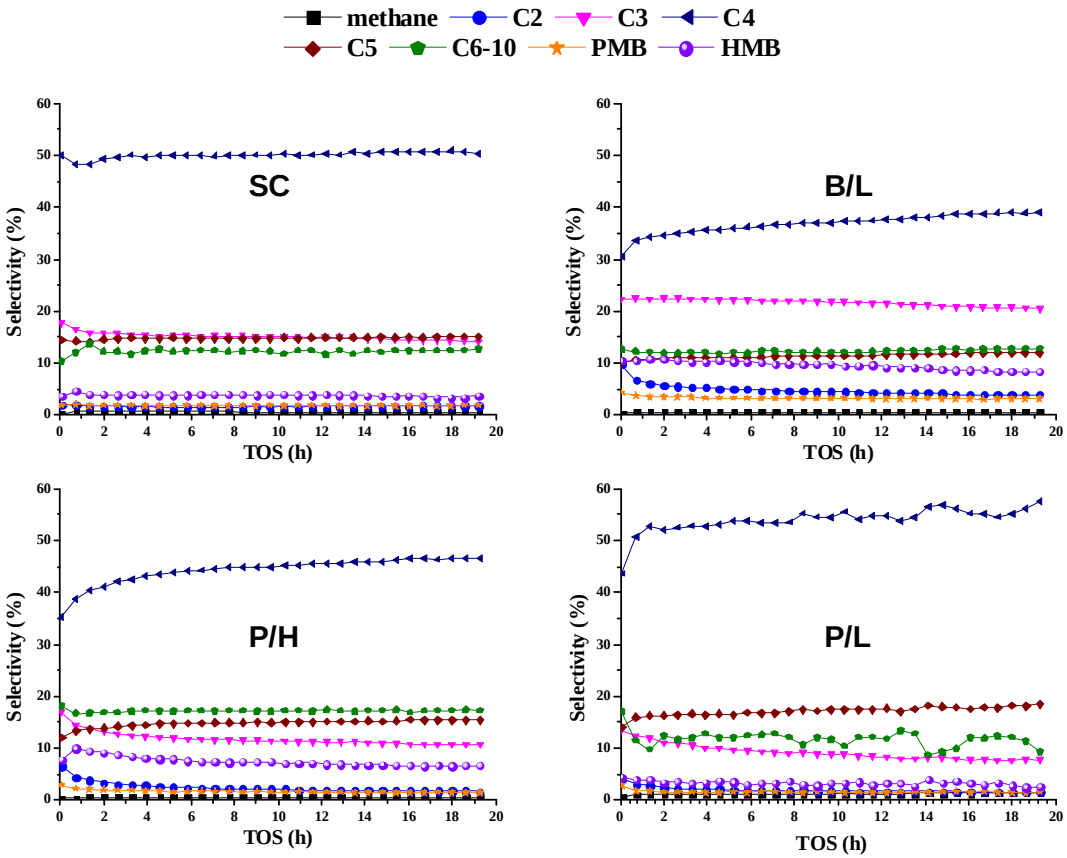

Fig. 15.8: Product selectivities as a function of time on stream for all catalysts studied at 350 °C and WHSV 0.93. All samples were measured with the PLOT-Q system.

When the temperature is decreased to 350 °C at the same space velocity, the selectivities are seen to change a little compared to the higher temperature of 450 °C. As can be seen from figure 15.8, selectivity towards C4 is very dominant under these conditions. The selectivity towards hexamethylbenzene is also seen to be high, especially for P/H and B/L. In addition, methane selectivity is practically less than 1 % for all samples throughout the experiments, which is significantly lower than at 450 °C. It is again noted that the C4 to C5 ratio, although higher than at 450 °C, is relatively stable when comparing all samples and at all conversions. These experiments have been performed on the PLOT-Q column, meaning that comparisons to the results at higher temperature are not necessarily straightforward, but in figure 15.9 comparisons of selectivities at the same percentage conversion of methanol are attempted.

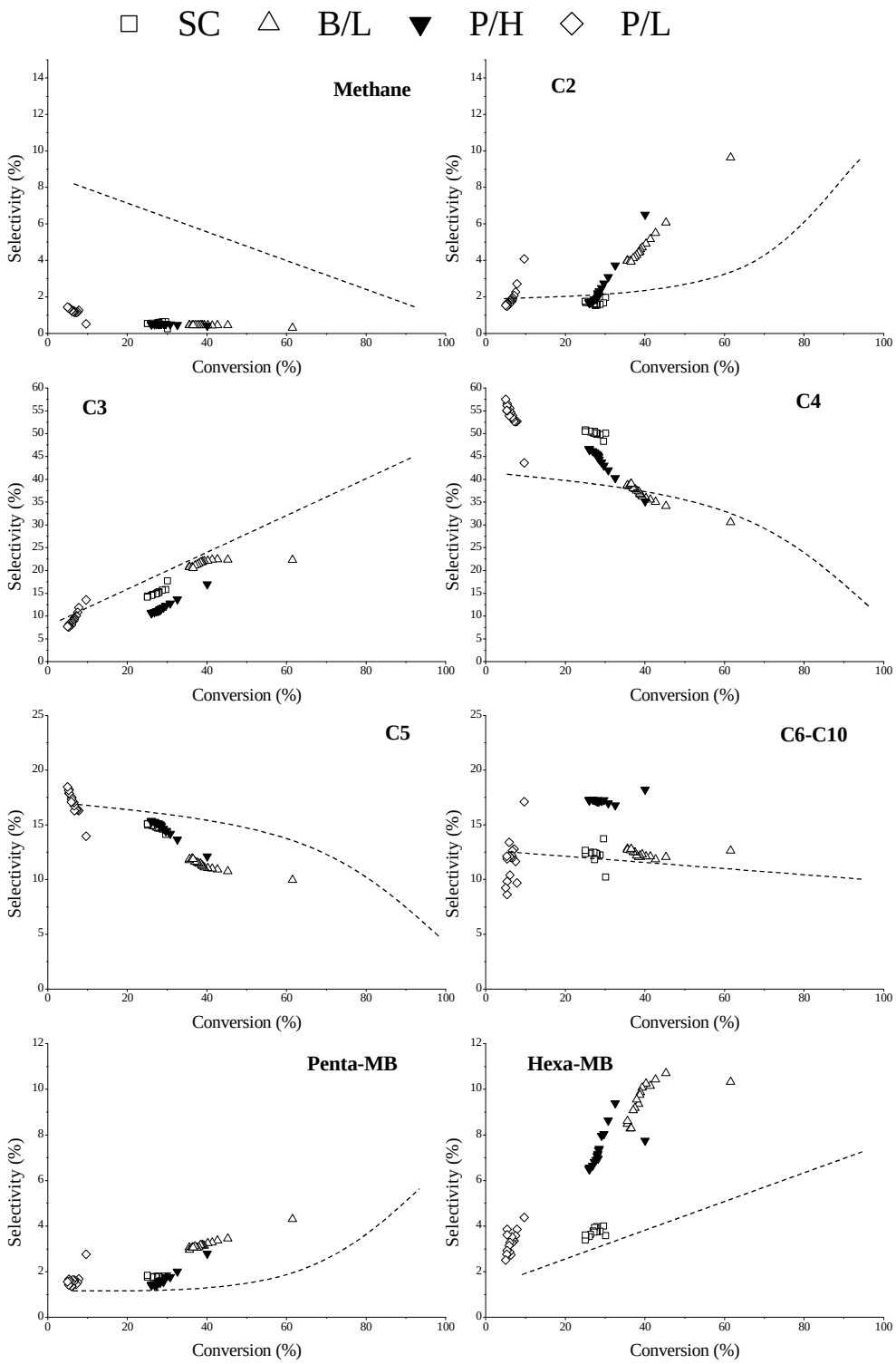

Fig. 15.9: Selectivities towards all product fractions at 350 °C plotted as a function of total conversion. The dashed lines are the approximate trend lines found at 450 °C.

When comparing the measured selectivities at 350 °C with the approximate trend lines for selectivity versus conversion at 450 °C (from figure 15.5), two striking differences are observed. Firstly, the selectivity towards methane is much lower at 350 °C than at 450 °C and secondly, the selectivity to hexamethylbenzene is significantly higher at conversion above 10 %. Even though the PLOT-Q column has problems analysing hexamethylbenzene, the amount eluted has previously been found to be smaller than the actual content in effluent and not larger (at least for experiments not run over several days).

While these two differences are clear enough to conclude that it is not simply an effect of the different GC column from that used at 450 °C, other smaller differences also exist from the experiments at 450 °C. For example, the C4 and C2 selectivity plots are a bit different. For C2 undue attention should not be paid to the fact that selectivity is somewhat higher than at 450 °C as the PONA column distinguishes poorly between C1 and C2. While this is true for the methane fraction as well, the differences in methane selectivity with temperature are large enough to be assumed significant. What is interesting with the C2 fraction, however, is the fact that all samples except SC show a decrease in selectivity with time on stream which is steeper than the trend line from the 450 °C experiments. The opposite trend, a steep increase in selectivity with time on stream, is also visible for C4. It is also interesting to note that these trends are not observed in sample SC.

The selectivity to pentamethylbenzene also appears a bit higher than at 450 °C, and the selectivity towards lower aromatics in SC (not shown) is also found to be higher at the lower temperature (1.7 % and 1 % selectivity at 450 °C and 350 °C, respectively). As the selectivity towards hexamethylbenzene is also higher, it appears safe to conclude that formation of aromatics is more favoured at the lower temperature. This may be explained by the fact that formation of aromatics becomes thermodynamically more favourable when the temperature is lowered. It should also at this point be noted that the selectivity towards hexamethylbenzene as a function of conversion has been lower for SC than for the other samples at both temperatures (if only considering the time before the abnormal values found towards the end of the 450 °C experiment).

As formation of aromatics is greater at this temperature, it is also expected that HTI values are higher. For the C2 and C3 HTI this is not observed, but a plot of the internal distribution of

C4 species (figure 15.10) reveals clear differences from what was observed at 450 °C (recall figure 15.6). At 450 °C, the selectivity to both i- and n- butane was below 3 % of the total C4 fraction for both P/L and SC, except above 70 % conversion where (for SC) the relative amount of i-butane increased sharply to ~8 % as conversion increased to 83 % (the highest measured for the sample). At 350 °C, i-butane constitutes ~4 % of the total C4 fraction at 10 % total conversion, rising to ~10 % at 30 % conversion and rising all the way to nearly 50 % when conversion is 63 %. Curiously, the selectivity to n – butane is zero in all samples.

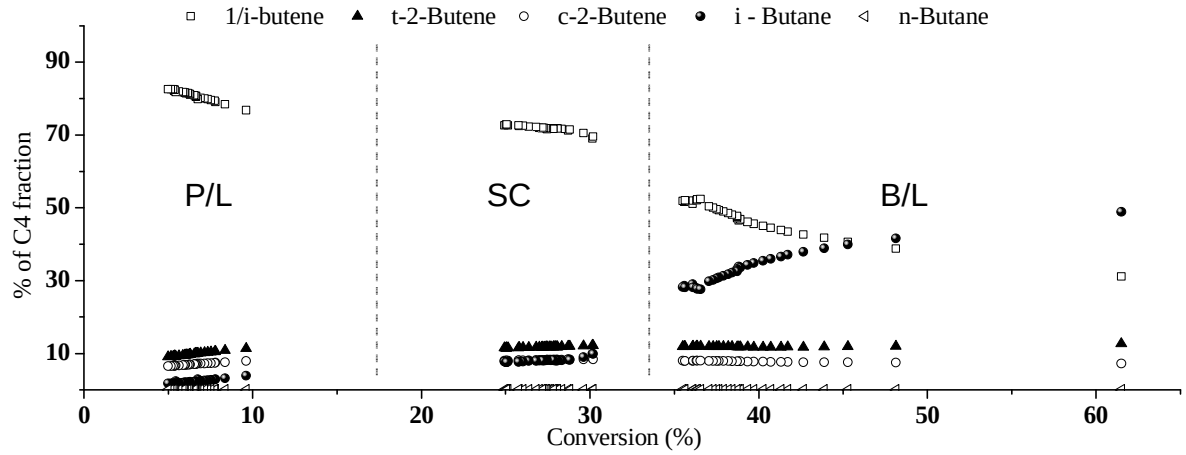

Fig. 15.10: Internal distribution of C4 species at 350 °C. The dashed lines divide analysis points for different samples.

Figure 15.10 is a composite of selectivity points at differing times on stream for three samples assembled to observe a trend over a larger range of conversion levels. This means that it cannot be ruled out that difference between the samples or due to varying degree of deactivation also factor into the differences in the composition of the C4 fraction. However, the good correlations between selectivities and methanol conversion found between the samples throughout this work, regardless of degree of deactivation or time on stream, provides strength to the extrapolation. In addition P/H (which has not been plotted to conserve the clarity of the figure) bridges the gap

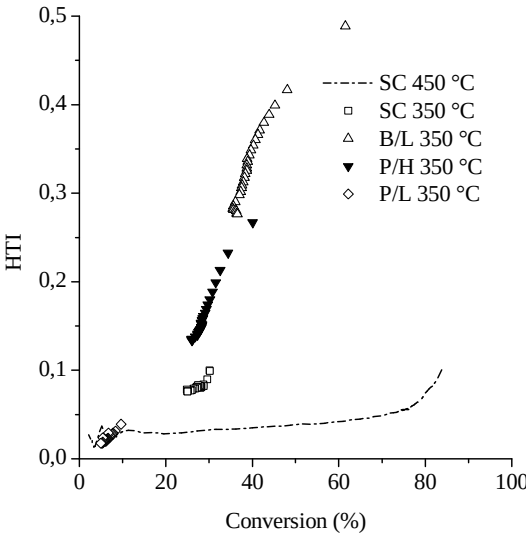

Fig. 15.11: C4 HTI as a function of conversion for all samples at 350 °C. The dash-dotted line, representing the C4 HTI of SC at 450 °C, is included for comparison.

between SC and B/L very nicely, overlapping with the displayed points of both at either end of its conversion range. The increased alkane formation at 350 °C compared to at 450 °C, shown in figure 15.11, fits very nicely with the observed increase in selectivity to aromatics at the lower temperature. These facts can be taken as evidence that hydrogen transfer reactions are favoured at the lower temperature. It is also interesting to note that the ratio of branched to linear C4 remains the same throughout the available conversion range, indicating that i - butane is formed nearly exclusively from i - butene.

15.2.3 Selectivities when space velocity is varied at 450 ℃

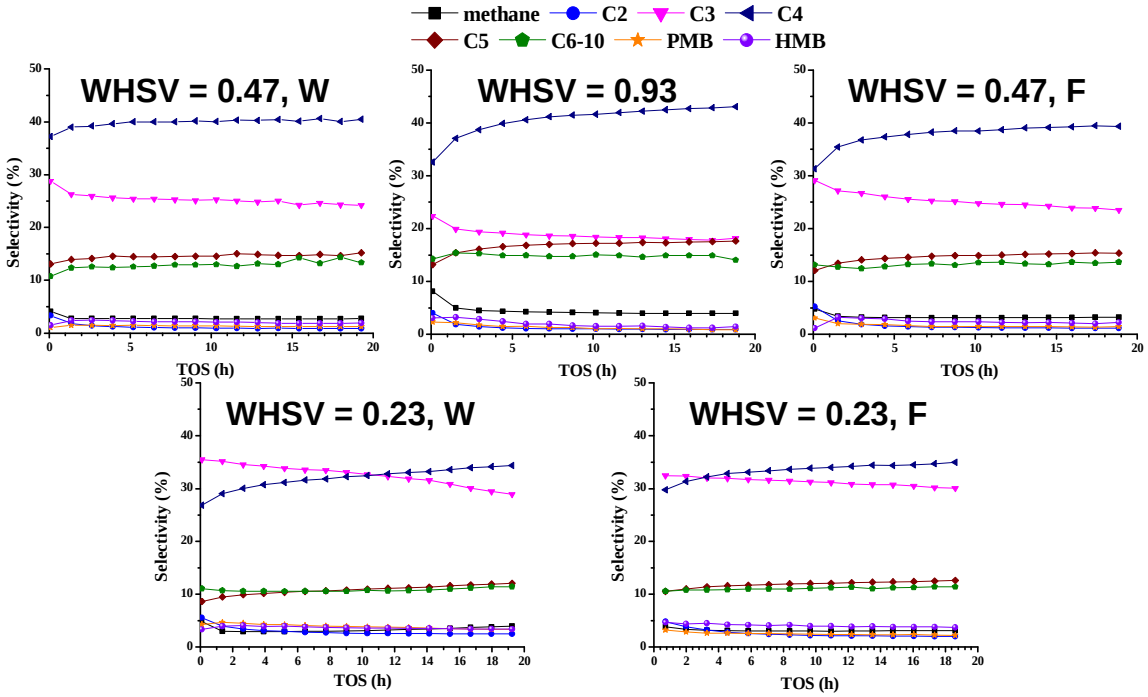

Fig. 15.12: Selectivity as a function of time on stream when the space velocity is varied at 450°C. W signifies a change in catalyst mass, while F signifies a variation in flow rate varied. The catalyst is P/L, but selectivities of the WHSV = 0.93 are slightly different those shown earlier as all experiments shown here were performed using the PLOT-Q column.

When the space velocity was decreased, the conversion increased (as found in chapter 15.1.3). It also increased somewhat more when the catalyst mass was increased than when flow rate was decreased. Selectivities for these experiments with sample P/L are shown in figure 15.12. Trends found under these conditions are not very different from those found for catalysts at the same conversion levels at 450 °C and WHSV 0.93 h^{-1}. However, the selectivities change a bit more than expected (based on change in conversion) during the first hours on stream.

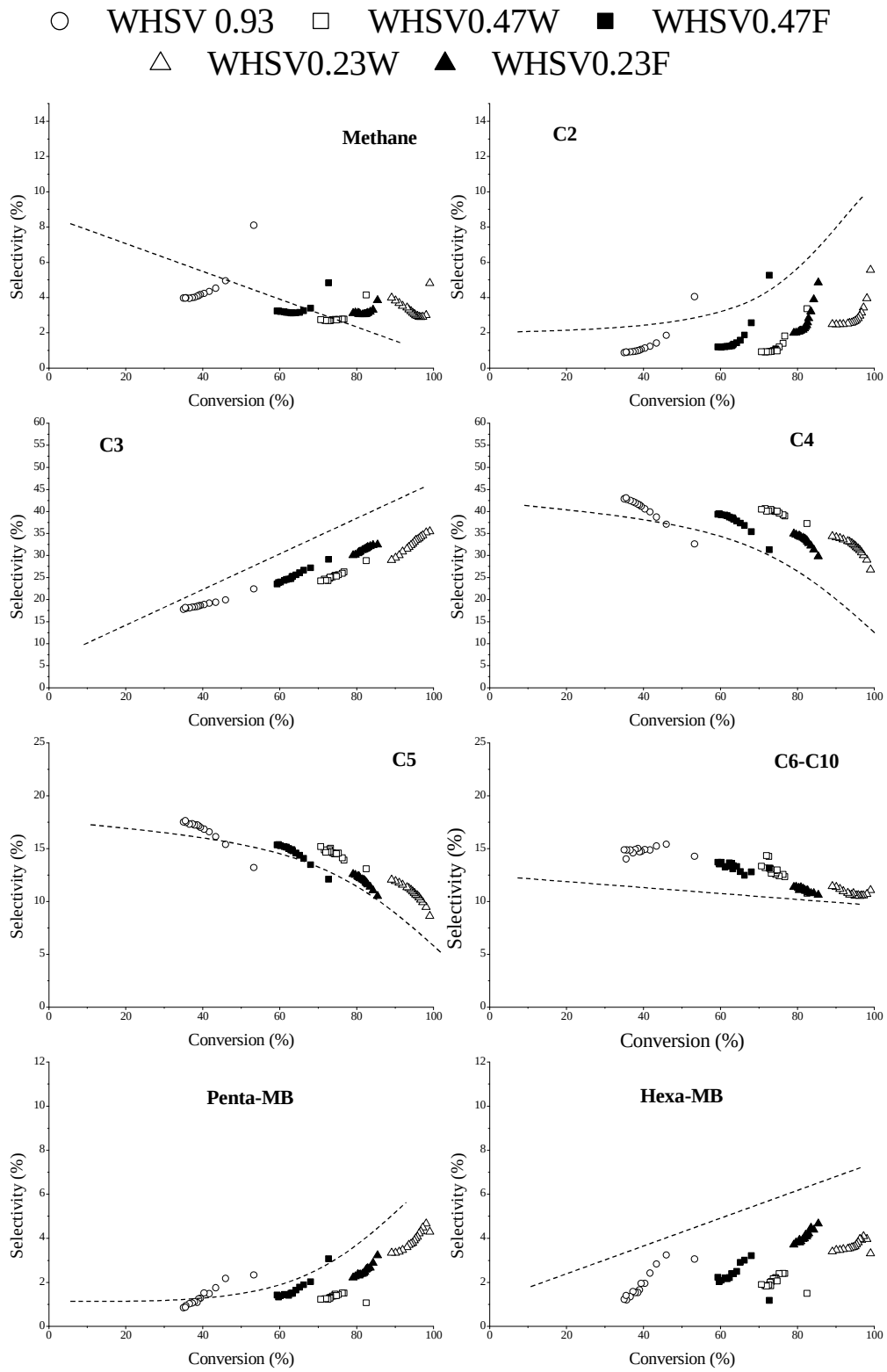

Fig. 15.13: Plots of the selectivity to each product fraction as a function of total methanol conversion. Marks W and F means that mass of catalyst or flow rate, respectively, has been changed to achieve the lower space velocity. The dashed line is included as a comparison to the approximate trend line found for all catalysts at 450 °C and WHSV 0.93 h^{-1}.

Figure 15.13 compares the selectivity towards different product fractions with the trends found earlier at 450 °C (chapter 15.2.1). The selectivity trends seem to mostly be the same when higher conversion is achieved through a decrease in WHSV as those observed when catalysts of different acid site densities or different degree of deactivation were compared. Many of the small differences observed can be ascribed to the difference in GC column. A look at figure 15.5 will reveal that the points of SC (the only sample in that figure measured with PLOT-Q) is placed on the same side of the trend line as the points in figure 15.13 for all fractions except C3. This means that although it is possible that more C4, C5 and C6-7 aliphatics is produced at lower space velocity at the cost of less C2 and C3, undue attention should not be paid from these deviations from the established trends. The aromatics of the C6-10 fraction and the selectivity to pentamethylbenzene correspond very well with that observed for SC at WHSV 0.93 h^{-1} at all degrees of deactivation, so the small deviations in the selectivity to hexamethylbenzene is attributed to the poor quantification of this compound in the GC with the PLOT-Q column.

A look at the distribution of C4 species versus total conversion also appears very similar to that observed for SC throughout its conversion range (recall figure 15.6). As expected from this, the C4 HTI, plotted in figure 15.14 is quite similar to that found for SC throughout the whole range the latter's whole range of deactivation. The main difference is that each experiment varies more than expected due to their short range of conversion levels. It is also observed that the HTI increases to an even higher level when conversion increases to more than what has been observed for SC.

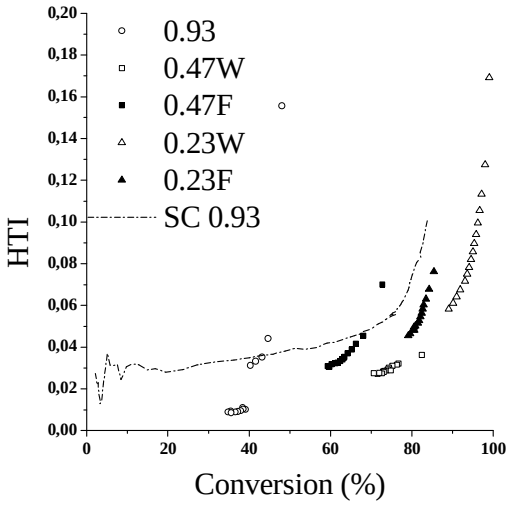

Fig. 15.14: C4 HTI as a function of conversion for P/L at different WHSV. W and F is for changed sample weight or flow rate, respectively. The dash-dotted line, representing the C4 HTI of SC at WHSV 0.93, is included for comparison.

While a lot of the observed trends may be the same whether a given conversion is reached by changing the space velocity, the sample or the degree of deactivation, the plots in this section also strongly imply that the time spent on stream is also of some importance. While it has been pointed out briefly before (especially for B/L and P/H), figure 15.13 shows quite clearly that change in C2 selectivity is greater than the trend line during the beginning of the experiments, while flattening out at longer time on stream. To a smaller degree, the opposite trend is also witnessed for the C4 fraction. The HTI also changes quite drastically for some of the samples during the first hours of testing, as witnessed by figure 15.14.

15.2.4 Selectivities at low conversion

In order to gain a possible insight into what products are closest to primary products, an attempt to extrapolate the observed trends down to zero conversion was made. A series of experiments were thus performed where the aim was achieving as low conversion as possible. This was accomplished by increasing the flow rate of methanol fed over catalyst sample SC at a temperature of 350°C. Table 15.2 displays the total percentage conversion of methanol and the selectivities observed at WHSV 0.93, 2.49 and 4.98 h^{-1} after 5 minutes on stream. For the two latter space velocities, conversion and selectivities were also checked after 2 and 10 minutes, but the results were hardly discernible from those found after 5 minutes.

Table 15.2: Conversion and selectivities of sample SC at WHSV 0.93, 2.49 and 4.98 h^{-1} (top to bottom). The C6 + fraction contains only aliphatics, while the aromatics previously considered part of the C6-10 fraction have now been placed in a separate fraction called lower aromatics.

Conversion (%)	C1	C2	C3	C4 =	C4 -	C5	C6 +	Lower Aromatics	Penta -MB	Hexa - MB
30,2	0,2	2,0	17,7	45,1	5,0	14,4	8,5	1,7	1,8	3,6
10,7	0,4	1,9	13,3	53,6	2,7	16,6	7,6	2,0	0,6	1,2
3,9	1,1	1,5	10,4	57,1	2,2	17,4	7,1	0,7	0,0	2,6

What is clearly evident from table 15.2 is that as the conversion is decreased, the ratio of C4 to C3 increases sharply. This is in line with the trends observed earlier both at 350 °C and 450 °C, but it should be noted that the selectivity to C3 decreases too little to assume an extrapolation to zero at lower conversion. It should also be added that at the lowest conversion, isobutene constitutes nearly 80 % of the C4 fraction. Further, it can be seen that

the C5 fraction increases when conversion is decreased, also in line with earlier observed trends at both temperatures. It should be noticed that the ratio of C4 to C5 remains more or less constant during the observed changes in conversion.

Apart from this a number of smaller trends are noticed, such as an increase in selectivity to C1 and a decreasing selectivity to C2 and all aromatics with decreasing conversion. These trends are all in line with previous observations. C4 HTI is also seen to decrease with decreasing conversion. The values for penta- and hexa- methylbenzene in table 15.2 are not necessarily trustworthy at the lowest conversions, but a clear decrease has occurred between 30 % and 10 % conversion. The observed decrease in both C6 + and lower aromatics as space velocity is increased goes counter to the trend line of C6-10 plotted in figure 15.5, but this trend was never very clear in any of the previous plots, and especially not at 350 °C.

15.2.5 Comparison of selectivities with other large pore zeotypes

When comparing the selectivity of the H-SAPO-5 studied here with other zeolitic materials, the most logical structures to look at are H-Beta and H-Mordenite, as they have similar pore dimensions to SAPO-5. However, as both structures are silicoaluminates, their acidic strength is expected to be higher than that of H-SAPO-5. When comparing H-SAPO-5 to aluminosilicates with similar structures, it is possible that selectivity differences are caused by the difference in acid strength. The structure of H-Beta (recall figure 3.1) consists of a three dimensional network of slightly elliptic large 12-ring channels (7.7 x 6.6 Å[8]) in addition to somewhat smaller 12-rings (5.6 x 5.6 Å[8]). Mordenite has somewhat smaller one dimensional 12-ring channels (7 x 6.5 Å[8]) with very narrow 8-rings connecting the 12-ring channels.

For both of these zeolites C3 and C4 compounds constitute large fractions of the methanol converted when acid site densities and conditions are comparable to the H-SAPO-5 samples tested in this work (see [165] for H-Mordenite selectivities and [142, 161, 165] for H-Beta). Both catalysts are also reported to produce relatively large amounts of C5 + and aromatics together with meagre yields of C1 and C2. A similar product distribution has also been reported by Salehirad and Anderson[166] for H-ZSM-12, which has even narrower 12-rings than mordenite. It has also been reported by Yuen[17] that H-SSZ-24 (AFI structure) has

virtually identical selectivities to H-SAPO-5, but unfortunately they have published few details.

Some of the trends in selectivity found here for H-SAPO-5 are also reported for these catalysts. For example, an increase in temperature leads to an increase in methane and a decrease in C4 HTI and aromatics over both H-Mordenite and H-Beta[142, 165]. However, of the three catalysts mentioned, only H-Beta displays a tendency to favour C4 over C3 when conversion is lowered similarly to the observations in this work for H-SAPO-5. Even in H-Beta, the trend is not as strongly evident, and more C3 relative to C4 is produced than in H-SAPO-5. While the catalysts mentioned here provide similar selectivities as H-SAPO-5, it should be mentioned that both H-Mordenite and H-Beta appears to possess higher capacities for methanol conversion before deactivation under most conditions reported.

A look through the literature and comparisons with the work performed here might give the impression that channel sizes is the only important factor in determining selectivities, while acid strength plays a less important role. However, closer comparisons of the results from this work with Bjørgens extensive studies of H-Beta[142] (The catalyst with the most similar structure to AFI that has been thoroughly studied) nevertheless reveals some interesting small differences. Some examples of comparisons made between dealuminated H-Beta of comparable acid site density and H-SAPO-5 at the same temperatures and degrees of conversion are plotted in figure 15.15. In addition to H-Beta's higher selectivity

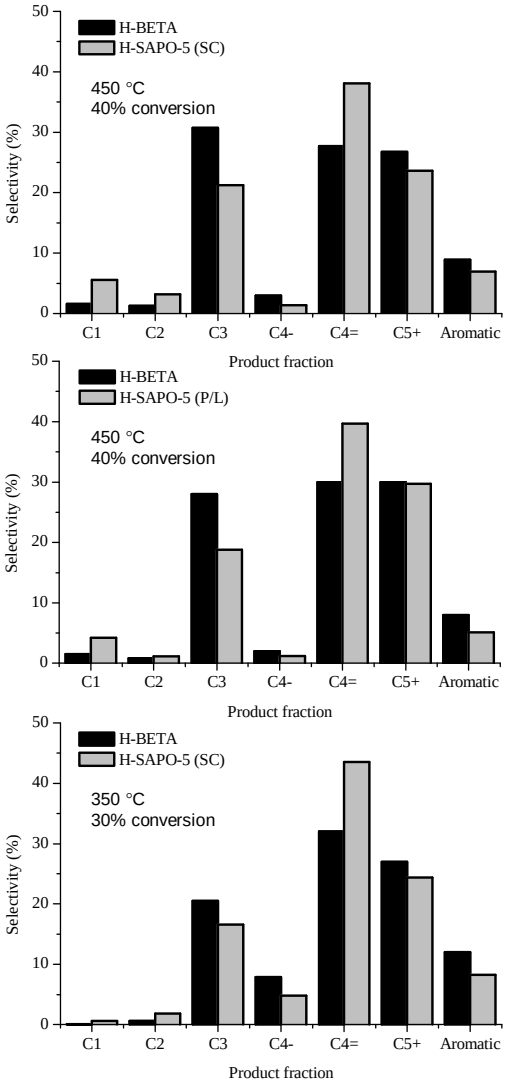

Fig. 15.15: Comparisons between H-Beta tested by Bjørgen[142] and H-SAPO-5 samples from this work. The comparisons are made at the same conversion and temperature, but at different space velocities and degrees of deactivation. The H-Beta plotted in the middle figure is more severely dealuminated than the others, and is compared to P/L instead of SC.

toward C3 and C5+ and lower selectivity toward C1, C2 and C4, it appears that H-Beta also produces more butane and aromatics (and thus has a higher HTI index). These differences are visible at most comparable conditions. The H-Beta tests used for comparisons in figure 15.15 are performed with catalysts of lower acid site density than the H-SAPO-5 samples and higher space velocity than used in this work. However, the selectivity to butane and aromatics are reported to increase both with decreasing space velocity and increasing acid site density[142], so larger differences are expected at more similar conditions.

While the increased selectivity to aromatics can be explained with reference to the larger space available in the channel intersections of H-Beta, it might also be explained by the difference in acid strength. A relation between the acid strength and the occurrence of hydride transfer reactions has been suggested by Yuen et al[17]. In addition, it has also been reported by Hazari et al[167] and Bercaw et al[168-170] that in a homogenous system of methanol conversion, the more strongly acidic InI_3 catalyses hydride transfer reactions more efficiently than ZnI_2. While this is an interesting hypothesis, the influence of the framework cannot be ruled out when comparing H-Beta to H-SAPO-5. A study of the selectivities of isostructural catalysts of differing acid strength such as H-SAPO-5 and H-SSZ-24 might provide valuable insights.

15.2.6 Summary of selectivities and hints to reaction mechanism

At the conditions employed, the major products of methanol conversion over H-SAPO-5 are C3-C5 alkenes. The remainder of the product spectrum comprises methane, ethane and alkenes larger than five carbon atoms in addition to aromatics and alkanes. Penta- and hexa-methylbenzenes are most prominent among the aromatics fraction. It is also evident that the C4 alkenes formed are not in equilibrium and, especially at low conversion, the dominant isomer is isobutene. Overall, the products from the MTH reaction over H-SAPO-5 are similar to those reported for other 12-ring zeolite catalysts, and especially to those of zeolite H-Beta. The main differences in selectivity from H-Beta are that H-SAPO-5 produces less aromatics and alkanes and that a higher amount of C4 hydrocarbons are produced relative to C3. Observed selectivities throughout this work appear very insensitive to acid site densities, space velocity or to the degree of deactivation of the catalyst, although they are seen to

change when the temperature is changed. Thus, apart from temperature, they appear to depend mainly on the percentage conversion of methanol at that given time.

A distinct tendency for the product selectivities to change during the first hour on stream was found in some of the tested catalyst samples. In particular the selectivity to C2, C4 and the HTI value was observed to undergo rapid changes in the beginning of an experiment. While there is no easy explanation for this phenomenon, it seems likely that a change in reaction mechanism takes place during this time. This effect seems especially pronounced in catalysts B/L and P/H, in which it can possibly also be linked to the change in percentage conversion observed during the same period. On the other hand, SC shows little or no indication of these initial changes. From this it would be natural to link the effects to the amounts of defects in the samples since FTIR reveals that while all other samples possess OH groups not related to Brønsted sites created by substitution of Si for P, SC has few or no such OH groups. B/L and P/H on the other hand, show higher amounts of P-OH, Si-OH and Al-OH groups than the others. The presence of acidic sites of either Lewis or Brønsted type possessing a greater acid strength than the bridging OH groups might explain the observed initial selectivity change as these may catalyse hydrogen transfers efficiently, but deactivate fast. However, from CO adsorption measurements, OH groups other than Si-OH-Al found appeared weak and would thus be assumed catalytically inactive. This decreases the likelihood of strong acid sites as the explanation, but it is also possible that they are present in amounts too small to observe from the relatively poor FTIR data obtained in this work.

The most prominent trends in selectivities of methanol conversion over H-SAPO-5 are those shown by the C3, C4 and C5 species. Increasing methanol conversion causes an increase in the selectivity towards C3 to increase and a decrease in the selectivity to the C4 fraction at all conditions studied. Relative amounts of C3 and C4 hydrocarbons produced at a given methanol conversion does not change significantly when conditions are changed. The C5 fraction also follows the same trend as the C4 fraction, and the ratio C4/C5 appears nearly independent of the degree of methanol conversion. Of all conditions studied so far only the temperature appears to affect this ratio, giving a higher relative selectivity to C4 at 350 °C than at 450 °C. In addition to this, the selectivity to aromatics (in particular penta- and hexa-methylbenzene) increases with higher conversion, matching an observed increase in alkane formation. Both the selectivity to aromatics and the HTI value is significantly higher at 350

°C than at 450 °C. Methane formation is significant at 450 °C, while at 350 °C it is much lower. At both temperatures, methane selectivity increases with decreasing conversion. The trends in selectivities toward the C2 and C6-10 fractions are not very clear, but a decrease in selectivity to C2 has been observed when decreasing conversion.

As for mechanistic insight, this is limited from only the data obtained so far. From the similarity in selectivity with H-Beta, it would be natural to assume that the mechanisms of olefin formation are similar as well. Previous mechanistic studies on H-Beta conclude that methylbenzenes are key intermediates in a hydrocarbon pool mechanism (see e.g. [56, 64, 76]). However, it is possible that the lower amount of methylbenzenes present in H-SAPO-5 will decrease their importance as intermediates. The lower selectivity to aromatics in H-SAPO-5 could be related to a decreased ability to perform intermolecular hydrogen transfers in the less acidic SAPO catalyst. One observation that is hard to reconcile with a methylbenzene-based hydrocarbon pool mechanism is the stability of the C5/C4 ratio during changes in methanol conversion. While methylation of butenes to yield pentenes has been reported as a plausible reaction over zeolites during methanol conversion by Svelle et al[72, 171], a sequence where isobutene is produced from methylbenzenes and subsequently methylated should lead to lower C5 selectivity at lower conversion since butene would then be closer to a primary product than pentene. A more fitting explanation for the stable ratio is that both isobutene and pentene is formed from a common precursor, which would mean that the ratio of the two species would depend only on their relative rates of formation from this precursor. Neither the paring reaction nor the exocyclic methylation (the two most common explanations for elimination of olefins from methylbenzenes[1]) accounts for production of pentenes. Thus, formation of both isobutene and pentenes directly from a common precursor would most likely proceed through cracking of a higher alkene.

15.3 Reactivity of aromatics retained in the catalyst

15.3.1 Flushing studies

Flushing experiments similar to those performed by Arstad and Kolboe[53] on SAPO-34 and Bleken et al[70] on both H-SAPO-34 and its zeolite analogue H-SSZ-13 was performed on samples P/L and SC. The aim of the experiments was to determine the relative reactivity of methylbenzenes in H-SAPO-5. This was done by comparing the composition of retained hydrocarbons in a sample exposed to methanol for 20 minutes to that of a sample left at reaction temperature in a stream of inert gas for 1 hour after 20 minutes of methanol exposure. Experiments were performed at 350 °C and WHSV 0.47 h^{-1} and the composition of the effluent was analysed, and confirmed equal, after 15 minutes to ensure reproducibility.

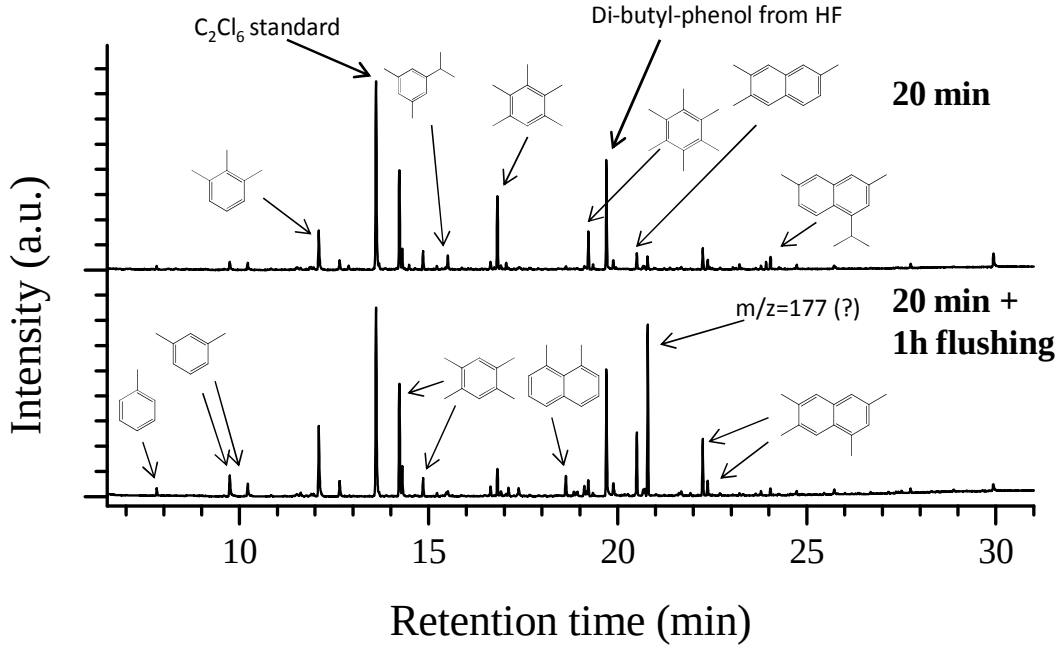

Fig. 15.16: Composition of the retained hydrocarbons in sample P/L after exposure to methanol for 20 minutes (top) and after flushing with He for 1 hour after methanol exposure (bottom). C_2Cl_6 is an internal standard while dibutyl phenol appears to be an impurity in the HF used. The peak eluted after 20.8 minutes (m/z = 177) is also assumed an impurity. Isomeric identities of the compounds are not known.

Results for sample P/L (figure 15.16) reveal that the major components of the retained hydrocarbons are methylbenzenes and methylnaphthalenes. Especially tetra-, penta-, hexa-, and tri- methylbenzenes are prominent in the chromatograms, but it is also worthy of note that a small fraction of propyl substituted compounds are present. When the catalyst was flushed

for 1 hour with helium it could be seen that the fraction of penta- and hexa- methylbenzene decreased together with the propyl substituted compounds. The toluene, xylene, trimethylbenzene and methylnaphthalene fractions, on the other hand, increased. Tetramethylbenzene fractions remain relatively unchanged, possibly increasing a little. A decrease in the intensity of the higher methylbenzenes during flushing was interpreted by Arstad and Kolboe as decomposition into light alkenes and lower methylbenzenes[53]. Thus, the instability of penta- and hexa- methylbenzenes in H-SAPO-5 during flushing indicates that they are active for olefin formation. While the propyl substituted compounds are also unstable, it is uncertain whether they are reaction intermediates or if they are formed from reactions between propene and aromatics.

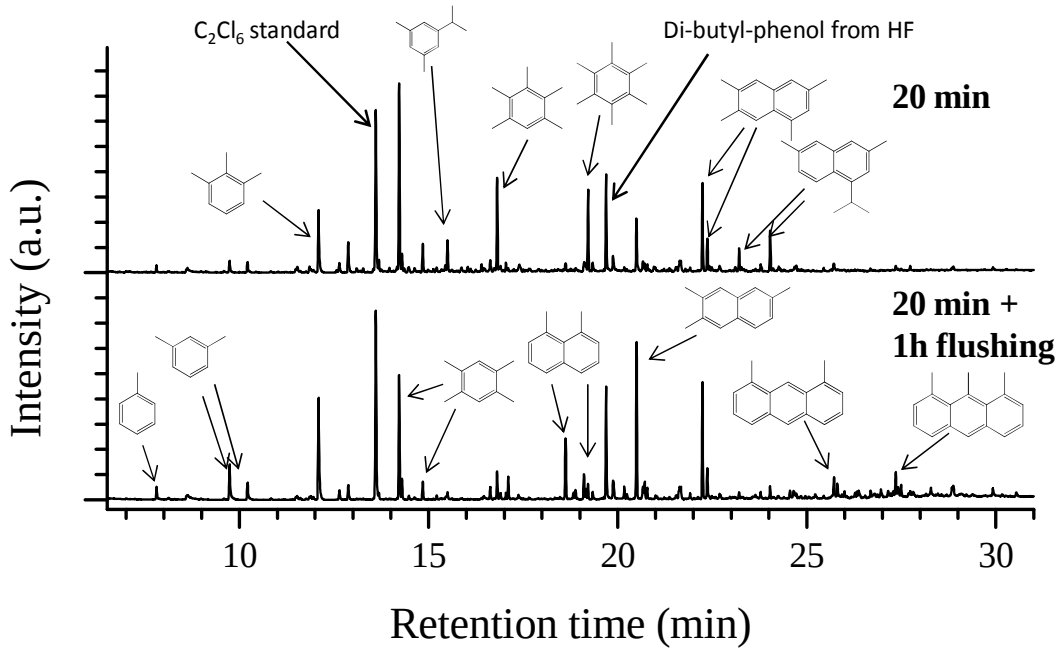

Fig. 15.17: Composition of the retained hydrocarbons in sample SC after exposure to methanol for 20 minutes (top) and after flushing with He for 1 hour after methanol exposure (bottom). C_2Cl_6 is an internal standard while dibutyl phenol appears to be an impurity in the HF used. The isomeric distributions of compounds are not known.

Figure 15.17 displays the chromatograms from identical experiments with sample SC, which is known to be more active for methanol conversion than P/L. This is also evident from the fact that the amount of retained hydrocarbons is higher in the former sample, easily observable both from the colour of the CH_2Cl_2 extract and the higher intensity of the hydrocarbon peaks by GC-MS. While the composition of its retained hydrocarbons after 20 minutes is similar to that of P/L, significantly greater amounts of methylnaphthalenes are

observed. As the catalyst is flushed with inert gas, the amount of propyl substituted compounds together with hexa- and penta- methylbenzene are seen to decrease. Just as observed for P/L, the decrease in these compounds is accompanied by an increase in lower methylbenzenes and methylnaphthalenes. However, methylphenanthrenes are also visible in the extracts from SC and, also unlike P/L, the tetramethylbenzene fraction has decreased after flushing.

Together, the results from the two samples strongly suggest that penta- and hexa-methylbenzenes are active for olefin formation. However, while the results from H-SAPO-34 of Bleken et al[70] indicated that tetramethylbenzenes are not active, such a conclusion is hard to draw for H-SAPO-5. Even though no decrease was observed after flushing for P/L, a clear decrease is observed in SC. It is possible that the lower methylbenzenes are flushed out of the catalyst channels when flushing, as their diffusivities would be greater than for the larger compounds. However, if this is the cause of the tetramethylbenzene decrease it should also be visible in P/L, as diffusivity for TPA in the latter sample is known to be higher than in SC (recall chapter 11.3). IR results of the two samples also indicate similar acid strength, so the ability to protonate should be the same in both samples, and thus a difference in reactive hydrocarbon pool compounds is not expected. Whatever the reason for the difference between the two samples, the fact remains that it cannot be concluded whether or not tetramethylbenzene is active for product formation in H-SAPO-5.

A few other interesting observations from the flushing experiments also include the fact that neither penta- nor hexa- methylbenzene disappears completely after flushing for one hour. This indicates a relatively low overall reactivity of the methylbenzenes in the catalysts compared to H-SAPO-34 results by Arstad and Kolboe[53], where hexamethylbenzene disappeared after only a few minutes. As the amount of methylnaphthalenes was seen to increase with flushing, it is also likely that a significant amount of the methylbenzenes form naphthalenes rather than eliminate olefins. The propyl-substituted aromatics are more unstable during flushing and are completely gone after 1 hour. As they appear in relatively large amounts, it would be of interest to find out whether they are reaction intermediates or simply products of back-reactions with propene.

15.3.2 Switching studies

By following the incorporation of ^{13}C atoms after a switch from ^{12}C to ^{13}C methanol, it is possible to assess the reactivity of the molecules confined in the catalyst. This type of experiments led to the discovery by Bjørgen et al[74, 75] that olefins are mostly generated by an alkene- based cycle during methanol conversion on H-ZSM-5. When applied to H-SAPO-5, sample SC was exposed to unlabelled methanol at 450 °C (WHSV was 0.47 h^{-1}) for 18 minutes before switching to a feed of ^{13}C labelled methanol. The incorporation of ^{13}C into the olefin products and the retained aromatics was then analysed after 0.5, 1 and 2 minutes after the switch.

Figure 15.18 shows the content of ^{13}C in the major light alkene products and the aromatics retained in the catalyst as a function of the time after switching to labelled feed. From this figure, it is evident that the incorporation of ^{13}C is faster in the effluent than in the retained methylbenzenes (and methylnaphthalenes). Although not shown, incorporation of ^{13}C into dimethyl ether was observed to occur slightly faster than for isobutene. If figure 15.18 is compared to the results of similar experiments for H-Beta[61, 76], differences are clearly observable. While the rate of ^{13}C incorporation in H-Beta is similar in the olefin products and retained aromatics, figure 15.18 reveals that the incorporation into aromatics is significantly slower than that of the olefin products in H-SAPO-5. The observed incorporation of ^{13}C and high degree of scrambling in the aromatics indicate that they are active for olefin formation and not simply spectator species. However, the slower incorporation into the aromatics compared to the olefinic products provides a strong indication that a reaction path to olefins not involving methylbenzenes as intermediates also exists. In analogy with the conclusions of Bjørgen et al[74] for H-ZSM-5, it appears likely that the dual cycle concept applies to H-SAPO-5 as well, which would mean that olefins can be formed either via an alkene cycle based on methylation and cracking reactions or from methylbenzene intermediates.

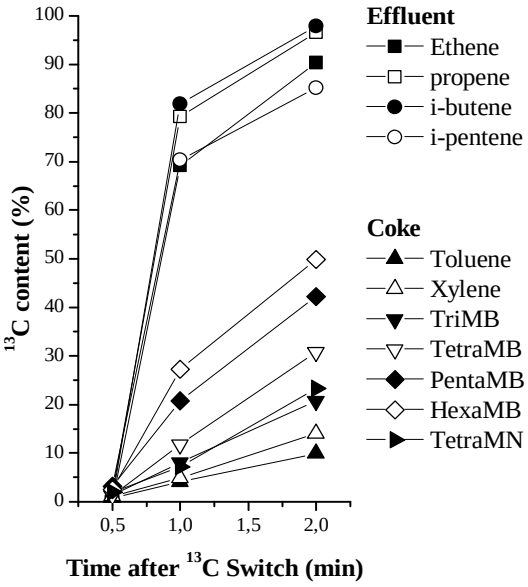

Fig. 15.18: The evolution of ^{13}C content in both the effluent and retained aromatics with time after switch to labelled feed.

Incorporation rates of labelled carbons can also be seen from figure 15.18 to be faster for the highly methylated benzenes than for the less substituted. This suggests that the higher methylbenzenes such as penta- and hexa- methylbenzene are the most reactive of the retained aromatics. Such an order of reactivities correspond well with the results from flushing studies (chapter 15.3.1) and also with previous results from H-SAPO-34 by Arstad and Kolboe[52]. Tetramethylnaphtalene also shows some incorporation of ^{13}C with time, but whether this is due to it being reactive in itself or if it is simply formed from higher methylbenzenes with labelled carbons is not known.

The difference in incorporation rate between alkenes in the effluent is difficult to explain. It is possible that aromatic intermediates are responsible for a larger fraction of the ethene formed than for propenes and butenes, giving a slower incorporation of ^{13}C in the former. Pentene formation from methylbenzene intermediates, on the other hand, appears unlikely as neither of the proposed mechanisms for elimination of alkenes from methylbenzenes leads to a C5 alkene. A satisfactory explanation for the slower incorporation of ^{13}C into isopentene has not been found, but it is possible that the rate of diffusion comes into play. As the catalyst crystals used are relatively large, the lower diffusivity of pentene compared to butene may cause a delay in its elution from the zeolitic channels.

15.4 Co-feeding of benzene and methanol

15.4.1 Hydrocarbons retained in the catalyst

A series of experiments were performed in which methanol and benzene were co-fed over catalyst sample P/L at temperatures between 230 and 350 °C. WHSV of benzene and methanol were 1.6 h^{-1} and 4 h^{-1} respectively, giving a molar ratio of methanol to benzene feed of 6.2. These space velocities were chosen in an attempt to form predominately hexamethylbenzene inside the catalyst. Olefins were produced at all temperatures under these conditions, and the composition of the effluent is discussed in the next section.

Figure 15.19 shows the chromatograms of the CH_2Cl_2 extracts from dissolved catalyst samples after 90 minutes of co-reaction. The low amount of coke present in the samples and the fact that quartz dilution was used during the reaction made quantification difficult and the chromatograms are of somewhat poor quality, but the trends as the temperature is increased are still clear, however. At low temperatures the dominating species are diphenylmethanes, while a transition towards higher methylbenzenes and naphthalenes occurs at higher temperatures. Diphenylmethanes have been reported by Svelle et al[172] as possible intermediates in transmethylation reactions between methylbenzenes.

In general, the chromatograms from co-feeding at temperatures above 250 °C look similar to those of the catalysts reacted with methanol at 450 °C (see chapter 15.3.1). Tetramethylbenzenes constitutes the largest fractions, while penta- and hexa- methylbenzenes together with tri- and tetra- methylnaphthalenes follow as other major components. The same propyl substituted methyl -benzenes and -naphthalenes as observed before are also present in these experiments. However, differences include the presence of diphenylmethane at all temperatures, together with a higher proportion of methylnaphthalenes to methylbenzenes. The latter may be caused simply by the longer time on stream before analysis in these experiments. There also appears to be smaller ethyl substituted compounds present and in particular the peak at ~ 12 minutes does not consist of exclusively trimethylbenzenes in these experiments, but is the

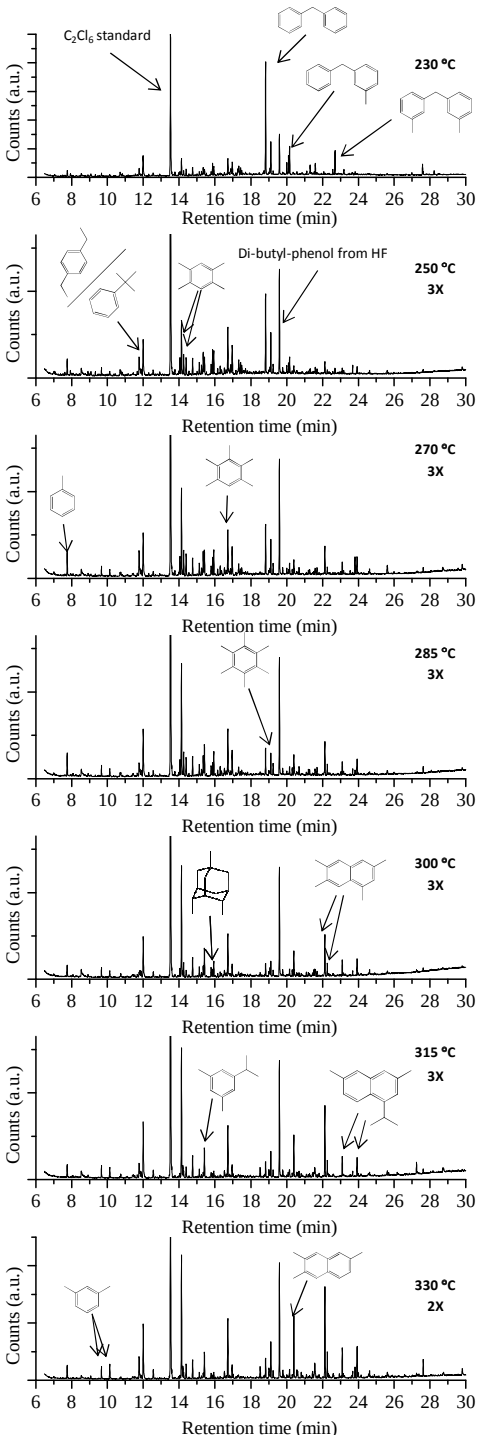

Fig. 15.19: Hydrocarbon extracts from samples exposed to a mixture of benzene and methanol for 90 minutes at different temperatures. Isomers of methylbenzenes and methylnaphthalenes have not been distuinguished. The chromatograms are shown at different magnifications.

result of an overlap between several species. The NIST database suggests both diethyl- and isobutyl- benzene, but neither the exact nature nor the relative amounts of compounds in this elution peak were determined. Adamantanes, in particular trimethyladamantanes, were also present in the extracts during co-feeding. Adamantane species have also been reported during methanol conversion over H-SAPO-34 by Bleken[151] at low temperatures, but their role in the reaction was not elucidated.

When comparing the retained hydrocarbons found here to a similar series of co-feeding experiments over H-Beta performed by Bjørgen et al[64], a number of differences are immediately evident. Where Bjørgen et al found a transition from almost exclusively hexamethylbenzene and 1,2,3,3,4,5-hexamethyl-6-methylene-1,4-cyclohexadiene (HMMC) at low temperatures to a mixture of higher methylbenzenes and methylnaphthalenes at higher temperatures, these results from H-SAPO-5 show a much broader spectrum of compounds. Especially the fact that HMMC is not observed at all in H-SAPO-5 is interesting and may mean that the heptamethylbenzenium cation is not as important in this catalyst as in H-Beta (HMMC being the conjugate base of the heptamethylbenzenium cation). It is possible that this is a space issue, as the lack of channel intersections in the AFI structure means there is less available space than in H-Beta. In addition, the lower acid strength of H-SAPO-5 may lead to slower methylation reactions than in H-Beta. Methylnaphthalenes are formed at very low temperatures in H-SAPO-5 compared to H-Beta, possibly indicating that they are more important as reaction intermediates in H-SAPO-5. Even if this is not the case, their formation must be much more favoured in the latter catalyst. These relatively large differences in the retained material imply that reaction mechanisms in H-SAPO-5 may be different from that of H-Beta. When considering the differences in this work compared to that of Bjørgen for H-Beta, it should be noted that the total conversion in Bjørgen's[64] experiments was much higher, especially at the higher temperatures.

15.4.2 Effluent analysis

In conjunction with studies of the retained material after co-feeding of methanol and benzene (at WHSV 4 h^{-1} and 1.6 h^{-1} respectively), the effluent composition was also analysed. Gas sampling and analysis by GC was performed after 5, 45 and 85 minutes on stream at all temperatures investigated. For the effluent, these temperatures were: 230, 250, 270, 285, 300,

315, 330 and 350 °C. Selectivities from all experiments are included in appendix J, while only the differences from what has been previously observed with only methanol feed are discussed here.

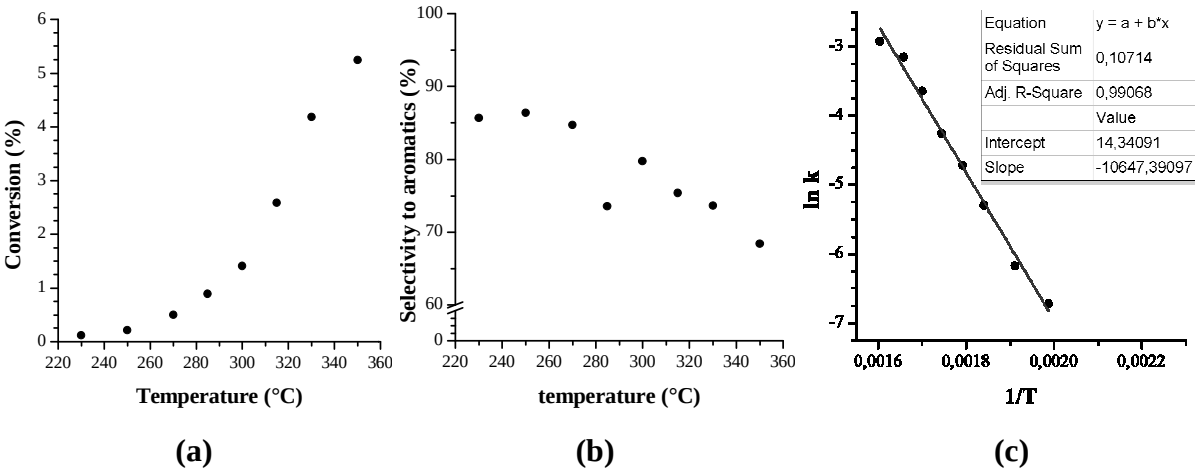

Fig. 15.20: Plots of total conversion (a) and selectivity to aromatics (b) after 5 minutes on stream, as a function of reaction temperature. An Arrhenius plot based on the assumption that the only reaction taking place is methylation of benzene is shown in (c).

As is shown in figure 15.20a, the conversion after five minutes (calculated by treating methanol, dimethyl ether and benzene as reactants) is low under the conditions employed here. It can also be observed to increase with temperature. Products consist mostly of aromatic species, as shown by the plot of selectivity to aromatics after 5 minutes on stream in figure 15.20b. The internal distribution varies somewhat with time on stream and temperature, but toluene is the dominant aromatic species at nearly all conditions. Although quantitative analysis of the distribution of other aromatics is difficult at low conversion, the selectivities to penta - and hexa- methylbenzenes are generally higher than other methylbenzenes (except toluene). This is likely due to the fact that methylation becomes progressively easier as the number of methyl groups on the benzene ring increases[173]. Diphenylmethane (not seen during conversion of methanol alone) is also eluted at the lower temperatures.

If it is assumed that the only reaction taking place during the co-feeding experiments is methylation of benzene, it is possible to calculate the apparent activation energy for the reaction. Even though this assumption is not correct, the value obtained can still provide an approximate value for the reaction. Figure 15.20c shows an Arrhenius plot where the reaction is treated as first order. From this, the apparent activation energy is found to be ~88 kJ /mol. It

is of interest to see that this is close to 30 kJ /mol higher than the value found for the same reaction in H-Beta[174]. The higher activation energy is likely due to the lower acid strength of H-SAPO-5, and this might in turn lead to other mechanistic differences in hydrocarbon formation over the two catalysts.

When co-feeding methanol and benzene, production of aliphatics occurs even at 230 °C, which is noteworthy as no products were observed when methanol alone was fed over SC at 300 °C. While feed rates were different for the two experiments, this still indicates that the presence of aromatics has an initiating function on the formation of hydrocarbons. The distribution of aliphatics in the products is fairly similar to what has been observed during reactions of methanol only, with isobutene as the most abundant species. However, as shown in figure 15.21, the addition of benzene to the feed has shifted the distribution somewhat towards lighter species. The comparison in the figure is made at similar conversion levels and the same temperature, but the space velocities were different. The larger amount of aromatics present in the catalyst when co-feeding benzene would be expected to increase the importance of the methylbenzene cycle relative to the alkene cycle in a dual cycle mechanism. Thus, the increased selectivity to C2 and C3 relative to C4 during co-reaction with benzene may indicate that formation of the former two proceeds mainly via methylbenzene intermediates, while formation of C4 does not. As Svelle et al[61] has found that lower methylbenzenes produce lighter olefins than higher methylbenzenes, there is also the possibility that the higher amount of toluene and xylenes present during co-reaction experiments causes the observed shift in selectivities. However, the fact that penta- and hexa- methylbenzene was present even at the lowest temperatures, and has been shown to be much more reactive than the lower methylbenzenes, decreases the likelihood of this.

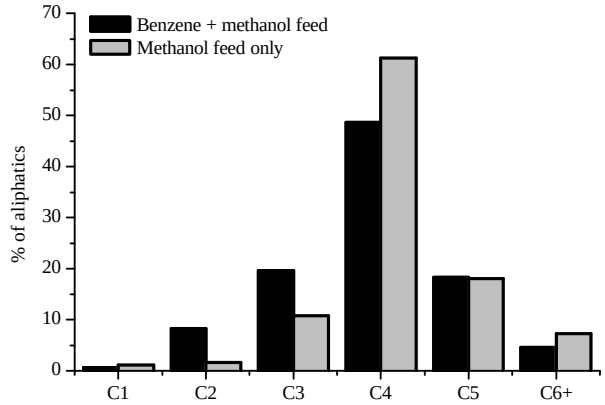

Fig. 15.21: Comparison of the relative selectivity of differently sized aliphatics when methanol is fed alone (grey) and when methanol and benzene is co- reacted (black) at 350 °C.

Even if the selectivities were not identical during benzene and methanol co- reaction to what was observed when methanol is reacted alone, the same trends were observed when selectivity is plotted as a function of conversion. This means that, similarly to what was found in chapter 15.2, the selectivity to C2 increased slightly with higher conversion, while the selectivity to methane was highest at lower conversion. The ratio between C4 and C5 was hardly affected by changes in conditions during co-feeding experiments, just as was found during methanol conversion. Curiously, the ratio was lower in co-feeding experiments than when only methanol is fed, meaning that more C5 was produced when benzene is present in the feed. The C5 species produced were still predominantly isopentenes.

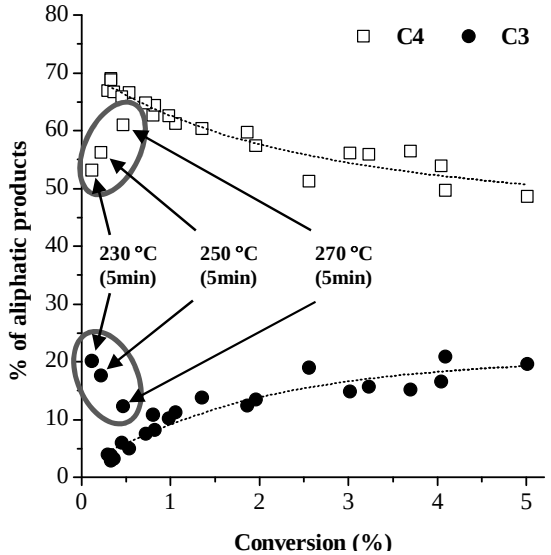

Fig. 15.22: Amount of C3 and C4 species formed during co-feeding of methanol and benzene, plotted as a function of the total conversion of both reactants.

Figure 15.22 reveals that the C3 and C4 formation also follows the same trends as observed during methanol conversion, namely that the former increased while the latter decreased with rising conversion. The shapes of the curves mirror each other closely, which may indicate a mechanistic link between the formations of these species. While the shape of the curves would lead to the assumption that C4 is formed before C3 (as the selectivity to C4 increases when conversion decreases), the evolution of selectivities at the lowest temperatures indicates the opposite. The deviating points that are highlighted in figure 15.22 correspond to the C3 and C4 selectivities after 5 minutes at the three lowest temperatures. Here, the ratio between C4 and C3 is much lower than expected, but increases both with increasing temperature and time on stream (both parameters also leading to higher conversion). This might mean either

that another mechanism operates early in the reaction at low temperatures, or it may indicate that the reaction has been slowed sufficiently to hinder formation of C4 from C3. If the latter is the case, reaction from C3 to C4 would then be assumed to proceed very fast during other conditions studied.

The simplest reaction from propene to a C4 species would be through a methylation reaction, where addition of a CH_3^+ group to the propene double bond would lead to a C4 alkene via a carbocation by either of the paths shown in figure 15.23.

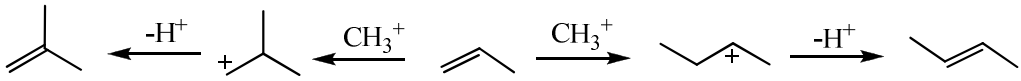

Fig. 15.23: simplified scheme for the addition of CH_3^+ to either side of a propene double bond

As shown in the figure, the path to isobutene leads through an unstable primary carbocation, while the methylation to a linear butene proceeds through a more stable secondary carbocation. Thus, it would be expected that methylation of propene would predominantly yield linear butenes, which is also what has been found experimentally by Svelle et al[72]. As the dominant C4 species formed in H-SAPO-5 is isobutene it is likely that, if this is indeed formed from propene, an indirect mechanism is responsible. Such a mechanism may for instance be based on successive methylations of propene to larger olefins, which then undergo cracking to produce isobutene and other alkenes. Cracking reactions in zeolites are likely to yield branched alkenes[32].

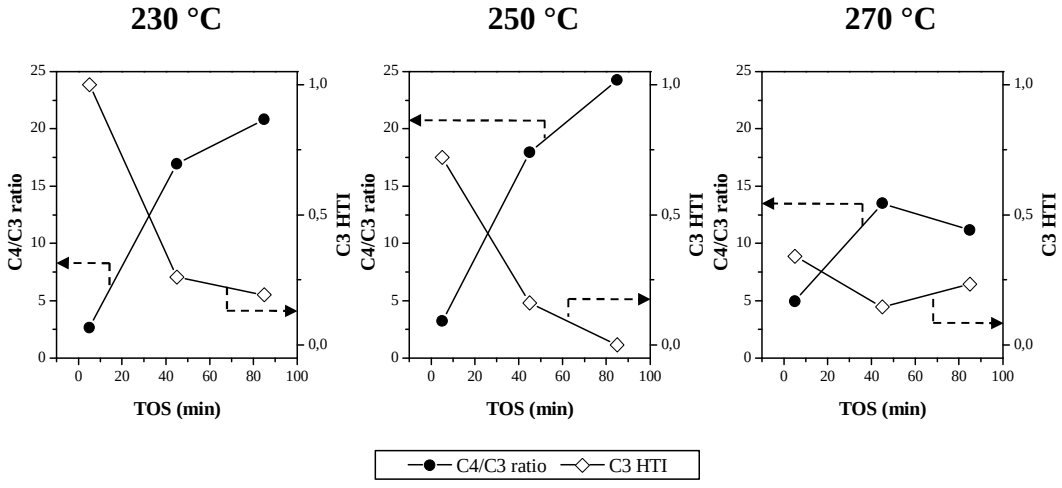

Fig. 15.24: Plots of the ratio of C4 to C3 aliphatics formed (left axes, filled circles) and the C3 HTI (right axes, open diamonds) as a function of the time on stream at different temperatures. For more details on conversion and selectivities, see appendix J.

Another observation in favour of propene being a precursor to C4 is shown in figure 15.24. These plots show that the ratio between C4 and C3 formed shows an inverse correlation with the C3 HTI ratio. This may be taken as an indication that formation of propane inhibits or competes with the formation of C4 species. If propene is assumed to be a precursor for both C4 and propane, this may lead to results similar to those found here. It should be noted that at higher temperatures the C3 HTI is near zero at all times on stream, and that C4 formation was dominant at low conversion in those experiments (as shown in figure 15.22). Figure 15.25 displays a simplified reaction scheme of the two possibly competing reactions of propene. These are the reaction to propane, via protonation and hydride transfer from another hydrocarbon, or to isobutene via successive methylation and cracking.

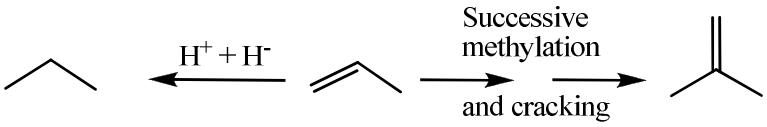

Fig. 15.25: Possible reactions of propene over H-SAPO-5

15.4.3 Use of isotopically labelled methanol

To further elucidate the mechanism of olefin formation from hydrocarbon pool compounds, the co-feeding of methanol and benzene was also performed with ^{13}C labelled methanol. If the olefin elimination from methylbenzenes proceeds via a ring contraction (paring type) mechanism, it is expected that one carbon atom from the aromatic ring is incorporated in every olefin produced. If the elimination proceeds by an exocyclic methylation route, this would not be the case. By synthesising the active methylbenzenes from ^{12}C benzene and ^{13}C methanol, it should be possible to determine what mechanism dominates. Figure 15.26 provides a simplified account of the expected difference in isotopic distribution for the paring and exocyclic methylation mechanisms. In the figure, the stars represent labelled carbons. Even though figure 15.26 uses the heptamethylbenzenium cation as starting point and splits off propene, the isotope patterns are expected to be the same for other methylbenzenes and/or if ethene or isobutene is eliminated.

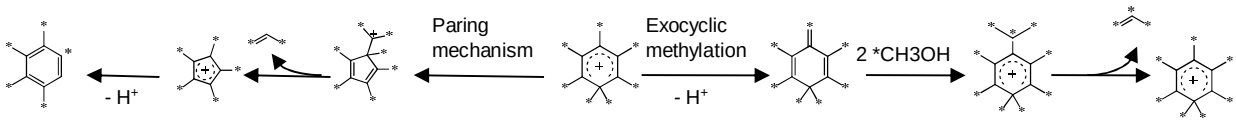

Fig. 15.26: Simplified reaction scheme of paring and exocyclic methylation pathways to splitting off propene from a heptaMB$^+$ cation with ^{13}C labelled methyl groups.

The experiment was based on work by Bjørgen et al[64] on H-Beta, where strong indications of the paring mechanism dominating were obtained. Even though the retained hydrocarbons in H-SAPO-5 are different, the experiment was expected to be able to discriminate between the two mechanisms here also. Even though the product distribution of methanol conversion over H-SAPO-5 is similar to that observed over H-Beta, indications of different reaction mechanisms have been observed. For instance, reactions involving methylbenzenes appear from isotopic switching experiments (chapter 15.3.2) to be less important in H-SAPO-5 than in H-Beta. Hints to indirect formation of isobutene from propene have also been observed and discussed earlier.

In these experiments similar conditions were utilised as those from unlabelled co-feeding experiments, but sample SC was used instead of P/L. In order to improve the quality of data for the retained compounds, no quartz dilution was used and the mass of catalyst was doubled. As more catalyst was dissolved, the methylbenzene peaks became more intense and isotopic analysis became more reliable. One problem with these experiments was that formation of pure ^{13}C methylbenzenes (or with one or two ^{12}C atoms) became very prominent when the conversion of reactants was higher than a few percent. This led to difficulties in interpreting the isotopic distribution data and made it necessary to work at very low conversion. The apparent preference for forming methylbenzenes high in ^{13}C rather than successively methylating benzene may be caused by a path where higher methylbenzenes are formed directly from ^{13}C- rich light alkenes. As higher methylbenzenes are more easily methylated than lower methylbenzenes[173], such species would preferably be methylated instead of the ^{12}C benzene. Figure 15.27 shows an example of a mechanism to form trimethylbenzene from propene that has been proposed by Sassi et al[56] during methanol conversion over H-Beta, which may also operate in H-SAPO-5.

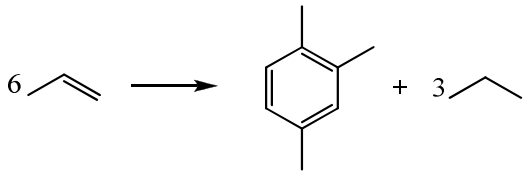

Fig. 15.27: Reaction of propene to trimethylbenzene and propane, from [56].

In order to suppress formation of more aromatics during the co-reaction of ^{13}C methanol and ^{12}C benzene, the conversion was kept low and the molar ratio of benzene to methanol in the feed was increased to 1:3. Optimal conditions were found to be a reaction temperature of 250 °C, and WHSV 0.8 h^{-1} and 1 h^{-1} for benzene and methanol respectively, in addition to a 10ml/min flow of pure helium. This led to a conversion of 1.13 % and 90% selectivity to methylbenzenes (predominantly toluene). The distribution of aliphatics was similar to that observed in earlier co-feeding experiments. Figure 15.28 shows the isotopic distribution in penta- and hexa- methylbenzene retained in the catalyst after 2.5 minutes of co-reaction.

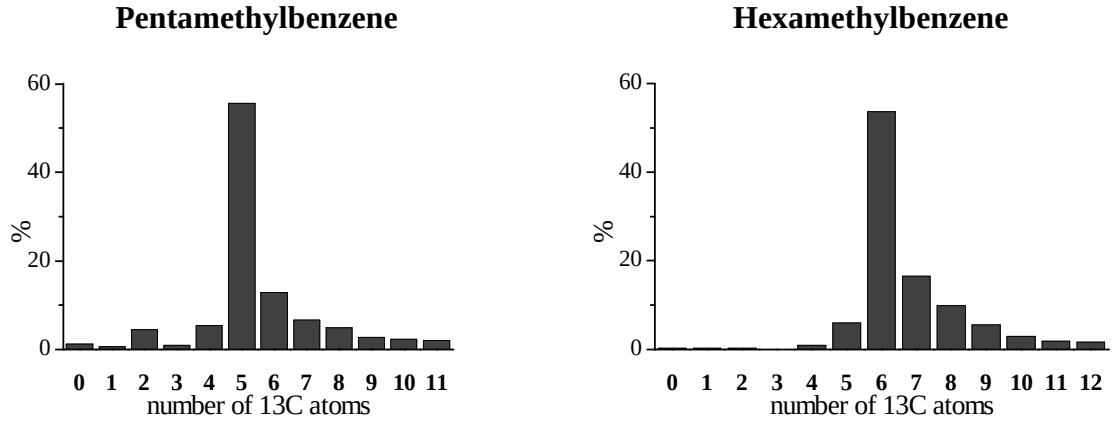

Fig. 15.28: Distribution of ^{13}C atoms in penta- (left) and hexa- methylbenzene (right) during co-reaction of ^{12}C benzene and ^{13}C methanol over sample SC.

The above figure reveals that under these conditions most of the penta- and hexa-methylbenzene is formed from methylation of ^{12}C benzene. What is also visible is that some degree of scrambling of labelled carbon into the benzene ring takes place. The scrambling patterns are not very different from those observed by Bjørgen et al[64] and may thus indicate that a paring type mechanism is taking place. However, scrambling of the methylbenzenes may also occur in processes not related to alkene eliminations as suggested by e.g. Sassi et al[56].

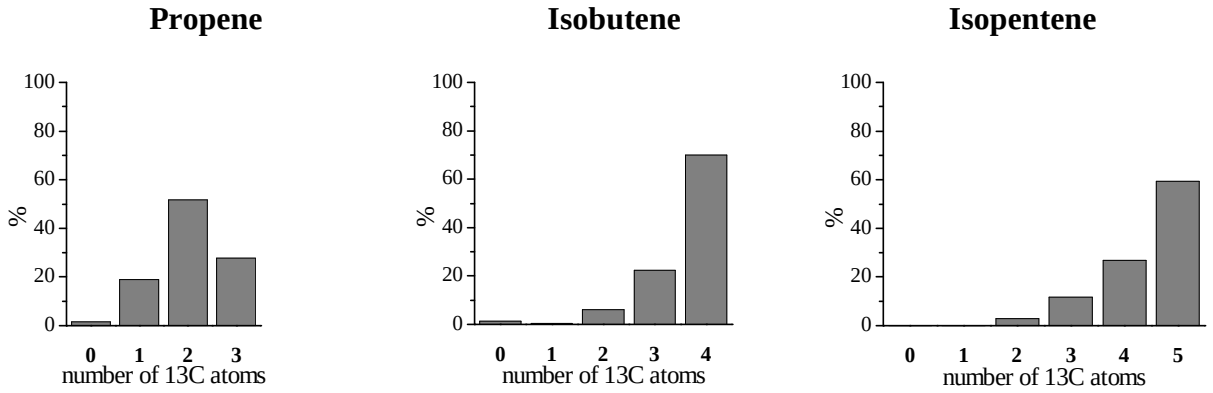

Fig. 15.29: Distribution of ^{13}C atoms in the major olefin products during co-reaction of ^{12}C benzene and ^{13}C methanol over sample SC.

Figure 15.29 shows the distribution of ^{13}C atoms in the three major olefin products: propene, isobutene and isopentene. Of these, propene has a significantly lower content of ^{13}C than the other two (68% in propene, ~90% in i-butene and i-pentene) and molecules with one ^{12}C are overrepresented compared to a random distribution. This fits well with a mechanism where the olefin is eliminated from methylbenzenes by a mechanism involving ring contraction, such as a paring type mechanism. While this is true for the propene effluent, most isobutene molecules appear to consist of only ^{13}C atoms, which is not consistent with a paring mechanism.

Propene and isobutene thus appear to be formed by two different mechanisms. While it is possible that isobutene is also formed from methylbenzenes, but by a mechanism not involving scrambling, certain factors makes this appear unlikely. First, the exocyclic methylation mechanism is not usually associated with isobutene formation. Secondly, indications of the importance of alkene-based mechanisms and the close link between propene and isobutene formation makes an indirect reaction from propene to isobutene more likely. Thirdly, the ^{13}C content in isopentene is suspiciously similar to that of isobutene, increasing the likelihood of a common reaction mechanism for the two. Such a common mechanism of formation fits poorly with an aromatics-based cycle.

Isotopic distributions of other compounds were difficult to achieve in this experiment due to the low concentrations in the reactor effluent and inside the catalyst. In the case of ethene, however, other experiments do indicate that the ^{13}C content in ethene is always lower than in propene (which again is always lower than in isobutene). This, together with the increased

ethene formation observed when co-feeding benzene, points to a methylbenzene-based mechanism similar to how propene is formed being responsible for ethene formation.

The paring mechanism, which eliminates olefins through a ring contraction, is assumed here to be responsible for propene formation. In spite of this, it should be noted that other reaction mechanisms can also account for the observed scrambling. For instance, Arstad et al[175] has investigated mechanisms proceeding through ring expansions which could also account for the observed scrambling. Even if olefin elimination occurs via ring expansion rather than contraction, these are both carbocation-based mechanisms. Thus, the results of this work indicate that even if the acid strength of H-SAPO-5 is lower than that of high-silica zeolites, a carbocation-based mechanism is preferred for elimination of olefins from methylbenzenes rather than a mechanism based on methylation of a double bond such as the exocyclic methylation reaction.

15.5 Summary and proposal of a reaction mechanism

The work performed here on H-SAPO-5 reveals that the various catalyst samples tested differ significantly in activity and lifetime. Indications of mechanistic differences early in the methanol conversion reaction in the more defective samples have also been found. Nevertheless, all samples share the same general trends in their product selectivities. These trends and the product distributions in H-SAPO-5 are very similar to that of the large-pore zeolite H-Beta. Dissimilarities include a higher ratio of C4/C3 hydrocarbons in H-SAPO-5 in addition to a lower amount of alkanes and aromatics produced. At conditions similar to those employed in this work, hydrocarbon formation from methanol over H-Beta has been determined to proceed mainly through methylbenzene intermediates. These are successively methylated and eliminate propene and isobutene via a paring-type (ring contraction) mechanism[61, 64]. Because of the similarities in product selectivity, it would appear likely that the same mechanisms operate over H-SAPO-5. In spite of this, isotopic switching experiments show that methylbenzene intermediates are of less importance in H-SAPO-5 than beta, and co-feeding of benzene and methanol indicates that isobutene is not formed in a paring mechanism from methylbenzenes. Fundamental mechanistic differences must therefore exist in the generation of hydrocarbons over the two catalysts. From indications that the presence of aromatics boosts methanol conversion and that olefins are formed from

methylbenzenes in H-SAPO-5, aromatics-based mechanisms are unlikely to be insignificant. However, another mechanism must operate in conjunction with this to explain the slower incorporation of fresh methanol into the aromatics than into the light alkene products. As mechanisms based on successive alkene methylation and cracking have been invoked previously for other catalytic systems, it appears likely that such mechanisms operate in H-SAPO-5 as well. Alkene based mechanisms are reported as the most likely paths to light hydrocarbons in catalysts where steric constraints limits the formation of higher methylbenzenes[61, 73-77, 79]. It is also the preferred explanation in low temperature generation of branched aliphatics both in zeolites[176] and over InI_3 and ZnI_2 catalysts[167-170].

Any mechanistic explanation for methanol conversion over H-SAPO-5 must account for the trends in the three major product fractions: propene, butenes and pentenes. The selectivity towards the first of these always increases with increasing conversion of methanol, while the latter two show the opposite trend. Co-feeding of benzene and methanol at low temperatures also hints to a link between propene and isobutene, possibly that formation of the latter proceeds from the former. The ratio between C4 and C5 species has been observed to remain constant with changing methanol conversion under similar conditions, but to depend on the reaction temperature, which may be indicative of formation from a common precursor. Formation of propene has been found to occur by the paring reaction from higher methylbenzenes, but as fresh methanol is incorporated faster into propene than aromatics, this cannot be the only pathway to propene formation.

In light of this it is proposed that a methylbenzene-based hydrocarbon pool produces propene, and that this propene reacts further to form other products. As direct methylation to form isobutene has been established as unlikely, this is assumed to occur by an indirect mechanism. If the further reactions of propene are based on methylation, it would be readily methylated as long as methanol or dimethyl ether is present and this would account for the observed increase in selectivity to propene with increasing conversion, since less of these methylating agents would be present at higher conversion. Further assuming that hexamethylbenzene is the predominant intermediate for propene formation through a paring reaction, a simplified reaction scheme would look like figure 15.30.

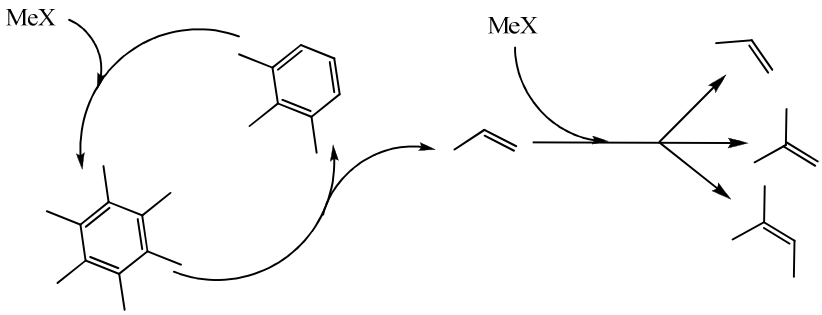

Fig. 15.30: Simplified scheme of a reaction mechanism where propene is formed from a paring reaction and further reacts to C3-C5 alkenes. MeX denotes a methylating agent.

MeX in figure 15.29 signifies any methylating agent, most likely methanol, dimethyl ether or a methoxy group inside the zeolite. The indirect reaction from propene and back to propene is included to account for the rapid incorporation of labelled carbons into propene after isotopic switching. While the methylbenzene cycle indicated in figure 15.30 proceeds from hexamethylbenzene to trimethylbenzene, this may in principle be a transition from any methylbenzene to one that is less substituted by three methyl groups. However, flushing and switching experiments indicate that hexamethylbenzene is the most reactive. Even though the heptamethylbenzenium cation has not been observed in H-SAPO-5, this is not proof that it does not exist. It cannot therefore be ruled out that the path to propene formation goes through this species in the same manner as reported previously for H-Beta[64].

When considering how propene can react to form higher alkenes, it is instructive to look at a sequence of methylation products. The reactions are assumed to proceed through carbocations that can be deprotonated to form alkenes. If the most highly substituted carbocations and alkenes are favoured at each step, such a sequence up to a C8 alkene would look like that shown in figure 15.31. When considering the final cation in that figure it is noteworthy that, unlike its predecessors, it is able to isomerise and crack via β-scission in several ways without the formation of an (unstable) primary carbocation. Indeed, methylation sequences similar to this has been invoked both by Ahn et al[176] and by Hazari and Bercaw et al[167-170] to explain product distributions in zeolites at low temperature and by ZnI_2 or InI_3, respectively. Ahn et al[176] also explains formation of isobutene by assuming β-scission of C8+ carbocations.

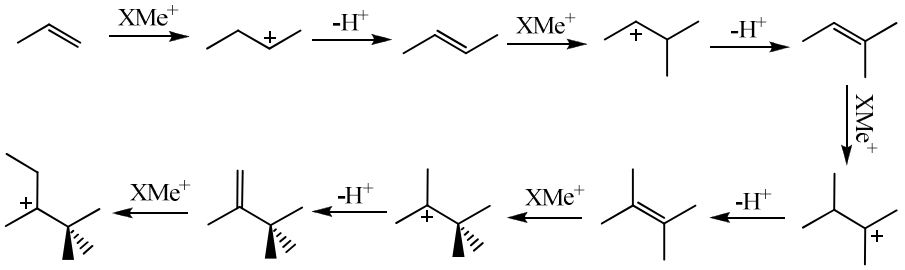

Fig. 15.31: Successive methylation sequence from propene to a 2,2,3-trimethylpentyl cation.

While it is possible to continue the sequence to larger species, alkenes containing more than eight carbons have not been observed in H-SAPO-5 during this work. A C8 species may undergo cracking either to form two C4 species or to C3 and C5, which would nicely account for the observed constancy in the C5/C4 ratio during changes in conversion. If they were primarily formed from the same species, this ratio would not be dependent on the availability of methylating agents. This would not be true if they were produced from different species in the methylation sequence of figure 15.31. Considering the 2,2,3-trimethylpentyl cation, isomerisation to species which can plausibly undergo β-scission to either isobutene and an isobutyl cation or to isopentene and a propyl cation should be possible. The cations formed may be deprotonated to form isobutene and propene. These reactions are outlined in figure 15.32. Of these, β-scission to yield two isobutenes is assumed to be fastest as the rate of reaction from a tertiary to another tertiary carbocation is much higher than from tertiary to secondary[32]. This, and the generation of two molecules from one reaction, would account for the higher selectivity to isobutene than isopentene observed in H-SAPO-5.

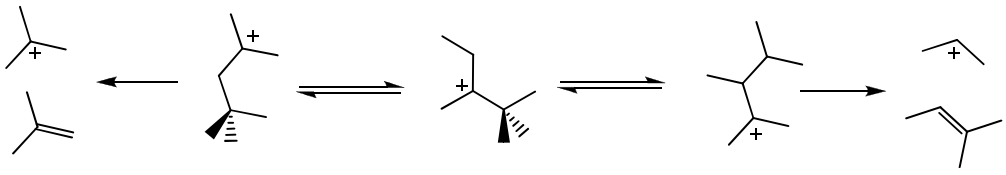

Fig. 15.32: Possible reaction scheme for formation of isobutene, isopentene and propene from a 2,2,3-trimethylpentyl cation by isomerisation and β-scission.

So far, the formation of the major products has been discussed. Of the more minor products, the increased production of ethene when benzene is added to the feed indicates formation from methylbenzenes. Considering methane production, any alkene may in principle crack to form this, but formation of a primary carbocation would be necessary. It is for this reason assumed that most of the methane is produced directly from methanol in accord with what

was observed for H-SAPO-34 by Dahl and Kolboe[45]. On a related note, cracking of e.g. C6 species to propenes in the same manner as proposed for H-ZSM-5[61] may also occur, but it is assumed that further methylation to C8 before cracking is more favourable, since this would involve more highly substituted carbocations. It is further assumed that alkenes and alkylbenzenes can undergo cyclisation and form more unsaturated species, with accompanied production of alkanes to maintain hydrogen balance. This then leads to a proposed mechanism which is very similar to that proposed for methanol conversion over H-ZSM-5 by Bjørgen et al[74], but where key intermediates and product distribution differ. The proposed mechanism is illustrated in figure 15.33 and consists of two cycles. Cycle 1 is based on methylbenzenes and assumes that ring-contraction of hexamethylbenzene is the cycle's main pathway to propene and ethene. Cycle 2 consists of methylation of propene to C8 and cracking to form propene, isobutene and isopentene. While the cycles represent parallel reaction mechanisms, transition from one cycle to another is assumed to occur frequently.

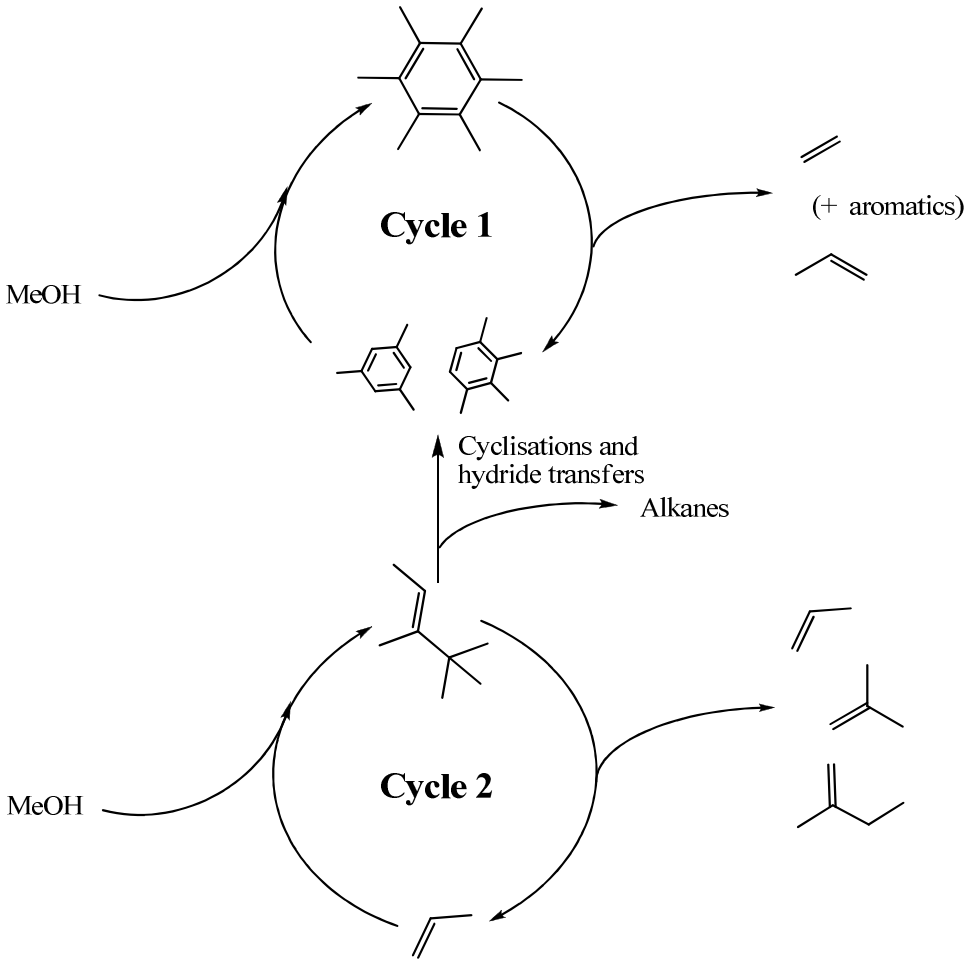

Fig. 15.33: Proposed mechanism of olefin formation during methanol conversion in H-SAPO-5

It should be stressed that the proposed mechanism as shown in figure 15.33 is not necessarily completely correct. Nevertheless, it fits well with the major observations of this work and should provide a good working hypothesis. This can then be used as a scaffold on which to base further studies of the system. One observation that has not been accounted for in the mechanistic proposal is the decreased C4/C5 ratio found in the products when benzene is added to the feed (recall figure 15.21). The reason for this change has not been determined, but it is possible that the larger amount of ethene and propene leads to more reactions between these. Reactions between propene and ethene may possibly lead to pentenes.

Finally, a question presents itself: why does olefin formation in other zeolitic MTH catalysts such as H-SAPO-34 and H-Beta occurs mainly by methylbenzene intermediates, while alkene based mechanisms appear more important in H-SAPO-5? Many possibilities exist here, but it would be instructive to look first at the differences between the systems. H-SAPO-34 possesses a structure with cages connected by very small apertures. It is conceivable that since molecules larger than propene are trapped inside the cages, these will eventually form methylbenzenes. Lesthaeghe et al[177] have also shown that formation of hexamethylbenzene in the CHA structure is more favourable than in H-Beta. As the methylbenzenes cannot leave the structure, addition of methanol and elimination of alkenes is likely to continue for some time. In H-Beta on the other hand, the methylbenzenes are free to diffuse out of the structure in the same manner as in H-SAPO-5. However, it is possible that the higher rate of hydrogen transfers in the (more strongly acidic) structure of H-Beta preferentially causes higher alkenes to form aromatics rather than crack by β-scission. This would then provide more active methylbenzenes and a shift favouring cycle I may occur. It should also be noted that the channel intersections in H-Beta provide a more spacious environment than in H-SAPO-5, which may favour cycles based on bulky methylbenzene intermediates and possibly cause more favourable conditions for formation of the highly reactive heptamethylbenzenium. This cation has not been observed so far in H-SAPO-5. Another interesting observation is that from the work by Ahn et al[176], it appears as if similar mechanisms as those proposed here for H-SAPO-5 dominate in H-Beta at lower temperatures. The main difference between their work and the study presented herein may be the increased rate of hydrogen transfer reactions in H-Beta, which could be responsible for “trapping” many of the larger hydrocarbons as less reactive alkanes, thus preventing them from cracking to form lower alkenes.

16 Conclusions and further work

While H-SAPO-5 is an active catalyst for methanol conversion, the samples produced in this work require low space velocities to convert an appreciable percentage of the feed. The overall conversion capacities before deactivation are not very high compared to other tested MTH catalysts. The major hydrocarbon products are C3-5 alkenes and methylbenzenes. Selectivity results indicate that degree of deactivation, acid site density or WHSV does not play a large role in determining selectivity as a function of methanol conversion, which implies that reactions appear independently at discrete acid sites. Deactivation is therefore assumed to primarily cause an acid site to become unavailable, while not affecting other sites in line with Janssens[81] kinetic model of deactivation in zeolites. Differences in deactivation rates have been observed between the differently synthesised samples. While a correlation between BET surface area and longer lifetime was found, it was hard to correlate the observations with other characterisation results. It is assumed that structural defects and possibly blocked channels are parts of the explanation, but this is by no means certain.

H-SAPO-5 has been shown to produce similar products as those observed when converting methanol over other twelve-ring zeolites, in particular zeolite H-Beta. However, a decreased selectivity to aromatics and alkanes is observed in H-SAPO-5, implying a lower hydrogen transfer activity. H-SAPO-5 also shows a higher preference for producing butenes rather than propene when compared to H-Beta. In addition to this, a higher apparent activation energy for methylation of benzene was found in H-SAPO-5. In spite of the similarities in product distribution, results indicate differences in the mechanisms of product formation compared to those reported for H-Beta. Based on the observations in this work, a mechanism where two cycles operate semi-independently of each other has been proposed. One cycle is based on methylbenzene intermediates and the paring reaction, while the other is based on successive methylations and cracking of alkenes. The proposed mechanism shares many similarities with mechanisms proposed for methanol conversion over H-ZSM-5.

As a hypothesis on the olefin formation mechanism in H-SAPO-5 has been provided, the logical next step would be to validate (or disprove) it. Several new experiments can be performed with this in mind. As 2,2,3-trimethylpentene has been proposed as a central intermediate in the alkene cycle, feeding this compound over a H-SAPO-5 sample would be

highly informative. If the cracking products are not consistent with the proposed mechanism, this will go a long way towards disproving the proposed mechanism. Similarly, co-feeding propene and methanol should generate C4-C8 species according to the mechanistic proposal. The above suggested co-feeding of methanol and propene may also be indicative of how much propene is produced from each of the mechanistic cycles if the dual cycle mechanism is not disproved. Also, hexamethylbenzene with ^{13}C methyl groups may be synthesised ex-situ and fed over the catalyst together with methanol to allow observation of elimination reactions from methylbenzenes with labelled methyl groups at higher conversion than what was managed in this work. If higher conversion is attainable without generating large amounts of pure ^{13}C methylbenzenes, it may be possible to analyse more species than C3-C5 alkenes. For example, the origins of ethene may be confirmed. Measurements of activation energies for different methylation reactions in H-SAPO-5 and subsequent comparisons with more strongly acidic zeolites may also prove valuable in determining which reactions are favoured upon changing the acid strength. Theoretical methods may also be employed for this purpose.

To determine whether the mechanistic differences observed in H-SAPO-5 and H-Beta are indeed caused by acid strength differences and not the difference in pore structure, a direct comparison of isostructural materials would be beneficial. It is possible to synthesise the zeolite isostructural to H-SAPO-5, SSZ-24 with acid site densities close to those of sample P/L in this work[135]. A Comparison between isostructural samples could prove invaluable in determining the role of acid strength in MTH applications. While such a study was recently performed by Bleken et al[70, 151], the CHA topology used in those studies limited the compounds that can be introduced due to its narrow channels. As bulky intermediates could not be utilised in co-feeeding experiments, mechanistic studies were difficult.

As causes of deactivation during the methanol-to-hydrocarbons process is generally poorly understood, further studies on the different catalyst samples found to differ in deactivation rate would be of interest. To gain insight into the reasons for the differing lifetimes, it would likely be necessary to characterise the samples more thoroughly. NMR methods should be employed to investigate compositions of the samples, but it would also be necessary to find a way to better characterise structural defects. Studies of both the nature and the amount of coke in the samples at various times on stream and degrees of deactivation may also be informative.

Appendix

A. Complete overview of syntheses performed

Syntheses performed using TPA template

Sample	Phase(s) obtained	H_2O	Al_2O_3	P_2O_5	SiO_2	TPA	Oven	Synth time	Temp	Notes
MWE01-2	AFI	50	1.0	0.6	0.40	2.1	Static	24.00h	200℃	
MWE01-4	AFI	50	1.0	0.6	0.40	2.1	Static	24.00h	200℃	
MWE04	AFI	50	1.0	0.6	0.40	2.1	Static	24.00h	200℃	
MWE05	AFI	50	1.0	0.6	0.40	2.1	Static	24.00h	200℃	
MWE06	AFI	50	1.0	0.6	0.40	2.1	Static	24.00h	200℃	
MWE07	AFI	50	1.0	0.8	0.40	2.1	Static	24.00h	200℃	
MWE08	AFI	50	1.0	1.0	0.40	2.1	Static	24.00h	200℃	
MWE09	AFI	50	1.0	1.0	0.40	2.1	Static	24.00h	200℃	I
MWE10-1	AFI/ tridymite	80	1.0	1.0	0.40	2.1	Static	24.00h	200℃	II
MWE10-2	AFI	80	1.0	1.0	0.40	2.1	Static	24.00h	200℃	II
MWE10-3	AFI	80	1.0	1.0	0.40	2.1	Static	24.00h	200℃	II
MWE10-4	AFI	80	1.0	1.0	0.40	2.1	Static	24.00h	200℃	II
MWE11	AFI	50	1.0	1.0	0.40	2.1	Old tumbler	23.00h	200℃	
MWE12	AFI	50	1.0	1.0	0.40	2.1	Old tumbler	23.00h	200℃	
MWE13	AFI	55	1.0	1.0	0.40	2.1	Old tumbler	23.00h	200℃	
MWE14	AFI	80	1.0	1.0	0.40	2.1	Old tumbler	23.00h	200℃	
MWE15	AFI	50	1.0	1.0	0.40	2.1	Old tumbler	24.00h	200℃	
MWE16	AFI	50	1.0	1.0	0.40	2.7	Old tumbler	24.00h	200℃	
MWE17	AFI	50	1.0	1.0	0.40	3.3	Old tumbler	24.00h	200℃	
MWE18	AFI	50	1.0	1.0	0.40	3.9	Old tumbler	24.00h	200℃	
MWE19	AFI	50	1.0	1.0	0.40	3.9	Old tumbler	24.00h	180℃	
MWE20	AFI	30	1.0	1.0	0.40	3.9	Old tumbler	24.00h	180℃	
MWE21	AFI	80	1.0	1.0	0.40	3.9	Old tumbler	24.00h	180℃	
MWE24	AFI	50	1.0	1.0	0.40	3.9	Old tumbler	16.00h	180℃	
MWE25	AFI	80	1.0	1.0	0.40	3.9	Old tumbler	16.00h	180℃	
MWE26	AFI	80	1.0	1.0	0.40	3.9	Old tumbler	16.00h	180℃	
MWE28	AFI	50	1.0	1.0	0.40	3.9	Old tumbler	8.00h	180℃	
MWE29	AFI	50	1.0	1.0	0.60	3.9	Old tumbler	8.00h	180℃	
MWE30	AFI	50	1.0	1.0	0.80	3.9	Old tumbler	8.00h	180℃	
MWE31	AFI	50	1.0	1.0	0.20	3.9	Old tumbler	16.00h	180℃	
MWE32	AFI	50	1.0	1.0	0.75	3.9	Old tumbler	16.00h	180℃	
MWE33	AFI	50	1.0	1.0	1.00	3.9	Old tumbler	16.00h	180℃	
MWE34	AFI	50	1.0	1.0	1.50	3.9	Old tumbler	16.00h	180℃	
MWE37	AFI	50	1.0	1.0	0.40	3.9	Old tumbler	4.00h	180℃	
MWE38	AFI	50	1.0	1.0	1.00	3.9	Old tumbler	4.00h	180℃	
MWE39	AFI	50	1.0	1.0	0.40	3.9	Old tumbler	16.00h	200℃	
MWE40	AFI	100	1.0	1.0	0.40	3.9	Old tumbler	16.00h	200℃	
MWE41	AFI	50	1.0	1.0	1.00	3.9	Old tumbler	16.00h	200℃	
MWE42	AFI	100	1.0	1.0	1.00	3.9	Old tumbler	16.00h	200℃	
MWE45	AFI	50	1.0	1.0	0.40	3.9	Old tumbler	4.00h	200℃	
MWE46	AFI	50	1.0	1.0	1.00	3.9	Old tumbler	4.00h	200℃	

I: Carried out in large autoclave (150ml liner)

II: Series with varying ageing time. The same gel was used for all four, with ageing times: 1h, 1 day, 2 days and 3 days respectively for 10-1 to 10-4.

TEA template

Sample	Phase(s)	H2O	Al	P	Si	temp	Oven	Synth time	Temp	Notes
MWE22	CHA(+AFI)	50	1,0	1,0	0,40	3,9	Old tumbler	24,00h	180℃	
MWE23	CHA/AFI	50	1,0	1,0	0,40	3,9	Old tumbler	16,00h	180℃	
MWE27	CHA/AFI	50	1,0	1,0	0,40	3,9	Old tumbler	8,00h	180℃	
MWE35	AFI/amorphous	50	1,0	1,0	0,40	3,9	Old tumbler	4,00h	180℃	
MWE36	CHA/amorphous	50	1,0	1,0	1,00	3,9	Old tumbler	4,00h	180℃	
MWE43	AFI/CHA	50	1,0	1,0	0,40	3,9	Old tumbler	4,00h	200℃	
MWE44	AFI/CHA	50	1,0	1,0	1,00	3,9	Old tumbler	4,00h	200℃	
MWE47	CHA	50	1,0	1,0	1,00	3,9	Old tumbler	4,50h	180℃	
MWE48	CHA/AFI	50	1,0	1,0	0,50	3,9	Old tumbler	4,50h	180℃	
MWE49	AFI/CHA	50	1,0	1,0	0,25	3,9	Old tumbler	4,50h	180℃	
MWE50	AFI(CHA)	50	1,0	1,0	0,00	3,9	Old tumbler	4,50h	180℃	
MWE51	AFI	50	1,0	1,0	0,25	3,9	Old tumbler	3,50h	200℃	
MWE52	AFI(CHA)	50	1,0	1,0	0,50	3,9	Old tumbler	3,50h	200℃	
MWE53	CHA	50	1,0	1,0	1,00	3,9	Old tumbler	3,50h	200℃	
MWE54	amorphous	100	1,0	1,0	1,00	3,9	Old tumbler	3,50h	200℃	
MWE55	AFI(CHA)	50	1,0	1,0	0,25	3,9	Old tumbler	3,50h	220℃	
MWE56	AFI(CHA)	50	1,0	1,0	0,50	3,9	Old tumbler	3,50h	220℃	
MWE57	AFI/CHA	50	1,0	1,0	1,00	3,9	Old tumbler	3,50h	220℃	
MWE58	AFI	50	1,0	1,0	2,00	3,9	Old tumbler	3,50h	220℃	
MWE59	AFI(CHA)	50	1,0	1,0	1,50	3,9	Old tumbler	4,50h	180℃	
MWE60	AFI	50	1,0	1,0	0,10	3,9	Old tumbler	4,50h	180℃	
MWE61	AFI(CHA)	50	1,0	1,0	0,20	3,9	Old tumbler	4,50h	180℃	
MWE62	AFI/CHA	50	1,0	1,0	0,25	3,9	Old tumbler	4,50h	180℃	
MWE63	AFI(CHA)	50	1,0	1,0	0,25	3,9	Old tumbler	4,00h	200℃	
MWE64	AFI/CHA	50	1,0	1,0	0,50	3,9	Old tumbler	4,00h	200℃	
MWE65	CHA/AFI	50	1,0	1,0	0,75	3,9	Old tumbler	4,00h	200℃	
MWE66	CHA/AFI	50	1,0	1,0	1,00	3,9	Old tumbler	4,00h	200℃	
MWE67	CHA/AFI	50	1,0	1,0	0,75	3,9	Old tumbler	4,50h	180℃	
MWE68	AFI/CHA	50	1,0	1,0	2,00	3,9	Old tumbler	4,50h	180℃	III
MWE69	AFI/CHA	50	1,0	1,0	1,00	3,9	Static	5,00h	200℃	
MWE134	AFI/CHA/+ unknown	50	1,0	1,0	0,25	3,9	Old tumbler	3,50h	220℃	III
MWE135	AFI/CHA/+ unknown	50	1,0	1,0	0,05	3,9	Old tumbler	3,50h	220℃	III
MWE136	AFI/CHA/+ unknown	50	1,0	1,0	0,25	3,9	Old tumbler	3,50h	220℃	III
MWE137	AFI/CHA/+ unknown	50	1,0	1,0	0,25	3,9	Old tumbler	3,50h	220℃	III
MWE150	amorphous/AFI	50	1,0	1,0	0,10	3,9	Magnetic	3,00h	200℃	
MWE151	AFI/amorphous	50	1,0	1,0	0,10	3,9	Magnetic	3,25h	200℃	
MWE152	AFI	50	1,0	1,0	0,10	3,9	Magnetic	3,50h	200℃	
MWE157	AFI/amorphous	50	1,0	1,0	0,10	3,9	Magnetic	3,50h	200℃	
MWE158	AFI	50	1,0	1,0	0,10	3,9	Magnetic	3,75h	200℃	
MWE159	AFI	50	1,0	1,0	0,10	3,9	Magnetic	4,00h	200℃	
MWE164	AFI/CHA	50	1,0	1,0	0,10	3,9	Magnetic	7,00h	180℃	IV
MWE165	AFI/CHA	50	1,0	1,0	0,10	3,9	Magnetic	4,25h	180℃	
MWE166	AFI	50	1,0	1,0	0,10	3,9	Magnetic	4,50h	180℃	
MWE167	AFI/CHA	50	1,0	1,0	0,10	3,9	Magnetic	4,25h	180℃	
MWE168	AFI/CHA	50	1,0	1,0	0,10	3,9	Magnetic	4,50h	180℃	
MWE169	AFI/CHA	50	1,0	1,0	0,10	3,9	Magnetic	4,45h	180℃	
MWE170	No product	50	1,0	1,0	0,10	3,9	Magnetic	4,50h	200℃	
MWE171	CHA/AFI	50	1,0	1,0	0,05	3,9	Magnetic	4,50h	200℃	
MWE172	CHA/AFI(AEI?)	50	1,0	1,0	0,05	3,9	Magnetic	4,50h	200℃	
MWE173_M1	AFI/amorphous	50	1,0	1,0	0,10	3,9	New Tumbler	3,50h	200℃	
MWE173_M2	AFI/CHA/amorphous	50	1,0	1,0	0,10	3,9	New Tumbler	3,50h	200℃	
MWE174_M3	CHA/AFI/amorphous	50	1,0	1,0	0,05	3,9	New Tumbler	3,50h	200℃	
MWE174_M4	CHA/AFI/amorphous	50	1,0	1,0	0,05	3,9	New Tumbler	3,50h	200℃	
MWE175_M1	CHA/AFI/amorphous	50	1,0	1,0	0,05	3,9	New Tumbler	4,00h	200℃	
MWE175_M2	AFI	50	1,0	1,0	0,05	3,9	New Tumbler	4,00h	200℃	

MWE176_M3	AFI	50	1,0	1,0	0,10	3,9	New Tumbler	4,00h	200℃	
MWE176_M4	AFI	50	1,0	1,0	0,10	3,9	New Tumbler	4,00h	200℃	
MWE177	No product	50	1,0	1,0	0,10	3,9	New Tumbler	4,50h	180℃	
MWE178_1	AFI(CHA)	50	1,0	1,0	0,10	3,9	New Tumbler	4,25h	200℃	
MWE178_2	AFI(CHA)	50	1,0	1,0	0,10	3,9	New Tumbler	4,25h	200℃	
MWE179	CHA	50	1,0	1,0	0,50	3,9	New Tumbler	4,25h	200℃	
MWE180	CHA/amorphous	50	1,0	1,0	0,50	3,9	New Tumbler	4,25h	200℃	
MWE181_1	AFI/CHA	50	1,0	1,0	0,10	3,9	New Tumbler	4,50h	200℃	
MWE181_2	AFI/CHA	50	1,0	1,0	0,10	3,9	New Tumbler	4,50h	200℃	
MWE182	CHA/AEI?(AFI)	50	1,0	1,0	0,50	3,9	New Tumbler	4,50h	200℃	
MWE183	CHA/AEI?(AFI)	50	1,0	1,0	1,00	3,9	New Tumbler	4,50h	200℃	
MWE184	CHA/AEI?/AFI	50	1,0	1,0	0,10	3,9	New Tumbler	5,00h	200℃	
MWE185	CHA/AEI?/AFI	50	1,0	1,0	0,10	2,0	New Tumbler	5,00h	200℃	
MWE186	CHA	50	1,0	1,0	0,50	3,9	New Tumbler	5,00h	200℃	
MWE187	CHA	50	1,0	1,0	1,00	3,9	New Tumbler	5,00h	200℃	
MWE188	AFI/CHA	50	1,0	1,0	0,10	3,9	New Tumbler	4,00h	200℃	
MWE189	CHA	50	1,0	1,0	0,25	3,9	New Tumbler	4,00h	200℃	
MWE200	CHA/AEI?	50	1,0	1,0	0,10	2,0	New Tumbler	4,00h	200℃	
MWE191	AFI	50	1,0	1,0	0,25	2,0	New Tumbler	4,00h	200℃	
MWE192	CHA/AFI	50	1,0	1,0	0,10	3,9	New Tumbler	4,00h	200℃	
MWE193	AFI (CHA)	50	1,0	1,0	0,10	3,9	New Tumbler	4,00h	200℃	V
MWE194	CHA/AEI?(AFI)	50	1,0	1,0	0,10	2,0	New Tumbler	4,00h	200℃	
MWE195	CHA/AEI?/AFI	50	1,0	1,0	0,10	2,0	New Tumbler	4,00h	200℃	
MWE196_M1	AFI/amorphous	50	1,0	1,0	0,10	3,9	New Tumbler	4,00h	200℃	V
MWE196_M2	AFI	50	1,0	1,0	0,10	3,9	New Tumbler	4,00h	200℃	V
MWE196_M3	AFI	50	1,0	1,0	0,10	3,9	New Tumbler	4,00h	200℃	V
MWE196_M4	AFI	50	1,0	1,0	0,10	3,9	New Tumbler	4,00h	200℃	V
MWE197_M5	AFI	50	1,0	1,0	0,10	3,9	New Tumbler	4,00h	200℃	V
MWE197_M12	AFI	50	1,0	1,0	0,10	3,9	New Tumbler	4,00h	200℃	V
MWE197_M13	AFI	50	1,0	1,0	0,10	3,9	New Tumbler	4,00h	200℃	V
MWE198	None	50	1,0	1,0	0,10	3,9	New Tumbler	4,00h	200℃	V
MWE201	AFI	50	1,0	1,0	0,10	3,9	New Tumbler	4,00h	200℃	V
MWE202	AFI	50	1,0	1,0	0,10	3,9	New Tumbler	4,00h	200℃	V
MWE203	AFI	50	1,0	1,0	0,10	3,9	New Tumbler	4,25h	200℃	VI
MWE204	AFI	50	1,0	1,0	0,10	3,9	New Tumbler	4,25h	200℃	VI

III: Ludox AS-40 used as silica source

IV: 150ml autoclave used

V: Seeded with plate-like sample

VI: Seeded with TPA sample

Syntheses performed with cyclohexylamine template[VI]

Sample	Phase(s)	H2O	Al	P	Si	cHA	Oven	Synth time	Temp	Notes
MWE02-2	AFI/CHA	107	1,0	1,0	4,00	1,2	Static	3,00h	200℃	
MWE02-6	AFI/CHA	107	1,0	1,0	4,00	1,2	Static	3,00h	200℃	
MWE03-4	AFI/CHA	107	1,0	1,0	4,00	1,2	Static	3,00h	200℃	
MWE03-6	AFI/CHA	107	1,0	1,0	4,00	1,2	Static	3,00h	200℃	
MWE03-7	AFI/CHA	107	1,0	1,0	4,00	1,2	Static	3,00h	200℃	

VI: A few attempts were made to reproduce the synthesis of Young[95] from "Verified Syntheses of Zeolitic Materials". After a few trials with no luck, it was decided to pursue other recipes instead.

Microwave Syntheses

Sample	Phase(s)	H2O	Al	P	Si	TEA	Oven	Synth time	Temp	Notes
MWE71	AFI/amorphous	50	1,0	1,0	1,00	3,9	Microwave	0,33h	190℃	
MWE72	AFI	50	1,0	1,0	1,00	3,9	Microwave	0,66h	190℃	
MWE73	AFI	50	1,0	1,0	1,00	3,9	Microwave	0,50h	190℃	
MWE74	AFI	50	1,0	1,0	1,00	1,0	Microwave	0,50h	190℃	
MWE75	AFI/dense	50	1,0	1,0	1,00	3,9	Microwave	0,50h	190℃	VII
MWE76	AFI	50	1,0	1,0	1,00	6,0	Microwave	0,50h	190℃	
MWE77	AFI/dense	50	1,0	1,0	0,10	1,0	Microwave	0,50h	190℃	
MWE78	AFI	50	1,0	1,0	0,10	3,9	Microwave	0,50h	190℃	
MWE79	AFI/amorphous	50	1,0	1,0	0,10	3,9	Microwave	0,50h	190℃	
MWE80	AFI	50	1,0	1,0	0,50	3,9	Microwave	0,50h	190℃	VII
MWE81	AFI	50	1,0	1,0	0,50	3,9	Microwave	0,50h	190℃	III
MWE82	AFI	50	1,0	1,0	0,50	3,9	Microwave	0,50h	190℃	III, VII
MWE83	AFI	50	1,0	1,0	0,50	3,9	Microwave	0,50h	190℃	III
MWE84	AFI	50	1,0	1,0	0,25	3,9	Microwave	1,00h	160℃	III
MWE85	AFI	50	1,0	1,0	1,00	3,9	Microwave	1,00h	160℃	III
MWE86	No product	50	1,0	1,0	0,25	3,9	Microwave	1,50h	160℃	III
MWE87	No product	50	1,0	1,0	1,00	3,9	Microwave	1,50h	160℃	III
MWE88	No product	50	1,0	1,0	0,25	3,9	Microwave	1,00h	160℃	III
MWE89	No product	50	1,0	1,0	0,25	3,9	Microwave	1,50h	160℃	III
MWE90	No product	50	1,0	1,0	0,25	3,9	Microwave	2,00h	160℃	III
MWE91	AFI	50	1,0	1,0	0,10	3,9	Microwave	0,75h	180℃	III
MWE92	AFI/dense	50	1,0	1,0	0,25	3,9	Microwave	0,75h	180℃	III, VII
MWE93	AFI/dense	50	1,0	1,0	0,50	3,9	Microwave	0,75h	180℃	III, VII
MWE94	AFI	50	1,0	1,0	1,00	3,9	Microwave	0,75h	180℃	III
MWE96	AFI	50	1,0	1,0	1,00	3,9	Microwave	0,66h	190℃	III
MWE97	AFI/dense	50	1,0	1,0	1,00	3,9	Microwave	0,50h	180℃	III, VII
MWE98	AFI/dense	50	1,0	1,0	1,00	10,0	Microwave	0,50h	180℃	III, VII
MWE99	AFI	50	1,0	1,0	0,10	10,0	Microwave	0,50h	180℃	III
MWE100	AFI	50	1,0	1,0	0,10	3,9	Microwave	0,50h	180℃	III
MWE101	AFI	50	1,0	1,0	1,00	3,9	Microwave	1,00h	190℃	III, VIII
MWE103	AFI/dense	50	1,0	1,0	1,00	3,9	Microwave	1,50h	190℃	III, VII, VIII
MWE104	AFI/dense	50	1,0	1,0	1,00	3,9	Microwave	2,00h	190℃	III, VII, VIII
MWE105	AFI/dense	50	1,0	1,0	0,10	3,9	Microwave	0,50h	180℃	III
MWE106	AFI/dense	50	1,0	1,0	0,10	3,9	Microwave	0,50h	180℃	III, VII
MWE107	AFI/dense	50	1,0	1,0	0,12	3,9	Microwave	0,58h	180℃	III
MWE108	No product	50	1,0	1,0	1,00	3,9	Microwave	0,75h	190℃	III, VIII
MWE109	AFI/dense	50	1,0	1,0	1,00	3,9	Microwave	1,00h	190℃	III, VII, VIII
MWE110	AFI	50	1,0	1,0	1,00	3,9	Microwave	1,00h	180℃	III, VIII
MWE111	AFI/dense	50	1,0	1,0	1,00	3,9	Microwave	1,25h	180℃	III, VII, VIII
MWE112	AFI/dense	50	1,0	1,0	0,10	3,9	Microwave	1,00h	180℃	III, VIII
MWE113	AFI/dense	50	1,0	1,0	0,10	3,9	Microwave	1,25h	180℃	III, VII, VIII
MWE114	AFI	50	1,0	1,0	0,50	3,9	Microwave	0,50h	180℃	III, IX
MWE115	AFI	50	1,0	1,0	1,00	3,9	Microwave	0,50h	180℃	III
MWE116	No product	50	1,0	1,0	0,10	3,9	Microwave	0,50h	190℃	III
MWE117	AFI	50	1,0	1,0	0,10	3,9	Microwave	0,50h	190℃	III
MWE118	AFI	50	1,0	1,0	1,00	3,9	Microwave	0,50h	190℃	III
MWE119	AFI	50	1,0	1,0	1,00	3,9	Microwave	0,50h	190℃	III
MWE120	No product	50	1,0	1,0	0,10	3,9	Microwave	1,00h	180℃	III, VIII
MWE121	No product	50	1,0	1,0	1,00	3,9	Microwave	1,00h	180℃	III, VIII
MWE122	Amorphous (AFI)	50	1,0	1,0	0,10	3,9	Microwave	1,25h	180℃	III
MWE123	AFI	50	1,0	1,0	0,10	3,9	Microwave	1,00h	180℃	III
MWE124	AFI, dense	50	1,0	1,0	1,00	3,9	Microwave	1,25h	180℃	III
MWE125	AFI	50	1,0	1,0	1,00	3,9	Microwave	1,00h	180℃	III
MWE126	AFI	50	1,0	1,0	0,10	3,9	Microwave	0,50h	190℃	III
MWE127	amorphous	50	1,0	1,0	0,10	3,9	Microwave	0,58h	190℃	III

MWE128	AFI	50	1,0	1,0	0,10	3,9	Microwave	0,66h	190℃	III
MWE129	No product	50	1,0	1,0	0,10	3,9	Microwave	0,33h	190℃	III
MWE130	No product	50	1,0	1,0	0,10	3,9	Microwave	0,41h	190℃	III
MWE131	No product	50	1,0	1,0	0,10	3,9	Microwave	0,50h	190℃	III
MWE132	No product	50	1,0	1,0	0,10	3,9	Microwave	0,58h	190℃	III
MWE133	AFI	50	1,0	1,0	0,10	3,9	Microwave	0,66h	190℃	III
MWE138	AFI	50	1,0	1,0	1,00	3,9	Microwave	0,41h	190℃	III
MWE139	AFI	50	1,0	1,0	1,00	3,9	Microwave	0,50h	190℃	III
MWE140	AFI	50	1,0	1,0	1,00	3,9	Microwave	0,58h	190℃	III
MWE141	AFI	50	1,0	1,0	1,00	3,9	Microwave	0,66h	190℃	III
MWE142	No product	50	1,0	1,0	0,10	3,9	Microwave	0,33h	180℃	
MWE143	No product	50	1,0	1,0	0,10	3,9	Microwave	0,41h	180℃	
MWE144	No product	50	1,0	1,0	0,10	3,9	Microwave	0,50h	180℃	
MWE145	No product	50	1,0	1,0	0,10	3,9	Microwave	0,58h	180℃	
MWE146	No product	50	1,0	1,0	0,10	3,9	Microwave	0,50h	180℃	
MWE147	No product	50	1,0	1,0	0,10	3,9	Microwave	0,58h	180℃	
MWE148	No product	50	1,0	1,0	0,10	3,9	Microwave	0,66h	180℃	
MWE149	No product	50	1,0	1,0	0,10	3,9	Microwave	0,75h	180℃	
MWE153	amorphous	50	1,0	1,0	0,10	3,9	Microwave	0,66h	180℃	
MWE154	AFI/amorphous	50	1,0	1,0	0,10	3,9	Microwave	0,75h	180℃	
MWE155	AFI	50	1,0	1,0	0,10	3,9	Microwave	0,83h	180℃	
MWE156	AFI	50	1,0	1,0	0,10	3,9	Microwave	0,91h	180℃	
MWE160	AFI	50	1,0	1,0	0,10	3,9	Microwave	0,75h	180℃	
MWE161	AFI	50	1,0	1,0	0,10	3,9	Microwave	0,83h	180℃	
MWE162	amorphous	50	1,0	1,0	0,10	3,9	Microwave	0,91h	180℃	
MWE163	AFI	50	1,0	1,0	0,10	3,9	Microwave	0,91h	180℃	

III: Ludox AS-40 used as silica source

VII: Known to have ventilated

VIII: Slow heating (45-60 minutes to T_{max})

IX: From this point on, thermocouple was inserted into reference mixture instead of water.

B. List of catalytic tests performed

- Flow rates listed are total flow rates of He and reactant combined
- Where P, flow or WHSV is given as two values, the first is benzene: (benzene;MeOH)
- P/L 2* denotes a reproduced synthesis of P/L. As results were different from the original batch, no further testing with this sample was performed.

Exp #	Sample	T (°C)	Mass (mg)	Quartz (Y/N)	P_{feed} (mbar)	Flow (ml/min)	WHSV (h^{-1})	Stopped after	Comments
MWE501	P/H	350	100	Y	130	30	3.03		Test run
MWE502	P/H	350	60	Y	130	30	5.06		Test run
MWE503	P/H	350	60	Y	40	30	1.56		Test run
MWE504	P/H	350	60	Y	40	30	1.56		Test run
MWE505	P/H	400	60	Y	40	30	1.56		Test run
MWE506	P/H	450	60	Y	40	30	1.56		Test run
MWE507	P/H	450	100	Y	40	30	0.93	19.5 h	
MWE508	P/H	450	100	Y	40	30	0.93	19.5 h	
MWE509	P/H	450	100	Y	40	30	0.93	19.5 h	
MWE510	P/H	450	50	Y	40	15	0.93	19.5 h	
MWE511	P/H	450	50	Y	40	15	0.93	19.5 h	
MWE512	P/H	450	100	Y	40	30	0.93	19.5 h	
MWE513	P/H	450	100	Y	40	30	0.93	19.5 h	
MWE514	P/H	450	100	Y	40	30	0.93	19.5 h	
MWE515	P/H	450	50	Y	40	15	0.93	19.5 h	
MWE516	P/L	450	50	Y	40	15	0.93	19.5 h	
MWE517	P/L	450	50	Y	40	15	0.93	19.5 h	
MWE518	P/L	450	50	Y	40	15	0.93	19.5 h	
MWE519	P/L	450	50	Y	40	15	0.93	19.5 h	
MWE520	P/L	450	50	Y	40	15	0.93	19.5 h	
MWE521	P/L	450	50	Y	40	15	0.93	19.5 h	
MWE522	P/L	450	50	Y	40	15	0.93	19.5 h	
MWE523	P/L	450	50	Y	40	15	0.93	19.5 h	
MWE524	P/H	450	50	Y	40	15	0.93	19.5 h	
MWE525	P/H	450	50	Y	40	15	0.93	19.5 h	
MWE526	B/L	450	50	Y	40	15	0.93	19.5 h	
MWE527	B/L	450	50	Y	40	15	0.93	19.5 h	
MWE528	B/H	450	50	Y	40	15	0.93	19.5 h	
MWE529	B/H	450	50	Y	40	15	0.93	44 h	
MWE530	P/L	450	50	Y	40	15	0.93	19.5 h	
Rig rebuilt									
MWE531	P/L	450	50	Y	40	15	0.93	19.5 h	
MWE532	P/L	450	50	Y	40	15	0.93	19.5 h	
MWE533	P/L	450	100	Y	40	15	0.47	19.5 h	
MWE534	P/L	450	100	Y	40	15	0.47	19.5 h	
MWE535	P/L	450	200	Y	40	15	0.23	19.5 h	
MWE536	P/L	450	50	Y	40	15	0.93	19.5 h	
MWE537	P/L	450	50	Y	40	15	0.93	19.5 h	
MWE538	P/L	450	50	Y	40	15	0.93	19.5 h	
MWE539	P/L	450	50	Y	40	15	0.93	19.5 h	
MWE540	P/H	450	50	Y	40	15	0.93	19.5 h	

column changed									
MWE541	P/L	450	50	Y	40	15	0.93	19.5 h	
MWE542	P/L	450	50	Y	40	15	0.93	19.5 h	
MWE543	P/L	450	50	Y	40	7,5	0.47	19.5 h	
MWE544	P/L	450	50	Y	40	3,7	0.23	19.5 h	
MWE545	P/L	450	50	N	40	15	0.93	19.5 h	
MWE546	P/L	350	50	Y	40	15	0.93	19.5 h	
MWE547	P/L	450	50	Y	40	15	0.93	19.5 h	
MWE548	P/H	350	50	Y	40	15	0.93	19.5 h	
MWE549	B/L	350	50	Y	40	15	0.93	19.5 h	
MWE550	P/L	450	200	Y	40	15	0.23	19.5 h	
MWE551	P/L	300	50	Y	130;60	10;6	2.0;1.35	90 min	^{12}C MeOH + ^{12}C Benzene
MWE552	P/L	250	50	Y	130;60	10;6	2.0;1.35	90 min	^{12}C MeOH + ^{12}C Benzene
MWE553	P/L	230	50	Y	130;60	20;7	4.0;1.6	90 min	^{12}C MeOH + ^{12}C Benzene
MWE554	P/L	250	50	Y	130;60	20;7	4.0;1.6	90 min	^{12}C MeOH + ^{12}C Benzene
MWE555	P/L	270	50	Y	130;60	20;7	4.0;1.6	90 min	^{12}C MeOH + ^{12}C Benzene
MWE556	P/L	285	50	Y	130;60	20;7	4.0;1.6	90 min	^{12}C MeOH + ^{12}C Benzene
MWE557	P/L	300	50	Y	130;60	20;7	4.0;1.6	90 min	^{12}C MeOH + ^{12}C Benzene
MWE558	P/L	315	50	Y	130;60	20;7	4.0;1.6	90 min	^{12}C MeOH + ^{12}C Benzene
MWE559	P/L	330	50	Y	130;60	20;7	4.0;1.6	90 min	^{12}C MeOH + ^{12}C Benzene
MWE560	P/L	350	50	Y	130;60	20;7	4.0;1.6	90 min	^{12}C MeOH + ^{12}C Benzene
MWE561	P/L	370	50	Y	130;60	20;7	4.0;1.6	90 min	^{12}C MeOH + ^{12}C Benzene
MWE562	P/L	300	50	N	130;60	20;7	4.0;1.6	3 min	^{12}C MeOH + ^{12}C Benzene
MWE563	P/L	300	100	N	130;60	20;7	2.0;0.8	3 min	^{12}C MeOH + ^{12}C Benzene
MWE564	P/L	300	100	N	130;60	20;7	2.0;0.8	3.5 min	^{13}C MeOH + ^{12}C Benzene
MWE565	P/L	300	100	N	130;60	20;7	2.0;0.8	3.5 min	^{13}C MeOH + ^{12}C Benzene
MWE566	P/L	300	100	N	130;60	20;7	2.0;0.8	2.5 min	^{13}C MeOH + ^{12}C Benzene
MWE567	P/L	250	100	N	130;60	20;7	2.0;0.8	3.5 min	^{13}C MeOH + ^{12}C Benzene
MWE568	P/L	250	100	N	130;60	20;7	2.0;0.8	2.5 min	^{13}C MeOH + ^{12}C Benzene
MWE569	SC	450	50	Y	40	15	0.93	19.5 h	
MWE570	P/L	250	100	N	130;60	20;7	2.0;0.8	2.5 min	^{13}C MeOH + ^{12}C Benzene
MWE571	P/L	350	100	N	40	15	0.47	20 min	
MWE572	SC	450	50	Y	40	15	0.93	50 h	
MWE573	P/L	350	100	N	40	15	0.47	80 min	20 min MeOH + 60 min pure He
MWE574	SC	450	50	Y	40	15	0.93	50 h	
MWE575	P/L	450	100	Y	40	15	0.47	19.5 h	
MWE576	P/L	450	100	Y	40	15	0.47	19.5 h	
MWE577	P/L 2*	450	50	Y	40	15	0.93	19.5 h	
MWE578	P/L 2*	350	100	N	40	15	0.47	20 min	
MWE579	P/L 2*	350	100	N	40	15	0.47	80 min	20 min MeOH + 60 min pure He
MWE580	SC	300	50	N	40	45	2.77	5 min	no conversion observed
MWE581	SC	350	50	N	40	40	2.47	12 min	
MWE582	SC	350	50	Y	40	15	0.93	19.5 h	
MWE583	SC	350	50	N	40	80	4.93	6 min	
MWE584	SC	350	100	N	40	15	0.47	20 min	
MWE585	SC	350	100	N	40	15	0.47	80 min	20 min MeOH + 60 min pure He
MWE586	SC	300	100	N	130;60	20;7	2.0;0.8	3.5 min	^{13}C MeOH + ^{12}C Benzene
MWE587	SC	300	100	N	130;60	20;7	2.0;0.8	2.5 min	^{13}C MeOH + ^{12}C Benzene
MWE588	SC	300	100	N	60	7	0.8	2.5 min	Only benzene + 20ml/ min He feed
MWE589	SC	300	100	N	130;60	20;7	2.0;0.8	3.5 min	^{13}C MeOH + ^{12}C Benzene
MWE590	SC	450	50	N	40	15	0.93	20 min	^{12}C to ^{13}C MeOH switch after 18 min
MWE591	SC	450	50	N	40	15	0.93	19 min	^{12}C to ^{13}C MeOH switch after 18 min
MWE592	SC	450	50	N	40	15	0.93	18.5 min	^{12}C to ^{13}C MeOH switch after 18 min
MWE593	SC	450	50	N	40	15	0.93	21 min	^{12}C to ^{13}C MeOH switch after 18 min
MWE594	SC	300	100	N	130;60	10;7	1.0;0.8	2.5 min	^{13}C MeOH,^{12}C Benzene, 10ml/min He
MWE595	SC	300	100	N	130;60	10;7	1.0;0.8	3.5 min	^{13}C MeOH,^{12}C Benzene, 10ml/min He
MWE596	SC	250	100	N	130;60	10;7	1.0;0.8	3.5 min	^{13}C MeOH,^{12}C Benzene, 10ml/min He
MWE597	SC	250	100	N	130;60	10;7	1.0;0.8	2.5 min	^{13}C MeOH,^{12}C Benzene, 10ml/min He

C. Calculation of Weight Hourly Space Velocity (WHSV)

If the partial pressure of reactant is known (determined by the temperature in bubble saturators), the flow of reactant can be found from the total flow:

$$Flow(total) \cdot \frac{p(feed)}{P} = Flow(feed)$$

When the flow rate of feed is known, the mass of feed per time can be found by use of the ideal gas law:

$$m(feed) = \frac{PV \cdot M}{RT}$$

WHSV (the mass of feed per mass of catalyst per time) is then found from:

$$WHSV = \frac{m(feed)}{m(catalyst) \cdot hour}$$

D. Calculations based on results from GC analyses

All conversion and selectivity data of catalytic tests presented in this work has been calculated from the observed peaks from on-line effluent analysis by GC-FID. The FID detector has been assumed to have the same response to all non-oxygenate hydrocarbons, so a response factor 1 has been employed for these. For methanol and dimethyl ether, response factors based on previous calibration were used. As such, corrected peak areas used were:

Hydrocarbons (HC):

$$A_{corr}(HC) = \frac{A(HC)}{1}$$

DME:

$$A_{corr}(MeOH) = \frac{A(MeOH)}{0.773}$$

MeOH:

$$A_{corr}(DME) = \frac{A(DME)}{0.592}$$

The corrected areas were proportional to the number of carbon atoms in each analysed compound. Thus, if equal areas are found for ethene and butene the actual concentration of butene in the effluent will be half as high as that of ethene. Formulas for calculating conversion and product selectivities are given below:

Conversion

Conversion of reactants was calculated from the GC-FID peaks by the formula:

$$Conversion = \frac{\sum A_{corr}\,(products)}{\sum A_{corr}\,(products) + \sum A_{corr}\,(reactants)} \cdot 100\ \%$$

Selectivity

Product selectivity for a given product *i* can be found from:

$$Selectivity = \frac{A_{corr}\,(i)}{\sum A_{corr}\,(products)} \cdot 100\ \%$$

E. Calculation of (Al+P)/Si from NH_3 TPD

The density of acid sites in mol/g can be found from the weight loss in the chemisorption region. The (Al+P)/Si ratio was then found by assuming that the framework consists of equal amounts P and Al in TO_2 groups with an average molar mass $M(TO_2) = 60.98$.

$$Acidity = \left(\frac{\%\, Weight\ Loss}{100}\right)\left(\frac{1}{M(NH_3)}\right) = \frac{n(NH_3)}{m(TO_2) + m(SiO_2)} = \frac{n(SiO_2)}{m(TO_2) + m(SiO_2)}$$

$$m(TO_2) + m(SiO_2) = 1$$
$$\Rightarrow Acidity = n(SiO_2) = n(NH_3)$$

$$n(TO_2) * M(TO_2) + n(NH_3) * M(SiO_2) = 1$$
$$n(TO_2) = \frac{1 - n(NH_3) * M(SiO_2)}{M(TO_2)}$$

$$\frac{Al + P}{Si} = \frac{n(TO_2)}{n(SiO_2)} = \frac{1 - n(NH_3) * M(SiO_2)}{M(TO_2) * n(NH_3)}$$

F. Reproducibility

Poor reproducibility of the catalytic tests was a major issue for a long time during the initial stages of the work presented here. For this reason many identical experiments were performed numerous times as can be inferred from the list of experiments in appendix B. Results of early experiments using sample P/H at identical conditions are shown in figure F.1a.

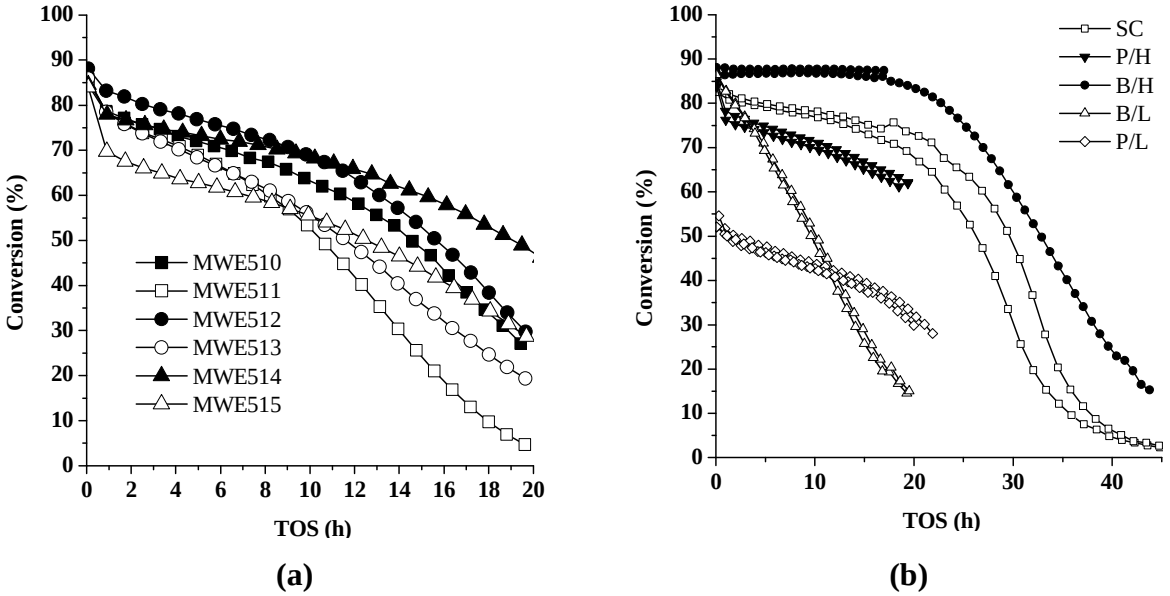

Fig. F.1: (a) Reproducibility checks for P/H at identical conditions during early stages of testing. (b) Improved reproducibility of tests at 450 °C and WHSV 0.93 h^{-1} during later testing. SC was analysed on the PLOT-Q column, while all others in the plots were analysed by the PONA column.

Measures to improve the reproducibility included cleaning of nearly all GC parts and improving insulation and heating of the transfer line from reactor to GC. In addition, in-situ calcination of the catalyst in pure oxygen at 550 °C prior to each experiment was made standard practice. It was also discovered that leakages in the reactor system apparently led to decreased catalyst lifetime.

With time (and much work) reproducibility was significantly improved, as shown by figure F.1b. However, perfect reproducibility for long tests was never achieved, as is witnessed from the plot of SC. It should be noted that even when strange results were obtained for catalyst lifetimes, the selectivity trends discussed throughout this work still held.

After the rig was rebuilt, the reproducibility was also confirmed satisfactory.

G. Old and new rig comparison

A comparison of conversion as a function of time on stream for catalyst P/L on the HP-PONA GC column and on the rebuilt rig with a PLOT-Q column is given below in figure G.1. Conditions were WHSV 0.93 and 450 °C. It is apparent from the figure that the shape of the curve was changed, but the overall activity and lifetime was relatively similar. The reason for the differing curve shape is not known, but the difference was reproducible.

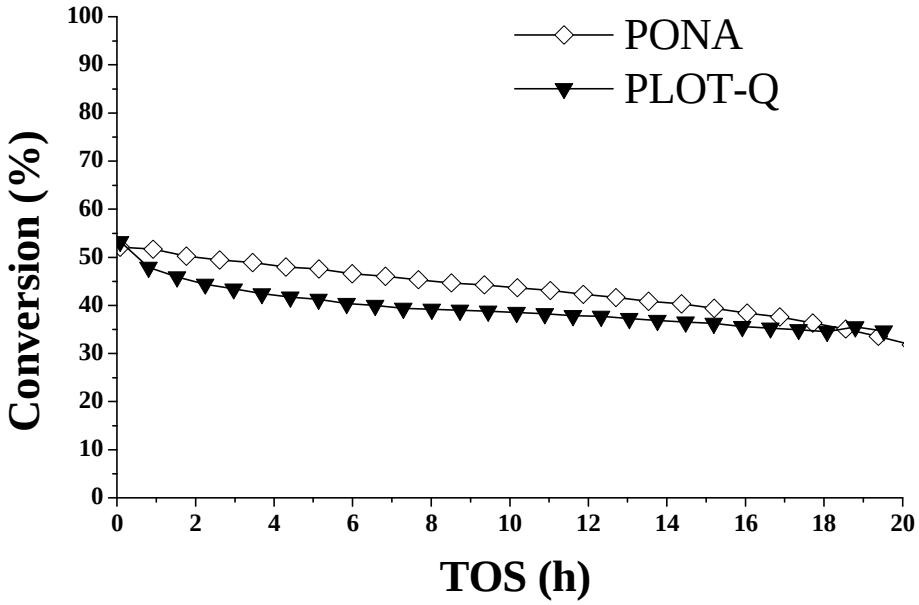

Fig. G.1: Conversion vs TOS for PONA and PLOT-Q system

Product selectivities from the experiments shown above in figure G.1 are shown below in figure G.2. Some differences are apparent, but the C3-C5 fractions are very similar. While the PLOT-Q offered superior resolution of the light olefins, analysis of hydrocarbons with more than 8 carbons was difficult due to a noisy baseline at higher temperatures. Especially the Hexamethylbenzene peak was very broad, and as seen in figure G.2 the peak area varies significantly between measurements. Overall, the results obtained before and after the rig was rebuilt were similar enough that the same trends were apparent. It should be noted that even if the hexamethylbenzene signal is higher on the PLOT-Q column for these experiments, the general trend appeared to show the opposite.

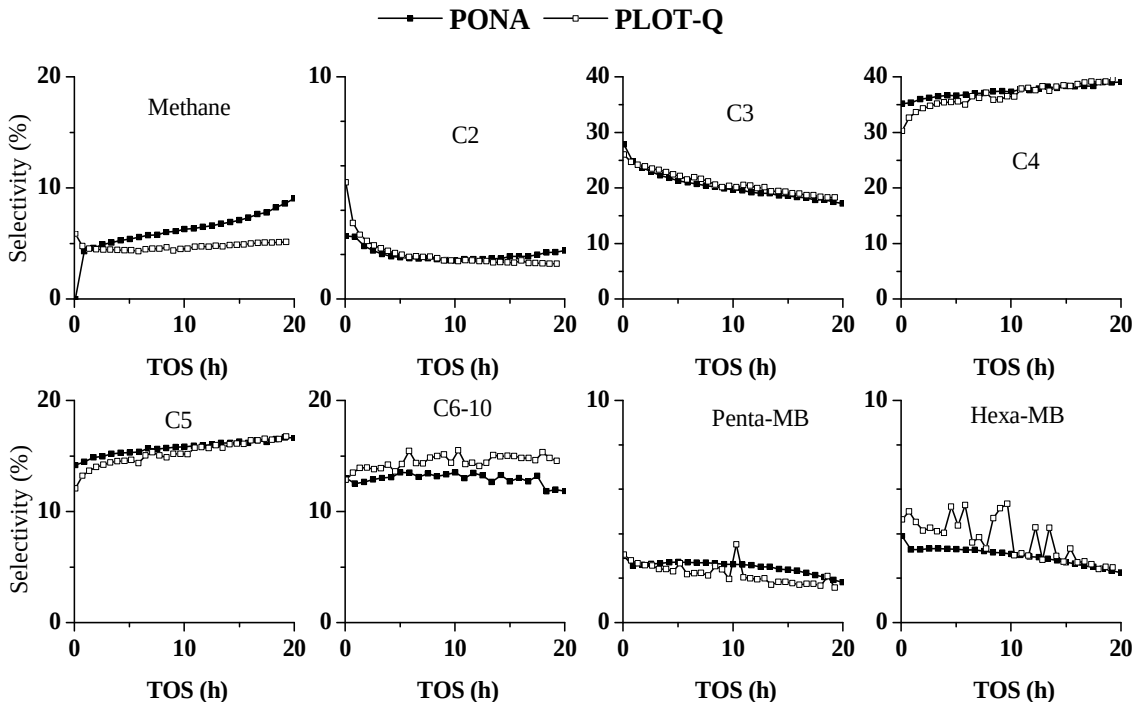

Fig. G.2: Selectivities of the same experiments as shown in figure G.1. Note the differences in Y-axis scale.

H. Use of quartz dilution

During many of the catalytic tests performed in this work, the catalyst was diluted with 1:5 parts quartz. The reason for using quartz was to have a larger catalyst bed (as per the recommendations of Dautzenberg[160], but it was found that analysis of spent catalyst was made difficult by its presence. However, in hindsight it appears that the quartz did not have much influence on the results of testing, as shown by the two experiments in figure H.1. Both tests are of sample P/L at 450 °C and WHSV 0.93 h^{-1}, but one is performed without quartz dilution. No significant differences in the selectivities were found either.

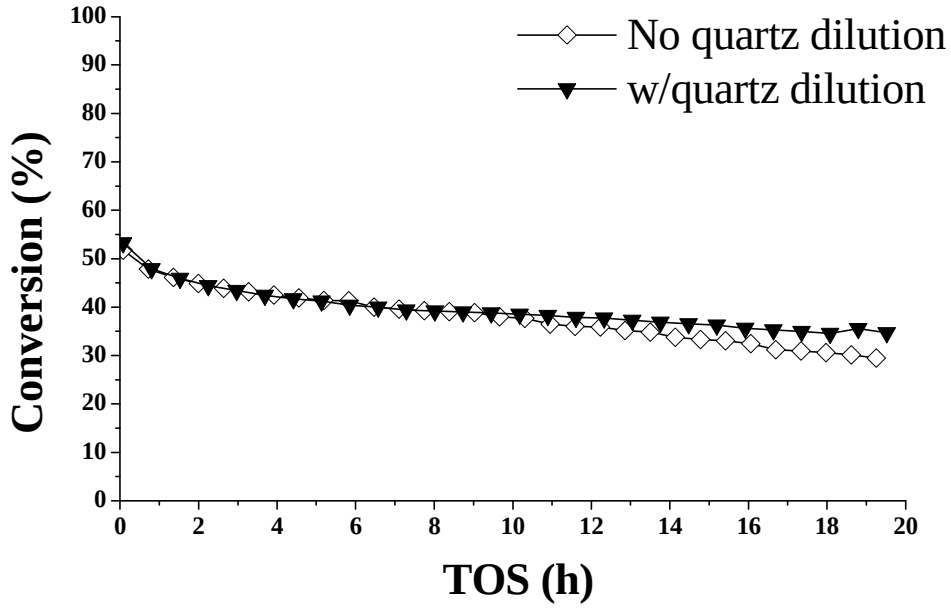

Fig. H.1: Conversion vs TOS for PONA and PLOT-Q system

I. Some characteristics of the catalytic testing setup

Temperature gradients in the reactor oven

In order to ensure that the catalyst bed was placed at a position in the oven where temperature was stable during catalytic tests, measurements of the temperature gradients in the oven that would be used were performed. Figure I.1 displays the temperature of the oven when set to 368 °C (insulated as would be done for a catalytic test) as a function of the distance from the bottom of the oven. As the highest and most stable temperature was found between 5 and 6 cm from the bottom, a reactor was constructed where the catalyst bed would always be placed at this height.

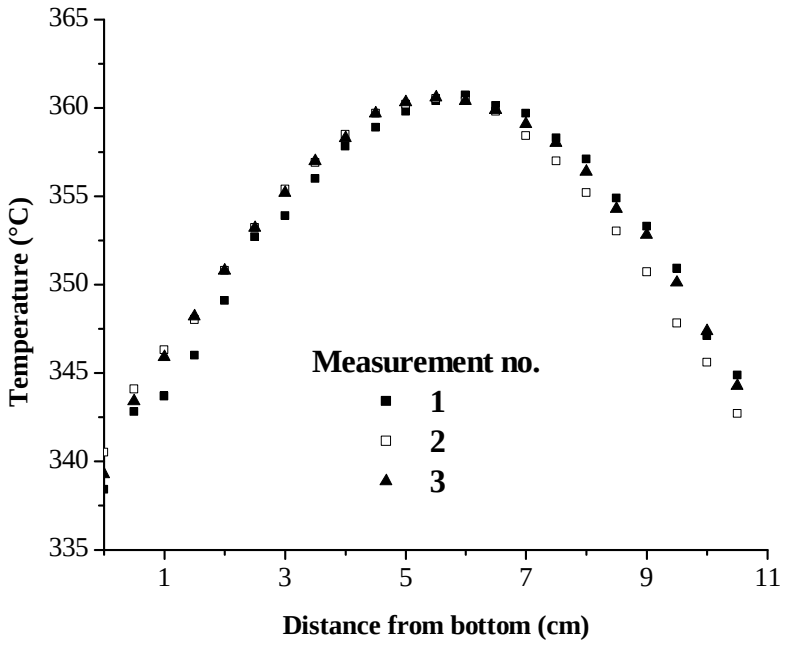

Fig. I.1: Temperature as a function of the height from the bottom in the oven used to heat the catalyst bed during catalytic experiments.

Latency and mixing of feed

After the rig was rebuilt to match the scheme shown in figure 14.1, a measurement of the time required for a fresh reactant to reach the catalyst was performed by switching from a pure oxygen feed to a pure helium feed. The flow rate of the helium was 15 ml/min. MS signals of both gases are shown in figure I.2 as a function of the relative time after switch, both on linear and logarithmic scales. It was found that close to one minute passed before the helium signal started to increase. While the long tube from the reactor to the MS probably increased the time before detection it was also found that during switching trials hardly any ^{13}C hydrocarbons was found in the effluent after 30 seconds.

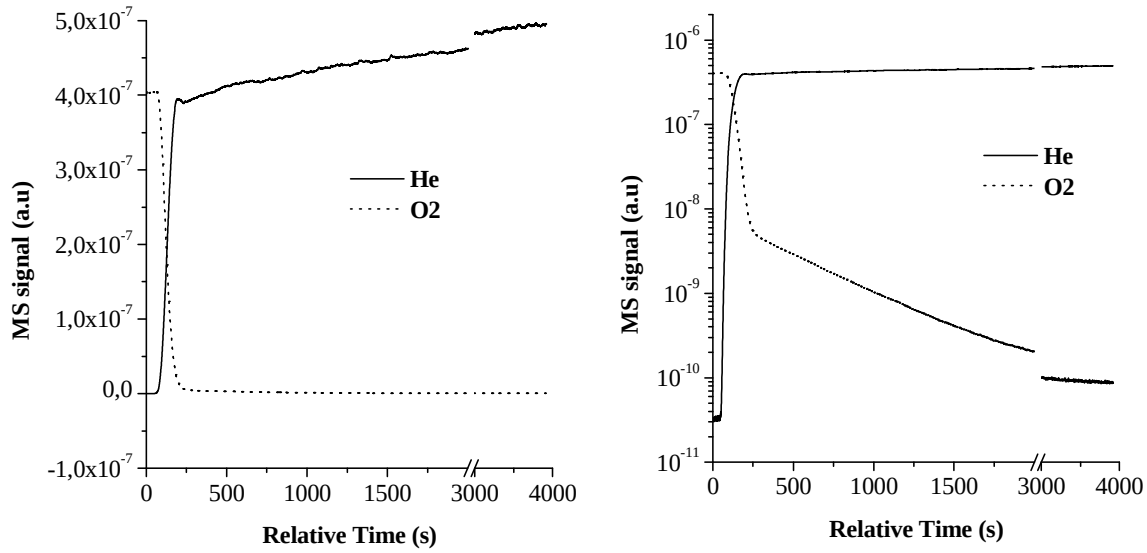

Fig. I.2: Signal by MS of He and O_2 from the outlet of the catalytic reactor after a switch from the latter gas to the former.

In addition to the delay before fresh feed contacts the catalyst, it was also found that a significant amount of time passed before the atmosphere in the reactor achieved equilibrium. From the first detection of helium entering the system, a period of ~2 minutes followed where oxygen and helium was mixed, and even after this nearly an hour passes before complete the oxygen is completely removed from the reactor. While the partial pressure of oxygen can be assumed negligible after a few minutes, the reactor hardly qualifies as a plug-flow reactor.

J. Conversion and selectivity data from co-feeding

Tables J.1, J.2 and J.3 display the conversion and selectivity of the co-reaction between benzene and methanol discussed in chapter 15.4.2. The three tables show the results at all temperatures after 5, 45 and 85 minutes on stream, respectively.

Table J.1: Effluent composition after co-feeding methanol and benzene for 5min.

T (°C)	Conv. (%)	Aliphatics						Aromatics	
		C1	C2	C3	C4	C5	C6+	Toluene	Other
230	0,12	0,75	0,00	2,42	6,38	2,46	0,00	72,58	15,40
250	0,22	0,33	0,49	2,40	7,67	2,76	0,00	75,75	10,60
270	0,47	0,12	0,46	1,88	9,32	3,50	0,00	77,48	7,25
285	0,80	0,15	0,97	2,85	16,57	5,92	0,00	64,38	9,16
300	1,35	0,22	0,95	2,79	12,25	4,08	0,00	66,57	13,13
315	2,56	0,10	1,92	4,66	12,61	4,81	0,50	48,50	26,90
330	4,09	0,10	2,44	5,49	13,09	4,75	0,51	43,86	29,77
350	5,02	0,20	2,63	6,18	15,34	5,78	1,45	47,26	21,17

Table J.2: Effluent composition after co-feeding methanol and benzene for ~ 45min.

T (°C)	Conv. (%)	Aliphatics						Aromatics	
		C1	C2	C3	C4	C5	C6+	Toluene	Other
230	0,30	1,10	0,79	2,16	36,51	14,00	0,00	23,40	22,05
250	0,33	0,00	0,50	1,63	29,22	10,98	0,00	39,04	18,64
270	0,54	0,17	0,51	1,93	26,11	10,49	0,00	51,22	9,56
285	0,83	0,19	0,72	2,31	18,35	6,97	0,00	54,04	17,42
300	1,06	0,19	1,04	2,77	15,10	5,59	0,00	65,79	9,50
315	1,96	0,13	1,23	2,91	12,44	4,56	0,43	57,96	20,34
330	3,23	0,17	1,49	3,74	13,35	4,62	0,52	53,87	22,24
350	4,04	0,20	1,83	4,61	15,08	5,44	0,86	52,51	19,46

Table J.3: Effluent composition after co-feeding methanol and benzene for ~ 80min.

T (°C)	Conv. (%)	Aliphatics						Aromatics	
		C1	C2	C3	C4	C5	C6+	Toluene	Other
230	0,36	0,85	0,52	1,79	37,22	15,50	0,00	13,40	30,73
250	0,33	0,27	0,38	1,33	32,11	12,63	0,00	36,46	16,82
270	0,46	0,18	0,46	2,00	22,38	8,98	0,00	59,38	6,61
285	0,72	0,21	0,85	2,18	18,81	7,01	0,00	61,62	9,32
300	0,99	0,20	0,88	2,40	14,82	5,41	0,00	69,07	7,22
315	1,87	0,15	0,89	2,47	11,87	4,24	0,25	61,22	18,91
330	3,02	0,23	1,24	3,31	12,53	4,51	0,50	56,94	20,73
350	3,70	0,20	1,60	4,09	15,19	5,31	0,56	54,21	18,83

K. List of chemicals used

Chemical	Manufacturer	Purity
Catapal B	SASOL / Vista	-
Ludox® AS-40	Sigma-Aldrich	-
Cab-O-Sil M5	Riedel-de Haën	-
Orthophosphoric acid	Merck	85 %
Tri-n-propylamine	Fluka	>98 %
Triethylamine	Fluka	>99.5 %
Cyclohexylamine	Fluka Analytical	>99 %
Al-iPr	Fluka	>98 %
Methanol	VWR / Prolabo	99.8%
Benzene	Riedel-de Haën	> 99.5 %
13C methanol	Cambridge Isotope Laboratories	>99 %
HF	Merck	40 % in H_2O
CH2Cl2	VWR / Prolabo	99.8 %
Hexamethylbenzene	Aldrich	99 %
Durene (1,2,4,5-TMB)	Fluka	Purum
CO gas (3.7)	AGA	99.97 %
He gas (5.0)	AGA	99.999 %
H_2 gas (4.5)	AGA	99.995 %
N_2 gas	AGA	-
O_2 gas	AGA	-

References

[1] S. Kvisle, T. Fuglerud, S. Kolboe, U. Olsbye, K.-P. Lillerud, B. V. Vora, in *Handbook of Heterogeneous Catalysis* (Eds.: G. Ertl, H. Knözinger, F. Schüth, J. Weitkamp), Wiley-VCH, **2008**, pp. 2950-2965.

[2] G. A. Olah, *Angewandte Chemie - International Edition* 44, **2005**, 2636.

[3] I. Chorkendorff, J. W. Niemantsverdriet, *Concepts of modern catalysis and kinetics*, 2nd edition, Wiley-VCH, **2007**

[4] A. Dyer, *An Introduction to Zeolite Molecular Sieves*, 1st edition, John Wiley & sons, **1988**

[5] E. M. Flanigen, in *Introduction to Zeolite Science and Practice*, 2nd ed. (Eds.: H. van Bekkum, E. M. Flanigen, P. A. Jacobs, J. C. Jansen), Elsevier, **2001**, pp. 11-36.

[6] IZA Commission of Natural zeolites, http://www.iza-online.org/natural/default.htm (Accessed: 13.08.09)

[7] S. T. Wilson, in *Introduction to Zeolite Science and Practice*, 2nd ed. (Eds.: H. v. Bekkum, E. M. Flanigen, P. A. Jacobs, J. C. Jansen), Elsevier, **2001**, pp. 229-260.

[8] C. Baerlocher, L. B. McCusker, Database of Zeolite Structures, http://www.iza-structure.org/databases/ (Accessed: 06.05.10)

[9] D. S. Coombs, A. Alberti, T. Armbruster, G. Artioli, C. Colella, E. Galli, J. D. Grice, F. Liebau, J. A. Mandarino, H. Minato, E. H. Nickel, E. Passaglia, D. R. Peacor, S. Quartieri, R. Rinaldi, M. Ross, R. A. Sheppard, E. Tillmans, G. Vezzalini, *European Journal of Mineralogy* 10, **1998**, 1037.

[10] C. Baerlocher, W. M. Meier, D. H. Olson, *Atlas of Zeolite Framework Types*, 5th edition, Elsevier, **2001**

[11] British Zeolite Association (BZA), www.bza.org (Accessed: 30.12.09)

[12] L. B. McCusker, C. Baerlocher, in *Introduction to Zeolite Science and Practice* (Eds.: H. van Bekkum, E. M. Flanigen, P. A. Jacobs, J. C. Jansen), Elsevier, **2001**, pp. 37-67.

[13] IUPAC, IUPAC Gold Book, http://goldbook.iupac.org/ (Accessed: 07.02.10)

[14] W. Löwenstein, *American Mineralogist* 39, **1954**, 92.

[15] R. Szostak, *Molecular Sieves - Principles of Synthesis and Identification*, Van Nostrand Reinhold, **1989**, pp. 205-281.

[16] S. T. Wilson, B. M. Lok, C. A. Messina, T. R. Cannan, E. M. Flanigen, *Journal of the American Chemical Society* 104, **1982**, 1146.

[17] L.-T. Yuen, S. I. Zones, T. V. Harris, E. J. Gallegos, A. Auroux, *Microporous Materials* 2, **1994**, 105.

[18] G. F. Froment, W. J. H. Dehertog, A. J. Marchi, *Catalysis* 9, **1992**, 1.

[19] B. M. Lok, C. A. Messina, R. L. Patton, R. T. Gajek, T. R. Cannan, E. M. Flanigen, *U.S. patent 4,440,871*, **1984.**

[20] B. M. Lok, C. A. Messina, R. L. Patton, R. T. Gajek, T. R. Cannan, E. M. Flanigen, *Journal of the American Chemical Society* 106, **1984**, 6092.

[21] E. M. Flanigen, B. M. Lok, R. L. Patton, S. T. Wilson, *Pure and Applied Chemistry* 58, **1986**, 1351.

[22] M. Kustova, M. S. Holm, C. H. Christensen, Y.-H. Pan, P. Beato, T. V. W. Janssens, F. Joensen, J. Nerlov, *Studies in Surface Science and Catalysis* 174 A, **2008**, 117.

[23] J. F. Haw, *Physical Chemistry Chemical Physics* 4, **2002**, 5431.

[24] J. Weitkamp, M. Hunger, in *Introduction to Zeolite Science and Practice*, 3rd revised edition ed. (Eds.: J. Cejka, H. Van Bekkum, A. Corma, F. Schüth), Elsevier, **2007**, pp. 787-835.

[25] D. Barthomeuf, in *Acidity and Basicity of Solids* (Eds.: J. Fraissard, L. Petrakis), Kluwer Academic Publishers, **1994**, pp. 375-390.

[26] U. Schubert, N. Hüsing, *Synthesis of Inorganic Materials*, 2nd edition, Wiley-VCH, **2005**

[27] J. C. Jansen, in *Introduction to Zeolite Science and Practice*, 2nd ed. (Eds.: H. v. Bekkum, E. M. Flanigen, P. A. Jacobs, J. C. Jansen), Elsevier, **2001**, pp. 175-227.

[28] S. T. Wilson, in *Verified Syntheses of Zeolitic Materials*, 2nd revised ed. (Ed.: H. Robson), Elsevier, **2001**, pp. 27-31.

[29] H. Robson (Editor), *Verified Syntheses of Zeolitic Materials*, 2nd edition, Elsevier, **2001**

[30] C. S. Cundy, P. A. Cox, *Microporous and Mesoporous Materials* 82, **2005**, 1.

[31] J. A. Moulijn, M. Makkee, A. Van Diepen, *Chemical Process Technology*, John Wiley & Sons, Ltd, **2001**

[32] J. A. Martens, P. A. Jacobs, in *Introduction to zeolite science and practice* (Eds.: H. van Bekkum, E. M. Flanigen, P. A. Jacobs, J. C. Jansen), Elsevier, **2001**, pp. 633-667.

[33] M. Stöcker, *Microporous and mesoporous materials* 29, **1999**, 3.

[34] C. D. Chang, A. J. Silvestri, *Journal of Catalysis* 47, **1977**, 249.

[35] J. F. Haw, W. Song, D. M. Marcus, J. B. Nicholas, *Accounts of chemical research* 36, **2003**, 317.

[36] Lurgi press release 28.11.06, http://www.lurgi.com/website/SingleNews.125.0.html?&L=1&cHash=1364154788&tx_ttnews[backPid]=110&tx_ttnews[pS]=1261117241&tx_ttnews[pointer]=2&tx_ttnews[tt_news]=75 (Accessed: 07.05.10)

[37] UOP LLC press release 30.01.08, http://www.uop.com/pr/releases/eurochem%20mto%20release%20final.pdf (Accessed: 07.05.10)

[38] UOP LLC press release 07.12.05, http://www.uop.com/pr/releases/Total%20MTO.pdf (Accessed: 07.05.10)

[39] ExxonMobil presentation, World CTL conference 2008, France, http://www.exxonmobil.com/apps/refiningtechnologies/pdf/Coal_to_Liquids_CTL.pdf (Accessed: 07.05.10)

[40] Haldor Topsøe AS press release 08.12.09, http://www.topsoe.com/news/News/2009/081209.aspx (Accessed: 25.01.10)

[41] R. M. Dessau, *Journal of Catalysis* 99, **1986**, 111.

[42] R. M. Dessau, R. B. LaPierre, *Journal of Catalysis* 78, **1982**, 136.

[43] T. Mole, J. A. Whiteside, D. Seddon, *Journal of Catalysis* 82, **1983**, 261.

[44] B. E. Langner, *Applied Catalysis A: General* 2, **1982**, 289.

[45] I. M. Dahl, S. Kolboe, *Catalysis Letters* 20, **1993**, 329

[46] I. M. Dahl, S. Kolboe, *Journal of Catalysis* 149, **1994**, 458.

[47] I. M. Dahl, S. Kolboe, *Journal of Catalysis* 161, **1996**, 304.

[48] M. Hunger, M. Seiler, A. Buchholz, *Catalysis Letters* 74, **2001**, 61.

[49] W. Song, D. M. Marcus, H. Fu, J. O. Ehresmann, J. F. Haw, *Journal of the American Chemical Society* 124, **2002**, 3844.

[50] D. Lesthaeghe, V. Van Speybroeck, G. B. Marin, M. Waroquier, *Angewandte Chemie - International Edition* 45, **2006**, 1714.

[51] Ø. Mikkelsen, P. O. Rønning, S. Kolboe, *Microporous and Mesoporous Materials* 40, **2000**, 95.

[52] B. Arstad, S. Kolboe, *Journal of the American Chemical Society* 123, **2001**, 8137.

[53] B. Arstad, S. Kolboe, *Catalysis Letters* 71, **2001**, 209.

[54] W. Song, J. F. Haw, J. B. Nicholas, C. S. Heneghan, *Journal of the American Chemical Society* 122, **2000**, 10726.

[55] T. Mole, G. Bett, D. Seddon, *Journal of Catalysis* 84, **1983**, 435.

[56] A. Sassi, M. A. Wildman, H. J. Ahn, P. Prasad, J. B. Nicholas, J. F. Haw, *Journal of physical Chemistry B* 106, **2002**, 2294.

[57] W. Song, H. Fu, J. F. Haw, *Journal of physical Chemistry B* 105, **2001**, 12839.

[58] M. Bjørgen, U. Olsbye, S. Kolboe, *Journal of Catalysis* 215, **2003**, 30.

[59] J. F. Haw, J. B. Nicholas, W. Song, F. Deng, Z. Wang, T. Xu, C. S. Henegan, *Journal of the American Chemical Society* 122, **2000**, 4763.

[60] P. W. Goguen, T. Xu, D. H. Barich, T. W. Skloss, W. Song, Z. Wang, J. B. Nicholas, J. F. Haw, *Journal of the American Chemical Society* 120, **1998**, 2650.

[61] S. Svelle, U. Olsbye, F. Joensen, M. Bjørgen, *The Journal of physical Chemistry C - Letters* 111, **2007**, 17981.

[62] R. F. Sullivan, C. J. Egan, G. E. Langlois, R. P. Sieg, *Journal of the American Chemical Society* 83, **1961**, 1156.

[63] W. v. E. Doering, M. Saunders, H. G. Boyton, H. W. Earhart, E. F. Wadley, W. R. Edwards, *Tetrahedron* 4, **1958**, 178.

[64] M. Bjørgen, U. Olsbye, D. Petersen, S. Kolboe, *Journal of Catalysis* 221, **2004**, 1.

[65] W. Song, J. B. Nicholas, A. Sassi, J. F. Haw, *Catalysis Letters* 81, **2002**, 49.

[66] B. Arstad, J. B. Nicholas, J. F. Haw, *Journal of the American Chemical Society* 126, **2004**, 2991.

[67] D. M. McCann, D. Lesthaeghe, P. W. Kletnieks, D. R. Guenther, M. J. Hayman, V. Van Speybroeck, M. Waroquier, J. F. Haw, *Angewandte Chemie - International Edition* 47, **2008**, 5179.

[68] M. Bjørgen, F. Bonino, B. Arstad, S. Kolboe, K.-P. Lillerud, A. Zecchina, S. Bordiga, *ChemPhysChem* 6, **2005**, 232.

[69] M. Bjørgen, F. Bonino, S. Kolboe, K.-P. Lillerud, A. Zecchina, S. Bordiga, *Journal of the American Chemical Society* 125, **2003**, 15863.

[70] F. Bleken, M. Bjørgen, L. Palumbo, S. Bordiga, S. Svelle, K.-P. Lillerud, U. Olsbye, *Topics in Catalysis* 52, **2009**, 218.

[71] S. Svelle, P. O. Rønning, S. Kolboe, *Journal of Catalysis* 224, **2004**, 115.

[72] S. Svelle, P. O. Rønning, U. Olsbye, S. Kolboe, *Journal of Catalysis* 234, **2005**, 385.

[73] S. Svelle, F. Joensen, J. Nerlov, U. Olsbye, K.-P. Lillerud, S. Kolboe, M. Bjørgen, *journal of the American Chemical Society* 128, **2006**, 14770.

[74] M. Bjørgen, S. Svelle, F. Joensen, J. Nerlov, S. Kolboe, F. Bonino, L. Palumbo, S. Bordiga, U. Olsbye, *Journal of Catalysis* 249, **2007**, 195.

[75] M. Bjørgen, K.-P. Lillerud, U. Olsbye, S. Svelle, *Studies in Surface Science and Catalysis* 167, **2007**, 463.

[76] M. Bjørgen, F. Joensen, K.-P. Lillerud, U. Olsbye, S. Svelle, *Catalysis Today* 142, **2009**, 90.

[77] S. Teketel, M. Sc. thesis, University of Oslo, **2009**.

[78] S. Teketel, S. Svelle, K.-P. Lillerud, U. Olsbye, *ChemCatChem* 1, **2009**, 78.

[79] S. Teketel, S. Svelle, K.-P. Lillerud, P. Beato, U. Olsbye, *Manuscript in preparation* **2010**.

[80] M. Guisnet, P. Magnoux, *Applied Catalysis A: General* 212, **2001**, 83.

[81] T. V. W. Janssens, *Journal of Catalysis* 264, **2009**, 130.

[82] H. S. Cerqueira, G. Caeiro, L. Costa, F. Ramôa Ribeiro, *Journal of Molecular Catalysis A - Chemical* 292, **2008**, 1.

[83] B. P. C. Hereijgers, F. Bleken, M. H. Nilsen, S. Svelle, K.-P. Lillerud, M. Bjørgen, B. M. Weckhuysen, U. Olsbye, *Journal of Catalysis* 264, **2009**, 77.

[84] D. Mores, E. Stavitski, M. H. F. Kox, J. Kornatowski, U. Olsbye, B. M. Weckhuysen, *Chemistry - A European Journal* 14, **2008**, 11320.

[85] J. M. Bennet, J. P. Cohen, E. M. Flanigen, J. J. Pluth, J. V. Smith, *ACS Symposium Series* 218, **1983**, 109.

[86] R. A. Van Nordstrand, D. S. Santilli, S. I. Zones, *ACS Symposium Series* 368, **1988**, 236.

[87] J. Caro, F. Marlow, K. Hoffman, C. Striebel, J. Kornatowski, I. Girnius, M. Noack, P. Kolsch, *Studies in Surface Science and Catalysis* 105, **1997**, 2171.

[88] D. Wang, Z. K. Tang, G. D. Li, J. S. Chen, *Nature* 408, **2000**, 50.

[89] J. A. Rabo, R. J. Pellet, P. K. Coughlin, E. S. Shamshoum, *Studies in Surface Science and Catalysis* 46, **1989**, 1.

[90] S. Bordiga, L. Regli, D. Cocina, C. Lamberti, M. Bjørgen, K.-P. Lillerud, *Journal of Physical Chemistry B* 109, **2005**, 2779.

[91] Z.-M. Cui, Q. Liu, W. Song, L.-J. Wan, *Angewandte Chemie - International Edition* 45, **2006**, 6512.

[92] J. Chen, P. A. Wright, S. Natarajan, J. M. Thomas, *Studies in Surface Science and Catalysis* 84, **1994**, 1731.

[93] H. Weyda, H. Lechert, *Zeolites* 10, **1990**, 251.

[94] J. M. Campelo, F. Lafont, J. M. Marinas, M. Ojeda, *Applied Catalysis A: General* 192, **2000**, 85.

[95] D. Young, in *Verified Syntheses of Zeolitic Materials*, 2nd revised ed. (Ed.: H. Robson), Elsevier, **2001**, pp. 93-94.

[96] D. Demuth, G. D. Stucky, K. K. Unger, F. Schüth, *Microporous Materials* 3, **1995**, 473.

[97] X. Qinhua, Y. Aizhen, B. Shulin, X. Kaijun, *Proceedings of the 7th International Zeolite Conference* **1986**, 835.

[98] L. Wang, C. Guo, S. Yan, X. Huang, Q. Li, *Microporous and Mesoporous Materials* 64, **2003**, 63.

[99] D. Tian, W. Yan, X. Cao, J. Yu, R. Xu, *Chemistry of Materials* 20, **2008**, 2160.

[100] S. H. Jhung, J.-S. Chang, Y. K. Hwang, S.-E. Park, *Journal of Materials Chemistry* 14, **2004**, 280.

[101] S. H. Jhung, Y. K. Hwang, J.-S. Chang, S.-E. Park, *Microporous and Mesoporous Materials* 67, **2004**, 151.

[102] S. H. Jhung, J.-S. Chang, J. S. Hwang, S.-E. Park, *Microporous and Mesoporous Materials* 64, **2003**, 33.

[103] S. H. Jhung, J.-S. Chang, D. S. Kim, S.-E. Park, *Microporous and Mesoporous Materials* 71, **2004**, 135.

[104] J. W. Yoon, S. H. Jhung, Y. H. Kim, S.-E. Park, J.-S. Chang, *Bulletin of the Korean Chemical Society* 26, **2005**, 558.

[105] Y. Xu, P. J. Maddox, J. W. Couves, *Journal of the Chemical Society - Faraday Transactions* 86, **1990**, 425.

[106] U. Lohse, R. Bertram, K. Jancke, I. Kurzawski, B. Parlitz, E. Loffler, E. Schreier, *Journal of the Chemical Society - Faraday Transactions* 91, **1995**, 1163.

[107] P. Concepción, J. M. Lopez Nieto, A. Mifsud, J. Perez-Pariente, *Zeolites* 16, **1996**, 56.

[108] Ø. B. Vistad, D. E. Akporiaye, K. P. Lillerud, *Journal of Physical Chemistry B* 105, **2001**, 10437.

[109] S. M. Yang, S. I. Wang, C. S. Huang, *Studies in Surface Science and Catalysis* 61, **1991**, 429.

[110] J. W. Niemantsverdriet, *Spectroscopy in Catalysis - An Introduction*, 3rd completely revised and enlarged edition, Wiley-VCH, **2007**

[111] D. Brandon, W. D. Kaplan, *Microstructural Characterization of Materials*, John Wiley & Sons, **1999**

[112] S. Jørgensen, *Lecture notes for SEM module* **2007**.

[113] P. Norby, *Current Opinion in Colloid & Interface Science* 11, **2006**, 118.

[114] F. Di Renzo, *Catalysis Today* 41, **1998**, 37.

[115] M. Ganschow, G. Schulz-Ekloff, M. Wark, M. Wendschuh-Josties, D. Wöhrle, *Journal of Materials Chemistry* 11, **2001**, 1823.

[116] S. Seelan, A. K. Sinha, *Journal of Molecular Catalysis A - Chemical* 215, **2004**, 149.

[117] M. M. J. Treacy, J. B. Higgins, *Collection of Simulated XRD Powder Patterns for Zeolites*, Elsevier, **2001**

[118] K. Jansen, in *Verified Syntheses of Zeolitic Materials*, 2nd ed. (Ed.: H. Robson), Elsevier, **2001**, pp. 39-42.

[119] E. A. Eilertsen, M. Sc. thesis, University of Oslo, **2008**.

[120] G. Finger, J. Richter-Mendau, M. Bülow, J. Kornatowski, *Zeolites* 11, **1991**, 443.

[121] M. Choi, K. Na, J. Kim, Y. Sakamoto, O. Terasaki, R. Ryoo, *Nature* 461, **2009**, 246.

[122] S. Braunaer, P. H. Emmet, E. Teller, *Journal of the American Chemical Society* 60, **1938**, 309.

[123] A. Jentys, J. A. Lercher, in *Introduction to Zeolite Science and Practice* (Eds.: H. Van Bekkum, E. M. Flanigen, P. A. Jacobs, J. C. Jansen), Elsevier, **2001**, pp. 345-386.

[124] K. S. W. Sing, D. H. Everett, R. A. W. Haul, L. Moscou, R. A. Pierotti, J. Roquerol, T. Siemeniewska, *Pure and Applied Chemistry* 57, **1985**, 603.

[125] C. Y. Chen, S. I. Zones, *Microporous and Mesoporous Materials* 104, **2007**, 39.

[126] Y. Traa, S. Sealy, J. Weitkamp, in *Molecular Sieves, Vol. 5*, Springer - Verlag, **2007**, pp. 103-154.

[127] C. Y. Chen, S. I. Zones, A. W. Burton, S. A. Elomari, S. Svelle, *Studies in Surface Science and Catalysis* 172, **2007**, 329.

[128] D. L. Pavia, G. M. Lampman, G. S. Kriz, *Introduction to spectroscopy*, Third edition, Brooks/Cole - Thomson Learning, **2001**, pp. 13-101.

[129] H. Günzler, H.-U. Gremlich, *IR spectroscopy - an introduction*, Wiley - VCH, **2002**

[130] A. Zecchina, G. Spoto, S. Bordiga, *Physical Chemistry Chemical Physics* 7, **2005**, 1627.

[131] A. Zecchina, G. Spoto, S. Bordiga, in *Handbook of Vibrational Spectroscopy, Vol. 4* (Eds.: J. Chalmers, P. Griffiths), John Wiley & Sons, **2001**, pp. 1-30.

[132] ChemSpider, http://www.chemspider.com (Accessed: 24.03.10)

[133] TA Instruments - TGA Evaluation of Zeolite Catalysts, www.tainstruments.com/library_download.aspx?file=TA231.PDF (Accessed: 24.03.10)

[134] T. Düren, F. Millange, G. Férey, K. S. Walton, R. Q. Snurr, *Journal of Physical Chemistry C* 111, **2007**, 15350.

[135] Y. Kubota, H. Maekawa, S. Miyata, T. Tatsumi, Y. Sugi, *Microporous and Mesoporous Materials* 101, **2007**, 115.

[136] P. Brandão, A. Philippou, N. Hanif, P. Ribeiro-Claro, A. Ferreira, M. W. Anderson, J. Rocha, *Chemistry of Materials* 14, **2002**, 1053.

[137] V. R. Choudhary, S. D. Sansare, *Journal of Thermal analysis* 32, **1987**, 777.

[138] S.-I. Lee, H. Chon, *Journal of the Chemical Society - Faraday Transactions* 93, **1997**, 1855.

[139] N. J. Tapp, N. B. Milestone, L. J. Wright, *Journal of the Chemical Society, Chemical Communications* **1985**, 1801.

[140] C. Halik, J. A. Lercher, H. Mayer, *Journal of the Chemical Society - Faraday Transactions* 84, **1988**, 4457.

[141] O. V. Saure, M. Sc. thesis, University of Oslo, **2009**.

[142] M. Bjørgen, cand. scient. thesis, University of Oslo, **2000**.

[143] A. Ojo, J. Dwyer, J. Dewing, P. J. O'Malley, A. Nabhan, *Journal of the Chemical Society - Faraday Transactions* 88, **1992**, 105.

[144] B. Zibrowius, E. Löffler, M. Hunger, *Zeolites* 12, **1992**, 167.

[145] L. M. Kustov, S. A. Zubkov, V. B. Kazansky, L. A. Bondar, *Studies in Surface Science and Catalysis* 69, **1991**, 303.

[146] L. Kubelková, S. Beran, J. A. Lercher, *Zeolites* 9, **1989**, 539.

[147] S. G. Hedge, P. Ratnasamy, L. M. Kustov, V. B. Kazansky, *Zeolites* 8, **1988**, 137.

[148] M. Bjørgen, *Personal Communication* **2010**.

[149] D. W. Breck, *Zeolite molecular sieves*, reprint w/corrections & revisions, Robert E. Krieger Publishing Company, **1984**

[150] F. Schüth, D. Demuth, B. Zibrowius, J. Kornatowski, G. Finger, *Journal of the American Chemical Society* 116, **1994**, 1090.

[151] F. Bleken, M. Sc. thesis, University of Oslo, **2007**.

[152] NIST Chemistry WebBook, http://webbook.nist.gov/chemistry/ (Accessed: 02.05.10)

[153] D. A. McCaulay, A. P. Lien, *Journal of the American Chemical Society* 73, **1951**, 2013.

[154] D. Barthomeuf, A. de Mallmann, I*ndustrial & Engineering Chemistry Research* 29, **1990**, 1435.

[155] J. A. Lercher, A. Jentys, in *Introduction to Zeolite Science and Practice* (Eds.: J. Cejka, H. van Bekkum, A. Corma, F. Schüth), Elsevier, **2007**, pp. 435-476.

[156] M. J. Franco, A. Mifsud, J. Perez-Pariente, *Zeolites* 15, **1995**, 117.

[157] L. M. Harwood, C. J. Moody, J. M. Percy, *Experimental Organic Chemistry*, second edition, Blackwell Science Ltd., **1999**

[158] D. C. Harris, *Quantitative Chemical Analysis*, 7th edition, W. H. Freeman and Company, **2007**, pp. 528-553.

[159] P. O. Rønning, Dr. Scient thesis, University of Oslo, **1998**.

[160] F. M. Dautzenberg, *ACS Symposium Series* 411, **1989**, 99.

[161] M. Bjørgen, S. Kolboe, *Applied Catalysis A: General* 225, **2002**, 285.

[162] M. Bjørgen, F. Joensen, M. S. Holm, U. Olsbye, K.-P. Lillerud, S. Svelle, *Applied Catalysis A: General* 345, **2008**, 43.

[163] D. Chen, T. Moljord, T. Fuglerud, A. Holmen, *Microporous and Mesoporous Materials* 29, **1999**, 191.

[164] D. R. Stull, E. F. Westrum, G. C. Sinke, *The Chemical Thermodynamics of Organic Compounds*, John Wiley & Sons, **1969**

[165] Ø. Mikkelsen, Dr. Scient thesis, University of Oslo, **1998**.

[166] F. Salehirad, M. W. Anderson, *Journal of the Chemical Society - Faraday Transactions* 94, **1998**, 1911.

[167] N. Hazari, J. A. Labinger, V. J. Scott, *Journal of Catalysis* 263, **2009**, 266.

[168] J. E. Bercaw, P. L. Diaconescu, R. H. Grubbs, R. D. Kay, S. Kitching, J. A. Labinger, X. Li, P. Mehrkhodavandi, G. E. Morris, G. J. Sunley, P. Vagner, *Journal of Organic Chemistry* 71, **2006**, 8907.

[169] J. E. Bercaw, P. L. Diaconescu, R. H. Grubbs, N. Hazari, R. D. Kay, J. A. Labinger, P. Mehrkhodavandi, G. E. Morris, G. J. Sunley, P. Vagner, *Inorganic Chemistry* 46, **2007**, 11371.

[170] J. E. Bercaw, N. Hazari, J. A. Labinger, V. J. Scott, G. J. Sunley, *Journal of the American Chemical Society* 130, **2008**, 11988.

[171] S. Svelle, B. Arstad, S. Kolboe, O. Swang, *Journal of Physical Chemistry B* 107, **2003**, 9281.

[172] S. Svelle, U. Olsbye, K.-P. Lillerud, S. Kolboe, M. Bjørgen, *Journal of the American Chemical Society* 128, **2006**, 5618.

[173] B. Arstad, S. Kolboe, O. Swang, *Journal of Physical Chemistry B* 106, **2002**, 12722.

[174] M. Visur, M. Sc. thesis, University of Oslo, **2010**.

[175] B. Arstad, S. Kolboe, O. Swang, *Journal of Physical Chemistry A* 109, **2005**, 8914.

[176] J. H. Ahn, B. Temel, E. Iglesia, *Angewandte Chemie - International Edition* 48, **2009**, 3814.

[177] D. Lesthaeghe, B. De Sterck, V. Van Speybroeck, G. B. Marin, M. Waroquier, *Angewandte Chemie - International Edition* 46, **2007**, 1311.